Boundary Conditions for Vapor-Solid Interfaces

In the Context of Vapor Phase Crystal Growth by Physical Methods.

by

J.P. Caputa
B.Eng., University of Victoria (2005)

A Thesis Submitted in Partial Fulfillment of the
Requirements for the Degree of

Master of Applied Science

in the Department of Mechanical Engineering

Boundary Conditions for Vapor-Solid Interfaces

In the Context of Vapor Phase Crystal Growth by Physical Methods.

by

J.P. Caputa
B.Eng., University of Victoria (2005)

Supervisory Committee

Dr. Henning Struchtrup, Co-supervisor
(Department of Mechanical Engineering)

Dr. Sadik Dost, Co-supervisor
(Department of Mechanical Engineering)

Dr. Rustom Bhiladvala, Department Member
(Department of Mechanical Engineering)

Supervisory Committee

Dr. Henning Struchtrup, Co-supervisor
(Department of Mechanical Engineering)

Dr. Sadik Dost, Co-supervisor
(Department of Mechanical Engineering)

Dr. Rustom Bhiladvala, Department Member
(Department of Mechanical Engineering)

Abstract:

Non-equilibrium boundary conditions based upon kinetic theory and linear irreversible thermodynamics are applied to the interface kinetics in vapor crystal growth of unitary and binary materials. These are compared to equilibrium boundary conditions in a simple, 1D closed ampoule physical vapor transport model. It is found that in cases where the diffusive impedance is negligible and when system pressure is low, surface kinetics play an important role in limiting the mass transport. In cases where diffusion is the dominant transport impedance, and/or when the pressure in the system is high, the kinetic impedances at the interfaces are negligible, as impedances due to diffusion and latent heat transport at the interfaces become more significant. The non-equilibrium boundary conditions are dependent upon the sticking coefficient of the surface. An experiment to estimate the sticking coefficient on solid surfaces is proposed. The non-equilibrium theory also predicts significant temperature jumps at the interfaces.

Table of Contents

List of Tables

List of Figures

ACKNOWLEDGEMENTS

I would like to thank:

My Wife,
Catherine Suzanna Esther Gabor-Caputa

My Mom and Dad,
Ewa and Kris Caputa

My Sister,
Uszula Caputa

My Supervisors,
Henning Struchtrup and Sadik Dost

Other Helpfull Folk,
Neil Armour, Jordan Roszman, Brian Lent, Armando Tura, Mike Fischer, Sandro Schopfer, Anirudh Rana, Peyman Taheri, Rustom Bhiladvala, Andrew Rowe, Sean Bell, Mehdi Camus, and many others that I may have missed.

Finally, I would especially like to thank the Canadian Space Agency and Auto 21 for kindly funding this research.

DEDICATION

For Cathy

Nomenclature

Symbols

Latin

Symbol	Description	Unit
c	Mole density.	$\frac{\mathrm{mol}}{\mathrm{m}^3}$
C_n	Integration constant n.	Varies
$\bar{C}_p$	Constant pressure specific heat.	$\frac{\mathrm{J}}{\mathrm{mol\,K}}$
$\bar{C}_v$	Constant volume specific heat.	$\frac{\mathrm{J}}{\mathrm{mol\,K}}$
D_{ab}	Binary diffusion coefficient.	$\frac{\mathrm{m}^2}{\mathrm{s}}$
ΔT	Temperature jump.	K
f	Speed distribution function.	$\frac{\mathrm{s}^3}{\mathrm{m}^6}$
$\bar{g}$	Mole specific Gibbs free energy.	$\frac{\mathrm{J}}{\mathrm{mol}}$
$\hat{g}$	Thermal part of the Gibbs free energy.	$\frac{\mathrm{J}}{\mathrm{mol}}$
$\bar{h}$	Mole specific enthalpy.	$\frac{\mathrm{J}}{\mathrm{mol}}$
$\Delta\bar{h}_{sv}$	Latent heat of sublimation.	$\frac{\mathrm{J}}{\mathrm{mol}}$
I_k^a	Diffusion flux of constituent a.	$\frac{\mathrm{mol}}{\mathrm{m}^2\,\mathrm{s}}$
J_i, J	Total mole flux vector, scalar.	$\frac{\mathrm{mol}}{\mathrm{m}^2\,\mathrm{s}}$
J_i^a, J_a	Partial mole flux vector, scalar.	$\frac{\mathrm{mol}}{\mathrm{m}^2\,\mathrm{s}}$
J_i^+, J_i^-	Mole flux away/towards a solid surface.	$\frac{\mathrm{mol}}{\mathrm{m}^2\,\mathrm{s}}$
k	Boltzmann Constant.	$\frac{\mathrm{J}}{\mathrm{K}}$
Kn	Knusden number.	None
K_p	Equilibrium reaction constant.	Varies
ΔK	Supersaturation in terms of K_p.	Varies
l_{ab}	Component of the $\mathcal{L}_{ab}$ matrix.	Varies
m	Particle mass.	kg
M, M_w	Molecular weight.	$\frac{\mathrm{g}}{\mathrm{mol}}$
p, p_a	Pressure, partial pressure of a.	Pa
p_{sat}, p_{sat}^a	Saturation pressure, sat. partial pressure.	Pa
Δp	Supersaturation.	Pa
q_i, q	Non-convective heat flux vector, scalar.	$\frac{\mathrm{J}}{\mathrm{m}^2\,\mathrm{s}}$
r_{ab}	Component of the $\mathcal{R}_{ab}$ matrix.	Varies
R_c	Scattering kernel.	None

Latin (Continued)

Symbol	Description	Unit
R_u	Universal gas constant.	$\frac{\mathrm{J}}{\mathrm{mol\,K}}$
S	Entropy.	$\frac{\mathrm{J}}{\mathrm{K}}$
$\bar{s}$	Mole specific entropy.	$\frac{\mathrm{J}}{\mathrm{mol\,K}}$
$\hat{s}$	Thermal component of the entropy.	$\frac{\mathrm{J}}{\mathrm{mol\,K}}$
t	Time.	s
t_{ij}	Stress tensor.	Pa
T	Temperature.	K
T_w	Wall temperature.	K
$\bar{u}$	Mole specific internal energy.	$\frac{\mathrm{J}}{\mathrm{mol}}$
v_i, v	Mass centric velocity vector, scalar.	$\frac{\mathrm{m}}{\mathrm{s}}$
$\tilde{v}_i$, $\tilde{v}$	Mole centric velocity vector, scalar.	$\frac{\mathrm{m}}{\mathrm{s}}$
v_i^a, v_a	Constituent a velocity vector, scalar.	$\frac{\mathrm{m}}{\mathrm{s}}$
w_i	Kinetic theory velocity vector.	$\frac{\mathrm{m}}{\mathrm{s}}$
x_i, x	Position vector, scalar.	m

Greek

Symbol	Description	Unit
χ	Mole fraction	None
γ	Reaction coefficient	None
κ	Thermal conductivity	$\frac{\mathrm{W}}{\mathrm{m}}$
Λ	Effective heat transfer coefficient	$\frac{\mathrm{J}}{\mathrm{m^3\,s}}$
$\bar{\mu}_a$	Mole specific chemical potential of α	$\frac{\mathrm{J}}{\mathrm{mol}}$
θ_s	Sticking coefficient	None
σ	Bulk entropy generation	$\frac{\mathrm{J}}{\mathrm{m^3\,K}}$
σ_s	Surface entropy generation	$\frac{\mathrm{J}}{\mathrm{m^2\,K}}$
σ_{sb}	Stefan-Boltzmann constant	$\frac{\mathrm{W}}{\mathrm{m^2\,K^4}}$
ξ_i	Peculiar velocity vector	$\frac{\mathrm{m}}{\mathrm{s}}$
ζ	Equilibrium partial pressure ratio	None
ε	Surface emissivity	None

Script

Symbol	Description	Unit
$\mathcal{B}_{AB}$	Inverse of the diffusivity matrix.	$\frac{\mathrm{s}}{\mathrm{m^2}}$
$\mathcal{D}_{AB}$	Diffusivity matrix.	$\frac{\mathrm{m^2}}{\mathrm{s}}$
$\mathcal{J}_A$	Thermodynamic flux.	Varies
$\mathcal{L}_{AB}$	Phenomenological conductivity matrix.	Varies
$\mathcal{R}_{AB}$	Phenomenological resistivity matrix.	Varies
$\mathcal{S}$	Boltzmann collision term.	$\frac{1}{\mathrm{s}}$
$\mathcal{X}_A$	Thermodynamic force.	Varies

Subscripts and Superscripts

Symbol	Description
a, b, ν	Generic mixture constituents.
i, j, k	Physical vector indices.
A, B	Mathematical vector indices.
$I1, I2$	Interface 1, Interface 2.
Rx	Reaction.
s	Solid phase.
v	Vapor phase.
z	Inert mixture constituent.
0	Reference quantity.
$(\nu - 1)+$	Indicates a mixture of $\nu - 1$ active constituents and 1 inert constituent.

Acronyms

Acronym	Full Form
BC	Boundary condition
BTB	Binary transport in a binary system
BTT	Binary transport in a ternary system
BCF	Burton, Cabrera and Frank
CA	Closed ampoule
CE	Chapman-Enskog
CKB	Cipolla-Kjelstrup-Bedeaux
CVT	Chemical vapor transport
FVG	Fast vapor growth
HK	Hertz-Knudsen
KT	Kinetic Theory
LIT	Linear irreversible thermodynamics
NE	Non-equilibrium
PVT	Physical vapor transport
TLK	Terrace-Ledge-Kink
UTB	Unitary transport in a binary system
UTU	Unitary transport in a unitary system
VPG	Vapor phase growth

Chapter 1

Introduction

Effective manufacture of high quality semiconductor materials is a very active and important research field. Vapor crystal growth is a technique that is particularly applicable to II-VI compounds like cadmium telluride (CdTe) and zinc telluride (ZnTe) as well as ternary compounds such as cadmium zinc telluride ($Cd_{1-n}Zn_nTe$). The main advantage of vapor crystal growth over other techniques is the high crystal quality that can be obtained; crystals grown from vapor tend to have a lower concentration of point defects than those produced by other techniques [5, 6, 7].

Our research group is interested in improving the manufacture of high quality semiconductor materials from vapor. This research constitutes the first part of a multi-staged project to grow high quality binary and ternary semiconductors conductors from the vapor. Of particular interest are CdTe and $Cd_{1-n}Zn_nTe$. The development of successful vapor phase crystal growth (VPG) experiments requires accurate models. Such models can be used to optimize growth runs and reduce costly errors in the laboratory. An important component of such models are the boundary conditions. The research discussed in the following investigates the transport phenomena in VPG and develops a boundary condition framework for VPG models.

VPG falls into three main categories:

- Physical vapor transport (PVT), where phase transformations and simple non-catalytic chemical reactions take place at the interfaces.
- Chemical vapor transport (CVT), where material is incorporated into the growing crystal by complex chemical reactions.
- Vapor deposition, where only thin films are deposited upon surfaces well outside of the continuum regime [5, 3].

The present work focuses on PVT. In PVT, source material is sublimated and transported to a substrate located some distance from the source. The substrate can be a seed crystal of the same material or a surface of a different material. Growth by PVT is typically conducted within a growth vessel or ampoule. Transport is driven by the temperature difference between the source and the substrate. This temperature difference induces a free energy difference between the solids and the vapor, which in turn drives the mass transport.

The first attempts to grow semiconductor crystals from the vapor phase date back to before the 1960s [8]. PVT of semiconductor materials has been extensively reviewed several times over the decades. Faktor and Garrett produced an extensive monograph on the subject [9]; Brinkman reviewed semiconductor growth specifically [8]; recent progress was reviewed by Paorici and Attolini [5].

The vast majority of VPG models assume complete thermal and chemical equilibrium conditions at the growing interface (e.g. [10, 6, 11, 12, 9]). Some models do take into account non-equilibrium effects (e.g. [5, 13, 14, 15]); these assume the Hertz-Knudsen relationship for sublimation/deposition which has been shown to be inaccurate for both heat and mass transport (for a review, see [16]). The phenomenological approach has also been applied, but with limited justification for the choice of the transport coefficients [17]. Finally, the transport of latent heat out of the interface is commonly ignored, though some authors have addressed it [9, 18, 11, 10].

1.1 Objectives

1. To model the impedences to mass transport in PVT, and estimate the conditions at which each is important.
2. To study and recommend appropriate vapor-solid interface conditions for future PVT models.
3. To analyze the error between equilibrium and non-equilibrium interface conditions in the context of PVT.
4. To study heat transport at solid-vapor interfaces, and comment on its implications.

1.2 Methodology

Linear irreversible thermodynamics (LIT) combined with kinetic theory (KT) have been used to determine phenomenological boundary conditions for evaporation and condensation problems involving simple substances as well as binary and higher order mixtures within the continuum regime [19, 20, 21, 22]. In order to demonstrate the usefulness of the LIT and KT framework to determine interface conditions for continuum solid-vapor phase transition problems, such as those found in PVT crystal growth, we develop one dimensional advective/diffusive PVT models based upon those of Faktor and Garrett [9], replacing their equilibrium interface conditions (EIC) with non-equilibrium interface conditions (NEIC). We also introduce incorporate heat transport in the 1D model, which Faktor and Garrett negelcted. The

NEIC are derived from the linearization of KT results, and, following linear theory, are dependent upon only the equilibrium properties of the solid-vapor interface.

We use this model to solve 4 different transport problems using both EICs and NEICs:

- Transport of a single constituent without a background gas — unitary transport in a unitary system (UTU).
- Transport of a single constituent limited by diffusion in a stagnant background gas — unitary transport in a binary system (UTB).
- Transport of two constituents without a background gas — binary transport in a binary system (BTB).
- Transport of two constituents within a stagnant background gas — binary transport in a ternary system (BTT).

For our analysis of UTU and UTB, we use iodine (I_2) as the transported substance. I_2 is commonly used as a model substance in PVT experiments due to its low sublimation temperature [11]. For BTB and BTT we consider the binary semiconductor material cadmium telluride (CdTe). The solutions to our models predict temperature profiles, partial pressure profile, and, the steady-state mass flux and heat flux from the source to the substrate.

1.3 Thesis Structure

For the rest of this chapter (§1.4-1.8) the basic science behind VPG is reviewed qualitatively. Following that, the remainder of this thesis is structured as follows: In Chapter 2, the heat and mass transport model for the bulk phases (solid and vapor) is described; in Chapter 3 a non-equilibrium interface model based upon LIT is proposed; in Chapter 4 the relation between the surface physics, the KT interface expressions and the LIT phenomenological coefficients is discussed; Chapters 5 and 6 introduce the property data and solution method that are used to solve the aforementioned PVT problems; in Chapter 7 PVT of Iodine is modelled; in Chapter 8 PVT of CdTe is modelled; in Chapter 9, an experimental approach for obtaining interface transport coefficients is discussed, and, finally in Chapter 10, the findings of this thesis are summerized.

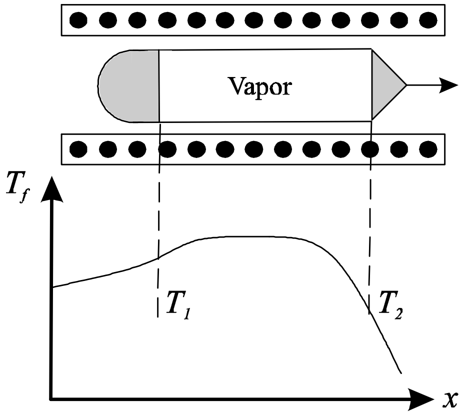

Figure 1.1: An example of a CA-PVT arrangement. The source material is placed on the left hand side and the growing crystal is on the right hand side. As the growing interface advances, the ampoule is translated to the right to maintain a constant temperature at the interface.

1.4 Overview of PVT Crystal Growth Techniques

Transport in PVT occurs by advection, convection[1] and diffusion. PVT methods have been applied to all sorts of materials and have been found to be particularly useful for II-VI semiconductors like CdTe [5, 8]. Although many different experimental arrangements exist for PVT crystal growth (see [8] for a review), these can be classified into three categories:

- Closed ampoule arrangements (CA-PVT) (Fig. 1.1): Here, the source and seed are sealed in a closed, evacuated ampoule. The ampoule is heated externally and has a temperature gradient imposed between the source and seed by some means. The advantage of this approach is its simplicity; the main disadvantage is that impurity vapors and excess vapor species tend to build up in the ampoule, restricting the transport rate or worse, poisoning the growth. Since these factors are difficult to control or measure, CA-PVT experiments are notorious for their lack of repeatability [8, 7, 5], though when extreme care is taken in the experimental preperation, repeatable experiments appear to be possible [12, 18, 10, 13, 11].

- Semi-closed ampoule arrangements (SC-PVT) (Fig. 1.2): This arrangement is a modification of the CA arrangement. A small effusion hole is added at the growth end and connected to vacuum. The idea here is to overcome the difficulties of the CA arrangement by allowing impurity vapors to escape during the initial heating of the ampoule. The effusion hole is sealed off by condensing

---

[1] Advection and convection are often understood as the same phenomena. In this thesis, we differentiate the two: we consider advection as flow driven by density differences in the vapor that are not induced by gravity; and convection is flow induced by buoyancy effects due to gravity.

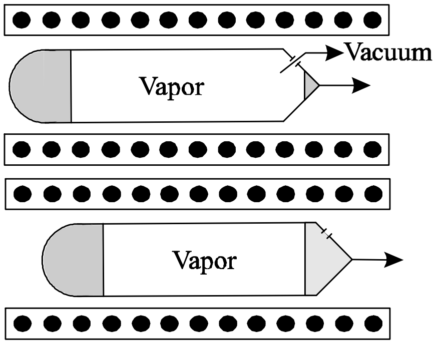

Figure 1.2: An example of seeded semi-closed PVT arrangement. Here, during the initial stages of the growth, the ampoule is connected to vacuum. As the seed crystal grows, the advancing crystal eventually seals off the effusion hole, and growth proceeds as in CA-PVT.

material shortly after growth begins. This arrangement, while solving some of the problems associated with CA techniques, still suffers from a lack of repeatability, since excess impurities and excess constituents can build up after the effusion hole closes [8, 7, 5].

- Semi-open ampoule arrangements (SO-PVT) (Fig. 1.3): In this arrangement, the ampoule is connected to vacuum during the entire experiment. Thus, impurity vapors as well as excess constituents can be continuously removed from the ampoule, greatly increasing the repeatability of the experiments. A background gas can be introduced into the growth ampoule and pumped out at the vacuum source to facilitate transport. This is the principle of the successful Markov-Davydov method, which is the only commercially implemented bulk vapor crystal growth method to date [5, 8]. Also worth mentioning is the promising multi-tube PVT method [5, 23] which thermally decouples the source and the seed crystals by storing them in seperate growth chambers, though the overall principle is very similar to that of the Markov-Davydov method. These techniques have the additional advantage of seperating the growing crystal from the wall of the ampoule, thus reducing the strain that typically develops in crystals grown in contact with the walls [5].

The experiments we analyze in this work are limited to the CA-PVT, although in principle, the interface model developed here could easily be extended to other techniques. The above is only a very general list of experimental techniques; and many subsets and modifications exist. For a complete review see [5, 8].

1.4.1 Macroscopic models

At the macroscopic level, the vapor-solid interface is considered a smooth surface. This surface may be flat or may have curvature. Indeed, the theory defining the equilibrium shape of crystal interfaces

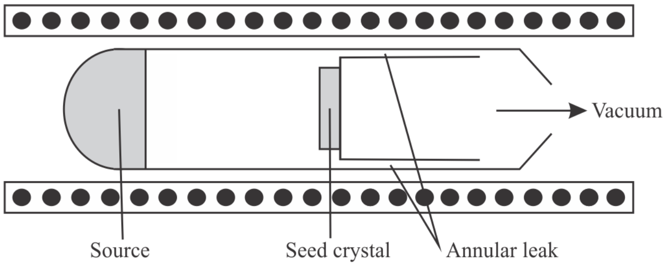

Figure 1.3: The Markov-Davydov SO-PVT arrangement. Impurities and excess constituents escape by the annular leak during the entire growth run.

was first developed by Gibbs well over 100 years ago [3]. These ideas were then furthered greatly by the introduction of Wulf's law, which can be used to describe the shape of single crystals [3, 24]. In our work, we are less concerned with the shape of the growing crystal, and more concerned with the transport of material across the interface.

In our literature review, we found that 1-D CA and SC-PVT models are either based upon, or are an alternative formulation of, the Faktor-Garrett model (e.g. [13, 12, 17, 6]). Other, more sophisticated 2D and 3D models capture convective and surface energy effects which lead to curvature developing at the crystal interface; these are ignored in the 1D models. It has been shown that both viscous and convective effects in PVT models can be significant, and often cannot be ignored [11, 25]. Thus any complete model of vapor crystal growth should consider these effects. For our purposes, however, we neglect these effects so that the interface conditions can be studied in the simplest

1.4.2 Transport by dissociative sublimation

Binary semiconductor materials dissociate upon sublimation, so that a chemical reaction takes place at the interface of the form,

$$\mathrm{AB(s)} \rightleftharpoons \gamma_{\mathrm{A}}\mathrm{A(v)} + \gamma_{\mathrm{B}}\mathrm{B(v)} \tag{1.1}$$

where A and B are the constituent species of the compound, $\gamma_{\mathrm{A}}, \gamma_{\mathrm{B}}$ are the corresponding stoichiometric coefficients. An early theoretical treatment of dissociative sublimation vapor phase growth was developed by Faktor et al. [26, 9] for the II-VI compound cadmium sulfide (CdS). The dissociative sublimation vapor crystal growth model has been applied frequently to the transport of binary and ternary semiconductor materials (e.g. [23, 17, 6, 27, 12]). As we shall confirm in Chapter 8, transport by dissociative sublimation poses serious challenges for obtaining fast, reproducable VPG growth rates of semiconductor materials due to large swings in vapor pressures of the binary vaporous species above the solid [9, 12], though it appears that these problems can be resolved either by careful source preperation [12], or by the

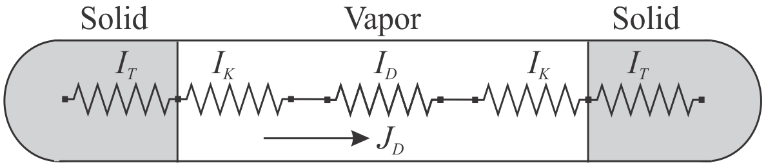

Figure 1.4: A schematic of the transport impedances in PVT crystal growth. I_T represents an impedance related to the transport of latent heat in or out of the interface, I_K is the impedance related to interfacial kinetics, I_D is an impedance related to diffusion in the bulk vapor. J_D is the mole flux.

application of SO-PVT methods [17, 23, 28].

1.4.3 Transport Impedances

Faktor and Garrett described vapor crystal growth as a series of sequencial processes [9]. As resistors in an electric circuit, each of these processes has an impedance associated with it. An example of this idea is given in for PVT in Fig. 1.4. In PVT, the main impedences are: the thermal impedance, caused by the release and absorption of the latent heat of sublimation during the solid-vapor/vapor-solid phase transformations; the kinetic impedance on solid surfaces, caused by the kinetics of the interphase mass transport; and, diffusive impedence, caused by bulk diffusion in the vapor. There may also be additional impedances, for example an impedence stemming from flow viscosity; however, in this work we restrict ourselves to transport with thermal, kinetic and diffusive impedances only.

1.5 Overview of Linear Irreversible Thermodynamics

The framework for LIT was first developed by Lars Onsager in 1931 [29, 30] with the introduction of the reciprocal relations. The complete theory of LIT was presented in its final form by de Groot and Mazur in their famous monograph titled *Non-Equilibrium Thermodynamics* first published in 1962 [31]. A substantially more modern review is given by Kjelstrup and Bedeaux [20].

The central premiss of LIT is the local equilibrium assumption, where, even though the macroscopic control volume is outside of equilibrium, equilibrium thermodynamic concepts can still be applied to the differential volume element; thus, a local Gibbs equation remains valid in each differential volume even though it is not valid for the overall system. With this assumption, balance laws for mass/moles, mass/mole concentration, momentum and energy can be combined to write a balance law for the entropy of the system, including the entropy generation terms. As a concequence of the second law of thermodynamics, the entropy generation terms must be nonegative, and can be manipulated into a linear product of entropic forces $\mathcal{X}_A$, such as the temperature gradient, and entropic fluxes $\mathcal{J}_A$, such as the heat flux, in the form

$$\sigma = \sum_A \mathcal{J}_A \mathcal{X}_A \geq 0. \tag{1.2}$$

For cases where the system is not far from equilibrium, it is postulated that the entropic forces can be written as a linear combination of the thermodynamic fluxes such that

$$\mathcal{J}_A = \sum_B \mathcal{L}_{AB} \mathcal{X}_B, \tag{1.3}$$

where $\mathcal{L}_{AB}$ is a matrix of phenomenological transport coefficients that is dependent upon equilibrium properties of the system. The reciprocal relations, state that $\mathcal{L}_{AB}$ is symmetric

$$\mathcal{L}_{AB} = \mathcal{L}_{BA}, \tag{1.4}$$

and positive-definite so as to prevent a 2nd law violation. This was proven for independent force/flux pairs by Onsager. A common pitfall here is to assume that any set of forces and fluxes can be related with a symmetric matrix; this is not correct. A symmetric $\mathcal{L}_{AB}$ matrix is obtained only for *independent* force/flux pairings defined as,

$$\mathcal{J}_A = \frac{dA_A}{dt}, \quad \text{and} \quad \mathcal{X}_A = \frac{dS}{dA_A}, \tag{1.5}$$

where A_A are the independent variables, t is time, and S is the entropy of the system. In other cases, non-symmetric matricies are encountered [32].

LIT is only valid for systems close to equilibrium. Other theories have been applied to systems far out of equilibrium [33, 34]. Nevertheless, LIT has been very successful in describing close-to-equilibrium phenomena in continuum, and can be used to define, from first principles, the appropriate constitutive assumptions required to derive the Euler, Navier-Stokes, Fick and Fourier transport equations complete with cross effects.

1.6 Overview of Kinetic Theory

The following is a short introduction to kinetic theory; for a comprehensive review see [35, 36]. In kinetic theory, the behavior of a system of atoms is described by the distribution function $f(x_i, t, w_i)$ which is defined such that $f(r_i, t, w_i)\, d\mathbf{w} d\mathbf{r}$ is the number of atoms with velocities in $\{\mathbf{w}, \mathbf{w} + d\mathbf{w}\}$ and positions in $\{\mathbf{r}, \mathbf{r} + d\mathbf{r}\}$ at time t. Given the distribution function, bulk properties such as mass density, momentum density, internal energy, pressure tensor and heat flux can be computed.

We are interested in sublimation and condensation on solid surfaces; we can use kinetic theory to find the mole flux,

$$J_i = cv_i = \iiint\limits_{-\infty}^{\infty} w_k f d\mathbf{w} \ , \tag{1.6}$$

and the energy flux,

$$Q_i = m \iiint\limits_{-\infty}^{\infty} \frac{1}{2} w^2 w_k f d\mathbf{w} \ , \tag{1.7}$$

where c is the mole density of the vapor, v_k is the center of mass velocity of the vapor, f is the speed distribution function of the vapor, and, w_k is the particle velocity.

The velocity distribution function must be a solution of the Boltzmann equation [37, 36]

$$\frac{\partial f}{\partial t} + w_k \frac{\partial f}{\partial x_k} = \mathcal{S}(f) \ , \tag{1.8}$$

where $\mathcal{S}$ denotes the collision term that describes the evolution of the distribution function. The balance laws for mass, momentum, and energy as well as the H-theorem (i.e., the second law) can be derived by suitable averaging of the Boltzmann equation over the microscopic velocity [37, 36]. The H-theorem can be used to show that entropy generation is always non-negative, and is only zero when $\mathcal{S}(f) = 0$; this then is the definition of equilibrium [36].

1.6.1 Distribution functions in the bulk vapor

When $\mathcal{S}(f) = 0$ the solution to the Boltzmann Equation (1.8) is the Maxwellian distribution,

$$f_M\left(p, T, \xi\right) = \frac{p}{kT}\left(\frac{m}{2\pi kT}\right)^{3/2} \exp\left(-\frac{m}{2kT}\xi^2\right) ; \tag{1.9}$$

where ξ is the peculiar velocity, defined as

$$\xi_i = w_i - v_i \ . \tag{1.10}$$

The Maxwellian is a Gaussian (normal) distribution in three dimensions.

Non-equilibrium solutions ($\mathcal{S}(f) \neq 0$) to (1.8) are considerably more complex. The Boltzmann equation can be solved numerically, either directly or by DSMC simulations [38], both of which are computationally expensive.

The Chapman-Enskog (CE) expansion gives an approximation of the distribution function, which is obtained from (1.8) by expansion in the Knudsen number Kn,which is the ratio of mean free path to the characteristic dimension. The zeroth order expansion gives the continuum Euler equations and the first order expansion adds the continuum Navier-Stokes and Fourier equations.

1.6.2 Distribution functions at the interface

When a vapor particle strikes the surface, it either adsorbs onto the interface or it bounces off. If it adsorbes on the interface, the particle either diffuses into a growth location, or it detaches back into the vapor. The details of these phenomena are discussed in §1.7. Sublimation is the exact reverse of this process, according to the principle of microreversibility [39, 40].

In both equilibrium and non-equilibrium, there is a constant flux of particles striking the interface, which are either condensing on the surface or reflecting back into the vapor. There is also a constant flow of particles subliming from the surface. We distinguish between the particles traveling towards and away from the interface, such that the net particle velocity distribution function at the interface is

$$f_{int} = \begin{cases} f^-, & w'_n \leq 0 \\ f^+, & w_n > 0 \end{cases}, \tag{1.11}$$

where f^- is the distribution of incident particles (negative velocity w'_n normal to the interface), and f^+ is the distribution of emitted particles (positive velocity w_n normal to the interface). In equilibrium, $f_{int} = f_m$; and $|f^-| = |f^+|$.

In both equilibrium and non-equilibrium, the distribution of emitted particles can be related to the distribution of incident particles [40, 41, 42, 37]

$$f^+ = \hat{\theta}_s(w_k, T_s) f_M \left[p_{sat}\left(T_s\right), T_s, w\right] + \frac{1}{|w_n|} \iiint\limits_{w'_n < 0} f^- R_c(w'_k \to w_k) \, |w'_n| \, d\mathbf{w}' \tag{1.12}$$

where $\hat{\theta}_s(w_k, T_s)$ is a sublimation probability function — the probability that a particle subliming from a surface at temperature T_s will have a velocity w_k; $R_c(w'_k \to w_k)$ is a reflection kernel. The first term of equation (1.12) describes the sublimating particles, and assumes the solid surface is in local equilibrium, i.e. the distribution of evaporating particles is always a Maxwellian at the surface temperature [39, 41]. The second term represents the reflected particles.

1.7 Overview of Microscopic Crystal Growth Theory

Although our model is fully macroscopic in nature, it is worth discussing the phenomena that occur at the interface of a growing crystal. The reader should be familiar with some elementary crystallography here, in particular the basic crystal structures and the index planes; the level discussed in any materials engineering textbook such as [43] should suffice.

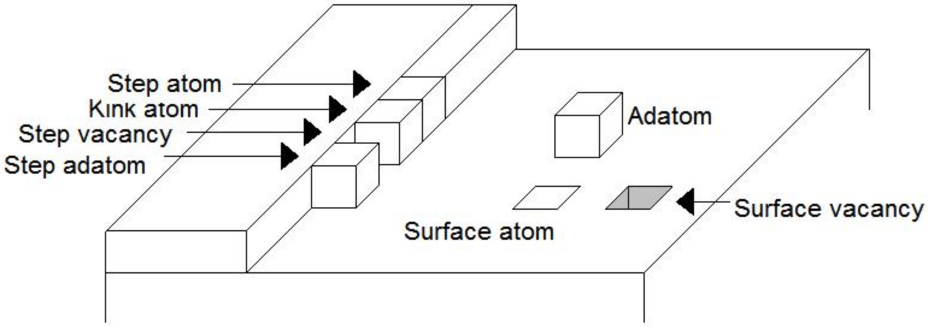

Figure 1.5: The surface structure of the Kossel crystal surface. All five of the possible surface positions in the kossel crystal TLK model are shown. *Image from Wikipedia, reproduced under the terms of the GPL.*

1.7.1 Atomistic structure of the interface

To begin, we consider a very simple crystal surface called a Kossel crystal [3]. The Kossel crystal is primarily a theoretical construct[2] in which, unlike real crystals, atoms are located at lattice points only. The kossel crystal surface can conveniently be represented by a square grid, with small cubes representing atoms. In Fig. 1.5 the (100) plane of a Kossel crystal surface is shown with a monatomic step; the types of surface defects are identified, including the allowed positions of surface atoms, normally called adatoms. This crystal surface model is called the terrace-ledge-kink (TLK) model, and was first formulated independently by Kossel [44] and Stranski [45]. With the advent of the scanning electron microscope, the TLK structure of real (non-Kossel) crystal surfaces has actually been observed; for example, Fig. 1.6 shows the TLK-type surface on the (001) plane of zincblende silicon.

The adatom positions identified in Fig. 1.5 are classified in terms of their bonding strength. In order of strength from weakest to strongest, the positions are:

- Adatom position: one nearest-neighbour (NN) bond.
- Step adatom position: two NN bonds.
- Kink position: Three NN bonds.
- Step position: Four NN bonds.

---

[2] In fact, under some conditions, the Kossel crystal does exist in solid metal Polonium, but otherwise is not found in nature [3].

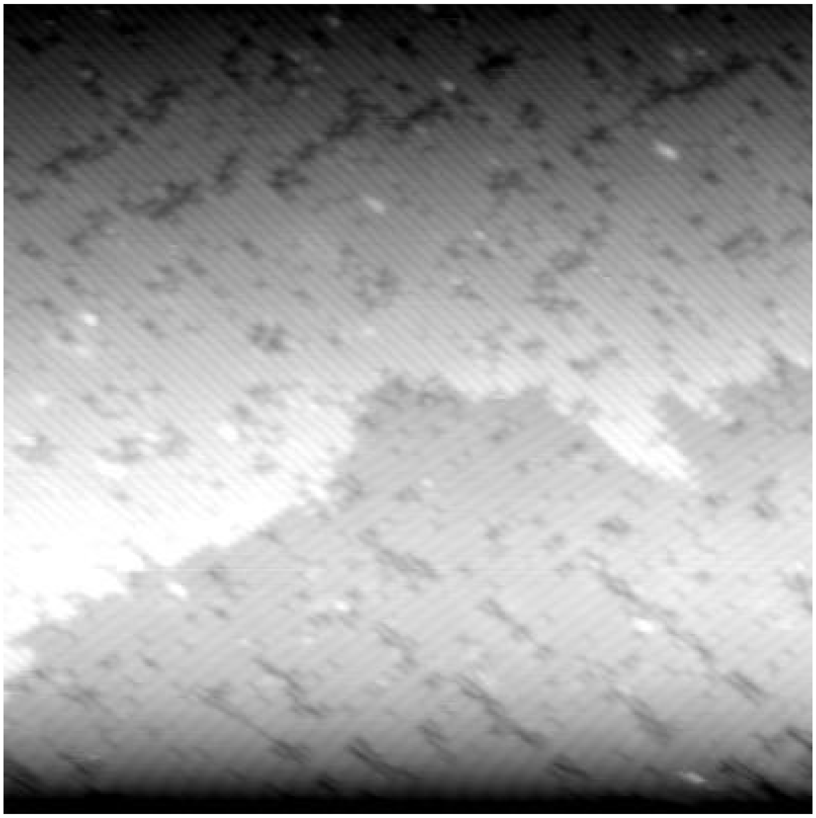

Figure 1.6: A scanning tunneling microscope image of a clean Si (100) surface. A step edge as well as many surface vacancies are shown. Many kink sites are visible along the terrace edge. *Image from Wikipedia, reproduced under the terms of the GPL.*

- Surface position: Five NN bonds.
- Lattice position: Six NN bonds.

More distant neighbors (second nearest and third nearest) also contribute to the bonding strength. By convention, adatoms in the adatom and step adatom positions are considered attached but not incorporated into the crystal structure — these adatoms can easily move about on the surface or return to the parent phase. Adatoms in the kink, step, surface or lattice positions are considered part of the solid phase [3, 39]

1.7.2 Transport between the vapor phase and the solid phase

Now that the basic surface structure has been identified, we turn our attention to the transport of atoms between the vapor phase and the solid phase. The transport of particles from the vapor phase to the solid phase is a multistaged process which includes adsorption — the process of attachment of gaseous molecules to exposed, non-gaseous surfaces; surface diffusion — the surface concentration-driven transport of adatoms from location to location upon the surface; and, finally, the incorporation into the lattice, which occurs when an adatom diffuses into or advects directly into a kink, step or surface position [3].

The probability that an incident particle will successfully become attached to the lattice, and thus transition into the solid phase is normally called the sticking probability [24]. This can be confusing to the reader because the probability that an atom adsorbes, but does not attach to a kink is also normally called the sticking probability [39]; for our purposes, we shall refer to the sticking probability as the probability that an atom becomes incorporated into the bulk by attachment to a kink (or stronger) site.

1.7.3 Adsorption

Adsorption is the process of attraction of gaseous molecules to exposed, non-gaseous surfaces. This phenomenon has applications in many fields of engineering, physics and chemistry, and is very well studied. There are two main types of adsorption — physisorption and chemisorption. In physisorption, the adatoms are held onto the surface by weak van-der-Waals type forces; in chemisorption, the adatoms are chemically bonded to the surface. In vapor crystal growth, we are concerned with chemisorption as opposed to physisorption [39, 9]. Adsorption is a very complex subject, and is highly dependent upon the condition of the surface. We limit our discussion here to a qualitative one only, for a full and proper review, see [39].

At a fixed temperature, the coverage of a surface by adatoms is a function of the vapor pressure above the surface. The simplest model of this is the Langmuir isotherm, which is limited to non-interacting adsorbates that constitute only one layer upon the surface. The Brunauer-Emmett-Teller isotherm is a more complex model, which can handle all types of adsorbates as well as multiple layers of adsorbates [39, 9].

Adatoms can only attach to energetically favorable sites on the surface. In the Kossel crystal, these sites correspond to the corner point of the lattice. These potential wells can be described in terms of distance from the surface and the kinetic energy of the adatom. Adsorption can be an activated or a non-activated process. In non-activated adsorption, less energetic particles are more likely to lose enough energy to get sucked in to a well. In activated adsorption, the particle must have enough energy to cross over an activation barrier, but still lose enough energy in the interaction with the interface so as to fall into the well [39]. This problem is more difficult than it seems; the theory was addressed for deep potential wells by Iche and Niozzers [46].

We were unable to identify an appropriate energy loss function for a growing crystal surface. Therefore, in our analysis, we shall always assume that the adsorption probability and by extension the sticking probability are independent of the particle energy. Even these constant adsorption probabilites can be a complex functions, as several steps may be involved in the adsorption process. Nevertheless, for many cases, an Arrhenius relationship for adsorption is sufficient to describe the phenomena [39]. The adsorption probability is then given as

$$\theta_{ads} = \exp\left[\frac{-\Delta U_{ads}}{kT_s}\right] \tag{1.13}$$

where ΔU_{ads} is the activation energy for adsorption, T_s is the temperature of the surface and k is the Boltzmann constant.

1.7.4 Surface diffusion

A newly adsorbed adatom will arrive at any of the locations shown in Fig. 1.5. If it arrives at a deep potential well, such as a kink, or a step vacancy, it will become strongly attached to the crystal lattice, and is unlikely to detach again. If, however, the adatom attaches in the adatom position or the step adatom position, it is only weakly held to the surface. While it may not have enough energy to escape the surface entirely, only a little bit of extra energy can cause it to jump from location to location on the crystal surface; this effect is called surface diffusion. Energy is exchanged between the surface and the adatoms as well as between adatoms. Much like diffusion in vapor, surface diffusion is driven by chemical potential differences on the surface, and can be described by Fick's law [3, 24, 47]. The phenomena involved in surface diffusion were reviewed in detail by Antczak and Ehrlich [47].

1.7.5 The Kink Site as an Energy Well

We have now established that in order for an adatom to reach a kink site, and thus become part of the crystal, it must adsorb onto the surface and than diffuse into a kink site. We can picture this process as an adatom jumping from potential well to potential well on the surface. Fig. 1.7 shows the activation energies involved in such a process as well as the energy wells that may exist. The solid line shows a simple Arrhenius type relationship for the adsorption probability that might exist for adsorption directly into a kink. The dotted line adds an additional potential well for the adsorbed position; it describes the more complex energy transitions an adatom might go through before falling into the kink potential well.

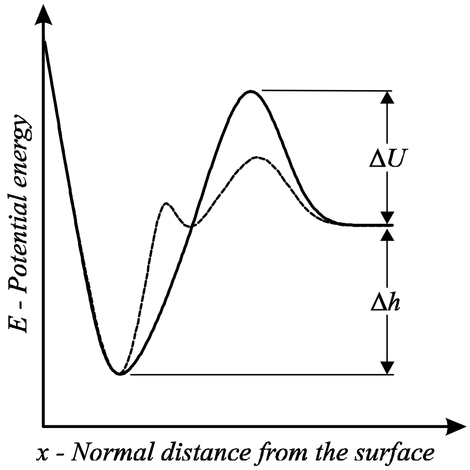

Figure 1.7: Arrhenius type energy barriers for a surface. ΔU is the height of the activation barrier and Δh is the latent heat of adsorption for the solid.

1.7.6 Driving Forces in Vapor Crystal Growth

Like all phase transformation processes, the growth of crystal surfaces is driven by differences in free energy between the parent phase (vapor) and the crystalline phase (solid)[3]. Small differences between the solid free energy and the vapor free energy can be approximated by a difference between the vapor pressure and the saturation pressure. In vapor crystal growth this is called the *supersaturation* of the vapor defined as $\Delta p = p_v - p_{sat}(T_s)$, where p_v is the pressure of the vapor phase and $p_{sat}(T_s)$ is the saturation pressure of the system at the temperature of the solid.

---

[3] In Chapter 3 we show that the temperature difference between the vapor and the solid must also play a role.

1.7.7 Growth of the Microscopic Surface

The definitive paper on the growth of microscopic surfaces is the famous paper by Burton, Cabrerra, and Frank [2]. This paper presents the first complete theory of microscopic surface growth, called the BCF-model. The BCF-model combines the already established step growth model (the TLK model) with the so-called screw dislocation growth mechanism, where small dislocations on nearly perfect surfaces introduce additional steps onto the surface. These steps grow outwards in a spiral form [3, 9]. This growth phenomenon was first predicted by theory and then experimentally confirmed [48].

According to the BCF-model and subsequent work, crystal growth from vapor takes place in one of several growth modes, these are [1]:

- 2-dimensional growth, as in Fig. 1.8(a): Layers growing on low index planes such as the (001) of a surface tend to be nearly-complete before new layers form. Bottlenecks in growth are strictly related to two-dimensional nucleation of clusters.
- 3-dimensional growth, as in Fig. 1.8(c): Here, multiple layers can grow at the same time. This type of growth is encountered on rough surfaces. [48, 2, 1].
- Stranski-Krastanov growth, as in Fig. 1.8(c): This type of growth is typically encountered in hetero-epitaxy, where a layers of material are grown on a substrate of a different type. We include it here for interests sake only [1].
- Step flow growth: This growth mode is a special case that occurs only on vicinal surfaces — surfaces which cut across the crystal lattice. Here, instead of growth on a flat surface, growth occurs on a series of steps that appear to travel across the crystal surface. [1, 2].

At low temperatures near equilibrium, growth tends to proceed by the 2-dimensional growth mechanism. As the temperature is increased past a certain temperature T_r, called the roughening temperature, the surface becomes rough, and growth proceeds by the 3-dimensional growth mechanism [1].

3D surface growth typically takes place on rough surfaces, where the kink density is very high. Growth proceeds by adatoms adsorbing directly into kinks, and the influence of surface nucleation and surface diffusion is negligible. This type of growth proceeds linearly in the supersaturation [3], and therefore can be accuratly modeled with LIT.

2D growth modes are more difficult to characterize than 3D growth. Growth by screw dislocations (Fig 1.9) has been shown to proceed with quadratic dependence on the supersaturation when the supersaturation is low, as in Fig. 1.11a.

Growth by the nucleation of 2D clusters (Fig. 1.10) on the other hand proceeds linearly with supersaturation, but requires a certain minimum critical supersaturation to be reached before nucleation can

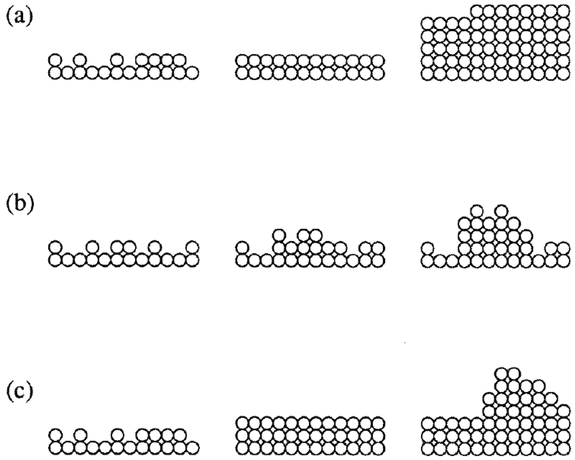

Figure 1.8: The three general types of surface growth. (a) Layer-by-layer 2-dimensional growth. (b) 3-dimensional growth where multiple layers can grow at the same time. (c) Stranski-Krastanov growth, which lies somewhere between (a) and (b) and generally only occurs in epitaxial growth. Image from [1].

occur, as in Fig. 1.11b. The slope of the dependence on supersaturation depends on whether growth proceeds layer-by-layer where no new layers are formed until the previous layer is complete, or by multi-layer growth. In both cases, the application of a linear law as determined from LIT to the growth of the crystal surface is inaccurate.

The step flow growth mode, which is often present on semiconductor surfaces growing near the vicinal plane and on high-index planes, proceeds linearly with supersaturation as the nucleation of new steps or the formation of growth spirals is not required. The linear laws are perfectly acceptable for this type of growth.

Since the expressions for the rates of advance of steps on a crystal surface are complex, and highly dependent upon the surface geometry, we shall assume that the kinetic theory of the growth of trains of steps can be approximated by the expression we derive for rough surfaces in Chapter 4.

1.7.8 Dependence on Growth Plane

Figure 1.12 shows the various planes on a Kossel crystal and the type of growth expected on each. Growth on the (111) plane exposes a rough surface, and growth proceeds by the 3D growth mechanism. Growth on the low index planes (100,010,001) takes place on smooth surface, and the 2D growth mechanisms are expected. Growth on the vicinal planes (011,110,101) proceeds by the step flow mechanisms.

It should be noted however that in crystal growth, especially bulk crystal growth, it is nearly impossible to obtain a perfect low index plane. Crystal growth typically proceeds on some high index plane near

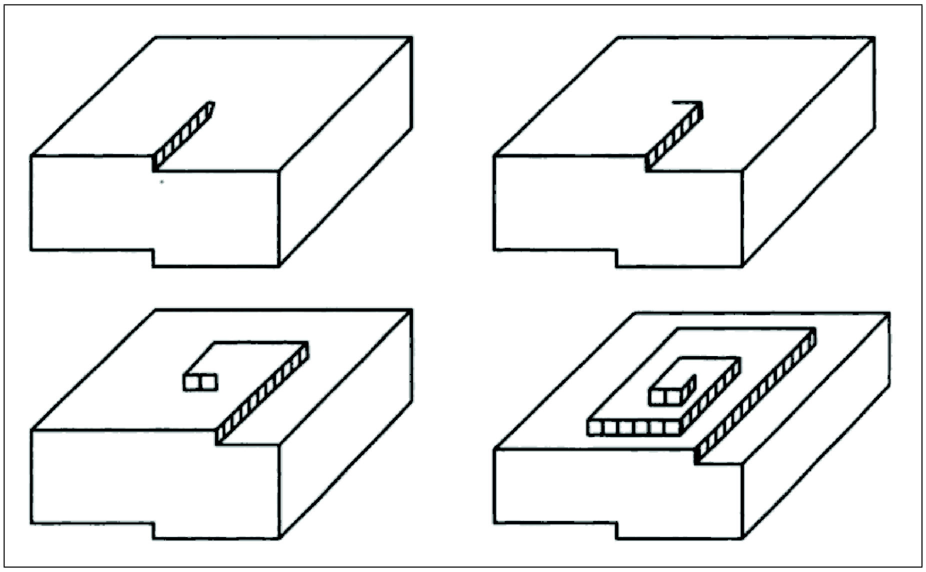

Figure 1.9: The growth spiral formation process is shown. Growth begins with the formation of a screw dislocation, which initiates a step. The step then grows as atoms attach to the mobile kink. The step spirals around as more atoms attach to the step, until a growth pyramid is formed [2]. Figure from [3].

one of the low index planes; thus, step flow can be important even on the low index, non-vicinal planes [3]. Due to this effect, it is likely that step flow mode to be the dominant growth mode on materials such as CdTe [49].

1.8 Overview of Cadmium Telluride

In this thesis we are mainly concerned with the growth of cadmium telluride (CdTe). CdTe is a II-VI semiconductor material. Modern interest in cadmium telluride (CdTe) dates back to 1947, when single

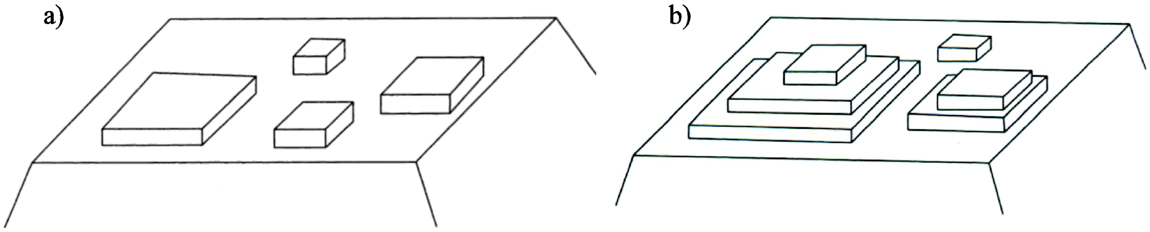

Figure 1.10: Growth by 2D nucleation. a) Growth proceeds layer-by-layer, where the layers tend to be fully completed before new layers nucleate. b) Multiple layers nucleate and grow concurrently. Figure from [3].

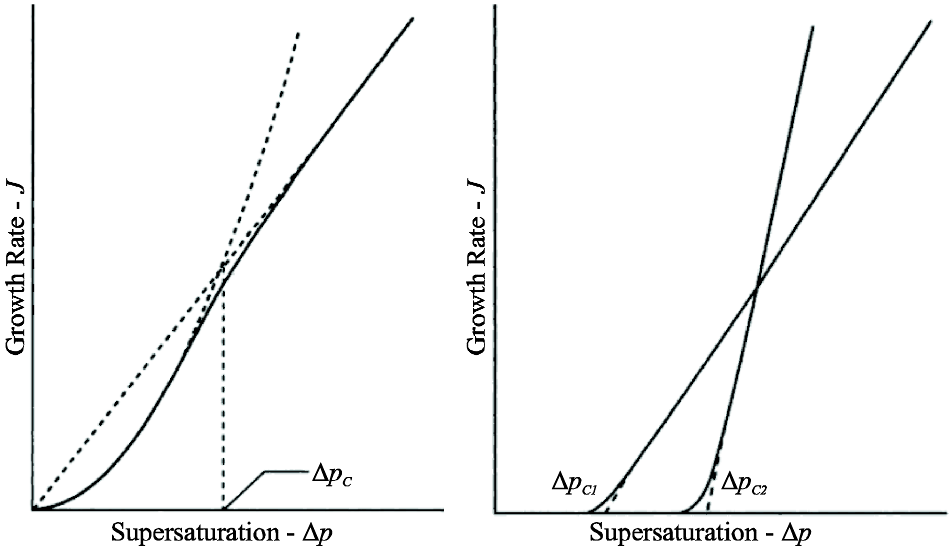

Figure 1.11: The supersaturation dependance of growth rate in the a) spiral growth and b) 2D nucleation mechanism. In a) Δp_C indicates the critical supersaturation at which growth transitions from parabolic dependence to linear dependence. In b) Δp_{C1} indicates the critical supersaturation at which 2D nuclei begin to form in multilayer growth. Δp_{C2} indicates the critical supersaturation at which 2D nuclei begin to form in layer-by-layer growth. Image from [3].

crystals of the material were first grown. Today, CdTe has important engineering applications. Its direct bandgap of 1.5 eV make it near optimum for photovoltaic cells. Its high atomic number, large bandgap and reasonable electron transport properties make it a good material for x-ray and gamma ray detection. Its high electro-optic coefficient and its low absorption constant have led to its consideration for electro-optic modulators, lenses, Brewster windows, partial reflectors and fiber optic devices [50]. Single crystals of CdTe can be grown using melt growth, solution growth or vapor growth techniques.

1.8.1 Crystal Structure

The different kinds of conventional crystal structures expected in real materials, such as the face-centred cubic or base centred cubic structures are reviewed in [43]. Elemental semiconductor materials such as silicon have a diamond cubic crystal structure. The structure consists of two interpenetrating face center cubic (FCC) sublattices with one sublattice displaced from the other by one quarter of the distance along a diagonal of the cube. All atoms are identical in the diamond lattice, and each atom in the diamond lattice is surrounded by four equidistant nearest neighbors that lie at the corners of a tetrahedron.

CdTe and other compound semiconductors have a zincblende lattice, as in Fig. 1.13. The zincblende

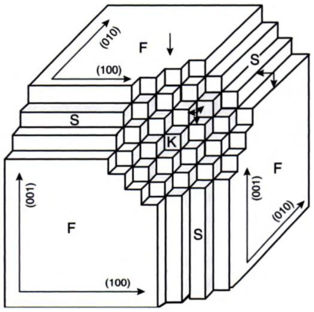

Figure 1.12: The dependence on surface condition on orientation in a Kossel crystal. Figure from [3].

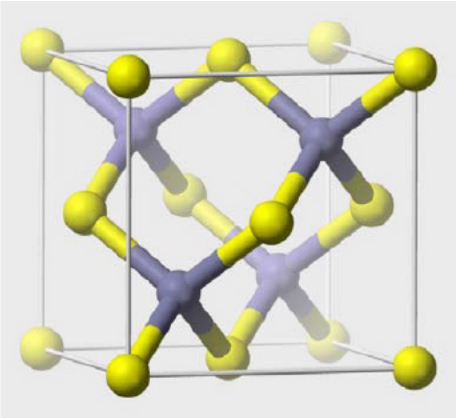

Figure 1.13: A unit cell of the zincblende crystal structure. The arrangement of the atoms is analogous to that of diamond. *Image from Wikipedia licensed under the terms of the GPL.*

lattice is identical in structure to the diamond lattice; however, one of the two face-centred-cubic (FCC) sublattices consists of a different species. Some semiconductors can have more than one type of crystal structure depending on the conditions in which they are grown. For example, the nitride semiconductors (GaN, InN, AlN) can crystallize in either the zincblende or the wurtzite structure [51]. In the particular case of CdTe, the surface of the crystal has a tendency to relax to the wurtzite crystal structure [52].

1.8.2 Composition

Figure 1.14 gives the T-X diagram for CdTe. CdTe can exist in solid form only at temperatures below its melting point at approximatly 1360 K. The melting point of CdTe is slightly non-stoichiometric. Non-stoichiometry in CdTe crystals occurs as a result of the dissolution of excess Cd or Te into the solid [53, 54]. We are interested in the lower temperatures in the diagram; here, the composition range of the solid material is quite large; the maximum composition range occurs at approximatly 1040 K.

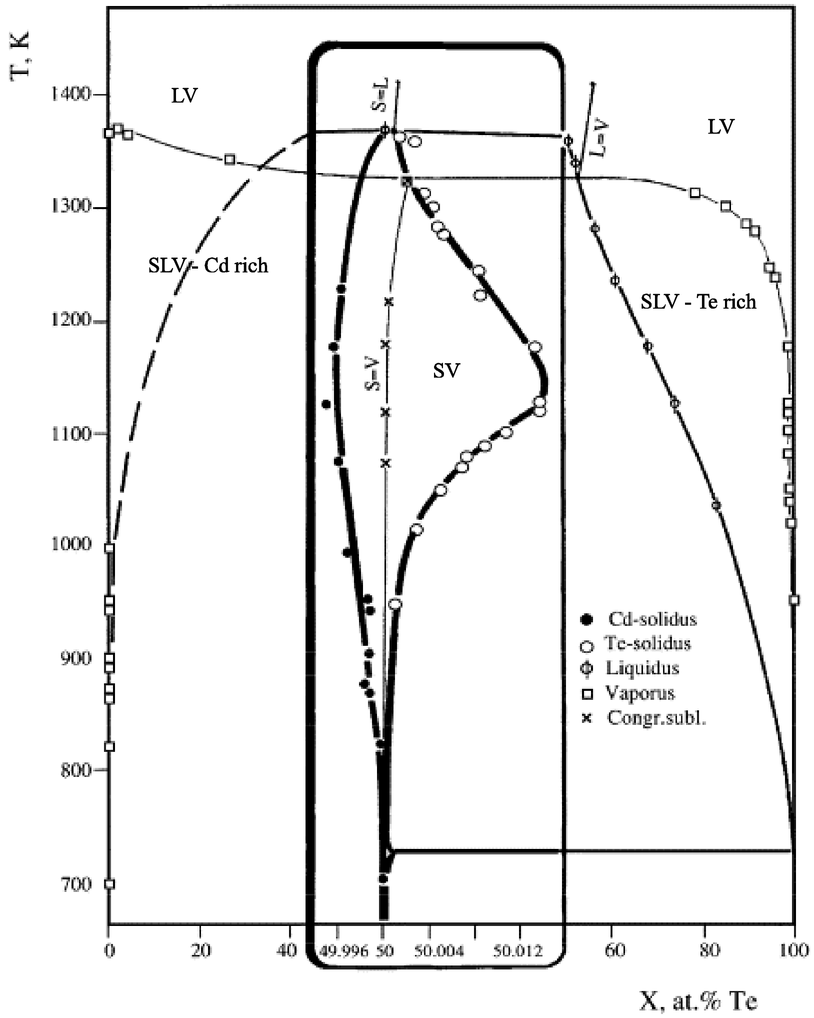

Figure 1.14: The temperature-composition projection of the phase diagram for CdTe. Solid cadmium telluride can only exist within a very narrow range of compositions (approximatly 49.996-50.012 %Te). Figure from [4]. *Figure used with permission from Elsevier.*

It is known that non-stoichiometric compounds have compromised semiconductor properties. Typically, the more stoichiometric the material is, the more suitable it is for use in a device [55]. It is apparent from Fig. 1.14 that growing stoichiometric material by VPG is challenging, as the range of possible compositions is largest at precisely the temperatures of interest for VPG of CdTe (1073-1173 K) [8]. Although it is possible to obtain stoichiometric material by VPG, it is clear from the phase diagram that it is challenging.

Chapter 2

Transport Model Part I - The Bulk Phases

This chapter describes the equations governing the transport in the bulk phases (solid, vapor) of the PVT model.

2.1 Preliminaries

Before proceeding, we must formally define our model domain, and the assumptions under which our derivation shall be made.

2.1.1 Model domain

The model domain is shown in Fig. 2.1. The bulk phases consist of the solid phase (source), of thickness x_0, located at the left hand side of the domain; a vapor phase extending from $x = 0$ to $x = x_2$ and a second solid phase (seed) extending from $x = x_2$ to $x = x_3$. We call the interface located at 0 Interface 1, and the interface located at x_2 Interface 2. Temperatures at the end of the solid material (x_0, x_3) are prescribed as T_0 and T_3. A wall temperature profile $T_w(x)$ is prescribed along the length of the domain as shown. The domain represents a tubular glass ampoule with inner diameter d_a.

2.1.2 Assumptions

We consider steady state transport only. These assumptions are discussed in more detail in §2.5.

Assumption 1 *: The vapor is considered an ideal gas mixture.*

Assumption 2 *: The solid is considered incompressible.*

Assumption 3 *: Convective and viscous effects are neglected.*[1]

Assumption 4 *: Thermal conductivities and specific heats are considered constant in terms of temperature within the bulk phases.*

---

[1] *Gravity driven convection as opposed to advection, which our model does consider.*

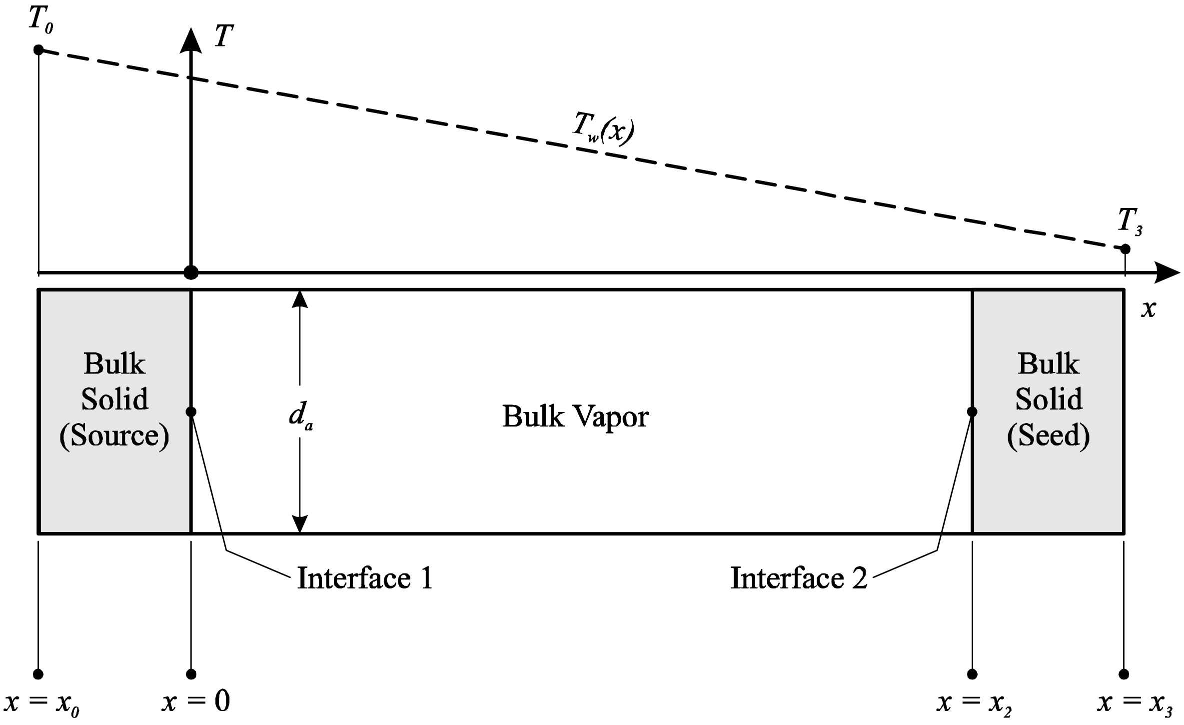

Figure 2.1: The model domain for the PVT model. A linear temperature profile is shown.

Assumption 5 *: The transport rate within the bulk phases is slow, so that second order and higher velocity terms may be neglected.*

Assumption 6 *: Local thermodynamic equilibrium is assumed within the model domain.*

Assumption 7 *: Radiative heat transfer from the crystal surfaces is ignored.*

We also consider the assumptions of *linearized diffusion theory* [32] to model the mass diffusion; these are,

Assumption 8 *: The diffusion coefficient is uniform and constant throughout the domain.*

Assumption 9 *: The density of the bulk vapor is considered constant in the diffusion term.*

Assumption 10 *: The total volume of the bulk vapor phase V is approximately constant.*

2.2 Definitions

In this section, we explicitly define the required quantities, all on a mole basis. The mole based quantities can be converted to mass based quantities using the molecular weight M.

2.2.1 Physical properties

We start with the mole density:

$$c = \sum_{a=1}^{\nu} c_a \ ; \tag{2.1}$$

where c_α is the partial mole density of constituent a. The mole fraction is defined as

$$\chi_a = \frac{c_a}{c}, \tag{2.2}$$

with the condition that

$$\sum_a \chi_a = 1. \tag{2.2b}$$

The total molecular weight of the mixture is given by the mole weighted average

$$M = \sum_a \chi_a M_a. \tag{2.3}$$

Since the vapor is an ideal gas mixture, the mole fraction is related to the partial pressure ratio by Dalton's law [56]

$$\chi_a = \frac{p_a}{\sum_a p_a} = \frac{p_a}{p}. \tag{2.4}$$

The mole-centric velocity is defined as

$$\tilde{v}_i = \sum_a \chi_a v_i^a \ ; \tag{2.5}$$

where v_i^a is the component velocity[2]. The mass-centric velocity is defined as

$$v_i = \sum_a \frac{\rho_\alpha}{\rho} v_i^a, \tag{2.6}$$

where $\rho_a = M_a c_a$, $\rho = Mc$ are the component and total mass densities respectively. The partial and total mole flux are defined as

$$J_i^a = c_a v_i^a \ , \tag{2.7}$$

and,

$$J_i = c\tilde{v}_i = \sum_a J_i^a. \tag{2.8}$$

We define the mole diffusion flux,

$$I_k^a = c_a \left(v_k^a - \tilde{v}_k\right) = J_k^a - \chi_a J_k. \tag{2.9}$$

which is subject to

$$\sum_a I_k^a = 0, \tag{2.10}$$

as a consequence of (2.2b) and (2.5).

2.2.2 Thermochemical properties

The thermochemical properties are defined considering assumptions 1 and 4. The internal energy for any ideal substance or mixture is given as

$$\bar{u}(T) = \sum_a \chi_a \bar{u}_a(T). \tag{2.11}$$

The enthalpy, defined as $\bar{h} = \bar{u} + \frac{p}{c}$, is obtained as

$$\bar{h}(T) = \sum \chi_\alpha \bar{h}_\alpha(T). \tag{2.12}$$

---

[2] In a pure substance, the mole centric velocity is always equal the mass centric velocity; this is true of mixture constituents as well, but not of the overall mixture.

For an incompressible solid, $\bar{u} = \bar{h}$; for an ideal gas with constant specific heats, $\bar{u}$ and $\bar{h}$ are given by

$$\begin{aligned} \bar{u} &= \bar{C}_v \left(T - T_0 \right), \\ \bar{h} &= \bar{C}_p \left(T - T_0 \right); \end{aligned}$$

where $\bar{C}_v$ is the constant pressure specific heat and $\bar{C}_p$ is the constant pressure specific heat. These can be related to one another by the universal gas constant

$$R_u = \bar{C}_p - \bar{C}_v. \tag{2.13}$$

In an ideal gas mixture

$$\bar{C}_v = \sum \chi_a \bar{C}_v^a, \tag{2.14}$$

$$\bar{C}_p = \sum \chi_a \bar{C}_p^a. \tag{2.15}$$

We will obtain specific heat values from empirical data.

When comparing enthalpies of the vapor phase and solid phase, it is important to ensure that all enthalpies are written in terms of the same reference condition. To do this, we must account for the latent heat of sublimation[3] $\Delta\bar{h}_{sv}$. For a system at reference temperature T_{ref}, the enthalpies for the solid and vapor phases are obtained as

$$\bar{h}_s(T) = \bar{C}_s(T - T_{ref}), \tag{2.16}$$

$$\bar{h}_v(T) = \bar{C}_v(T - T_{ref}) + \Delta\bar{h}_{sv}; \tag{2.17}$$

here, $\bar{C}_s$ is the heat capacity of the incompressible solid.

The entropy of an ideal gas is given as

$$\bar{s}(T, p) = \hat{s}(T) - R_u \ln \frac{p}{p_0}, \tag{2.18}$$

where $\hat{s}(T)$ is the thermal part of the entropy term; if the specific heat is constant

$$\hat{s}(T) = \bar{C}_p \ln \frac{T}{T_0}. \tag{2.19}$$

---

[3] For inert constituants, that exist only in the vapor phase, it is not necessary to account for the latent heat of sublimation.

For an ideal gas mixture, the entropy can be written as a sum of the constituent entropies,

$$\bar{s}(T,p) = \sum_a \chi_a \bar{s}_a(T,p_a) = \sum_a \chi_a \bar{s}_a(T,p) + R_u \sum_a \chi_a \ln \chi_a, \tag{2.20}$$

where the logarithmic term accounts for the entropy of mixing. For an ideal, incompressible solid, entropy is only a function of temperature, for constant specific heats as

$$\bar{s}_s(T) = \hat{s}_s(T) = \bar{C}_s \ln \frac{T}{T_0}. \tag{2.21}$$

The Gibbs free energy is defined as

$$\bar{g}(T,p) = \bar{h} - T\bar{s}. \tag{2.22}$$

For an incompressible solid, this is only a function of temperature. For an ideal gas, the Gibbs free energy can be split into a thermal and a hydraulic part, like the entropy,

$$\bar{g}(T,p) = \hat{g}(T) + R_u T \ln \frac{p}{p_0}; \tag{2.23}$$

where $\hat{g}(T) = \bar{h}(T) - T\hat{s}(T)$. In a mixture, the total molar Gibbs free energy is the mole average of the chemical potential μ_a of each constituent,

$$\bar{g}(T,p) = \sum \chi_a \bar{\mu}_a(T,p_a), \tag{2.24}$$

where

$$\bar{\mu}_a(T,p_a) = \hat{g}_a(T) + R_u T \ln \frac{p_a}{p_0}. \tag{2.25}$$

2.3 The Balance Laws

We define the bulk vapor equations assuming that the vapor constitutes a constant control volume for which we shall define the balance laws. The simplified form of these balance laws will define the governing equations for the transport problems.

The general form of a local balance law reads [57],

$$\frac{\partial c\bar{\varphi}}{\partial t} + \frac{\partial}{\partial x_k}\left(c\bar{\varphi}\tilde{v}_k + \bar{\phi}_k\right) = c\bar{\pi}. \tag{2.26}$$

Here, c is the mole density, $\tilde{v}_k$ is the total mole-centric velocity, φ is the quantity we are balancing, ϕ_k is the non-advective flux, and π is a production/supply term.

The reader should note that the Einstein summation has been invoked; for a review see any textbook on tensor calculus, (e.g., [58]).

2.3.1 The continuity equation

We begin by writing the mole balance, such that $\bar{\varphi} = 1$ in (2.26). Particles are transported only by convective fluxes, therefore $\bar{\phi}_k = 0$. Since we do not consider a reacting mixture, there are no sources of particles within the bulk, therefore, $\bar{\pi} = 0$. The partial continuity equation is then found for our model, written in one dimension as

$$\frac{\partial c_a}{\partial t} + \frac{\partial}{\partial x}(c_a v_a) = \frac{\partial c_a}{\partial t} + \frac{\partial}{\partial x} J_a = 0. \tag{2.27}$$

Given that we model steady state transport only, the equation simplifies to

$$\frac{dJ_a}{dx} = 0. \tag{2.28}$$

Integration of the partial continuity equations gives

$$J_a = c_a v_a = \text{constant}. \tag{2.29}$$

By summing (2.27) we obtain the continuity equation for the overall mixture

$$\frac{\partial c}{\partial t} + \frac{\partial}{\partial x} J = 0; \tag{2.30}$$

which simplifies to

$$\frac{dJ}{dx} = 0, \tag{2.31}$$

and as a consequence of this

$$J = \sum_a J_a = \text{constant}. \tag{2.32}$$

The continuity equation (2.27) can be written as a mass balance, with $\bar{\varphi} = M$ in (2.26)

$$\frac{\partial \rho}{\partial t} + \frac{\partial}{\partial x}(\rho v) = 0. \tag{2.33}$$

2.3.2 The mole transport equation

Straightforward manipulations of (2.27) and combination with (2.30) gives the mole transport equation,

$$c\frac{\partial \chi_a}{\partial t} + J\frac{\partial \chi_a}{\partial x} + \frac{\partial}{\partial x} I_a = 0; \tag{2.34}$$

which in steady state can be integrated and re-written as,

$$J_a = J\chi_a + I_a. \tag{2.35}$$

In the bulk solid phases, diffusion is negligible; $I_a = 0$. Therefore, for the solid phase, we have

$$J_a = J\chi_a. \tag{2.36}$$

One must be very careful to apply Eq. (2.36) to the solid phase only, and not to the vapor phase.

2.3.3 Momentum balance

Using the balance law framework (2.26), the momentum balance for the total mixture follows with $\bar{\varphi}_i = Mv_i$, where v_i is the mass-centric velocity, $\bar{\phi}_k = -t_{ik}$ is the stress tensor and $\bar{\pi} = a_i$ is the net acceleration vector, which gives the body force. The momentum balance is then

$$\rho\left(\frac{\partial v_i}{\partial t} + v_k\frac{\partial v_i}{\partial x_k}\right) - \frac{\partial t_{ik}}{\partial x_k} = \rho a_i. \tag{2.37}$$

Since we neglect all viscous forces [59],

$$t_{ik} = -p\delta_{ik}; \tag{2.38}$$

where δ_{ij} is the Kronecker delta. Since we consider only 1D steady state transport, (2.37) becomes

$$\rho v\frac{\partial v}{\partial x} + \frac{\partial p}{\partial x} = \rho a_i. \tag{2.39}$$

Finally, we apply Assumption 5, and thus neglect the second order terms in the velocity,

$$\frac{dp}{dx} = 0; \tag{2.40}$$

which upon integration gives

$$p = \text{constant}. \tag{2.41}$$

2.3.4 Energy Balance - The first law

Using the balance law framework (2.26), we identify the total energy as the sum of the kinetic and internal energy, such that $\varphi = u + \frac{1}{2}v^2$. Since the body forces are neglected, we may neglect the potential energy. The non-convective flux includes the heat flux and the stress tensor such that $\bar{\phi}_k = q_k - v_i t_{ik}$; for now we leave the supply term π undefined. The energy balance is then

$$c\frac{\partial}{\partial t}\left(\bar{u}+\frac{1}{2}v^2\right)+\frac{\partial}{\partial x_k}\left[c\tilde{v}_k\left(\bar{u}+\frac{1}{2}v^2\right)+q_k-v_it_{ik}\right]=c\pi. \tag{2.42}$$

Applying 5 and replacing the stress tensor with (2.38) we obtain

$$c\frac{\partial\bar{u}}{\partial t}+\frac{\partial}{\partial x_k}\left(J_k\bar{h}+q_k\right)=c\pi. \tag{2.43}$$

In one dimensional steady state, this simplifies to

$$\frac{d}{dx}\left(J\bar{h}+q\right)=c\pi. \tag{2.44}$$

Since the 1-D model cannot capture heat flux from the wall into the vapor directly, we use the supply term to incorporate this heat flux. For this, we define the supply term using Newton's law of cooling as [60],

$$c\pi=\Lambda\left\{T_w(x)-T(x)\right\}; \tag{2.45}$$

where Λ is the effective heat transfer coefficient. The energy balance now becomes

$$\frac{d}{dx}\left(J\bar{h}+q\right)=\Lambda\left\{T_w(x)-T(x)\right\}. \tag{2.46}$$

2.3.5 Entropy Balance - The second law

In order to ensure consistency with what has been derived already, we avoid the balance law structure entirely, and instead derive the entropy balance using LIT [31, 20]. Assumption 6 allows us to use equilibrium thermodynamics at the microscopic scale, even though the overall system is not in equilibrium. We start by recalling the Gibbs equation for a mixture in mole specific quantities [56]

$$d\bar{u}=Td\bar{s}+\frac{p}{c^2}dc+\sum_a\bar{\mu}_a d\chi_a, \tag{2.47}$$

we rewrite the differential quantities as partial time derivatives to obtain,

$$c\frac{\partial\bar{s}}{\partial t}=\frac{c}{T}\frac{\partial\bar{u}}{\partial t}-\frac{p}{Tc}\frac{\partial c}{\partial t}-\frac{c}{T}\sum\bar{\mu}_a\frac{\partial\chi_a}{\partial t}. \tag{2.48}$$

We can replace the three time derivatives on the right hand side of the above with the energy balance (2.43), net continuity equation (2.30) and the advection-diffusion equation (2.27).

$$c\frac{\partial \bar{s}}{\partial t} = \frac{1}{T}\left[c\pi - \frac{\partial}{\partial x_k}\left(J_k\bar{h} + q_k\right)\right] + \frac{1}{T}\sum \bar{\mu}_a\left\{J\frac{\partial \chi_a}{\partial x_k} + \frac{\partial I_k^a}{\partial x_k}\right\}.$$

Careful manipulations lead to

$$c\frac{\partial \bar{s}}{\partial t} + \frac{\partial}{\partial x_k}\left[\frac{1}{T}\left(J_k h - \sum J_k^a \mu_a + q_k\right)\right] = \sigma \geq 0; \tag{2.49}$$

where the entropy generation is given by

$$\sigma = \left(q_k + J_k h\right)\frac{\partial}{\partial x_k}\left(\frac{1}{T}\right) - \sum J_k^a \frac{\partial}{\partial x_k}\left(\frac{\bar{\mu}_a}{T}\right). \tag{2.50}$$

Note that we have neglected the supply term in (2.46), this term is effectively a heat transfer term, and thus has been lumped in with q in (2.49). Equation (2.49) is not yet a proper balance law in the form of (2.26). Manipulations of the convective term in (2.49) lead to the identity,

$$\frac{1}{T}\left(J_k h - \sum J_k^a \bar{\mu}_a + q_k\right) = J\bar{s} + \frac{1}{T}\left(q_k - \sum I_k^a \bar{\mu}_a\right); \tag{2.51}$$

thus, we obtain the final, proper form of the entropy balance,

$$c\frac{\partial \bar{s}}{\partial t} + \frac{\partial}{\partial x}\left[J\bar{s} + \frac{1}{T}\left(q - \sum I_a \bar{\mu}_a\right)\right] = \sigma. \tag{2.52}$$

Galilean invariance requires that the entropy generation be independent of the frame of reference [31]. To verify this, we consider a transformation to a reference frame with velocity v'. Thus,

$$\begin{aligned} J' &= J + cv', \\ J_a' &= J_a + c_a v'. \end{aligned}$$

We substitute these into (2.50), and find,

$$\sigma' = \sigma + cv_k' h\frac{\partial}{\partial x_k}\left(\frac{1}{T}\right) - \sum c_a v_k' \frac{\partial}{\partial x_k}\left(\frac{\bar{\mu}_a}{T}\right).$$

Since $\sigma' = \sigma$ must be true, we must prove that

$$\bar{h}\frac{\partial}{\partial x_k}\left(\frac{1}{T}\right) - \sum \chi_a \frac{\partial}{\partial x_k}\left(\frac{\bar{\mu}_a}{T}\right) = 0.$$

We consider the Gibbs-Duhem equation, which for constant pressure is

$$\bar{s}dT + \sum_a \chi_a d\bar{\mu}_a = 0. \tag{2.53}$$

We replace the total differentials with partial derivatives in x; we also replace $\bar{s}$ using the definition of Gibbs free energy $\bar{g} = \bar{h} - T\bar{s}$, thus

$$-\left(\frac{\bar{g} - \bar{h}}{T}\right)\frac{\partial T}{\partial x_k} + \sum_a \chi_a \frac{\partial \bar{\mu}_a}{\partial x_k} = 0.$$

We now use $\bar{g} = \sum_a \chi_a \bar{\mu}_a$, and transform the derivatives by multiplying the expression by $\frac{1}{T}$,

$$-\bar{h}\frac{\partial}{\partial x_k}\left(\frac{1}{T}\right) + \sum_a \chi_a \bar{\mu}_a \frac{\partial}{\partial x_k}\left(\frac{1}{T}\right) + \frac{1}{T}\sum_a \chi_a \frac{\partial \bar{\mu}_a}{\partial x_k} = 0.$$

We can now combine derivatives and find

$$\bar{h}\frac{\partial}{\partial x_k}\left(\frac{1}{T}\right) - \sum_a \chi_a \frac{\partial}{\partial x_k}\left(\frac{\bar{\mu}_a}{T}\right) = 0. \tag{2.54}$$

Thus, we prove that $\sigma' = \sigma$.

2.4 Constitutive Assumptions

We now require expressions for the diffusion flux I_k^a, and the heat flux q_k. We obtain these from linear irreversible thermodynamics (LIT) as discussed in Chapter 1. By inspection, we see that the entropy generation (2.50) is in the form,

$$\sigma = \sum \mathcal{J}_A \mathcal{X}_A, \tag{2.55}$$

where $\mathcal{J}_A$ are thermodynamic fluxes and $\mathcal{X}_A$ are thermodynamic forces. Applying thermodynamic transformations described in [20] (2.50) becomes

$$\sigma = \left(q_k - \sum_a I_k^a h_a\right)\frac{\partial}{\partial x_k}\left(\frac{1}{T}\right) - \sum_a J_k^a \left(\frac{\partial \mu_a}{\partial x_k}\right)_T \tag{2.56}$$

where the derivative $\left(\frac{\partial \mu_a}{\partial x_k}\right)_T$ is taken at constant temperature. Since we have already shown that the entropy generation is independent of the frame of reference, we consider a frame where $J = 0$; as a result, (2.9) becomes

$$I_k^a = J_k^a.$$

We recall that $\sum I_k^a = 0$; thus, there are only $\nu - 1$ independent fluxes in the entropy generation term, where ν is the total number of mixture constituents. The entropy generation becomes

$$\sigma = q_k' \frac{\partial}{\partial x_k}\left(\frac{1}{T}\right) - \sum_a I_k^a \frac{\partial}{\partial x_k}\left(\mu_a - \mu_\nu\right)_T, \tag{2.57}$$

where

$$q_k' = q_k - \sum_a I_k^a \left(h_a - h_\nu\right) \tag{2.58}$$

is called the measurable heat flux [20]. Since the system is at constant pressure, the entropy generation can be further simplified to the form

$$\sigma = q_k' \frac{\partial}{\partial x_k}\left(\frac{1}{T}\right) - \sum_a I_k^a \frac{\partial}{\partial c_a}\left(\mu_a - \mu_\nu\right)_T \frac{\partial c_a}{\partial x_k}.$$

This form of the LIT reciprocity relation (1.3) can be written

$$\begin{bmatrix} q_k' \\ I_k^a \\ \vdots \\ I_k^n \end{bmatrix} = \begin{bmatrix} l_{qq} & l_{qa} & \cdots & l_{qn} \\ l_{aq} & l_{aa} & \cdots & l_{an} \\ \vdots & \vdots & \ddots & \vdots \\ l_{nq} & l_{an} & \cdots & l_{nn} \end{bmatrix} \begin{bmatrix} -\frac{1}{T^2}\frac{\partial T}{\partial x} \\ -\frac{\partial}{\partial c_a}\left(\mu_a - \mu_\nu\right)_T \frac{\partial c_a}{\partial x_k} \\ \vdots \\ -\frac{\partial}{\partial c_n}\left(\mu_n - \mu_\nu\right)_T \frac{\partial c_n}{\partial x_k} \end{bmatrix}. \tag{2.59}$$

where $n = \nu - 1$. The diffusion flux I_a and the measurable heat flux q' are governed by influences from both the concentration gradients and the temperature gradient in the vapor. Diffusion flux driven by the temperature gradient is called Soret diffusion, measurable heat flux driven by concentration gradients is called the Dufor effect [20]. Except in cases where the molecular weights of the mixture constituents are vary greatly, these effects can typically be neglected.

Assumption 11 *The Soret effect and Dufor effect are neglected in the bulk vapor; that is* $\{l_{qa}, ..., l_{qn}\} = 0$ *and* $\{l_{aq}, ..., l_{nq}\} = 0$.

The diffusion flux can now be defined from (2.59) in terms of Fick's law for an ideal gas mixture

$$I_k^a = -\sum_{b=1}^{\nu-1} l_{ab} \frac{\partial\left(\mu_b - \mu_\nu\right)_T}{\partial c_b} \frac{\partial c_b}{\partial x_k} = -\sum_{b=1}^{\nu-1} \mathcal{D}_{a\gamma} \frac{\partial c_\gamma}{\partial x_k}, \tag{2.60}$$

where $\mathcal{D}_{a\gamma}$is a non-symmetric diffusivity matrix. An expression for the total measurable heat flux can also be obtained

$$q' = -\frac{l_{qq}}{T_2}\frac{\partial T}{\partial x}. \tag{2.61}$$

This is in the form of Fourier's law, however the $-\frac{l_{qq}}{T_2}$ is *not* the thermal conductivity of the mixture. Instead, it is a conductivity term that is dependent upon the diffusion flux and concentration gradient in the mixture, and is not easy to obtain. We therefore assume

$$q \gg \sum I_a \left(h_a - h_\nu\right), \tag{2.62}$$

thus,

$$q = -\kappa\frac{\partial T}{\partial x} \simeq q' = -\frac{l_{qq}}{T_2}\frac{\partial T}{\partial x}. \tag{2.63}$$

This is Fourier's law for heat conduction, where κ is a the heat transfer coefficient.

2.4.1 Linearized Fick's law for diffusion

Fick's law is often considered in a linearized form [32]. The linearized Fick's law for a binary mixture,

$$I_k^a = -D_{ab}c\frac{\partial \chi_a}{\partial x_k}; \tag{2.64}$$

where D_{ab} is the binary diffusivity between the two constituents a and b. This assumes that the total density term is constant in the bulk vapor.[32]. Since our model assumes constant pressure, by the application of the ideal gas law and Dalton's law, the diffusion flux becomes

$$I_k^a = -\frac{D_{ab}}{R_u T}\frac{\partial p_a}{\partial x_k}; \tag{2.65}$$

where R_u is the universal gas constant.

For a higher order ($\nu > 2$) mixture, the linearized Fick's law is [32],

$$I_k^a = -c\sum_{\gamma=1}^{\nu-1}\mathcal{D}_{a\gamma}\frac{\partial \chi_\gamma}{\partial x_k}, \tag{2.66}$$

This equation can also be re-written using the ideal gas law and Dalton's law

$$I_k^a = -\frac{1}{R_u T}\sum_{\gamma=1}^{\nu-1}\mathcal{D}_{a\gamma}\frac{\partial p_\gamma}{\partial x_k}. \tag{2.67}$$

2.4.2 Diffusion coefficients

The binary diffusion coefficients can be obtained either through experiment, or through estimates based upon kinetic theory and statistical mechanics. In either case, the coefficients are usually only reported for one particular set of conditions (T, p); it is therefore important to understand how to adjust the binary diffusion coefficients for different conditions.

We begin by looking at the kinetic theory expression for the diffusion coefficient in a binary ideal gas mixture of constituents a and b [32],

$$D_{ab} = \hat{C}T^{3/2}\frac{\sqrt{(M_a + M_b)/(M_a M_b)}}{p\sigma_{ab}^2 \mathcal{S}_D}; \tag{2.68}$$

where $\hat{C}$ is a constant, σ_{ab} is the characteristic length, and $\mathcal{S}_D$ is the kinetic theory collision integral, which is dependent upon temperature. The kinetic theory expression can be approximated by the expression [61]

$$D_{ab} = CT^{1.75}\frac{\sqrt{(M_a + M_b)/(M_a M_b)}}{p\left\{\sqrt[3]{V_a} + \sqrt[3]{V_b}\right\}^2}; \tag{2.69}$$

where C is another constant, V_a and V_b are temperature independent molecular diffusion volumes of each particular species, discussed in more detail by Poling et al.[61]. This expression contains the full temperature dependency. We now assume we know one diffusion coefficient value D_{ab}^D at T_D and p_D; we can find the diffusion coefficient for any p and T by rewriting (2.69),

$$D_{ab}(T, p) = D_{ab}^D \frac{p_D}{p}\left(\frac{T}{T_D}\right)^{1.75}. \tag{2.70}$$

Thus, any given value for a diffusion coefficient can be adjusted to different conditions.

In a ternary system, the terms of the diffusivity matrix are different from the diffusion coefficients of the binary-pairs within the system. Determining these coefficients can be a complex problem for many substances; fortunately, the procedure is straightforward in an ideal gas mixture.

We consider a ternary ideal gas mixture of constituents, 1, 2 and 3 with composition $\{\chi_1, \chi_2, \chi_3\}$; the ternary diffusion coefficient matrix $\mathcal{D}$ can be obtained by first determining its inverse $\mathcal{B}_{AB}$ [32],

$$\mathcal{B}_{11} = \frac{\chi_1}{D_{13}[T, p(1-\chi_2)]} + \frac{\chi_2}{D_{12}[T, p(1-\chi_3)]} + \frac{\chi_3}{D_{13}[T, p(1-\chi_2)]}, \tag{2.71a}$$

$$\mathcal{B}_{12} = -\chi_1\left(\frac{1}{D_{12}[T, p(1-\chi_3)]} - \frac{1}{D_{13}[T, p(1-\chi_2)]}\right), \tag{2.71b}$$

$$\mathcal{B}_{21} = -\chi_2\left(\frac{1}{D_{12}[T, p(1-\chi_3)]} - \frac{1}{D_{23}[T, p(1-\chi_1)]}\right), \tag{2.71c}$$

$$\mathcal{B}_{22} = \frac{\chi_1}{D_{12}[T, p(1-\chi_3)]} + \frac{\chi_b}{D_{23}[T, p(1-\chi_1)]} + \frac{\chi_c}{D_{23}[T, p(1-\chi_1)]}. \tag{2.71d}$$

where $D_{12}\left[T, p\left(1-\chi_3\right)\right]$, $D_{23}\left[T, p\left(1-\chi_1\right)\right]$ and $D_{13}\left[T, p\left(1-\chi_2\right)\right]$ are the binary diffusion functions of the corresponding pairs determined by (2.70). Given that, by definition $\chi_3 = 1 - \chi_1 - \chi_2$, the ternary diffusivity matrix is now obtained as $\mathcal{D}(T, p, \chi_1, \chi_2) = \mathcal{B}^{-1}$.

2.4.3 Thermal Conductivities

Thermal conductivities for most solids have been measured and are found in the literature. Measured values for vapor thermal conductivity are more difficult to obtain, especially for the exotic substances we consider. We instead use estimates based upon kinetic theory to obtain these.

For both monatomic and polyatomic ideal gasses, the thermal conductivity can be estimated by the Modified Eucken model [61], where

$$\kappa_a(T) = \frac{\eta \bar{C}_v}{M'} \left(1.15 + \frac{2.03 R_u}{\bar{C}_v}\right). \tag{2.72}$$

M' is the molecular weight of the gas in units $\left[\frac{\mathrm{kg}}{\mathrm{mol}}\right]$; and η is the Chapman-Enskog viscosity of the gas, calculated as

$$\eta = \frac{26.69\sqrt{MT}}{d_c^2 \mathcal{S}_v} \tag{2.73}$$

for a basic estimate, the collision integral $\mathcal{S}_v$ is typically set to unity, d_c is the hard sphere particle diameter.

For a mixture the thermal conductivity of a mixture can be approximated by using the Wassiljeva equation [61]

$$\kappa_{mix} = \sum_{i=1}^{n} \frac{\chi_i \kappa_i(T)}{\sum_{j=1}^{n} \chi_j A_{ij}}; \tag{2.74}$$

where A_{ab} is calculated using the Mason and Saxena equation [61]

$$A_{ij} = \frac{\left[1 + \sqrt{\frac{\kappa_i}{\kappa_j}} \sqrt[4]{\frac{M_i}{M_j}}\right]^2}{\left[8\left(1 + \frac{M_i}{M_j}\right)\right]^{1/2}}. \tag{2.75}$$

2.4.4 Wall heat transfer coefficient

The transfer coefficient Λ in (2.46) can be written for the vapor as [60],

$$\Lambda_v = \frac{4H}{d_a}; \tag{2.76}$$

where H is the convective heat transfer coefficient. Since the flow velocity is low, and viscous effects are neglected, we assume the flow within the ampoule is laminar. Incorpera suggests a Nusselt number of 4.36 for heat transfer into a circular duct with constant heat flux, or 3.66 for constant wall temperature. Since we have neither, we pick a Nusselt number half way between these at 4.00. The estimated convective heat transfer coefficient now becomes [60],

$$H \simeq \frac{4.00\kappa}{d_a}. \tag{2.77}$$

Thus, the transfer coefficient becomes,

$$\Lambda_v = \frac{16H}{d_a}.$$

Although this assumption is somewhat questionable, it is certainly an improvement over other 1D PVT models which do not account for heat transfer in the bulk at all [9, 13].

For the bulk solid, heat transport into the center of the ampoule from the walls occurs purely by conduction. In can easily be deduced from the first law written over a differential section of the ampoule that the effective heat transfer coefficient in the bulk solid is [60]

$$\Lambda_s = \frac{8\kappa_s}{d_a^2}. \tag{2.78}$$

2.5 Discussion of Assumptions.

2.5.1 Steady State Modeling

Real crystal growth experiments have a transient contribution at the beginning and end of the run, as well as an ongoing evolution of the interface shape [24, 5]. Due to the low growth rate normally encountered in crystal growth experiments, the transient effects associated with the start and end of an experiment are relatively short lived when compared to the overall duration of the experiment. As for the evolution of the interface shape, the magnitude of this evolution is small when compared to the overall dimensions of the apparatus, again due to low growth rates [9]. We analyze the impact of the steady state assumption in Chapter 7.

2.5.2 1-Dimensional Modelling

The major limitation of a 1D model is that convective effects are neglected. These effects becomes important when the pressure within the growth ampoule becomes sufficiently high, as we show in Chapter 7. At lower pressures, the effects of convection in vapor crystal growth are a topic of continued research and debate [11, 5, 62]. Since we find that our model reproduces low pressure experimental results accurately (see Chapter 7 and Chapter 8), we believe that the 1D assumption and the resultant neglection of convection is justified.

2.5.3 Assumption 1: The vapor as an ideal gas mixture.

In single species diffusionless transport, the bulk vapor consists of only one species. The ideal gas assumption requires a compressibility factor of unity [56]. The dimensionless reduced pressure $p_r = \frac{p_v}{p_{cr}}$ and reduced temperature $T_r = \frac{T_v}{T_{cr}}$ are indicators of the vapor's compressibility. According to the Nelson-Obert generalized compressibility charts [56], compressibility remains within the range of 1.0 to 0.95 for high temperatures in excess of the critical temperature T_{cr} and low pressures, where p_r is no greater than 0.05. Since vapor growth takes place at high temperature and low pressure the ideal gas assumption is valid [9].

To confirm ideal gas behavior of the mixture, we consider the compressibility of the mixture, where the combined mixture compressibility is calculated by [56],

$$Z = \sum_{a=1}^{\nu} \chi_a Z_a; \tag{2.79}$$

where Z is the compressibility. If the resulting Z is near unity, the vapor mixture can be considered ideal. As in the case of a single species, the individual constituent compressibilities can be obtained from the Nelson-Obert charts. Since the temperature is high in vapor growth and the constituent partial pressures are low, the ideal gas assumption is valid.

2.5.4 Assumption 2: Incompressible solid.

Most solids can safely be assumed to be incompressible over the relatively low pressures and low pressures exhibited at the operating conditions characteristic of vapor crystal growth [9, 43].

2.5.5 Assumption 3: Convective and viscous effects are neglected.

We have already discussed convection. Viscosity can play a significant role in vapor crystal growth models [25], and is often incorporated, especially in more complex 2 or 3 dimensional models [11]. That being said, many other crystal growth experiments have growth rates low enough that viscous effects can be neglected. We demonstrate in Chapter 7 that under the conditions we consider, the magnitude of viscous losses is very small.

2.5.6 Assumption 4: Thermal conductivities, and specific heats are considered constant in terms of temperature within the bulk vapor.

This is a common assumption in vapor crystal growth models [9, 13]. In general, the temperature variation between the source and the seed are small, and thus the assumption is valid. We demonstrate the validity of this assumption in Chapter 5.

2.5.7 Assumption 5: The transport rate within the domain is slow, so that second order and higher velocity terms may be neglected.

This assumption has been frequently made in liquid-vapor-liquid transport models [63, 16, 40]. The assumption chiefly affects the momentum balance and the energy balance. In the momentum balance, this assumption leads to a constant pressure within the ampoule, which is very common in vapor crystal growth models [9, 12, 11, 13]. In the energy balance, we neglect the kinetic energy terms due to this assumption. The accuracy of this assumption can be easily checked once the total transport rate is estimated.

2.5.8 Assumption 6: Local thermodynamic equilibrium is assumed in the model domain.

This assumption is usually valid within the continuum regime, especially if the temperature and pressure gradients are relatively small [20]. In an ideal gas, the Knudsen number can be used to determine whether the gas is within the continuum regime. The Knudesen number is defined as the ratio of the mean free path to the critical dimension of the container, in our case the diameter of the ampoule. For an ideal gas, the Knudsen number is calculated [36],

$$\mathrm{Kn} = \frac{kT}{\sqrt{2}\pi d_c^2 p d_a}; \tag{2.80}$$

where k_b is the Boltzmann constant, d_c is the particle hard-sphere diameter that we use in Eq. (2.73) , p is the total pressure in the ampoule, and d_a is the ampoule diameter. For an ideal gas mixture, the mole weighted average d_c is used. The gas is considered within the continuum regime if $\mathrm{Kn} < 0.05$ [36]. We shall check the Knudsen number for each transport system to verify the validity of the local equilibrium assumption.

2.5.9 Assumption 7: Radiative heat transfer from the crystal surfaces is ignored.

As we shall see, this assumption is valid at low temperatures. The impact may be more severe however at larger temperatures. We discuss this assumption further in Chapter 7, 8 and 9.

2.5.10 Assumption 8: The diffusion coefficient is uniform and constant throughout the domain, and Assumption 9: The density of the bulk vapor is considered constant in the diffusion term.

Assumptions 8 and 9 are required in order to apply linearized diffusion theory. For the binary system, this assumption boiled down to neglecting the temperature variation within the bulk in the diffusion term; as we shall see, the error introduced by this assumption is negligible. In the ternary system, we also assume the diffusion coefficient matrix is constant throughout the domain. This might appear to the reader as a serious difficulty, as the composition of the vapor can change quite dramatically along the length of the domain [9]. Fortunately, it has been shown that the linearized diffusion theory is in good agreement with experimental results, even when the composition varies dramatically within the domain [32].

Chapter 3

Transport Model Part II - The Interface Model

In this chapter, we describe an interface model that allows us to derive non-equilibrium boundary conditions for sublimation and condensation. For the moment, we leave behind our bulk transport model and consider the general case of sublimation with a stationary, planar interface, as shown in Fig. 3.1. We introduce the following assumptions:

Assumption 12 *: The crystal interfaces are planar and retain their shape during growth.*

Assumption 13 *: In deviations from equilibrium, the solid surfaces retain their equilibrium properties at the interface temperature [39].*

Assumption 14 *: The solid phase is much denser than the vapor* $(c_s >> c_v)$ *.*

Assumption 15 *:The predominant surface growth modes are the step flow, and 3D (rough surface) growth modes.*

3.1 Interface Balance Laws

The balances of quantities at interfaces can be found using the jump condition framework. Jump conditions define the discontinuities in properties at interfaces [64]. Written out in full, the general form of a jump condition in terms of moles is:

$$\left\{c\varphi\left(\tilde{v}_k-\tilde{u}_k\right)+\phi_k\right\}_+ n_k-\left\{c\varphi\left(\tilde{v}_k-\tilde{u}_k\right)+\phi_k\right\}_- n_k=\Pi, \tag{3.1}$$

where the $+$ and $-$ subscripts represent the bulk vapor and bulk solid phases respectively, $\tilde{u}_k$ is the velocity of the interface, n_k is the interface unit normal vector, Π is the surface production term. We may re-write this in jump condition notation as

$$\left[\left[c\varphi\left(\tilde{v}_k-\tilde{u}_k\right)+\phi_k\right]\right] n_k=\Pi. \tag{3.2}$$

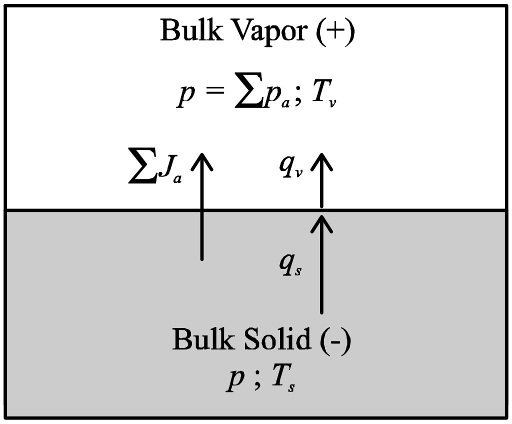

Figure 3.1: The 1-dimensional sublimation model. The temperatures and pressures as well as the mole fluxes and Fourier heat flux are shown. In this Chapter, we show that these fluxes constitute the thermodynamic fluxes as defined by the interface entropy generation (3.10).

For 1-dimensional transport (3.2) is simplified to

$$[[c\varphi\left(\tilde{v}-\tilde{u}\right)+\phi]]=\Pi. \tag{3.3}$$

3.1.1 Jump conditions for sublimation

We write the mole jump condition, considering (2.28) and (2.31). We replace φ with unity; the interface is stationary, so that $\tilde{u}$ is zero. Since, at least for now, we assume no reactions take place at the interface, Π is set to zero. The continuity jump conditions are then,

$$[[J]] = 0, \tag{3.4a}$$

$$[[J_a]] = 0. \tag{3.4b}$$

We now apply (3.3) to the momentum balance (2.37). In this case $\varphi = Mv$, and $\phi_k = -t_{ik}$ with no sources of momentum at the interface[1] $\Pi = 0$. Since the square velocity term vanishes per Assumption 5, the momentum jump gives

$$[[p]] = 0. \tag{3.5}$$

This is the classical pressure continuity expression valid for both liquids and solids [20, 39].

Next, we apply (3.3) to the energy balance (2.46), with $\varphi = u + \frac{1}{2}\tilde{v}^2$, $\phi = -\tilde{v}_k t_{ik} + q_i$ and no sources of

---

[1] Here, we assume that the surface energy, which our 1D model ignores is negligible.

energy at the interface[2] ($\Pi = 0$); we obtain,

$$\left[\left[J\bar{h} + q\right]\right] = 0. \tag{3.6}$$

Finally, we apply (3.3) to the entropy balance, (2.52). We set $\varphi = \bar{s}$, and $\phi = \frac{1}{T}\left(q_k - \sum I_a \bar{\mu}_a\right)$, with $\Pi = \sigma_s$. The ntropy jump across the interface is,

$$\left[\left[J\bar{s} + \frac{1}{T}\left(q_k - \sum_a I_a \bar{\mu}_a\right)\right]\right] = \sigma_s \geq 0; \tag{3.7}$$

where σ_s is the interface entropy generation. It is convenient to transform the interface generation in terms of the measurable heat flux q'

$$\left[\left[\sum_a J_a \bar{s}_a + \frac{1}{T} q'\right]\right] = \sigma_s \geq 0; \tag{3.8}$$

where, we recall the definition

$$q' = q - \sum_a I_a \bar{h}_a \tag{3.9}$$

3.2 Entropy Generation at the Interface

We combine (3.6) and (3.7) by eliminating the Fourier heat flux on the solid side of the interface; we also transform the entropy flux using identity (2.51). We thus obtain the entropy generation at the interface,

$$\sigma_s = \sum_a J_a \left[\frac{\bar{\mu}_a^s}{T_s} - \frac{\bar{\mu}_a^v}{T_v} + \bar{h}_v \left(\frac{1}{T_v} - \frac{1}{T_s}\right)\right] + q_v' \left(\frac{1}{T_v} - \frac{1}{T_s}\right) \geq 0; \tag{3.10}$$

where subscript s represents the solid and the subscript v represents the vapor. The entropy generation is in the form described by LIT (see Chapter 1), where

$$\sigma_s = \sum_A \mathcal{J}_A \mathcal{X}_A,$$

such that the thermodynamic fluxes are

$$\mathcal{J}_A = \{J_a, ..., J_\nu, q_v'\}$$

---

[2] If radiative heat transfer from the interface were incorporated into our model, it would be substituted into the energy balance as a source term. If we considered the surface energy at the interface, there would also be an additional contribution here.

and the corresponding thermodynamic forces are

$$\mathcal{X}_J^a = \frac{\bar{\mu}_a^s}{T_s} - \frac{\bar{\mu}_a^v}{T_v} + \bar{h}_v \left(\frac{1}{T_v} - \frac{1}{T_s}\right), \tag{3.11}$$

$$\mathcal{X}_q = \frac{1}{T_v} - \frac{1}{T_s}. \tag{3.12}$$

In equilibrium, the entropy generation at the interface must vanish ($\sigma_s = 0$) [31]. A part of LIT is requirement that that both the forces and fluxes vanish equally in equilibrium [31].Thus, $\mathcal{J}_A = 0$ and $\mathcal{X}_A = 0$. This gives the familiar equilibrium conditions: $T_v = T_s$ and $\bar{\mu}_a^s = \bar{\mu}_a^v$.

3.2.1 Reactive Sublimation

We now consider the special case of a reaction taking place at the interface during sublimation or condensation as is the case with CdTe (see Chapter 1). We consider a general reaction of the form

$$\mathrm{A_A ... A_\nu(s)} \rightleftharpoons \gamma_\mathrm{A} \mathrm{A_A(v)} + ... + \gamma_\nu \mathrm{A_\nu(v)} \tag{3.13}$$

which proceeds at reaction flux J_{Rx} where the subscript Rx indicates this is a reaction property. We take the total mole flux term of (3.10) and split it into solid and vapor parts,

$$\sum_a J_a \mathcal{X}_J^a = \sum_a J_a \frac{\bar{\mu}_a^s}{T_s} - \sum_a J_a \left[\frac{\bar{\mu}_a^v}{T_v} - \bar{h}_v \left(\frac{1}{T_v} - \frac{1}{T_s}\right)\right]; \tag{3.14}$$

the fluxes J_a are written for the vaporous products of (3.13); the J_a on the solid side are "virtual fluxes", fluxes that would be seen if a reaction were not taking place., and each flux corresponds to a product in (3.13). As we discussed in Chapter 2, the diffusion flux in the solid is negligible; thus, by Eq. (2.36) and (2.24)

$$\sum_a J_a \frac{\bar{\mu}_a^s}{T_s} = J_S \frac{\bar{g}_S}{T_s} \tag{3.15}$$

where J_S is the mole flux of the solid reactant. The constituent mole fluxes can be written in terms of the reaction flux J_{Rx} in the form

$$J_a = \frac{\gamma_a}{\sum_n \gamma_n} J_{Rx}. \tag{3.16}$$

where γ_n^v is written for the vaporous products only. As a consequence of (3.16), $J_S = J_{Rx}$. We recall that the Gibbs free energy for the ideal solid is a function of temperature only $\bar{g}_S\,(T_s, p) = \hat{g}_S(T_s)$ and that the the chemical potential for an ideal gas constituent is given by $\bar{\mu}_a(T, p_a) = \hat{g}_a(T) + R_u T \ln \frac{p_a}{p_0}$;

Eq. (3.14) with (3.15) and (3.16) becomes

$$\sum_a J_a \mathcal{X}_J^a = \frac{J_{Rx}}{\sum\limits_a \gamma_a} \left[\frac{\hat{g}_S(T_s)}{T_s} - \sum_a \gamma_a \frac{\hat{g}_a^v(T_v)}{T_v} - R_u \ln \prod_a \left(\frac{p_a}{p_0} \right)^{\gamma_a} + \right.$$

$$\left. + \sum_a \gamma_a \bar{h}_v \left(\frac{1}{T_v} - \frac{1}{T_s} \right) . \right] \tag{3.17}$$

We recall now that at equilibrium, the entropy generation, thermodynamic forces and thermodynamic fluxes must all vanish. We impose equilibrium conditions $\{T_v = T_s\,; p_a = p_{sat}^a(T_s)\}$ on (3.17) and find

$$\gamma_S \frac{\hat{g}_S(T_s)}{T_s} = \sum_a \gamma_a \frac{\hat{g}_a^v(T_s)}{T_s} + R_u \ln \{K_p(T_s)\} . \tag{3.18}$$

where

$$K_p(T) = \prod_a \left(\frac{p_{sat}^a}{p_0} \right)^{\gamma_a} = \exp \left[- \frac{\Delta \hat{g}_r^0(T)}{R_u T} \right] \tag{3.19}$$

is the equilibrium constant of the reaction. We introduce an analogous function for the actual partial pressures,

$$K_v = \prod_a \left(\frac{p_a}{p_0} \right)^{\gamma_a} . \tag{3.20}$$

Equations (3.18) and (3.20) substituted into (3.17) to give the final form of the thermodynamic force/flux pair in the presence of a chemical reaction at the interface,

$$\sum_a J_a \mathcal{X}_J^a = J_{Rx} \mathcal{X}_{Rx} \tag{3.21}$$

where,

$$\mathcal{X}_{Rx} = \frac{1}{\sum\limits_n \gamma_n} \left\{ R_u \ln \left[\frac{K_p(T_s)}{K_v} \right] + \sum_a \gamma_a \left[\left(\frac{\hat{g}_a^v(T_s)}{T_s} - \frac{\hat{g}_a^v(T_v)}{T_v} \right) + \bar{h}_v \left(\frac{1}{T_v} - \frac{1}{T_s} \right) \right] \right\} . \tag{3.22}$$

The second term of (3.22) is purely dependent upon the temperatures of the vapor and solid phases, and vanishes in equilibrium, where $T_s = T_v$.

3.2.2 Linearization of the forces

The thermodynamic forces we have now derived are non-linear in the temperature and partial pressure differences between the solid and the vapor phase. For small deviation from equilibrium the actual partial pressures, p_a, and actual temperatures T_v will differ only slightly from the saturation partial pressures p^a_{sat} and temperature T_s of the solid. We therefore linearize (3.11) and (3.12) by taking a Taylor series in terms of the temperature deviation from equilibrium $\Delta T = T_v - T_s$ and partial pressure deviations from equilibrium $\Delta p_a = p^a_{sat}(T_s) - p_a$ with regard to assumptions 1, 5, 13, and 14. After some manipulations and application of the thermodynamic property relations we obtain the linearized forces,

$$\mathcal{X}^a_J = \frac{R_u}{p^a_{sat}(T_s)}\Delta p_a; \tag{3.23a}$$

$$\mathcal{X}_q = -\frac{\Delta T}{T_s^2}. \tag{3.23b}$$

The chemical reaction force (3.22) can be linearized by taking a Taylor series expansion in terms of ΔT and $\Delta K = K_p(T_s) - K_v$. Remarkably, upon linearization we see that the temperature dependent part of (3.22) has a quadratic dependency on ΔT and thus vanishes completely in our linear model. The linearized force is then,

$$\mathcal{X}_{Rx} = \frac{\Delta K}{K_p(T_s)}. \tag{3.24}$$

This result matches the driving force used for CdTe transport by Laasch et al. [17].

In the crystal growth literature Δp_a is commonly referred to as the supersaturation of the vapor after its analogue in solution crystal growth [5]. For reactive systems, we shall term ΔK the chemical supersaturation.

3.2.3 Phenomenological coefficients

We recall that for small deviations from equilibrium the thermodynamic fluxes can be written as a linear product of the thermodynamic forces, as per LIT,

$$\mathcal{J}_A = \mathcal{L}_{AB}\mathcal{X}_B. \tag{3.25}$$

The entropy generation then becomes,

$$\sigma = \sum \mathcal{L}_{AB}\mathcal{X}_B\mathcal{X}_A > 0 \tag{3.26}$$

with the requirement that $\mathcal{L}_{AB}$ is a symmetric matrix of phenomenological conductivity coefficients that must be positive definite. For a unitary system,

$$\mathcal{L}^{(1)}_{AB} = \begin{bmatrix} l_{JJ} & l_{Jq} \\ l_{Jq} & l_{qq} \end{bmatrix}, \tag{3.27}$$

for systems of ν constituents

$$\mathcal{L}_{AB}^{(\nu)} = \begin{bmatrix} l_{aa}^{(\nu)} & \cdots & l_{an}^{(\nu)} & l_{aq}^{(\nu)} \\ \vdots & \ddots & \vdots & \vdots \\ l_{an}^{(\nu)} & \cdots & l_{nn}^{(\nu)} & l_{nq}^{(\nu)} \\ l_{aq}^{(\nu)} & \cdots & l_{nq}^{(\nu)} & l_{qq}^{(\nu)} \end{bmatrix} \tag{3.28}$$

or, in systems with a chemical reaction at the interface,

$$\mathcal{L}_{AB}^{(Rx)} = \begin{bmatrix} l_{RR} & l_{Rq} \\ l_{Rq} & l_{qq} \end{bmatrix}. \tag{3.29}$$

The phenomenological coefficients are functions of equilibrium properties only [20], such that,

$$\mathcal{L}_{AB}^{(1)} = f\left[T_{sat}, p_{sat}, \phi_{sat}\right], \tag{3.30}$$

$$\mathcal{L}_{AB}^{(\nu)} = f\left[T_{sat}, p_a^{sat}, ..., p_\nu^{sat}, \phi_{sat}\right], \tag{3.31}$$

$$\mathcal{L}_{AB}^{(Rx)} = f\left[T_{sat}, p_a^{sat}, ..., p_\nu^{sat}, \phi_{sat}\right], \tag{3.32}$$

where, in all cases, ϕ is a set of additional equilibrium properties of the surface that we leave undefined for now. We discuss these phenomenological coefficients in more detail in Chapter 4.

3.2.4 Phenomenological coefficients for dissociative sublimation

As we discussed in Chapter 1, the LIT phenomenological law only applies to independent force-flux pairings. In §3.2.1 we replaced the independent flux/force pairings for the mole fluxes with a single reaction flux. This reaction flux automatically imposes a dependency between the mole fluxes based upon (3.16).

As we have seen, the reactive sublimation model is the result of a transformation of the independent flux model; the only difference between the two is introduced during the linearization. We argue that the reactive and non-reactive sublimation models are equivalent so long as the dependency between the fluxes is enforced in both.

In Chapter 4, we discuss the phenomenological coefficients for non-reactive condensation of mixtures based upon kinetic theory. We were unable to find an equivalent model for reactive sublimation. We instead use the interface model Chapter 4 to determine the coefficients for reactive sublimation.

3.3 Interface Conditions for Sublimation and Condensation

So far, we have derived a non-equilibrium model for sublimation. In this section, we relate this model to boundary conditions at the interface. We begin by reviewing the equilibrium interface conditions (ICs).

3.3.1 Equilibrium ICs

Equilibrium ICs are based upon considering full thermal and chemical equilibrium at the interface. For the temperature at the interface we write

$$T_v = T_s, \tag{3.33}$$

and for the pressure(s) of the constituent(s)

$$p_a = p^a_{sat}(T_s). \tag{3.34}$$

If reactive sublimation is considered, we write

$$K_v = K_p(T_s) \tag{3.35}$$

3.3.2 Non-equilibrium ICs for non-reactive interfaces

We now use the LIT sublimation model to define non-equilibrium interface conditions (NEICs) for the condensation at solid-vapor interfaces[3].

For the condensation of a single species, the thermodynamic forces (3.23a,3.23b) and the fluxes $\{J_a, q\}$ are combined with (3.25) to give

$$\begin{bmatrix} J_a \\ q' \end{bmatrix} = \begin{bmatrix} J_a \\ -\kappa_v \frac{dT_v}{dx} \end{bmatrix} = \mathcal{L}^{(1)}_{AB}(T_s, p_{sat}, \phi_s) \begin{bmatrix} -\frac{R_u}{p^a_{sat}(T_s)}\Delta p_a \\ \frac{\Delta T}{T_s^2} \end{bmatrix}, \tag{3.36}$$

where the measurable heat flux q' is replaced by Fourier's law (2.63), as discussed in Chapter 2; κ_v is the thermal conductivity corresponding to the vapor and $\frac{dT_v}{dx}$ calculated at the interface.

For the binary system, where only one constituent condenses, we write,

$$\begin{bmatrix} J_a \\ 0 \\ -\kappa_v \frac{dT_v}{dx} \end{bmatrix} = \mathcal{L}^{(2)}_{AB}(T_s, p^a_{sat}, \phi_s) \begin{bmatrix} -\frac{R_u}{p^a_{sat}(T_s)}\Delta p_a \\ 0 \\ \frac{\Delta T}{T_s^2} \end{bmatrix}. \tag{3.37}$$

---

[3] We shall use exclusively equilibrium boundary conditions at the sublimating source interface. See §3.4.1.

For a binary system where both constituents condense

$$\begin{bmatrix} J_a \\ J_b \\ -\kappa_v \frac{dT_v}{dx} \end{bmatrix} = \mathcal{L}^{(2)}_{AB}(T_s, \zeta, \phi_s) \begin{bmatrix} -\frac{R_u}{p^a_{sat}(T_s)} \Delta p_a \\ -\frac{R_u}{p^b_{sat}(T_s)} \Delta p_b \\ \frac{\Delta T}{T_s^2} \end{bmatrix}, \tag{3.38}$$

where ζ is the saturation pressure ratio defined as

$$\zeta = \frac{p^a_{sat}(T_s)}{p^b_{sat}(T_s)}.$$

For a ternary system where two of three constituents condense

$$\begin{bmatrix} J_a \\ J_b \\ 0 \\ -\kappa_v \frac{dT_v}{dx} \end{bmatrix} = \mathcal{L}^{(3)}_{AB}(T_s, \zeta, \phi_s) \begin{bmatrix} -\frac{R_u}{p^a_{sat}(T_s)} \Delta p_a \\ -\frac{R_u}{p^b_{sat}(T_s)} \Delta p_b \\ 0 \\ \frac{\Delta T}{T_s^2} \end{bmatrix}. \tag{3.39}$$

3.3.3 NEICs for reactive interfaces

We consider a simple case of reactive condensation, where the reaction at the interface is of the form

$$\mathrm{AB(s)} \rightleftharpoons \gamma_{\mathrm{A}}\mathrm{A(v)} + \gamma_{\mathrm{B}}\mathrm{B(v)} \tag{3.40}$$

and proceeds with reaction flux J_{Rx} which can be related to J_{A} and J_{B} by (3.16). The thermodynamic forces (3.24,3.23b) and the fluxes $\{J_{Rx}, q\}$ are combined with (3.25) to give,

$$\begin{bmatrix} J_{Rx} \\ q \end{bmatrix} = \begin{bmatrix} J_{Rx} \\ -\kappa_v \frac{dT_v}{dx} \end{bmatrix} = \mathcal{L}^{(Rx)}_{AB}(T_1, \zeta, \phi_1) \begin{bmatrix} -\frac{\Delta K}{K_p(T_s)} \\ \frac{\Delta T}{T_s^2} \end{bmatrix}. \tag{3.41}$$

3.4 Discussion

Equilibrium ICs are based upon the idea that there is negligible resistance to sublimation and condensation at the interface. The NEICs converge to the Equilibrium ICs when the diagonal elements of $\mathcal{L}_{AB}$ are much larger than the thermodynamic forces; therefore, the Equilibrium ICs are valid when the transport coefficients in the $\mathcal{L}_{AB}$ are large compared to the thermodynamic forces.

3.4.1 Surface roughness and surface area

We introduced the concept of atomistic surface roughness in Chapter 1. We now consider how extreme surface roughness affects our choice of boundary conditions.

We define the mass flux in our ampoule as

$$J = \frac{4\dot{n}}{\pi d_a^2}, \tag{3.42}$$

where $\dot{n}$ is the total mole flow rate $\left[\frac{\mathrm{mol}}{\mathrm{s}}\right]$ and d_a is the inside diameter of the ampoule. This defines the flux onto the crystal only when the crystal is smooth, such that the surface area of the crystal is nearly that of the ampoule cross section. Due to extreme surface roughness, the measurable surface area of interfaces may be substantially greater than the cross sectional area of the ampoule, the most extreme case being a ground powder. For a volume of ground powder of identical sized spherical particles, the approximate total specific surface area is [65],

$$s \approx \frac{6}{\rho d_p} \frac{\mathrm{m}^2}{\mathrm{kg}}. \tag{3.43}$$

where ρ is the mass density of the powder particles, and d_p is the particle diameter. If we now consider a cylindrical ampoule with a ground-powder charge of thickness L' and mass m, we find the effective exposed surface area as,

$$A_s = \left(\frac{6m}{\rho d_p}\right) \frac{4}{\pi^2 d_a^3 L'}. \tag{3.44}$$

where d_a is the diameter of the ampoule. If $A_s >> \frac{1}{4}\pi d_a^2$.

$$J_{surface} = \frac{\dot{n}}{A_s} << \frac{4\dot{n}}{\pi d_a^2} = J. \tag{3.45}$$

For a fixed set of interface transport coefficients $\mathcal{L}_{AB}$, very small fluxes lead to very small forces; equilibrium conditions can be assumed. Hence, for a source material consisting of a ground powder or other extremely rough source material, equilibrium conditions can be assumed at the interface.

Chapter 4

Phenomenological Coefficients

In this chapter, we discuss the LIT phenomenological coefficients introduced in Chapter 3. Phenomenological coefficients can be obtained for vapor-surface interaction either experimentally [20] or from theory [20, 16, 22]. Here, we discuss the theoretical approach. We shall discuss the experimental approach as it applies to vapor-solid interaction in Chapter 9.

Kinetic theory (KT) can be used to formulate the laws for heat and mass transport at vapor-solid interfaces in a manner analogous to LIT. This KT formulation is more powerful than the LIT formulation, as the details of the vapor-surface interaction can be explicitly incorporated into the model.

Most attempts to use KT to determine LIT coefficients at surfaces have been concerned with bulk evaporation and condensation of liquids [21, 22, 20]. In these studies, KT is applied to the vapor phase only; the liquid is assumed to emit molecules at the equilibrium temperature and pressure of the interface, even in cases far outside of equilibrium [16, 20]. Surface science predicts the same behavior for solid surfaces [39]; thus, so far as KT is concerned, the vapor in contact with a solid surface behaves exactly the same way as vapor in contact with liquid. The differences lie in the surface interaction itself. We therefore argue that the LIT coefficients derived for liquid-vapor can be modified for solid-vapor interaction if the surface interaction is correctly taken into account.

Our group has previously used KT to model evaporation and condensation of simple liquids [16, 40]. These studies incorporated a particle impact energy dependent condensation probability function [66] into the KT surface interaction framework. This modification allowed KT models to accurately predict the large temperature jumps at liquid-vapor interfaces, as measured by Ward, Fang and coworkers [67]. It is likely that such a velocity dependent sticking probability, equivalent to the condensation probability, also exists for the solid surface, though so far as we can tell, no such function has been identified [68, 39]. We shall therefore stick to the more conventional KT model that considers the first moment of the sticking probability function $\hat{\theta}_s(w_k, T_z)$, defined as

$$\theta_s\left(T_s\right) = \iiint\limits_{w_n<0} \hat{\theta}_s(w_k, T_z) d\mathbf{w}. \tag{4.1}$$

This value, known as the sticking coefficient is subject to the condition

$$0 \leq \theta_s \left(T_s\right) \leq 1. \tag{4.2}$$

Physically, the sticking coefficient represents the fraction of particles that stick to the interface, independent of their impact energy.

4.1 The Interface at Equilibrium

We recall that in equilibrium the distribution of particles in the vapor must be the Maxwellian,

$$f_M \left(p, T, w\right) = \frac{p}{kT} \left(\frac{m}{2\pi kT}\right)^{3/2} \exp\left(-\frac{m}{2kT} w^2\right); \tag{4.3}$$

this must hold everywhere in the vapor, including right at the interface.

In equilibrium particles continue to sublime and condense upon the interface. Since there cannot be any entropy generation at the interface in equilibrium, the sublimation and condensation processes must be reversible; this concept is called microreversibility [39, 42, 41]. It is also required that the individual vapor-surface interactions are reciprocal, that is, they must be indistinguishable under a time reversal. This has been proven for condensing and non-condensing surfaces [42, 37].

In Chapter 1, we introduced the sublimation probability function $\hat{\theta}_s(w_k, T_s)$ — the probability that a particle sublimes from a surface at temperature T_s with a velocity between w_k and $w_k + dw_k$. As a consequence of reciprocity, the condensation mechanism must be identical to the sublimation mechanism, as must their probabilities of occurring. Therefore, the sublimation probability function must always be identical to the sticking (condensation) probability function [40]. The sticking coefficient (4.1) is then also identical to the sublimation coefficient.

4.1.1 The sticking probability function

For liquid surfaces, it has been shown that the condensation probability function[1] is likely a function of the incident normal velocity of particles, as vapor particles are more likely to condense if they penetrate into the liquid [16, 66]. Such a statement is not as easy to make for solid condensation due to the complex, coupled processes of adsorption and surface diffusion that take place on the solid surface [24, 3, 39]. The sticking probability function is directly proportional to the energy loss of an incident molecule as it transitions from the vapor phase to the solid phase [69]. An idealized theoretical model of this energy

---

[1] For vapor-liquid interactions, the sticking probability is normally called the condensation probability.

loss function was proposed by Iche and Nozières [46], though such a construct would require physical information about the surface that is not easy to obtain [24]. In the absence of activation barriers, it has been suggested that slower particles are more likely to stick than faster ones, which is opposite to the behavior of a liquid [39]. A simple form of such a sticking probability function, analogous to the Tsuruta form is

$$\hat{\theta}_s(w_k, T_s) = \theta_s\left(T_s\right)\exp\left(\frac{-w_n^2}{2kT_s}\right), \tag{4.4}$$

where ω, w_n is the normal velocity of the incident particle. The velocity dependent sticking probability must be considered to accurately predict the heat transport at the interface [16]. This is due to inaccuracy introduced in the computation of the energy flux integral (1.7) if the velocity dependence is ignored. This error does not arise in the mass flux integral (1.6), since velocity dependence does not affect the result.

4.1.2 Fluxes at the interface in equilibrium

The distribution of particles *subliming* off of the interface is given by the first term of the scattering expression (1.12)

$$f_s^+ = \hat{\theta}_s(w_k, T_s) f_M\left[p_{sat}\left(T_s\right), T_s, w\right], \tag{4.5}$$

and, since the system is in equilibrium,, $f_s^+ = f_s^-$. We can obtain the sublimation mole flux by inserting (4.5) into (1.6) and integrating over the half space pointing out of the interface; we compute the integrals based upon the assumption that the sticking probability is of the form in (4.4);

$$J_s^+ = \iiint\limits_{w_n>0}^{\infty} w_n \hat{\theta}_s(w_k) f_M\left[p_{sat}\left(T_s\right), T_s, w\right] d\mathbf{w} = \frac{\theta_s}{M}\sqrt{\frac{m}{2\pi kT_s}} p_{sat}(T_s). \tag{4.6}$$

We obtain the same result for the condensation flux,

$$J_s^- = \iiint\limits_{w_n<0}^{\infty} w_n \hat{\theta}_s(w_k) f_M\left[p_{sat}\left(T_s\right), T_s, w\right] d\mathbf{w} = \frac{\theta_s}{M}\sqrt{\frac{m}{2\pi kT_s}} p_{sat}(T_s), \tag{4.7}$$

thus confirming that the sublimation flux matches exactly the condensation flux.

We can also compute the equilibrium energy fluxes given by (4.5) inserted into (1.7) and integrating over the half space pointing out of the interface,

$$\begin{aligned} 0 \quad = \quad & Q_k^+ - Q_k^- = m \iiint\limits_{w_n>0}^{\infty} \frac{w^2}{2} \hat{\theta}_s(w_n, T_s) f_M \left[p_{sat}\left(T_s\right), T_s, w\right] d\mathbf{r} - \\ & - m \iiint\limits_{w_n<0}^{\infty} \frac{w^2}{2} \hat{\theta}_s(w_n, T_s) f_M \left[p_{sat}\left(T_s\right), T_s, w\right] d\mathbf{r}. \end{aligned} \tag{4.8}$$

We note that in kinetic theory Q_k is the total energy flux, including both the convective and non-convective heat fluxes. As an illustrative example, we make the simplifying assumption that, like the Tsuruta model, the sticking probability is a function of the particle normal velocity only [66]. The resulting energy flux expression is

$$Q_k^- = \frac{p_{sat}}{\sqrt{2\pi}} \sqrt{\left(\frac{m}{kT_s}\right)^3} \int\limits_0^{\infty} \hat{\theta}_s(w_n, T_s) \left(\frac{w_n^2}{2} + \frac{k}{m} T_s\right) \exp\left(-\frac{m}{2\pi kT} w_n^2\right) dw_n. \tag{4.9}$$

The same expression arises for the heat flux in the sublimation direction. When the sticking coefficient instead of the sticking probability function is used in the energy flux expression, Q_k becomes for both the sublimation and condensation directions

$$Q_k^+ = Q_k^- = 2\theta_s\left(T_s\right) \sqrt{\frac{2}{\pi}} p_{sat} \sqrt{\frac{k}{m} T_s}. \tag{4.10}$$

4.2 Hertz-Knudsen Condensation Model

The first attempt to write kinetic theory expressions for near-equilibrium interface mass transfer were produced by Hertz in 1882 [70] and Knudsen in 1915 [71]. Hertz-Knudsen (HK) law is based on the hypothesis that, near-equilibrium, the distribution function at the interface can be approximated by two Maxwellian distributions, where the incident molecules are at the same temperature but at a different pressure than the emitted molecules. The center-of-mass velocity of these distributions is assumed to be zero.

The classical HK mass flux is obtained by using (1.6) with the HK half-space distributions related to one another by (1.12),

$$J_k = \frac{\theta_s}{M} \sqrt{\frac{m}{2\pi kT_s}} \Delta p. \tag{4.11}$$

where, as before Δp is the supersaturation/subsaturation. The HK mole flux is now equivalent to the linear phenomenological law derived for UTU (3.36) assuming no temperature jump at the interface

$(\Delta T = 0)$

$$J_A = l_{JJ}\frac{R_u}{p_{sat}(T_s)}\Delta p. \tag{4.12}$$

The phenomenological coefficient for mass transport from HK is thus

$$l_{JJ}^{HK} = \frac{\theta_s}{M}\sqrt{\frac{m}{2\pi k T_s}}\frac{p_{sat}(T_s)}{R_u}, \tag{4.13}$$

with the remaining coefficients of $\mathcal{L}_{AB}^{(1)}$ set to zero.

The HK model has been applied to vapor growth from mixtures (e.g. [72, 73, 15, 68]). The resulting mixture phenomenological coefficients take the form

$$l_{aa}^{HK} = \frac{\theta_a}{M_a}\sqrt{\frac{m_a}{2\pi k T_s}}\frac{p_{sat}^a(T_s)}{R_u}, \tag{4.14}$$

for each condensing constituent a.

While the HK equation is a convenient and easy-to-derive model for sublimation and deposition, it has been shown to underestimate the sublimating mass flux by an approximate order of two [74, 16]. It is also useless for modelling heat transport at the interface; hence we neglect to compute the heat flux integrals.

The HK theory is frequently used when describing the growth rate of bulk crystals. Faktor and Garrett used HK theory combined with the Langmuirian adsorption model [9, 39] to estimate the interface transport coefficients for the growth of binary materials [26]. A similar model was used by Tempest and Ballentyne for studying the PVT of II-VI compounds [72, 73]. A HK based expression for crystal growth of general surfaces are given by Pimpinelli [24] and for different types of surfaces by Markov [3]. These are in agreement with the growth formulas given in the BCF model [2], which also made use of the HK law. Finally, the HK model was used in a fascinating interface stability analysis of Louchev [75].

4.2.1 Corrections to HK

A simple correction to the HK model is the Schrage model [76]. Schrage uses the same near-equilibrium argument as HK, but includes the net center-of-mass velocity of the vapor of the vapor in the equilibrium distributions. This results in the first-order ($v^2 \to 0$) mass flux expression [19, 77],

$$J = \frac{2\theta_s}{2-\theta_s}\frac{1}{M}\sqrt{\frac{m}{2\pi k}}\left[\frac{p_{sat}(T_s)}{\sqrt{T_s}} - \frac{p_v}{\sqrt{T_v}}\right], \tag{4.15}$$

In the limit $\theta_s \to 1$, the Schrage result reduced to the HK result multiplied by 2, thus accounting for the inaccuracy in the HK model. There is still some minor inaccuracy present, due to the neglection of the Knudsen layer — a transition layer of molecules near the interface, that is the result of strong non-equilibrium in the incident and emitted particles [74, 19]. A correction to account for the Knudsen layer in the Schrage model was derived [78].

It has been shown that the Schrage mass flux can also be obtained from the linearized CE distribution [19] which we discuss in the next section. Like the HK model, the Schrage model is not useful for determining the energy flux at the interface. We have found no evidence of the Schrage model being applied to vapor crystal growth.

4.3 Cipolla-Kjelstrup-Bedeaux Condensation Model

The classical HK model is a poor model for predicting the transport of heat and mass. The Schrage model predicts mass transport correctly, but remains inaccurate for heat flux. The heat flux problem is greatly improved by the Cipolla-Kjelstrup-Bedeaux (CKB) model, first derived by Cipolla et al. [21, 22] and modified to suit the LIT framework by Kjelstrup and Bedeaux [20].

The CKB model is based upon the linearized CE distribution. It assumes impact energy independent sticking probability and full accommodation of reflected molecules, meaning that the reflected molecules become thermalized on the surface and leave the interface in an equilibrium distribution at the temperature of the interface, just like subliming particles. Unlike the classical Schrage model, the CKB takes full account of the Knudsen layer at the interface and includes the energy flux.

We do not repeat the analysis of CKB, instead we give the latest results for the LIT phenomenological coefficients in terms of equilibrium properties of the solid phase.

The CKB phenomenological coefficients are reported in the form of a resistivity matrix, which is the inverse of the conductivity matrix introduced in Chapter 3, $\mathcal{R}_{AB} = \mathcal{L}_{AB}^{-1}$. For single species condensation, the resistivity matrix is of the form,

$$\mathcal{R}_{AB}^{(1)} = \begin{bmatrix} \hat{r}_{JJ}^{(1)} & \hat{r}_{Jq}^{(1)} \\ \hat{r}_{Jq}^{(1)} & \hat{r}_{qq}^{(1)} \end{bmatrix}. \tag{4.16}$$

The elements of $\mathcal{R}_{AB}^{(1)}$ are

$$\hat{r}_{JJ}^{(1)} = \frac{2R_u\sqrt{\pi}}{c_{sat}(T_s)\bar{v}_{MP}(T_s)}\left(\frac{1}{\theta_s} + \frac{1}{\pi} - \frac{23}{32}\right), \tag{4.17a}$$

$$\hat{r}_{qq}^{(1)} = \frac{\sqrt{\pi}}{4c_{sat}(T_s)R_uT_s^2\bar{v}_{MP}(T_s)}\left(1 + \frac{104}{25\pi}\right), \tag{4.17b}$$

$$\hat{r}_{Jq}^{(1)} = \hat{r}_{qJ} = \frac{2R_u\sqrt{\pi}}{8T_sc_{sat}\bar{v}_{MP}(T_s)}\left(1 + \frac{16}{5\pi}\right). \tag{4.17c}$$

Here, the the ideal gas law gives the saturation mole density $c_{sat}(T_s) = \frac{p_{sat}(T_s)}{R_u T_s}$, $\bar{v}_{MP}\left(T_s\right)$ is the mean particle velocity of the equilibrium vapor, calculated as,

$$\bar{v}_{MP}(T_s) = \sqrt{\frac{2R_u T_s}{M}}. \tag{4.18}$$

For the evaporation and condensation of mixtures of ν constituents, the resistivity matrix takes the form

$$\mathcal{R}_{AB}^{(\nu)} = \begin{bmatrix} \hat{r}_{aa}^{(\nu)} & \cdots & \hat{r}_{an}^{(\nu)} & \hat{r}_{aq}^{(\nu)} \\ \vdots & \ddots & \vdots & \vdots \\ \hat{r}_{a\nu}^{(\nu)} & \cdots & \hat{r}_{\nu\nu}^{(\nu)} & \hat{r}_{\nu q}^{(\nu)} \\ \hat{r}_{aq}^{(\nu)} & \cdots & \hat{r}_{nq}^{(\nu)} & \hat{r}_{qq}^{(\nu)} \end{bmatrix}, \tag{4.19}$$

where the elements of $\mathcal{R}_{AB}^{(\nu)}$ are:

$$\hat{r}_{ii}^{(\nu)} = \frac{R_u\sqrt{\pi}}{16 c_{sat}\bar{v}_{MP}}\left[1 + 32\left(\frac{1}{\theta_s^i} + \frac{1}{\pi} - \frac{3}{4}\right)\frac{1}{c_{sat}^i}\left(\sum_{a=1}^{\nu} c_{sat}^a \sqrt[4]{\frac{M_i}{M_a}}\right)\right], \tag{4.20a}$$

$$\hat{r}_{qq}^{(\nu)} = \frac{\sqrt{\pi}}{4R_u T_s^2 c_{sat}\bar{v}_{MP}}\left\{1 + \frac{104}{25\pi\left(\kappa\right)^2}\sum_{a=1}^{\nu}\left[\left(\chi_a\kappa_a\right)^2\frac{1}{c_{sat}^a}\left(\sum_{b=1}^{n} c_{sat}^b \sqrt[4]{\frac{M_a}{M_b}}\right)\right]\right\},$$

$$\hat{r}_{iq}^{(\nu)} = \frac{\sqrt{\pi}}{8T_s c_{sat}\bar{v}_{MP}}\left[1 + \frac{16\chi_i\kappa_i}{5\pi\left(\kappa\right)}\frac{1}{c_{sat}^i}\left(\sum_{a=1}^{\nu} c_{sat}^a \sqrt[4]{\frac{M_i}{M_a}}\right)\right], \tag{4.20b}$$

$$\hat{r}_{ij}^{(\nu)} = \frac{R_u\sqrt{\pi}}{16 c_{sat}\bar{v}_{MP}}. \tag{4.20c}$$

Here, $c_{sat} = \sum_a c_{sat}^a$, $\bar{v}_{MP} = \sum_a \chi_a \bar{v}_{mp}^a$.

4.3.1 Stagnant constituents in the CKB model

To our knowledge, the presence of stagnant, non-condensing constituents has not been considered explicitly in the CKB model. We have made the following modification to the model so as to account for one stagnant constituent. For a condensing mixture that contains one non-condensing constituent z, the phenomenological coefficients associated with the transport of across the interface z must vanish. Since z does not condense, its saturation pressure must be very large at T_s such that $c_{sat}^z = \frac{p_{sat}^z}{R_u T} \to \infty$. The resistivity matrix becomes

$$\mathcal{R}_{AB}^{(\nu-1)+} = \lim_{c_{sat}^b \to \infty} \mathcal{R}_{AB}^{(\nu)},$$

where the superscript + indicates the presence of a stagnant constituent. The $\mathcal{R}_{AB}^{(\nu-1)+}$ matrix elements

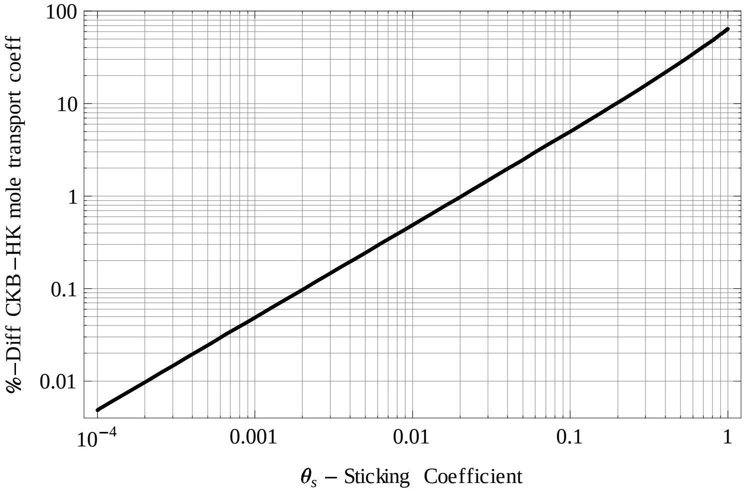

Figure 4.1: The difference between the HK and CKB interface mole transport coefficients plotted against the sticking coefficient. The difference is upwards of 60% when the sticking coefficient is unity. The thermochemical properties of iodine at 300 K were used in the analysis. (See Ch. 5)

are:

$$\hat{r}_{ii}^{(\nu-1)+} = \frac{R_u\sqrt{\pi}}{16c^i_{sat}\bar{v}_{MP}}32\left(\frac{1}{\theta^i_s}+\frac{1}{\pi}-\frac{3}{4}\right)\sqrt[4]{\frac{M_i}{M_z}}, \tag{4.21a}$$

$$\hat{r}_{zz}^{(\nu-1)+} = 0, \tag{4.21b}$$

$$\hat{r}_{qq}^{(n-1)+} = \frac{\sqrt{\pi}}{R_u T_s^2\bar{v}_{MP}}\left\{\frac{26}{25\pi}\sum_{a=1}^{\nu-1}\left[\frac{1}{c^a_{sat}}\left(\frac{\chi_a\kappa_a}{\kappa}\right)^2\sqrt[4]{\frac{M_a}{M_z}}\right]\right\},$$

$$\hat{r}_{iq}^{(\nu-1)+} = \frac{\sqrt{\pi}}{8T_s c^a_{sat}\bar{v}_{MP}}\frac{16\chi_i\kappa_i}{5\pi\kappa}\left(\frac{M_i}{M_b}\right)^{1/4}, \tag{4.21c}$$

$$\hat{r}_{zq}^{(\nu-1)+} = 0, \tag{4.21d}$$

$$\hat{r}_{zi}^{(\nu-1)+} = 0, \tag{4.21e}$$

$$\hat{r}_{ij}^{(\nu-1)+} = 0. \tag{4.21f}$$

4.3.2 Comparison to the HK model

In Fig.4.1 we plot the difference between the HK mole transport coefficient and the CKB mole transport coefficient. The thermochemical properties of Iodine were substituted in to the HK and CKB expressions, and a temperature of $T = 300\,\mathrm{K}$ was used.

We see that when the sticking coefficient is high, the HK and CKB coefficients differ by over 60%. When the sticking coefficient is very low, the HK and CKB model converge.

4.4 Phenomenological Coefficients for Dissociative Sublimation

In our literature review, we were unable to find a theoretical treatment of the phenomenological transport coefficients for dissociative sublimation. The phenomenological framework has been used in at least one case for the transport of CdTe [17], though in that case there was no justification for the choice of transport coefficient. We know that the phenomenological coefficients for dissociative sublimation must be of the form

$$\mathcal{R}_{AB}^{(Rx)} = \begin{bmatrix} \hat{r}_{RR} & \hat{r}_{Rq} \\ \hat{r}_{Rq} & \hat{r}_{qq} \end{bmatrix}, \tag{4.22}$$

which is the inverse of (3.29). We propose, based upon our argument in §3.2.4, that the phenomenological coefficients for non-reactive sublimation can be related to those for reactive sublimation.

We start by recalling (3.38) and replacing J_a and J_b using (3.16)

$$\begin{bmatrix} \frac{\gamma_a}{\gamma_a+\gamma_b} J_{Rx}\cdot \\ \frac{\gamma_b}{\gamma_a+\gamma_b} J_{Rx}\cdot \\ -\kappa_v \frac{dT_v}{dx} \end{bmatrix} = \mathcal{L}_{AB}^{(2)}(T_1, \chi_{sat}^a, \theta_s^a, \theta_s^b) \begin{bmatrix} -\frac{R_u}{p_{sat}^a(T_s)} \Delta p_a \\ -\frac{R_u}{p_{sat}^b(T_s)} \Delta p_b \\ \frac{\Delta T}{T_s^2} \end{bmatrix}. \tag{4.23}$$

The first and second row of (4.23) can be combined, in full form

$$\begin{aligned} J_{Rx} &= -R_u \left[\left(l_{aa}^{(2)} + l_{ab}^{(2)} \right) \frac{\Delta p_a}{p_{sat}^a(T_s)} + \left(l_{bb}^{(2)} + l_{ab}^{(2)} \right) \frac{\Delta p_b}{p_{sat}^b(T_s)} \right] + \\ &\quad + \left(l_{aq}^{(2)} + l_{bq}^{(2)} \right) \frac{\Delta T}{T_s^2}, & (4.24a) \\ -\kappa_v \frac{dT_v}{dx} &= -l_{aq}^{(2)} \frac{R_u}{p_{sat}^a(T_s)} \left[\Delta p_a \right] - l_{bq}^{(2)} \frac{R_u}{p_{sat}^b(T_s)} \Delta p_b + l_{qq}^{(2)} \frac{\Delta T}{T_s^2}. & (4.24b) \end{aligned}$$

We compare this result to (3.41) written in full form as

$$\begin{aligned} J_{Rx} &= -l_{RR} \frac{\Delta K}{K_p(T_s)} + l_{Rq} \frac{\Delta T}{T_s^2}, & (4.25a) \\ -\kappa_v \frac{dT_v}{dx} &= -l_{Rq} \frac{\Delta K}{K_p(T_s)} + l_{qq} \frac{\Delta T}{T_s^2}. & (4.25b) \end{aligned}$$

For the reaction flux we can thus conclude,

$$l_{RR} \frac{\Delta K}{R_u K_p(T_s)} = \left(l_{aa}^{(2)} + l_{ab}^{(2)} \right) \frac{\Delta p_a}{p_{sat}^a(T_s)} + \left(l_{bb}^{(2)} + l_{ab}^{(2)} \right) \frac{\Delta p_b}{p_{sat}^b(T_s)}, \tag{4.26}$$

and for the heat flux we find

$$l_{qq} = l_{qq}^{(2)}, \tag{4.27a}$$

$$l_{Rq} = l_{aq}^{(2)} + l_{bq}^{(2)}. \tag{4.27b}$$

The heat flux phenomenological coefficients are determined directly from the non-reactive phenomenological coefficients. This is not true of of the reaction flux coefficient since (4.26) cannot be solved directly; either an additional linearization is necessary, or a value can be found by direct comparison of the models. We choose the later option, as discussed in Chapter 9.

4.5 Sticking Coefficients

The phenomenological expressions from the CKB model are written in terms of sticking coefficients θ_s^i. We now examine simple HK based expressions for the growth of rough crystal surfaces from vapor, and extract the sticking coefficient. The expressions for the sticking coefficients on rough surfaces are included here for the sake of interest only. In this work, we do not calculate sticking coefficients for surfaces explicitly.

Markov describes the a growth of a single species in the presence of an activation barrier onto atomistically rough crystal surfaces [3] in terms of a relative roughness; his derivation follows. The equilibrium condensation mole flux in the presence of an activation barrier is

$$J_- = \beta \exp\left(-\frac{\Delta U}{kT_v}\right) \frac{1}{M}\sqrt{\frac{m}{2\pi k T_s}} p_{sat}(T_s), \tag{4.28}$$

here, ΔU is the height of the potential barrier as in Fig. 4.2, β is the relative roughness. The relative roughness is a ratio between the surface area containing favorable growth locations (kinks) over the surface area that does not; it ranges from unity when a surface is entirely covered in kinks to zero for a atomistically smooth surface. In equilibrium $J_+ = J_-$, thus the sublimation flux becomes,

$$J_+ = \beta \exp\left(-\frac{\Delta U}{kT_v}\right) \frac{1}{M}\sqrt{\frac{m}{2\pi k T_s}} p_{sat}(T_s). \tag{4.29}$$

Markov then assumed the HK law to determine the growth rate of the surface, this results in a net condensation flux of

$$J = \frac{\theta_s}{M}\sqrt{\frac{m}{2\pi k T_s}} \Delta p \tag{4.30}$$

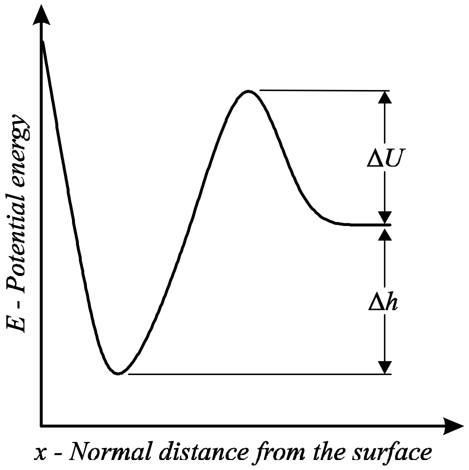

Figure 4.2: The potential diagram for a rough crystal surface that contains a potential barrier.

where the sticking coefficient is

$$\theta_s = \beta \exp\left(-\frac{\Delta U}{kT_v}\right). \tag{4.31}$$

An additional factor ξ can be added to indicate the fraction of adatoms that, upon encountering a kink site actually stick to it. The sticking probability then becomes,

$$\theta_s = \beta\xi \exp\left(-\frac{\Delta U}{kT_v}\right). \tag{4.32}$$

Depending upon the height of the potential barrier, the relative roughness and the probability that an atom will stick to a kink, the overall sticking coefficient can vary from zero to unity.

4.5.1 Extension to binary condensing species

The growth of binary crystal surfaces of II-VI compounds was considered by Tempest et al. [72]. As we have already discussed, II-VI compounds like CdTe have a tendency to sublime according to the reaction,

$$\mathrm{AB(s)} \rightleftharpoons \mathrm{A(v)} + \frac{1}{2}\mathrm{B_2(v)}. \tag{4.33}$$

This condensation behavior requires that atoms of both A and B_2 stick to the surface. Tempest formulated the sticking probability of B_2 as,

$$\theta_s^{B_2} = \beta^2 \xi_B^2 \exp\left(-\frac{\Delta U_d}{kT_v}\right) \tag{4.34}$$

where the ξ_B and β is squared to indicate that for every B_2 molecule that strikes the surface, two B adatoms must be accommodated in kinks, ΔU_d is the energy barrier for the dissociation of B_2 molecules into B adatoms. The sticking probability for A was given

$$\theta_s^A = \beta_A \gamma_A \tag{4.35}$$

So far as we could find, no simple direct relation was formulated to relate the kink density of A to the kink density of B that applies to bulk crystal growth.

4.5.2 Other growth modes

As we discussed in Chapter 1, we assume that the predominant growth modes of the substances considered are the 3D growth mode and the step flow growth mode. The sticking coefficient of the step flow growth mode is a much more complicated function than the sticking coefficient on a rough surface. It is dependent upon, among other things, the geometry and dimensions of the atomistic steps. This level of detail is outside the scope of this work, and thus we do not quantitatively discuss the form of the sticking coefficient expressions in the step flow growth mode. Instead, we direct the reader to the excellent reviews on the subject [24, 3].

4.5.3 Sticking coefficients for the systems of interest

As we have already discussed we limit ourselves in this thesis to the study of I_2 and CdTe PVT.

Abernathy et al. [25] studied the transport of I_2 limited by diffusion. The vapor pressure as well as the temperature of the interface was monitored closely. The supersaturation (difference between the saturation pressure and the vapor pressure) at the interface was found to be negligibly small over a large range of temperatures [25]. Therefore, it is likely that the average sticking coefficient on I_2 surfaces is near unity.

In the study of CdTe transport, we are concerned with the sticking coefficients of both Cd and Te_2. Sticking coefficients for these have been estimated for molecular beam epitaxial growth of CdTe films; for example, Waag et al. estimated the sticking coefficient of Cd to be 0.65, and the sticking coefficient of Te to be 0.76[2] for temperatures up to 390 °C [79]. Other measurement also can be found in the literature, however these are all taken at significantly lower temperatures than those typically used for bulk growth.

Recently, Fiederle et al.studied the deposition of CdTe thin films under microgravity in conditions similar to those of bulk vapor growth [10]. They estimated a value for the overall sticking coefficient of CdTe at approximately 820 °C as 0.003, though the methodology used to make this measurement was not entirely clear. We were unable to find any other measurements of the sticking coefficient of CdTe applicable to bulk growth.

---

[2] Waag used individual Te molecules rather than Te_2 molecules.

Chapter 5

Thermochemical Properties of the Bulk Phases

In this chapter we define all of the inputs into the models. In our analysis, we study the iodine – octaflurocyclobutane (I_2— C_4F_8) system for non-dissociative transport (UTU, UTB) following [11]; and we study the cadmium telluride – carbon monoxide (CdTe – CO) system for dissociative transport (BTB, BTT) following [12].

5.1 Iodine-Octafluorocyclobutane System Properties

5.1.1 Solid Properties

The properties for the bulk I solid are given in Tab. 5.1. Since we wish to compare to the experiments in [11], we need thermal properties of the solid near the experimental temperatures, which were all at approximately $315\,\mathrm{K} - 385\,\mathrm{K}$; the tabulated values are reasonably close to this range.

5.1.2 Vapor Properties

Vaporous iodine exists as I_2. The thermochemical properties for I_2 and C_4F_8 at 330 K are given in Tab. 5.2.

The saturation pressure of I_2 was obtained by taking a exponential least-square fit of data from [83], the result is

$$p_{sat}^{I_2}(T) = 5.028 \times 10^{-7} \exp\left[0.0625T\right] \quad \mathrm{Pa} \tag{5.1}$$

where T is in units K. We do not require the saturation vapor pressure of C_4F_8 since it acts as an inert background gas.

Property	Value [I]	Source
Molecular Weight M_w	$126.9\ \frac{\mathrm{g}}{\mathrm{mol}}$	[61]
Mole Density c	$388.73\ \frac{\mathrm{mol}}{\mathrm{m}^3}$ @ 300 K	[80]
Specific heat capacity $\bar{C}_s$	$27.22\ \frac{\mathrm{J}}{\mathrm{mol\,K}}$ @ 300 K	[80]
Thermal Conductivty κ	$0.449\ \frac{\mathrm{W}}{\mathrm{m\,K}}$ @ 300 K	[80]

Table 5.1: Properties of solid I.

Property	Value (I_2)	Value (C_4F_8)
Molecular weight M_w	253.8 $\frac{\mathrm{g}}{\mathrm{mol}}$	200 $\frac{\mathrm{g}}{\mathrm{mol}}$
Molecule critical dimension d_c	5.16 Å [61]	5.5 Å [81]
Heat of sublimation $\Delta\bar{h}_{sv}$	65.51 $\frac{\mathrm{kJ}}{\mathrm{mol}}$ [82]	N/A

Table 5.2: Properties of I_2 and C_4F_8 vapors.

The ideal gas specific heat capacity $\bar{C}_p$ of I_2 is obtained from [61]. We plot the specific heat capacity over temperature within the experimental range used by Rosenberger et al. ($315\,\mathrm{K} - 385\,\mathrm{K}$) in Fig. 5.1. We see that the specific heat capacity over this range does not change much; we use the average value $\bar{C}_p = 37.2\ \frac{\mathrm{J}}{\mathrm{mol\,K}}$. The constant volume specific heat capacity is found as $\bar{C}_v = \bar{C}_p - R_u = 28.9\frac{\mathrm{J}}{\mathrm{mol\,K}}$. The ideal gas specific heat capacity of C_4F_8 changes significantly over the experimental temperature range (Fig. 5.2). The expression for the $\bar{C}_p$ of C_4F_8 is [61],

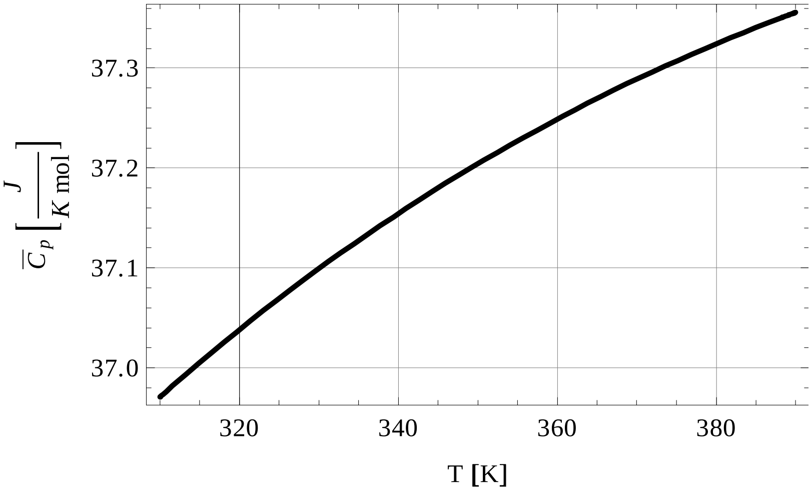

Figure 5.1: The constant pressure specific heat capacity of I_2 plotted over the experimental temperature range.

$$\bar{C}_p^{C_4F_8}(T) = 172.635 + 0.297(T-350) - 4.462\times10^{-4}\,(T-350)^2\ \frac{\mathrm{J}}{\mathrm{mol\,K}}. \tag{5.2}$$

We assume constant specific heats in our models. For each transport case, $\bar{C}_p^{C_4F_8}(T)$ shall be calculated at the average temperature of the scenario. The enthalpy of I_2 for UTU is given

$$\bar{h}(T) = \bar{C}_p^{I_2}\,(T - T_o) + \Delta h_{sv}^{I_2}. \tag{5.3}$$

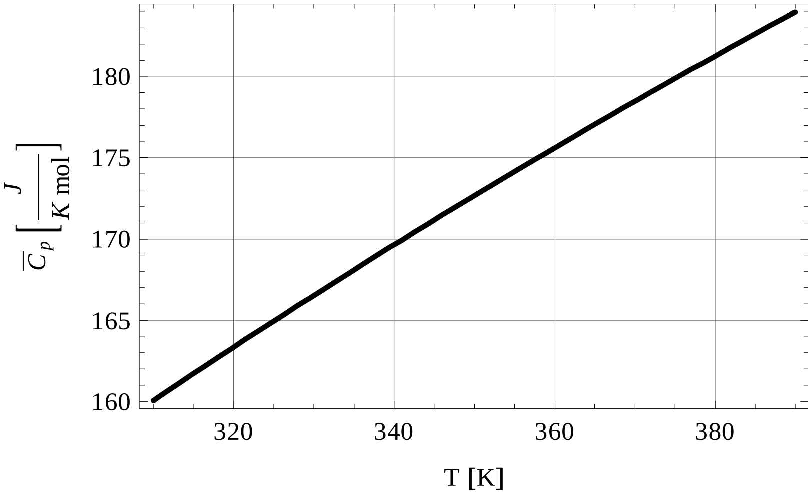

Figure 5.2: The constant pressure specific heat capacity of C_4F_8 plotted over the experimental temperature range.

In UTB, only the total enthalpy is ever calculated. This is obtained as,

$$\bar{h}(T) = \chi_{I_2}\left[\bar{C}_p^{I_2}(T - T_0) + \Delta h_{sv}^{I_2}\right] + \chi_{C_4F_8}\bar{C}_p^{C_4F_8}(\bar{T})(T - T_0). \tag{5.4}$$

The thermal conductivities can now be found using Eq. (2.72). For I_2 we get

$$\kappa(T) = 1.626 \times 10^{-3}\sqrt{T}\ \frac{\mathrm{W}}{\mathrm{m\,K}}. \tag{5.5}$$

with T in K and κ in $\frac{\mathrm{W}}{\mathrm{m\,K}}$. For C_4F_8, the result of (2.72) was an order of magnitude larger than empirical data [84]. We modify this by a correction factor equal to $\frac{1}{10}$. This corrects the calculated value while retaining the temperature relationship; thus

$$\kappa_{C_4F_8}(T) = -1.761 \times 10^{-9}\sqrt{T}\left(T^2 - 1364.1T - 46199.4\right)\ \frac{\mathrm{W}}{\mathrm{m\,K}}. \tag{5.6}$$

Both these expressions are valid only within the range $315\,\mathrm{K} - 386\,\mathrm{K}$.

The mixture thermal conductivity is obtained as a function of composition by (2.74). The resulting expression is quite long; we plot the mixture thermal conductivity in Fig. 5.3.For each transport case, we shall calculate the mixture thermal conductivities using average composition and average temperature for each set of temperatures.

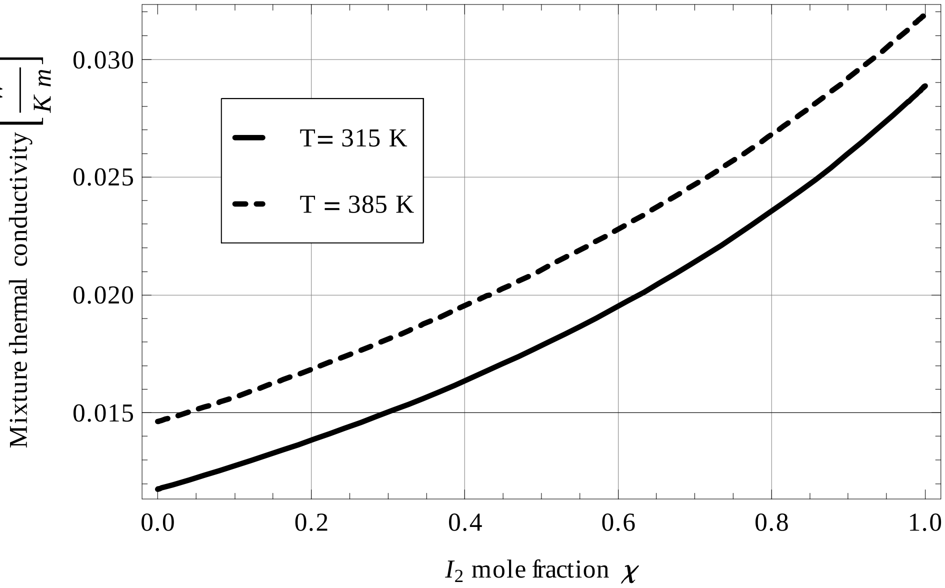

Figure 5.3: The thermal conductivity of the I_2- C_4F_8 mixture.

For the binary diffusion coefficient, we use reference data from [11] with Eq. (2.70):

$$D_{AB}(p,T) = D^0_{ab}\frac{p_0}{p}\left(\frac{T}{T_0}\right)^{1.75}. \tag{5.7}$$

where $D^0_{ab} = 6.9 \times 10^{-5}\,\frac{\mathrm{m}^2}{s}$, $p_0 = 4986\,\mathrm{Pa}$, $T_0 = 356\,\mathrm{K}$.

5.2 Cadmium Telluride - Carbon Monoxide System Properties

In our analysis of the BTB model we shall use a mixture of Cd and Te_2 over solid CdTe. For the BTT model we shall consider a ternary mixture of Cd, Te_2 and CO, following Palosz et al. [12]. CdTe growth experiments typically take place in the temperature range $1070\,\mathrm{K} - 1170\,\mathrm{K}$

5.2.1 Solid Properties

The properties of the bulk CdTe solid are given in Tab. 5.3 for several temperatures.

Since values near typical vapor growth temperatures ($1073-1173\,\mathrm{K}$) are not available, we shall use linear interpolation between the values to approximate the solid properties. Solid CdTe exists over a range of compositions; the phase diagram for the material is given in Fig. 1.14. The stoichiometric arrangement contains Cd and Te atoms only at lattice locations, as per the discussion in Chapter 1. Additional Cd

Property	Value	Source
Molecular Weight M_w	$240.0\ \frac{\mathrm{g}}{\mathrm{mol}}$	[61]
Mole Density c	$21.18 \frac{\mathrm{kmol}}{\mathrm{m}^3}$ @ 300 K	[85]
	$23.67\ \frac{\mathrm{kmol}}{\mathrm{m}^3}$ @ 1365 K	[86]
Specific heat capacity $\bar{C}_s$	$50.4\ \frac{\mathrm{J}}{\mathrm{mol\,K}}$ @ 300 K	[87]
	$57.6\ \frac{\mathrm{J}}{\mathrm{mol\,K}}$ @ 800 K	[87]
	$38.40\ \frac{\mathrm{J}}{\mathrm{mol\,K}}$ @ 1365 K	[86]
Thermal Conductivty κ	$0.449\ \frac{\mathrm{W}}{\mathrm{m\,K}}$ @ 300 K	[85]
	$1.5\ \frac{\mathrm{W}}{\mathrm{m\,K}}$ @ 1365 K	[86]

Table 5.3: Properties of solid CdTe.

Property	Value (Cd)	Value (Te_2)	Value (CO)
Molecular weight M	$112.5 \frac{\mathrm{g}}{\mathrm{mol}}$	$255.8 \frac{\mathrm{g}}{\mathrm{mol}}$	$28 \frac{\mathrm{g}}{\mathrm{mol}}$
Molecule critical dimension d_c	2.61 Å [12]	3.97 Å [12]	3.69 Å[12]

Table 5.4: The basic properties of Cd, Te_2 and CO

or Te molecules dissolve into interstitial sites in the crystal structure. As we shall see, this dissolution effect has a significant influence on the equilibrium composition of the vapor above the CdTe surface.

5.2.2 Vapor Properties

The basic properties of the vapor mixture constituents are given in Tab. 5.4. We obtain values for the specific heat capacity of Cd and Te_2 using the Benson method tabulation [61]; since data for Te_2 is not available, we use values for iodine vapor (I_2). The results are given in Tab. 5.5. We shall always calculate the total vapor enthalpy as opposed to the individual constituent enthalpies. We replace the partial heats of sublimation of each with the total heat of reaction, given by (5.17). In both BST and TST, we sum over all constituents such that,

$$\bar{h}(T) = \sum_a \chi_a \bar{C}_p^a \left(T - T_0\right) + \Delta \bar{h}_r^0(T) \tag{5.8}$$

To determine the thermal conductivity of Cd we use Eq. (2.72) with the values we have already determined. The calculated thermal conductivities between 1070 − 1170 K are more or less constant for all three constituents; we give the resulting conductivities in Tab. 5.5.

Constituant	$\bar{C}_p \left[\frac{\mathrm{J}}{\mathrm{mol\,K}}\right]$	$\kappa \left[\frac{\mathrm{W}}{\mathrm{m\,s}}\right]$
Cd	30 @ 1100 K	0.135
Te_2	38 @ 1100 K (I_2)	0.072
CO	35 @ 1120 K	0.218

Table 5.5: Thermal properties of Cd, Te_2 and CO vapors. These are all nearly constant in the temperature range 1070 K − 1170 K. Values from [61].

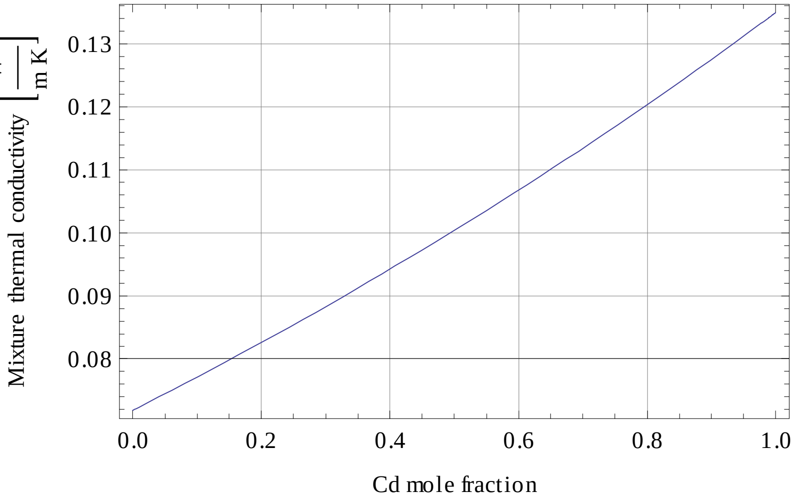

Figure 5.4: The thermal conductivity of the Cd – Te_2 vapor mixture as a function of composition.

Pairing	D_{AB} $\left[\mathrm{cm}^2/\mathrm{s}\right]$	p_0 [kPa]	T_0 [K]
Cd - CO	1.72	101	1163
Te_2 - CO	1.06	101	1163
Cd - Te_2	4.95	101	1163

Table 5.6: The binary diffusion coefficients on the Cd-Te_2-CO system.

For the mixture thermal conductivity, we use Eq. (2.74). The resulting thermal conductivity in the binary Cd-Te_2 system is plotted in Fig. 5.4; the thermal conductivity for the ternary system is plotted in Fig. 5.5.

In both BTB and BTT, the variations of thermal conductivity with composition are not extreme; values based upon the average composition within the system shall be used.

We obtain reference values from [12]. These are given in Tab. 5.6.

5.2.3 Saturation Pressure over Solid CdTe

We now consider the vapor mixture above solid CdTe at equilibrium. As discussed in Chapter 1, CdTe dissociates according to

$$\mathrm{CdTe(s)} \rightleftharpoons \mathrm{Cd(v)} + \sum_{n=1}^{7} \alpha_n \frac{1}{n} \mathrm{Te}_n\mathrm{(v)}, \tag{5.9}$$

where s indicates solid constituents and v indicates vaporous constituents. Whereas Cd exists exclusively as a monatomic molecule in the vapor, Te can exist as a monatomic molecule, a diatomic molecule, and a variety of polymers up to Te_7 [54, 88]. It has been demonstrated experimentally that at temperatures within the range $912\,\mathrm{K} - 1325\,\mathrm{K}$ the concentrations of polymers other than Te_2 are negligible [88]. Thus,

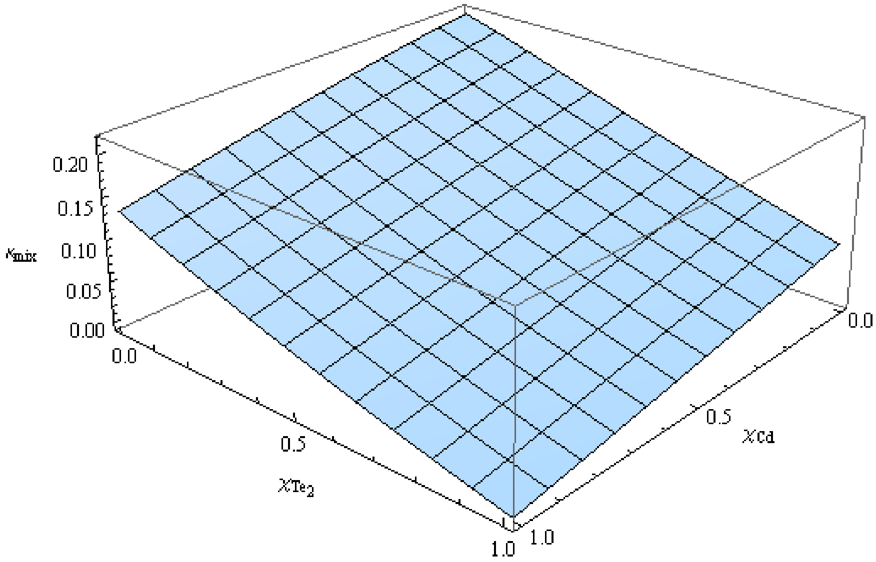

Figure 5.5: The thermal conductivity of the Cd – Te_2 – CO vapor mixture as a function of Cd and Te_2 mole fractions.

for our purposes, we assume that the dissociation reaction for CdTe takes the form

$$\mathrm{CdTe(s)} \rightleftharpoons \mathrm{Cd(v)} + \frac{1}{2}\mathrm{Te_2(v)}. \tag{5.10}$$

The equilibrium mixture of Cd and Te_2 vapors can have a wide range of compositions, depending upon the composition of the solid. The saturation pressure ratio is defined as

$$\zeta = \frac{p_{sat}^{Cd}}{p_{sat}^{Te_2}}. \tag{5.11}$$

The saturation pressures over solid CdTe must then be a function of T and ζ. We discuss ζ in more detail in §5.2.4. To determine the values for the saturation pressure, we consider first the law of mass action

$$\sum_{a=1}^{\nu} \gamma_a \bar{\mu}_a = 0. \tag{5.12}$$

where γ_a is the stoichiometric coefficient for each product and reactant, the product γ_a are taken as negative, the reactant γ_a are taken as positive; ν is the number of reactants and products in the reaction.

For (5.10) the law of mass action gives

$$0 = -\bar{\mu}_{CdTe}(T) + \bar{\mu}_{Cd}(T,p) + \frac{1}{2}\bar{\mu}_{Te_2}(T,p). \tag{5.13}$$

This can be written in terms of individual Gibbs free energies by considering equation (2.23) for the product vapors, and recalling that for a single species solid, as on the reactant side of (5.10), $\bar{\mu} = \bar{g}$.

$$0 = -\bar{g}_{CdTe}(T) + \bar{g}_{Cd}(T,p) + \frac{1}{2}\bar{g}_{Te_2}(T,p) + R_u T \ln\left(\chi_{sat}^{Cd}\sqrt{\chi_{sat}^{Te_2}}\right).$$

The Gibbs free energy change of the reaction is defined as $\Delta\bar{g}_r(T,p) = \sum_{a=1}^{\nu}\gamma_a\bar{g}_a$, thus we can write,

$$\chi_{sat}^{Cd}\sqrt{\chi_{sat}^{Te_2}} = \exp\left[-\frac{\Delta\bar{g}_r(T,p)}{R_u T}\right], \tag{5.14}$$

or, in terms of partial pressure, as

$$K_p(T) = p_{sat}^{Cd}(T,\zeta)\sqrt{p_{sat}^{Te_2}(T,\zeta)} = p_0^{3/2}\exp\left[-\frac{\Delta\hat{g}_r^0(T)}{R_u T}\right], \tag{5.15}$$

where $K_p(T)$ is the equilibrium constant of the reaction. The thermal part of the Gibbs free energy of reaction can be written in terms of enthalpy and entropy,

$$\Delta\hat{g}_r^0(T) = \Delta\hat{h}_r^0(T) - T\Delta\hat{s}_r^0(T). \tag{5.16}$$

Expressions for $\Delta\hat{h}_r^0$ and $\Delta\hat{s}_r^0$ have been obtained experimentally [88] as,

$$\Delta\hat{h}_r^0(T) = 308599 - \frac{736912}{T} - 13.0645T - 0.0095T^2 \ \frac{\mathrm{J}}{\mathrm{mol}}, \tag{5.17}$$

$$\Delta\hat{s}_r^0(T) = 297.654 - \frac{368456}{T^2} - 0.019T - 13.0718\ln T \ \frac{\mathrm{J}}{\mathrm{mol\,K}}. \tag{5.18}$$

The variation of these expressions with CdTe solid composition have been shown to be negligible over the range of possible solid compositions [88, 12, 54, 4]. Thus, for any CdTe composition, the saturation vapor pressures must satisfy (5.15). For any ζ the saturation pressures can be determined by solving (5.15) and (5.11) simultaneously.

5.2.4 Saturation pressure ratio

To relate the partial pressure ratio ζ to the composition of the solid, some knowledge of the solubility of Cd and Te in CdTe is required; these calculations were done independently by Greenberg [54] and by

Yellin and Szapiro [53]. In both cases it was found that ζ is extremely sensitive to composition, and even a 0.001 mol-% difference in the Cd to Te ratio can change the ζ by an order of magnitude, depending upon the temperature. Fig. 5.6 gives the relationship between the amount of dissolved tellurium and the partial pressure ratio of the equilibrium vapor. Tellurium or cadmium will dissolve into the solid until the corresponding tellurium or cadmium vapor pressure above the solid becomes large enough that a liquid phase of the excess constituent nucleates. Yellin and Szapiro determined the solid and vapor compositions at the point where the liquid phase nucleates; this was calculated only for the Te side, as the nucleation of liquid Cd is not typically seen in vapor growth experiments [53, 27, 12]; these values are given in Tab. 5.7.

Temp. $[K]$	Composition shift $[\text{mol} - \%]$	ζ
1073	$\delta Te > \delta Te_l$	3.0×10^{-4}
	$\delta Te = 0.005$	4.6×10^{-4}
	$\delta Cd = 0.005$	2.0×10^{4}
1173	$\delta Te > \delta Te_l$	0.021
	$\delta Te = 0.01$	0.084
	$\delta Te = 0.005$	0.22
	$\delta Cd = 0.05$	1.0×10^{4}

Table 5.7: Equilibrium vapor pressure ratios of CdTe above solids of corresponding composition as calculated in [53]. Here δTe_l refers to the composition at which liquid tellurium nucleates.

Fig. 5.6 gives the relationship between the composition of CdTe and the ζ as a function of composition and temperature.

From Tab. 5.7, it is clear that the variation of ζ within the SV region is quite extreme, and has serious implications on the vapor growth of CdTe, we shall discuss this in more detail in Chapter 8.

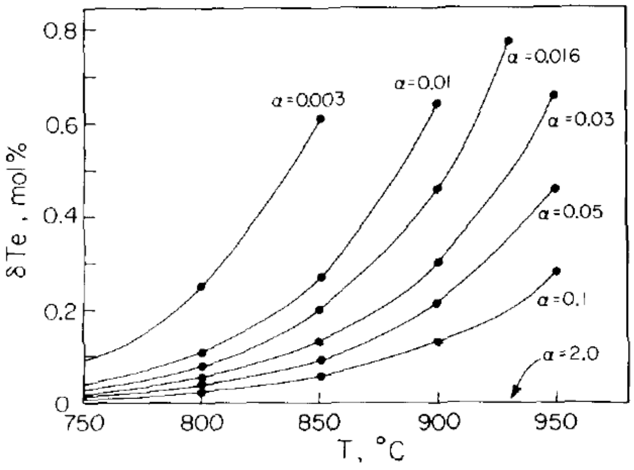

Figure 5.6: The relationship between the vapor equilibrium composition ratio ζ (here indicated as α) and the composition of the solid phase for tellurium rich compositions of CdTe as a function of temperature. *Used with permission from Elsevier.*

Chapter 6

Solution Generation Method

The complete set of equations and boundary conditions to describe the UTU, UTB, UTB and UTT problems have been obtained in the preceeding chapters. In this chapter, we combine these and describe our solution method.

6.1 Setup

We reconsider the arrangement in Fig. 6.1. The source interface at $x = 0$ is set to T_1; full thermal and chemical equilibrium is considered at this interface — we assume the source is a ground powder such that the surface area is very large[1]. The seed is located at $x = x_2$, the end of the solid seed is located at $x = x_3$, it is set to a temperature T_3. The wall temperature distribution is defined such that $T_w(0) = T_1$ and $T_w(x_3) = T_3$.

6.1.1 Frame of Reference

The interfaces in PVT are mobile. During transport, Interface 1 retreats in the $-x$ direction as the source material is depleated and Interface 2 advances in the $-x$ direction as the seed crystal grows (Fig. 6.1). We return to the continuity jump condition (3.4a), this time considering a mobile interface in the lab frame of reference. Interface 1 is located at $x = x_1$, and interface 2 is located at $x = x_1 + L$, the total flux jump conditions become, for Interfaces 1 and 2 respectively,

$$J - c_s^1 \tilde{u}_1 = J - c_v(x_1)\tilde{u}_1, \tag{6.1}$$

$$J - c_s^2 \tilde{u}_2 = J - c_v(x_1 + L)\tilde{u}_2. \tag{6.2}$$

---

[1] See the discussion in §3.4.1.

These equations can be solved for the interface velocities,

$$\tilde{u}_1 = -\frac{J}{c_{sol} - c_{vap}(x_1)}, \quad (6.3)$$

$$\tilde{u}_2 = -\frac{J}{c_{sol} - c_{vap}(x_1 + L)}; \quad (6.4)$$

here, the interfaces have different velocities which depend upon the density of the vapor. By Assumption 14 ($c_{sol} \gg c_{vap}$), the vapor density can be neglected against the solid density in the interface velocities, thus,

$$\tilde{u}_1 \simeq \tilde{u}_2; \quad (6.5)$$

the interfaces move at approximatly the same velocity. Therefore, a frame of reference attached to Interface 1 allows us to apply the static interface model of Chapter 3 with no modification.

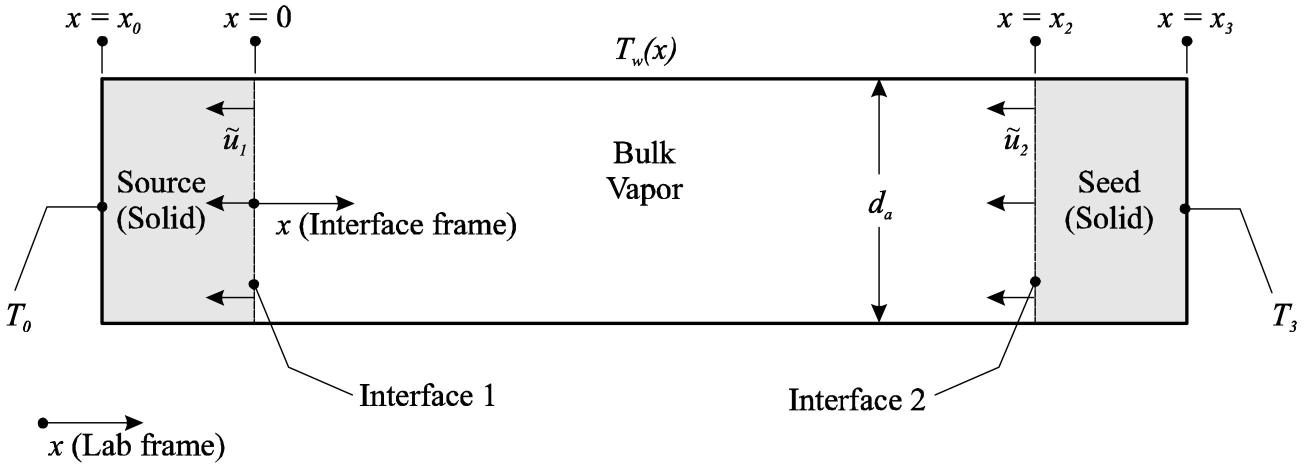

Figure 6.1: Frames of reference in the PVT model domain. The interface frame is attached to Interface 1; the lab frame is attached to the walls of the domain.

6.1.2 Wall temperature profiles

We shall use three types of temperature profiles. The first are linear wall temperature profiles of the form

$$T_w(x) = -\frac{T_1 - T_2}{x_2}x + T_1 \quad (6.6)$$

where T_1 is the perscribed wall temperature at Interface 1 and T_2 is the wall temperature at Interface 2. As we shall see, these are generaly *not* equal to the actual interface temperatures.

We shall also make use of a discontinuous temperature profile, given by

$$T_w(x) = \begin{cases} -\frac{T_1 - T_I}{x_I} x + T_1 & \text{if } x \leq x_I \\ -\frac{T_I - T_3}{x_3 - x_I} (x_I - x_2) + T_3 & \text{if } x_I < x \leq x_3 \end{cases} \tag{6.7}$$

Finally, we shall also make use of polynomial temperature profiles given by

$$T_w(x) = a_0 + a_1 x + a_2 x^2 + a_3^3 + a_4^4. \tag{6.8}$$

6.1.3 Controlled Parameters

For each transport problem, we set-up with reference to Fig. 6.1, the geometry of the problem:

- The distance between the left hand side end of the ampoule and the origin at Interface 1 x_0.
- The distance between Interface 1 and Interface 2, x_2.
- The distance between Interface 1 and the end of the ampoule x_3
- The diameter of the ampoule d_a.

We also set-up the temperatures,

- T_0, the temperature at the end of the source.
- T_3, the temperature at the end of the seed.
- T_w, the wall temperature profile.

We estimate the average temperature of the vapor in order to calculate the thermochemical properties $\{\bar{C}_p, \kappa, \text{etc.}\}$. For this, we use the wall temperature profile,

$$\bar{T}_v = \frac{1}{x_2} \int_0^{x_2} T_w(x) dx. \tag{6.9}$$

For the UTB and BTT problems we set the background gas fill pressure p_z^0. Finally, for the BTB and BTT problems, we set the vapor pressure ratio for the source material ζ_1.

6.2 Analytical solutions to the bulk transport equations

We now solve the bulk transport equations: the energy equation (2.46) and the mole transport equation(s) (2.35).

6.2.1 The energy equation

We combine the energy equation (2.46) with Fourier's law (2.63) and replace $\frac{d\bar{h}}{dx} = \bar{C}_p \frac{dT}{dx}$ under Assumption 4 to obtain the final form of the energy equation for the vapor,

$$-\frac{\kappa}{\Lambda}\frac{d^2T}{dx^2} + \frac{J\bar{C}_p}{\Lambda}\frac{dT}{dx} + T(x) = T_w(x). \tag{6.10}$$

The solution to this second order non-homogeneous ordinary differential equation (ODE), the solution to which can be found using the method of underdetermined coefficients. The solution is

$$T(x) = \mathcal{C}_2 \exp\left\{\frac{\bar{C}_pJ - \mathcal{A}}{2\kappa}x\right\} + \mathcal{C}_3 \exp\left\{\frac{\bar{C}_pJ + \mathcal{A}}{2\kappa}x\right\} + \mathcal{I}\left[T_w(x)\right]; \tag{6.11}$$

where, $\mathcal{A} = \sqrt{\left(\bar{C}_pJ\right)^2 + 4\kappa\Lambda}$, $\mathcal{C}_1$ and $\mathcal{C}_2$ are integration constants and $\mathcal{I}\left[T_w(x)\right]$ is an integral term that is dependent upon the wall temperature distribution,

$$\begin{aligned}\mathcal{I}\left[T_w(x)\right] \quad = \quad & \exp\left\{\frac{\bar{C}_pJ - \mathcal{A}}{2\kappa}x\right\}\left[-\frac{1}{\mathcal{A}}\int_x^1 \exp\left\{\frac{-\bar{C}_pJ + \mathcal{A}}{2\kappa}s\right\}\Lambda T_w(s)ds\, + \right. \\ & \left. + \exp\left\{\frac{x\mathcal{A}}{\kappa}\right\}\frac{1}{\mathcal{A}}\int_x^1 \exp\left\{\frac{\bar{C}_pJ + \mathcal{A}}{2\kappa}s\right\}\Lambda T_w(s)ds\right].\end{aligned} \tag{6.12}$$

The form of the solution is the same in both the solid and vapor phases; however, the coefficients and boundary conditions are different in every case. We use constants $\{C_0, C_1\}$ in the solid source, $\{C_2, C_3\}$ in the vapor, and $\{C_4, C_5\}$ in the solid seed.

6.2.2 The mole transport equations

In UTU (2.35) is trivial and need not be solved. For a UTB and BTB where the vapor mixture has two constituents a and b, (2.35) combined with the linearized Fick's law for a binary system (2.65) gives,

$$J_a = \frac{p_a\left(x\right)}{p}J - \frac{D_{ab}\left(\bar{T}, p\right)}{R_u\bar{T}}\frac{dp_a}{dx}. \tag{6.13}$$

where $\bar{T}$ is the average vapor temperature. An equivelant equation could be written for b, but only one equation is required since $p_b(x) = p - p_a(x)$. The solution to the non-homogeneous ODE is now obtained by integration:

$$p_a(x) = \frac{J_a p}{J} + C_6 \exp\left\{ \frac{J R_u \bar{T}}{p D_{az}\left(p, \bar{T}\right)} x \right\}, \tag{6.14}$$

where C_6 is an additional integration constant.

If the bulk vapor is a ternary mixture composed of a, b, and c, as in BTT, two linearized diffusion-advection equations are required; this results in a system of differential equations

$$\begin{bmatrix} J_a \\ J_b \end{bmatrix} = \frac{J}{p} \begin{bmatrix} p_a(x) \\ p_b(x) \end{bmatrix} - \frac{\mathcal{D}_{AB}\left[\bar{T}, p, \bar{\chi}_a, \bar{\chi}_b\right]}{R_u \bar{T}} \begin{bmatrix} \frac{dp_a}{dx} \\ \frac{dp_b}{dx} \end{bmatrix}; \tag{6.15}$$

where $\mathcal{D}_{AB}\left[\bar{T}, p, \bar{\chi}_a, \bar{\chi}_b\right]$ is the diffusivity matrix as defined by linearized diffusion theory. Constituents a and b were chosen arbitrarily here, an equivalent set could easily be written for a and c or b and c. The average diffusivities $\{\bar{\chi}_a, \bar{\chi}_b\}$ are calcaulated,

$$\bar{\chi}_a = \frac{1}{L} \int_0^L \frac{p_a(x)}{p}, \ \bar{\chi}_b = \frac{1}{L} \int_0^L \frac{p_b(x)}{p}. \tag{6.16}$$

The system (6.15) can be solved analytically, the solutions are obtained using Mathematica's DSolve function; these solutions are very long, and are omitted here for brevity. Two additional integration constants C_6, C_7 are introduced. Appropriate values for $\{\bar{\chi}_a, \bar{\chi}_b\}$ must still be found; we obtain these by an iterative scheme [32]:

1. Guess initial values $\bar{\chi}_a^0$ and $\bar{\chi}_b^0$.
2. Solve (6.15) for $p_a\left(x\right)$ and $p_b(x)$ using $\bar{\chi}_a^0$ and $\bar{\chi}_b^0$.
3. Solve the constraining equations[2] for the model parameters.
4. Estimate new average composition values using $\bar{\chi}_a^1 = \frac{1}{L} \int_0^L \frac{p_a(x)}{p} dx$ and $\bar{\chi}_b^1 = \frac{1}{pL} \int_0^L \frac{p_b(x)}{p} dx$
5. Test for convergence $\bar{\chi}_a^0 == \bar{\chi}_a^1?, \bar{\chi}_b^0 == \bar{\chi}_b^1?$ If true stop, else,
6. Set $\bar{\chi}_a^0 = \bar{\chi}_a^1$, $\bar{\chi}_b^0 = \bar{\chi}_b^1$ and repeat the procedure.

---

[2] See §6.4.

For initial guesses, the average equilibrium values for the source.

$$\bar{\chi}_a^0 = \frac{p_{sat}^a\left(\bar{T},\zeta_1\right)}{p_{sat}^a\left(\bar{T},\zeta_1\right)+p_{sat}^b\left(\bar{T},\zeta_1\right)+p_z^0} \tag{6.17a}$$

$$\bar{\chi}_b^0 = \frac{p_{sat}^b\left(\bar{T},\zeta_1\right)}{p_{sat}^a\left(\bar{T},\zeta_1\right)+p_{sat}^b\left(\bar{T},\zeta_1\right)+p_z^0} \tag{6.17b}$$

We found that the algoritim converges rapidly with these intial guesses; usually only 3 or 4 iterations are required for 3 digit precision.

6.3 Constraining Equations

The analytical solutions to the bulk phase transport must be constrained so as to solve for the unknown parameters. These include the transport rate J, the total pressure p, and the integration constants. These constraning equations (CEqs) fall into three categories: boundary conditions, conservation laws, and reaction relations.

6.3.1 Boundary conditions

Boundary conditions define the values of the analytical solutions at the interfaces as well as at the ampoule ends. At the LHS ampoule end we use:

$$T(x_0) = T_w(x_0) = T_0 \tag{6.18}$$

At Interface 1, we always use equilibrium interface conditionsfor each constituent:

$$T_v(0) = T_w(0) = T_1, \tag{6.19}$$

$$p_a(0) = p_{sat}^a(T_1). \tag{6.20}$$

At Interface 2, we occasionally use equilibrium interface conditions

$$T_v(x_2) = T_s(x_2), \tag{6.21}$$

$$p_a(x_2) = p_{sat}^a\left[T_s(x_2)\right]. \tag{6.22}$$

For reactive condensation, as described in §3.2.1, the equilibrium interface boundary condition is

$$K_v = K_p\left[T_s(x_2)\right] \tag{6.23}$$

We also use NE interface boundary conditions at Interface 2. These were defined in §3.3. We recall these: for a unitary system (UTU),

$$\begin{bmatrix} J_a \\ q \end{bmatrix} = \begin{bmatrix} J_a \\ -\kappa_v \frac{dT_v}{dx} \end{bmatrix} = \mathcal{L}^{(1)}_{AB}(T_s, p_{sat}, \theta_a) \begin{bmatrix} -\frac{R_u}{p^a_{sat}(T_s)} [\Delta p_a] \\ \frac{\Delta T}{T_s^2} \end{bmatrix}; \tag{6.24}$$

for a binary system with one condensing constituent (UTB),

$$\begin{bmatrix} J_a \\ 0 \\ q \end{bmatrix} = \begin{bmatrix} J_a \\ 0 \\ -\kappa_v \frac{dT_v}{dx} \end{bmatrix} = \mathcal{L}^{(1+)}_{AB}(T_s, p^a_{sat}, \theta_a) \begin{bmatrix} -\frac{R_u}{p^a_{sat}(T_s)} [\Delta p_a] \\ 0 \\ \frac{\Delta T}{T_s^2} \end{bmatrix}; \tag{6.25}$$

for a binary system with two condensing constituents (BTB),

$$\begin{bmatrix} J_a \\ J_b \\ q \end{bmatrix} = \begin{bmatrix} J_a \\ J_b \\ -\kappa_v \frac{dT_v}{dx} \end{bmatrix} = \mathcal{L}^{(2)}_{AB}(T_1, \zeta_2, \theta_a, \theta_b) \begin{bmatrix} -\frac{R_u}{p^a_{sat}(T_s)} [\Delta p_a] \\ -\frac{R_u}{p^b_{sat}(T_s)} [\Delta p_b] \\ \frac{\Delta T}{T_s^2} \end{bmatrix}; \tag{6.26}$$

for a ternary system with two condensing constituents (BTT),

$$\begin{bmatrix} J_a \\ J_b \\ 0 \\ q \end{bmatrix} = \begin{bmatrix} J_a \\ J_b \\ 0 \\ -\kappa_v \frac{dT_v}{dx} \end{bmatrix} = \mathcal{L}^{(2+)}_{AB}(T_1, \zeta_2, \theta_a, \theta_b) \begin{bmatrix} -\frac{R_u}{p^a_{sat}(T_s)} [\Delta p_a] \\ -\frac{R_u}{p^b_{sat}(T_s)} [\Delta p_b] \\ 0 \\ \frac{\Delta T}{T_s^2} \end{bmatrix}. \tag{6.27}$$

and, finally for a reactive condensation with two condensing constituents,

$$\begin{bmatrix} J_{Rx} \\ q \end{bmatrix} = \begin{bmatrix} J_{Rx} \\ -\kappa_v \frac{dT_v}{dx} \end{bmatrix} = \mathcal{L}^{(Rx)}_{AB}(T_1, \zeta_2, \theta_a, \theta_b) \begin{bmatrix} -\frac{\Delta K}{K_p(T_s)} \\ \frac{\Delta T}{T_s^2} \end{bmatrix}. \tag{6.28}$$

The phenomenological matricies $\mathcal{L}^{(n)}_{AB}$ were obtained as described in Chapter 4.

The final boundary condition is for the edge of the seed at $x = x_3$. Here, we always use a thermal equilibrium condition,

$$T(x_3) = T_w(x_3) = T_3. \tag{6.29}$$

Two additional boundary conditions for the interfaces can be obtained from the first law (3.6). When consistent reference values are chosen, this equation incorporates the effects of the latent heat of sublimation into the model. The conditions are, for Interface 1,

$$J\left\{\bar{C}_p\left[T_v(0)-T_{ref}\right]+(1-\chi_z)\,\Delta\bar{h}_{sv}\right\}-\kappa_v\frac{dT_v}{dx}(0)=J\left\{\bar{C}_s\left[T_s(0)-T_{ref}\right]\right\}-\kappa_s\frac{dT_s}{dx}(0)\,, \tag{6.30}$$

and for Interface 2,

$$J\left\{\bar{C}_p\left[T_v(x_2)-T_{ref}\right]+(1-\chi_z)\,\Delta\bar{h}_{sv}\right\}-\kappa_v\frac{dT_v}{dx}(x_2)=J\left\{\bar{C}_s\left[T_s(x_2)-T_{ref}\right]\right\}-\kappa_s\frac{dT_s}{dx}(x_2)\,. \tag{6.31}$$

6.3.2 Mass conservation

The conservation of mass (moles) within the bulk can be used to provide an additional constraining equation in situations where an inert background constituent z is present, as in UTB and BTT. This background gas exists only in the bulk vapor phase and cannot cross either interface such that its overall flux is [9]

$$J_z = 0. \tag{6.32}$$

For any choice of parameters, the total quantity of z is always constant and equal to a prescribed initial quantity N_z Since the volume of the vapor phase V is constant (assumption 10), the average mole density of z, $\bar{c}_z = \frac{N_z}{V}$, must also be constant. If $\bar{c}_z$ is constant, the ideal gas law can be used to determine a corresponding partial fill pressure p_z^0 in terms of the average temperature $\bar{T}$,

$$p_z^0 = \bar{c}_z R_u \bar{T} = \frac{1}{L}\int_0^L p_z(x)dx. \tag{6.33}$$

This equation provides an additional CEq if a background gas is present.

6.3.3 Reaction relations

The BTB and BTT cases considered in this thesis model the transport of CdTe. As we discussed in Chapter 5, CdTe undergoes a chemical reaction at the condensing interface. We assume the transport of CdTe is always stoichiometric (see Chapter 8). The two fluxes can be related to one another by [9]

$$J_{Cd} = 2J_{Te_2} \tag{6.34}$$

The ratio of saturation pressures at the condensing interface is an unknown ζ_2, and must be solved from boundary conditions (6.26) or (6.27).

6.4 Systems of Constraining Equations

CEq #	Parameter	Eq Sol.	NE Sol.
1.	p	(6.20)	(6.20)
2.	J_a	(6.22)	(6.24)
3.	C_0	(6.18)	(6.18)
4.	C_1	(6.19)	(6.19)
5.	C_2	(6.30)	(6.30)
6.	C_3	(6.21)	(6.24)
7.	C_4	(6.31)	(6.31)
8.	C_5	(6.29)	(6.29)

Table 6.1: The system of equations in the UTU transport problem. Eq Sol. corresponds to the equilibrium solution, NEq Sol. corresponds to the non-equilibrium solution.

CE #	Parameter	Eq Sol.	NE Sol.
1.	p	(6.20)	(6.20)
2.	J_a	(6.22)	(6.25)
3.	C_0	(6.18)	(6.18)
4.	C_1	(6.19)	(6.19)
5.	C_2	(6.30)	(6.30)
6.	C_3	(6.21)	(6.25)
7.	C_4	(6.31)	(6.31)
8.	C_5	(6.29)	(6.29)
9.	C_6	(6.33)	(6.33)

Table 6.2: The system of constraining equations in the UTB transport problem.

Table 6.1 gives the system of contraining equations in the UTU transport problem. Here, the solutions to parameters $\{p, C_0, C_1, C_2, C_3, C_4\}$ are linear and $\{J_a, C_5\}$ are non-linear. The UTB system of equations in given in Tab. 6.2. Here, the solutions to parameters $\{C_0, C_1, C_2, C_3, C_4\}$ are linear, the solutions to $\{C_5, C_6, J_{,}p\}$ are non-linear. The BTB system of equations in given in Tab. 6.3. Here, the solutions to parameters $\{C_0, C_1, C_2, C_3, C_4\}$ are linear, the solutions to $\{C_5, C_6, J_{,}p, \zeta_2\}$ are non-linear. The BTT system of equation is given in Tab. 6.4. Here, the solutions to parameters $\{C_0, C_1, C_2, C_3, C_4\}$ are linear, the solutions to $\{C_5, C_6, C_7, J_{,}p, \zeta_2\}$ are non-linear. For reactive boundary conditions in BTB, the system of equations is givne in Tab. 6.5. Here, the solutions to parameters $\{C_0, C_1, C_2, C_3, C_4\}$ are linear and the solution to $\{C_5, C_6, J_{Rx,}p\}$ are non-linear.

6.5 Equation Solving Software and Functions

For all solutions, we use Wolfram Mathematica 7 ©.

To solve for the analytical solution to the system of mole transport equations in the ternary system, we make use of the "DSolve" function. This function employs Mathematica's extensive, propriatary

CE #	Parameter	Eq Sol.	NE Sol.
1.	p	(6.20)	(6.20)
2.	J_a	(6.22)	(6.26)
3.	J_b	(6.34)	(6.34)
4.	C_0	(6.18)	(6.18)
5.	C_1	(6.19)	(6.19)
6.	C_2	(6.30)	(6.30)
7.	C_3	(6.21)	(6.26)
8.	C_4	(6.31)	(6.31)
9.	C_5	(6.29)	(6.29)
10.	C_6	(6.20)	(6.26)
11.	ζ_2	(6.22)	(6.26)

Table 6.3: The system of equations in the BTB transport problem. Note that the reference to Eq. (6.22) appears twice. This corresponds to seperate equations written for p_a and for p_b.

CE #	Parameter	Eq Sol.	NE Sol.
1.	p	(6.33)	(6.33)
2.	J_a	(6.22)	(6.27)
3.	J_b	(6.34)	(6.34)
4.	C_0	(6.18)	(6.18)
5.	C_1	(6.19)	(6.19)
6.	C_2	(6.30)	(6.30)
7.	C_3	(6.21)	(6.27)
8.	C_4	(6.31)	(6.31)
9.	C_5	(6.29)	(6.29)
10.	C_6	(6.20)	(6.20)
11.	C_7	(6.20)	(6.20)
12.	ζ_2	(6.22)	(6.27)

Table 6.4: The system of equations in the BTT transport problem. Note that the reference to Eq. (6.22) appears twice. This corresponds to seperate equations written for p_a and for p_b.

database of differential equations [89].

To solve the linear equations, we make use of the ”Solve” function. This function re-arranges the equations algebraically for the solution [89].

To solve the non-linear equations, we make use of the ”FindRoot” function. This function uses Newton's method with initial guesses to converge to an accuracy of six digits [89]. We make initial guesses based upon trial and error and knowledge of previous solutions; i.e., the equilibrium solution is used to make initial guesses for the non-equilibrium solution. If the guesses are close enough to a set of roots, Newton's method will converge to these roots. There is no guarantee that there is only one set of solutions for each transport problem; indeed, we occasionally find several solutions for each system of non-linear equations — however, we have found that only one set of real solutions exists for each transport problem; the remaining solutions are always complex. The real solutions we find tend to be realistic in that they do not violate the second law; are continuous in changes of parameters; and they are reasonably close to

CE #	Parameter	Eq Sol.	NE Sol.
1.	p	(6.20)	(6.20)
2.	J_{Rx}	(6.23)	(6.28)
3.	C_0	(6.18)	(6.18)
4.	C_1	(6.19)	(6.19)
5.	C_2	(6.30)	(6.30)
6.	C_3	(6.21)	(6.28)
7.	C_4	(6.31)	(6.31)
8.	C_5	(6.29)	(6.29)
9.	C_6	(6.20)	(6.20)

Table 6.5: The system of equations in the BTB transport problem considering reactive sublimation. Note that the reference to Eq. (6.28) appears twice. This corresponds to seperate equations written for p_a and for p_b.

experimental data, when applicable. Should the initial guesses be too far from the solution set, an error message of non-convergence is displayed.

Chapter 7

Physical Vapor Transport of Iodine

We now analyze the transport of Iodine (I_2) both without diffusion (UTU) and with diffusion in C_4F_8 (UTB) following [11]. We assume ampoule dimensions identical to those used by Rosenberger et al. [11]; these are given in Fig. 7.1.

7.1 UTU Results

We begin with the simplest case, transport without diffusion (UTU). We recall that UTU is limited only by the thermal impedances and the kinetic impedance. Fig. 7.2 gives the solutions to UTU with equilibrium interface conditions, HK interface conditions and CKB interface conditions; in each case $T_w(0) = 350\,\mathrm{K}$ and $T_w(x_2) = 340\,\mathrm{K}$. In the first row, we show the solution for the sticking coefficient equal to unity. In this case, all three solutions are nearly identical. There is a large negative temperature spike at the source, and a large positive temperature spike at the seed. The negative spike is the result of the absorption of latent heat as the transported material changes phase from solid to vapor. The positive spike is caused by the release of latent heat as the transported material becomes solid. In the equilibrium solution, the pressure is constant and equal to the saturation pressures of the interfaces; thus, the interface temperatures must be equal. In the CKB and HK solutions, the difference between the interface temperatures is very small, though as we see from Fig. 7.2, this must not always be the case. There is a small temperature jump at the seed interface in the CKB solution. This jump is the result of non-convective transport of heat across the interface.

The remaining rows of Fig. 7.2 show the UTU solutions with a reduced sticking coefficient. The equilibrium solution is, not surprisingly, unaffected. This is because the equilibrium interface conditions are independent of the sticking coefficient. At $\theta_s = 0.5$, the HK and CKB solutions remain nearly unchanged from the equilibrium solution; the thermal impedance remains dominant. At $\theta_s = 0.1$ the temperature spikes are reduced as a result of the lower overall transport rate, the kinetic impedance becomes more important. At $\theta_s = 0.01$, the transport rate is reduced even further, and the temperature spikes diminish. The kinetic impedance becomes the dominant transport impedance in the system.

In Fig. 7.3 we plot the equilibrium transport rate as a function of $T_w(0)$ for a linear temperature profile

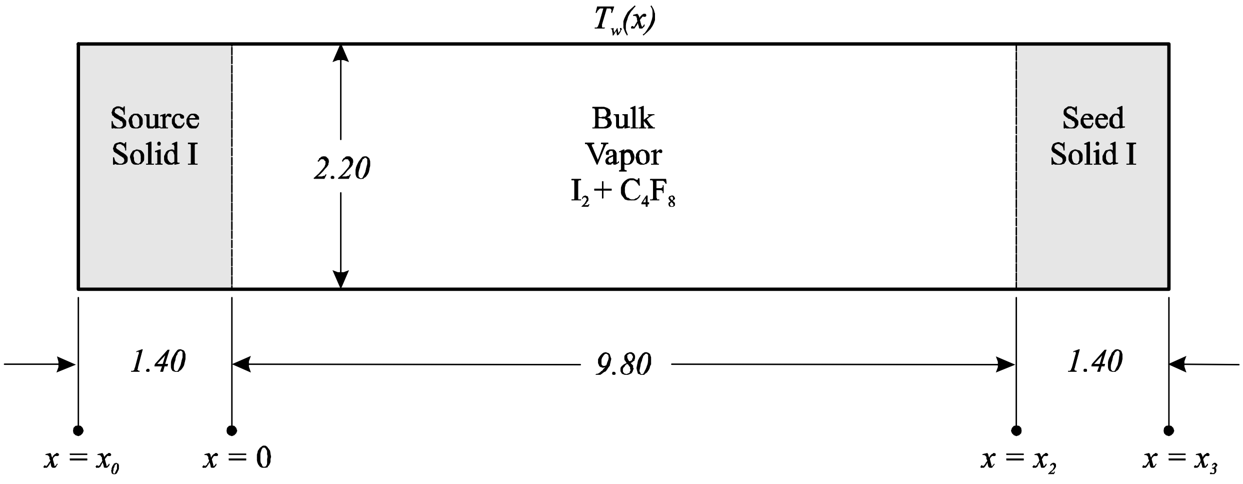

Figure 7.1: The ampoule dimensions for the I_2 transport experiments desciribed in [11]. We use the same dimensions in our analysis. All dimensions above are stated in cm.

with $dT_w/dx = -1\,\mathrm{K/\,cm}$ and $dT_w/dx = -2\,\mathrm{K/\,cm}$; we also give the percent difference between the equilibrium and non-equilibrium (CKB) solutions as a function of the sticking coefficient for both cases. We see that at a high source temperature, the difference between the equilibrium and non-equilibrium solutions is negligible, the thermal impedance is dominant; this confirms our results from Fig. 7.2. When the source temperature is lowered, the difference between the equilibrium and non-equilibrium solutions becomes more significant, even when the sticking coefficient is high. The kinetic impedance at the interface therefore becomes significant enough that it dominates over the latent heat impedance at these low temperatures. We see from Fig. 7.3 that this effect is not as a result of variations in the transport rate, which remains nearly constant as the source temperature is varied. Instead, this effect is caused by the coefficients in the $\mathcal{L}_{AB}$ matrix becoming small at low temperatures, thereby increasing the kinetic impedance at the interface. It is also noticeable that the doubling of the wall temperature gradient, while increasing the transport rate substantially, does not effect the difference between the equilibrium and non-equilibrium solutions much.

7.1.1 HK to CKB Comparison

From Fig. 7.2 we see that the difference between the HK mole flux and the CKB mole flux is negligible, at least in terms of the transport rate. This result is surprising, given the approximate factor 2 difference between the HK and CKB phenomenological coefficient (See Chapter 4). The supersaturation (Δp) in all three plots hints as to why this is the case; the factor 2 difference appears to express itself in

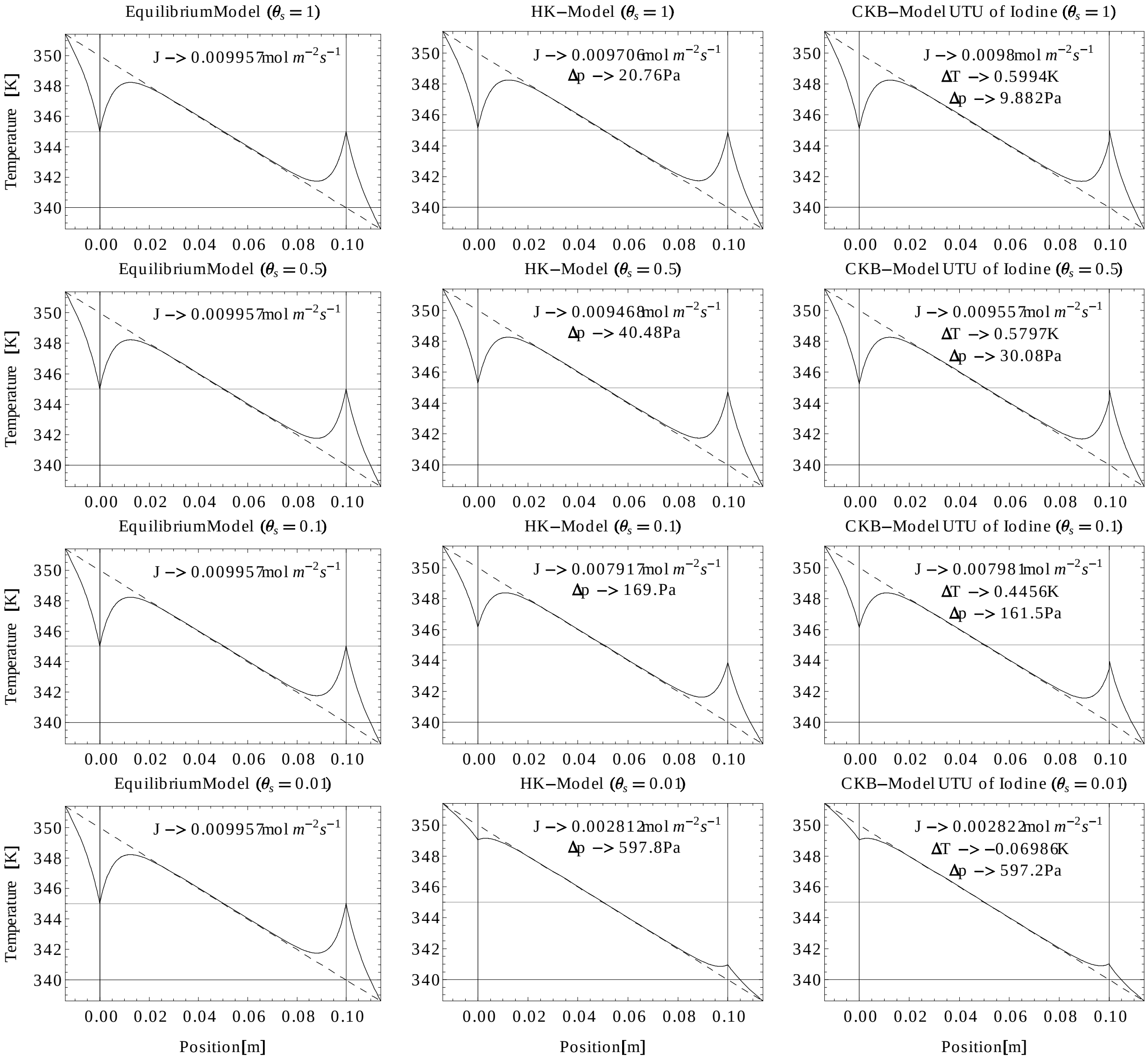

Figure 7.2: Solutions to the UTU problem using the equilibrium model, the HK-model and the CKB-model. The dashed line indicates $T_w(x)$. All cases are shown with the same temperature profile.

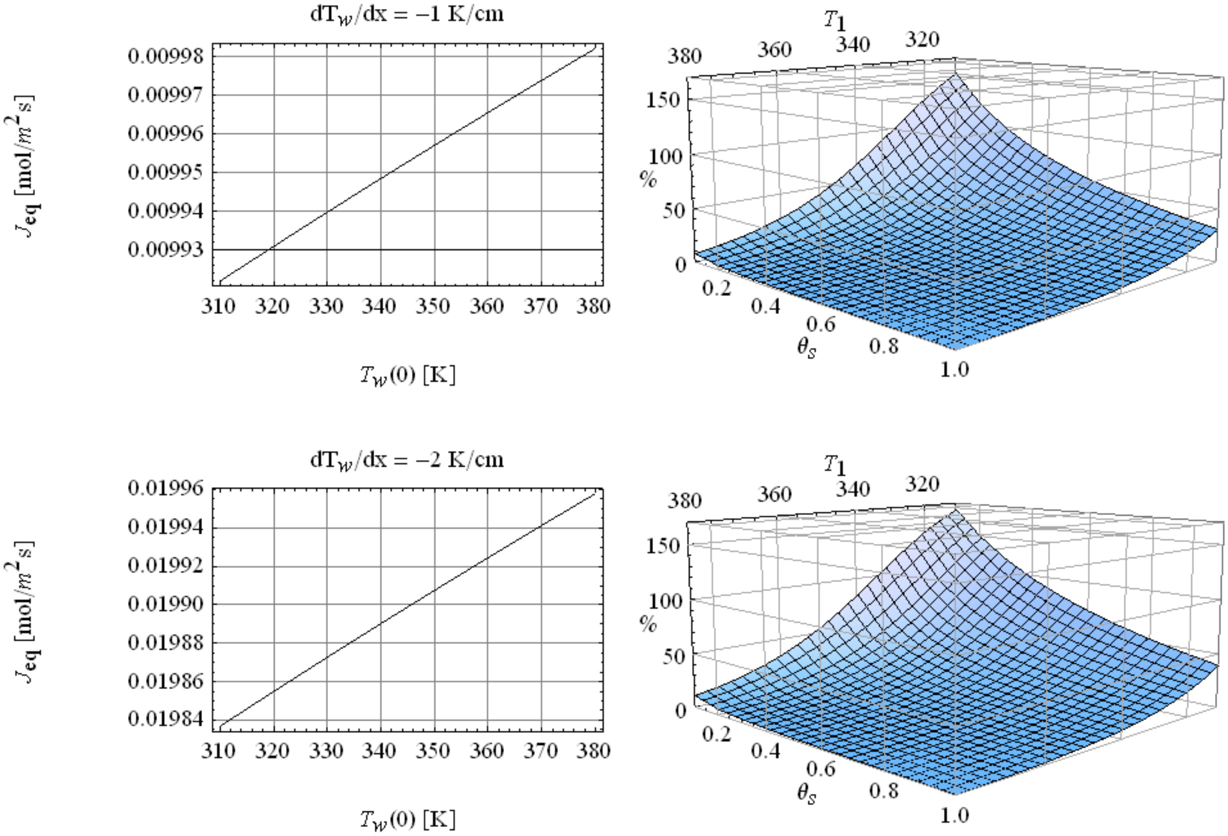

Figure 7.3: On the left, the equilibrium transport rate is given as a function of temperature. On the right, the percent difference between the equilibrium and CKB non-equilibrium solutions is given ($J_{eq} - J_{neq}$).

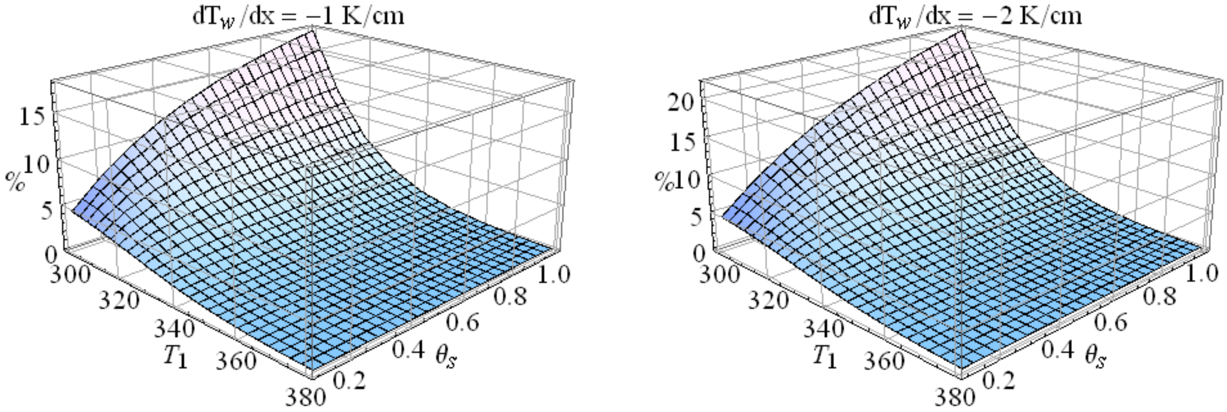

Figure 7.4: The percent difference the HK and CKB model solutions for the UTU problem with a linear temperature gradient. Under all conditions $J_{CKB} > J_{HK}$.

the supersaturation required to drive the interfacial transport, rather than in the transport rate itself. Therefore, at least in the above conditions, the difference between the HK and CKB interface conditions makes little difference in terms of the transport rate, which is limited by the thermal impedance, but significantly affect the supersaturation at the interface.

In Fig 7.4 we plot the %-difference between the CKB and HK mole flux solutions as a function of source temperature $T_w(0)$ and sticking coefficient. At high source temperatures, the difference between the mole flux in the HK solution and the CKB solution is negligible. As the source temperature is decreased, the difference between the two becomes more significant; with the HK model giving a lower transport rate than the CKB model. Since, as we explained in Chapter 4, the HK model is known to be inaccurate, we assume that the HK condition becomes invalid for both mole flux and interface temperature at low temperatures. At higher temperatures, the HK model is acceptable for the mole flux, but still gives erroneous values for the interface temperature. Given the results (Fig. 7.3), the kinetic impedance at the interface becomes insignificant at the high temperatures, where the HK and CKB models converge. Therefore, the HK model only appears to give accurate solutions when the kinetic impedance at the interface is insignificant.

Since the HK model is known to given inaccurate solutions under many circumstances, we abandon the model for the remainder of this thesis, and keep only the CKB and the equilibrium models.

7.2 UTB Results

We reconsider the system described in the previous section, this time containing a background gas, such that the UTB problem is now solved. We recall that the UTB problem adds a diffusive impedance to the already present thermal and kinetic impedances. We once again consider the moderate temperature case where $T_w(0) = 350\,\mathrm{K}$ and $T_w(x_2) = 340\,\mathrm{K}$; this time we use a unity sticking coefficient, and vary the quantity of background gas p_z^0 in the ampoule. We plot the temperature distribution as well as the partial pressure distribution for both the equilibrium and CKB interface conditions. The result is given in Fig. 7.5. As before, the equilibrium and CKB cases are nearly at the temperatures considered. When little background gas is present, the thermal impedance is dominant. As the background gas pressure p_z^0 is increased, the diffusive impedance becomes more significant. At a high background gas pressure, the temperature spikes in the vapor diminish, and the diffusive impedance becomes dominant. When the background gas pressure is increased further, a small negative temperature jump appears at the interface; this feature is discussed in §7.5.

Fig. 7.6 shows the relationship between the p_z^0, θ_s, and the difference between the equilibrium and CKB solutions for mole flux. The corresponding equilibrium mole fluxes are given in Fig. 7.7. The interplay between the three transport impedances becomes clearer. At high background gas pressure, the diffusive impedance becomes dominant, and the equilibrium and non-equilibrium solutions converge. At high temperatures, kinetic impedances are small, but do persist for longer across the range of fill pressures. This is because, at high temperatures, the saturation pressure of I_2 is also high, and therefore, the ratio of I_2 to C_4F_8 is higher; it takes a larger quantity of background gas for the diffusive impedance to become dominant. At low temperatures the kinetic impedance becomes significant, as before. However, once the background gas pressure is increased enough, the solutions still all converge, even for a very low sticking coefficient. The temperature gradient has a very small impact on these results.

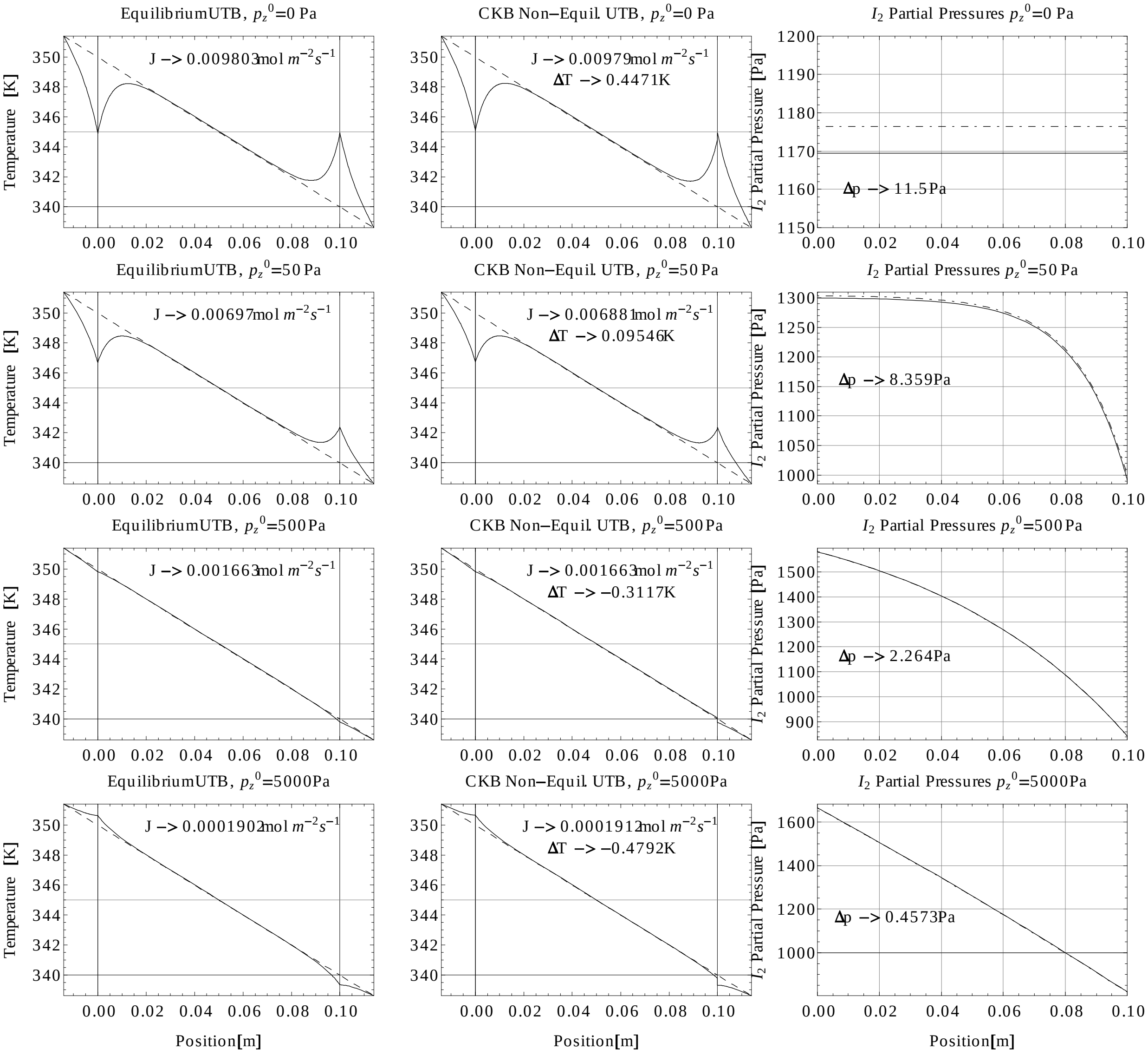

Figure 7.5: Temperature and partial pressure profiles for UTB transport of I_2 in a C_4F_8 background gas; p_z^0 indicates the fill pressure of C_4F_8. In the temperature profiles, the dashed line indicates the wall temperature distribution; in the partial pressure profile, the dashed line indicates the CKB solution, the solid line indicates the equilibrium solution.

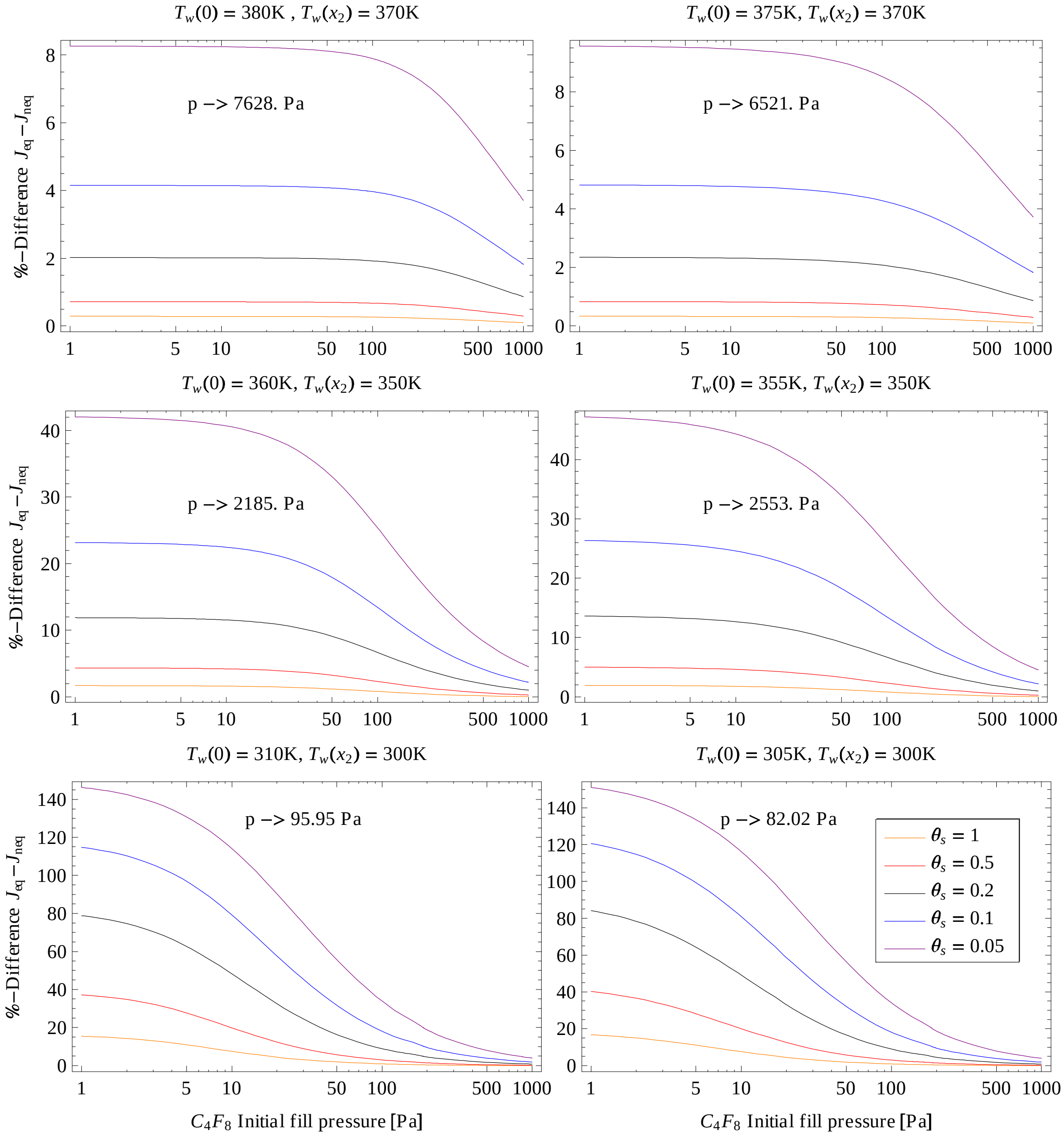

Figure 7.6: The %-difference between the equilibrium mole flux and non-equilibrium mole flux at several values of the sticking coefficient plotted over a range of background gas fill pressures. The pressure given indicates the total pressure in the equilibrium solution when no background gas is present. The plots on the left side have $\frac{dT_w}{dx} = -1\,\text{K}/\,\text{cm}$, plots on the right has side have $\frac{dT_w}{dx} = -0.5\,\text{K}/\,\text{cm}$.

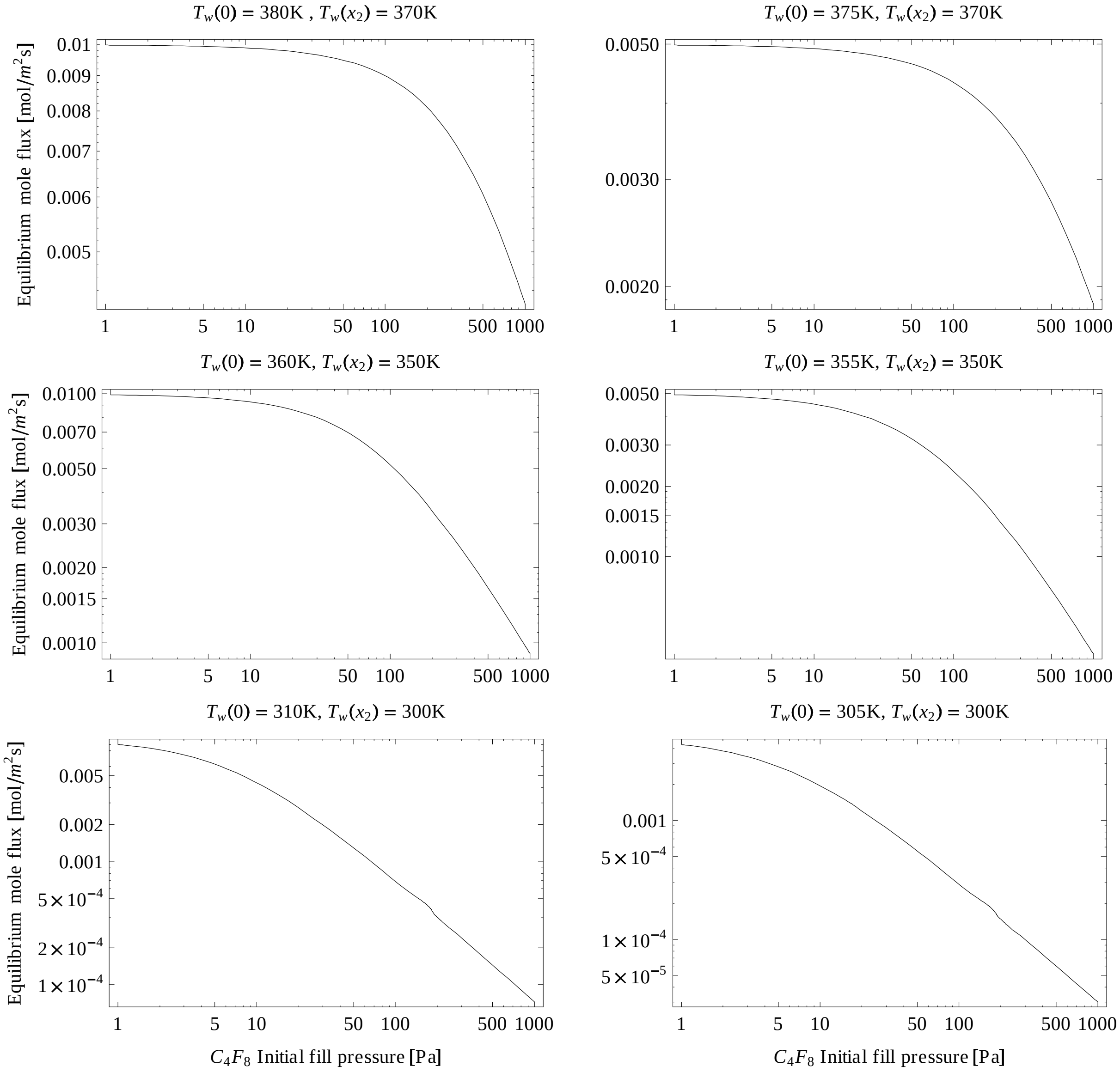
$T_w(0) = 380\text{K}$, $T_w(x_2) = 370\text{K}$

$T_w(0) = 375\text{K}$, $T_w(x_2) = 370\text{K}$

$T_w(0) = 360\text{K}$, $T_w(x_2) = 350\text{K}$

$T_w(0) = 355\text{K}$, $T_w(x_2) = 350\text{K}$

$T_w(0) = 310\text{K}$, $T_w(x_2) = 300\text{K}$

$T_w(0) = 305\text{K}$, $T_w(x_2) = 300\text{K}$

Figure 7.7: The equilibrium mole fluxes corresponding to Fig 7.6.

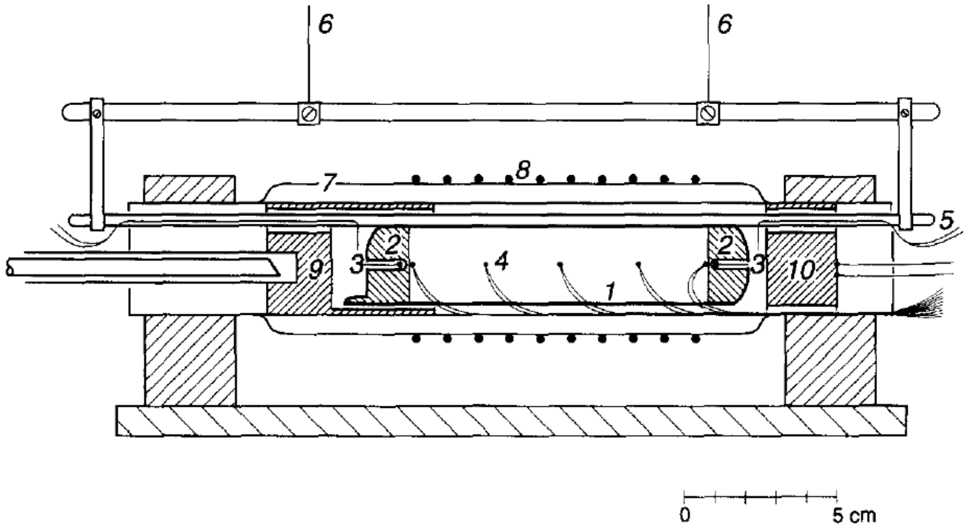

Figure 7.8: The I_2 transport experiment appartus used by Rosenberger et al. (1) is the sealed growth ampoule; (2) are the source and seed material; (3) are thermocouples measuring the temperature near the interfaces on the outside of the ampoule; (4) are thermocouples that measure the wall temperature profile; (5) are wires the support the ampoule; (6) is an analytical balance that measures the transport rate; (7) is a transparant vacuum jacket; (8) are the heating coils; (9, 10) are furnace end plugs. Figure from [11]. *Used with permission from Elsevier.*

7.3 Comparison to Experiment

7.3.1 Setup

Rosenberger et al. conducted a series of I_2 transport experiments in C_4F_8 [11]; a diagram of their experimental apparatus is given in 7.8.

The experimental results are given in Tab. 7.1; polynomial coefficients for the wall temperature profile were also reported; however, we were unable to reproduce the temperature profiles from the reported coefficients, and believe them to be inaccurate. We therefore approximated the wall temperature profile based upon the Fig. 3 in [11] and the reported interface temperatures. These temperature profiles are defined by (6.8). The dimensions of the experimental arrangement were given previously in Fig. 7.1.

We only investigate the low pressure transport cases as at higher background gas fill pressures convective and viscous effects, which, are ignored in our model were reported as significant [11].

7.3.2 Results

We used both the equilibrium and CKB models with $\theta_s = 1$, but found that the difference between them was negligible in all cases. Fig. 7.9 gives our results for the CKB model only. When the temperature

Case	Interface temps.		$\dot{m}$	J
	$T\,(0)$ [K]	$T\,(x_2)$ [K]	[g/ h]	[mmol/ m^2 s]
1	333	315	0.14	0.40
2	347	324	0.35	1.01
3	358	334	0.64	1.84
4	368	344	0.98	2.82
5	378	350	1.40	4.03

Table 7.1: Experimental data from the Rosenberger I_2 transport experiments [11]. Each run was conducted with initial fill pressure $p^0_{C_4F_8} = 1130\,\mathrm{Pa}$

(and thus the pressure) is low, the models reproduce the experimental data accurately (Cases 1-3). However, when the source temperature is increased (Case 4-5) both models become inaccurate.

7.3.3 Analysis

It is clear that our model appears to be valid at low temperatures, but breaks down at higher temperatures. Our model tends to greatly exaggerate the transport rate at high temperatures, at least with regard to the results in [11]. There are two possibilities: either there must be an additional transport impedance that our model does not account for, or the temperature profiles we use are incorrect. In this model we neglected convection, radiative heat transport and viscosity; a transport impedance arising from one or a combination of these may be the source of error here. Convective transport tends to speed up, rather than slow down transport [11]; this is likely not the cause of our error. Radiative heat transfer on the other hand can potentially inhibit the transport of latent heat at the interface, thus greatly increasing the thermal impedance. The magnitude of the viscous impedance should also be checked.

7.3.4 Radiative dissipation of the latent heat

We now attempt to quantify the impact of radiative heat transport on our model results. To model the effect of the radiative heat transfer, an additional supply term must be added to the interface energy balance such that the first law at the interfaces becomes,

$$J\left[C_p\left(T_v - T_{ref}\right) + \Delta h_{sv}\right] + q_v = JC_s\left(T_v - T_{ref}\right) + q_s + q_{rad} \tag{7.1}$$

We make the first order approximation that the radiative heat transport is independent of the wavelength of the radiation, and that heat is exchanged between gray surfaces [60]. Furthermore, we assume that the radiation is exchanged between a small, concave surface (the interface) with temperature equal to the solid temperature at the interface in a large cavity (the ampoule) with temperature equal to the

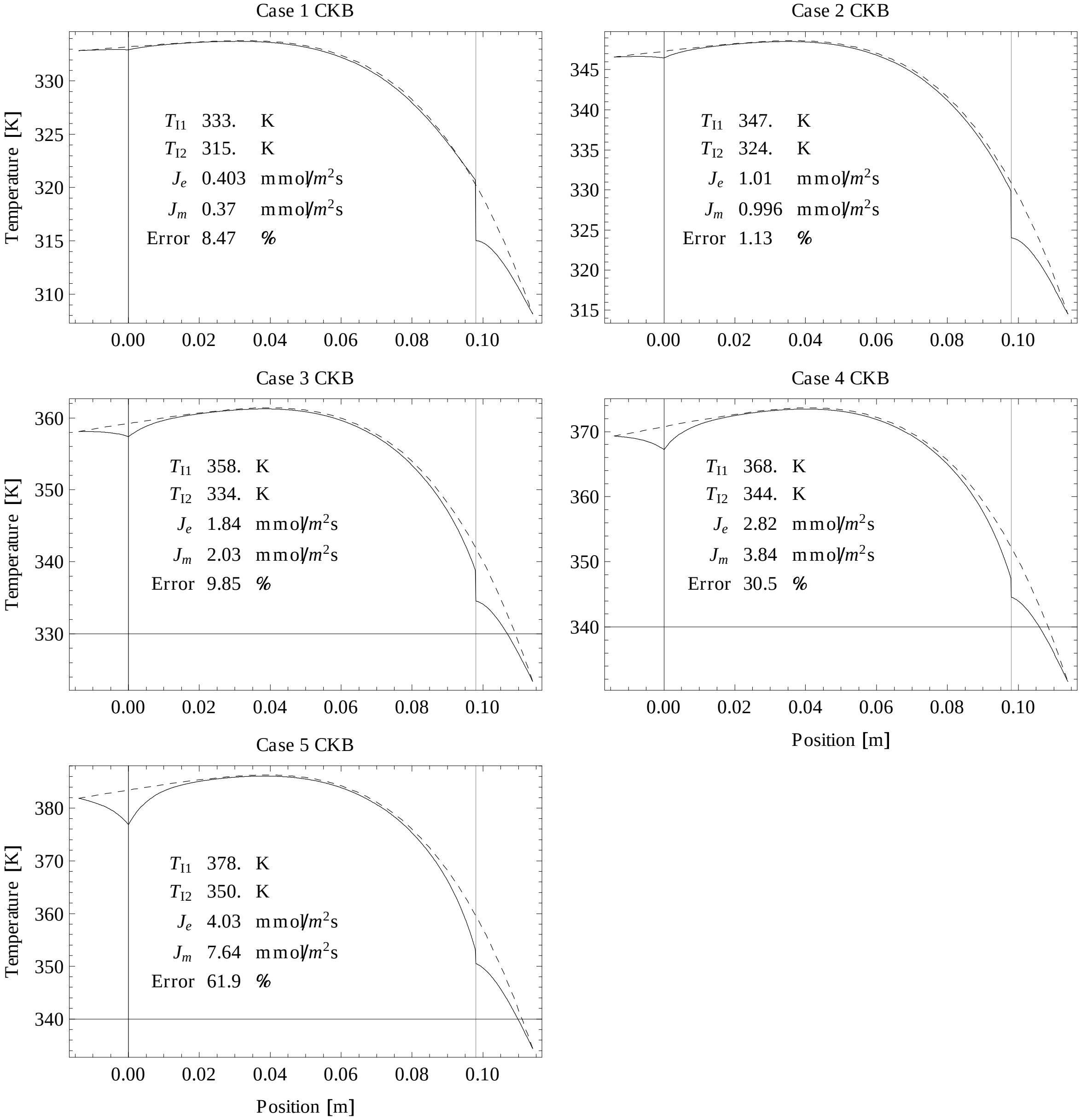

Figure 7.9: The results of the CKB-model of the Rosenberger el al. Iodine transport experiments [11]. Here T_{I1} is the Interface 1 temperature, T_{I2} in the Interface 2 temperature, J_E is the experimental mole flux, J_M is the model mole flux.

Case	$\tilde{v}_{avg}$
	[mm/ s]
1	68
2	143
3	205
4	244
5	284

Table 7.2: Calculated velocities in the CKB solution to the Rosenberger et al. experiments. [12].

average wall temperature. The radiative heat flux is then.

$$q_{rad} = \varepsilon\sigma \left[T_s^4 (x) - \bar{T}_w^4\right] \tag{7.2}$$

where σ is the Stefan-Boltzmann constant equal to $5.670 \times 10^{-8} \frac{\mathrm{W}}{\mathrm{m}^2\,\mathrm{K}^4}$ and ε is the gray body emissivity of the Iodine surface which we approximate as 0.80 since the surface is non-metallic [60]. This type of radiative transport expression has been applied successfully in previous radiative heat transport analysis of CA-PVT [90].

The results of the addition of radiative transfer to the CKB model are given in Fig. 7.10.

We see that the addition of radiation has not changed the results by much. If anything, the error has increased, rather than decreased. The model error is not caused by the neglection of radiation.

7.3.5 Viscous Impedance

Rosenberger and others suggest that viscosity play a significant role in physical vapor transport [25, 11]. In the UTB model, where one constituent is stagnant, the average total flow velocity can be found as

$$\tilde{v}_{avg} = \frac{R_u \bar{T}}{p} J \tag{7.3}$$

where $\bar{T}$ is the average vapor temperature. We calculate the average flow velocities based upon the CKB for Cases 1 - 5. These are given in Tab. 7.2.

These velocities are very small; nevertheless, Cases 4 and 5 have substantially larger velocities than the remaining cases. Viscosity may play a role. Using these velocities, the viscous impedance can be estimated by solving the Hagen-Poiseuille equation for pressure loss [91],

$$p\,(0) - p\,(x_2) = J \frac{8\mu x_2}{\bar{p}\,(d_a/2)^2} R_u \bar{T} \tag{7.4}$$

where, for the moment, we have assumed that total pressure is *not* constant, μ is the viscosity of C_4F_8 vapor (the majority constituent) reported as 0.011 mPa s [84]. For case 4, we calculate a pressure drop

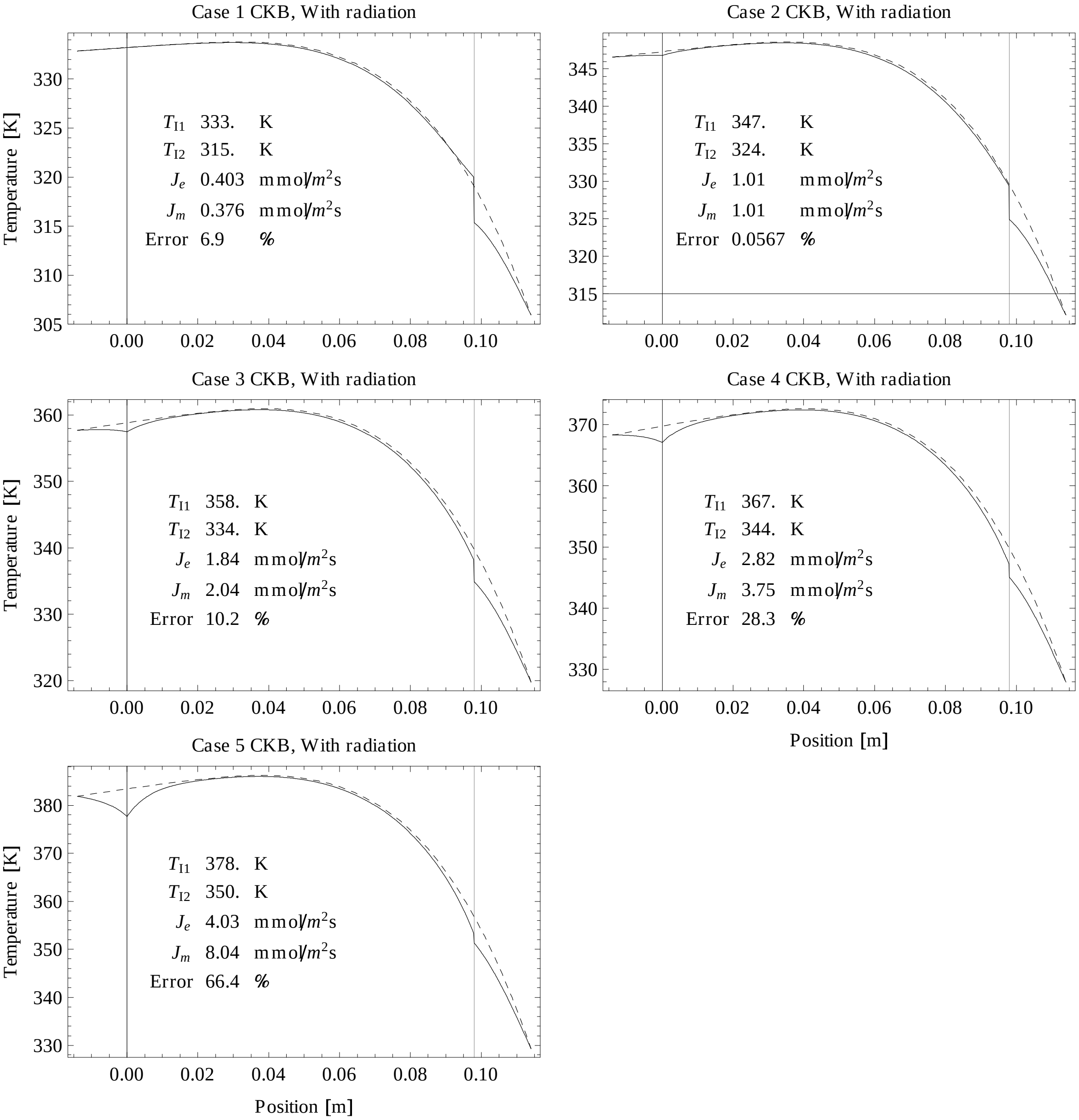

Figure 7.10: The results of the CKB model compared to the Rosenberger et al. experiment [11] when radiative heat transfer at the interfaces is included. The error between the experimental results remains high at high temperature.

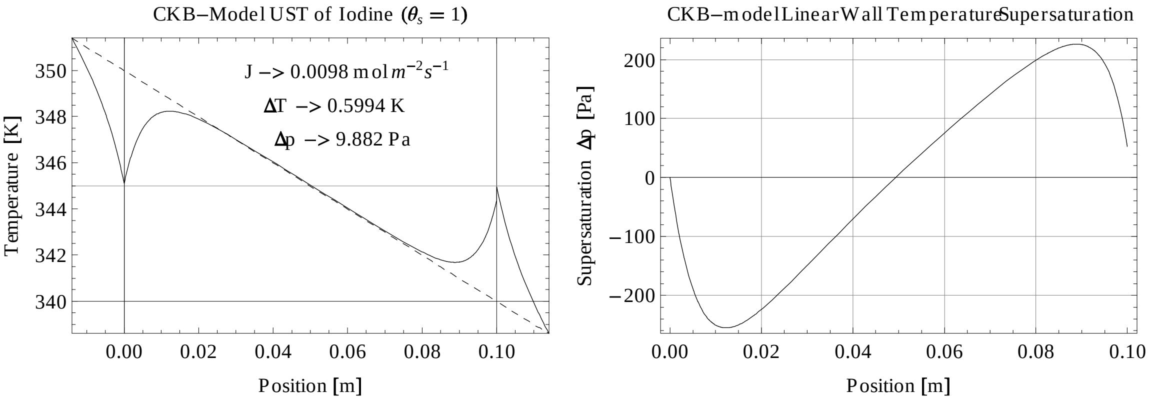

Figure 7.11: The supersaturation in the UST solution with a linear temperature profile. The maximum Δp occurs a distance back from the interface. Parasitic nucleation of additional crystals ahead of the interface is likely.

of 1.7 mPa, less than 1% of the total pressure; for Case 5, we calculate a pressure drop of 2.0 mPa, also less than 1% of the total pressure. Thus, in both cases, the viscous interaction is negligible.

We have ruled out all three neglected transport impedances in the system as the source of our error. Therefore, our error must be caused by the uncertainty in the temperature profile, which may be significant as the temperature profiles used in this analysis were approximated. The actual profiles used in the Rosenberger experiment are unknown.

7.4 Supersaturation and Stability

We have already studied plain, linear temperature profiles. We have also looked at more typical temperature profiles as in Fig. 7.9. In Fig. 7.11 we plot the supersaturation $\Delta p = p - p_{sat}\left[T(x)\right]$ for the UTU system along the length of the ampoule with a linear temperature profile $T_w(0) = 350\,\mathrm{K}$, $\frac{dT_w}{dx} = -1\,\mathrm{K/\,cm}$.

The supersaturation is very high everywhere past the midpoint of the vapor portion of the ampoule; the maximum occurs ahead of the interface rather than at the interface itself. This high supersaturation is likely to induce the nucleation of additional crystals ahead of the interface, which is commonly seen in vapor crystal growth experiments [9, 5]. This parasitic nucleation is very undesirable in vapor crystal growth as it tends to lead to unstable growth and growth of polycrystalline material. We observe a similar situation when a background gas is present, as shown in Fig. 7.12.

To reduce the likelihood of parasitic nucleation, it is wise to select a temperature profile so that the vapor

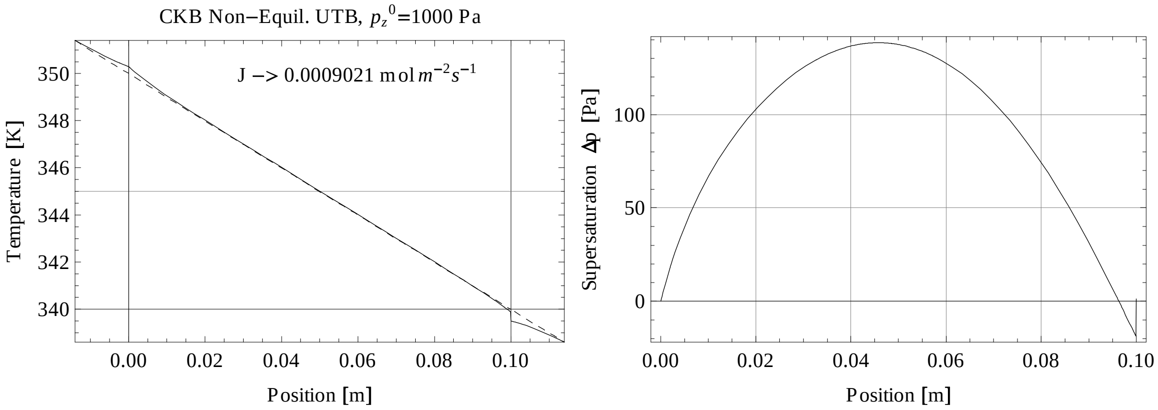

Figure 7.12: The temperature profile and supersaturation in UTB background within a background gas. The supersaturation is positive throughout the ampoule, expect right at the interface. Transport is driven by a small positive partial pressure jump at the interface. In this situation, parasitic nucleation is likely.

is supersaturated only near the interface, with the maximum Δp occurring at the interface [5, 9]. This is the basis of the well known constitutional supersaturation stability (CSS) criterion typically applied to solution growth, which was first proposed by Reed et al. [92] for PVT. The criterion is stated explicitly as

$$\frac{d}{dx}\left[\Delta p\right]\bigg|_{x_2} \geq 0; \tag{7.5}$$

the supersaturation must decrease with distance from the solid surface. If this condition is not met, aspirates growing out of the interface are likely to grow faster than the interface itself, causing the formation of dendrites and other undesirable forms.

It has been observed that stable interfaces exist in PVT even if the CSS criterion is violated [93], and other more complex analysis of stability have since superseded it [75].

7.4.1 Flat vapor temperature profile

The supersaturation problem can be solved by applying a flat temperature profile in the vapor, with a steep temperature gradient in the solid seed only. This sort of temperature profile could be obtained by cooling the seed material in some way. In Fig 7.13 we plot the result of such a transport case. We see that the vapor is not supersaturated anywhere along the length of the bulk, expect for right at the interface location. The CSS criterion is not violated. The situation is similar when a background gas is present; such a case is given in Fig. 7.14.

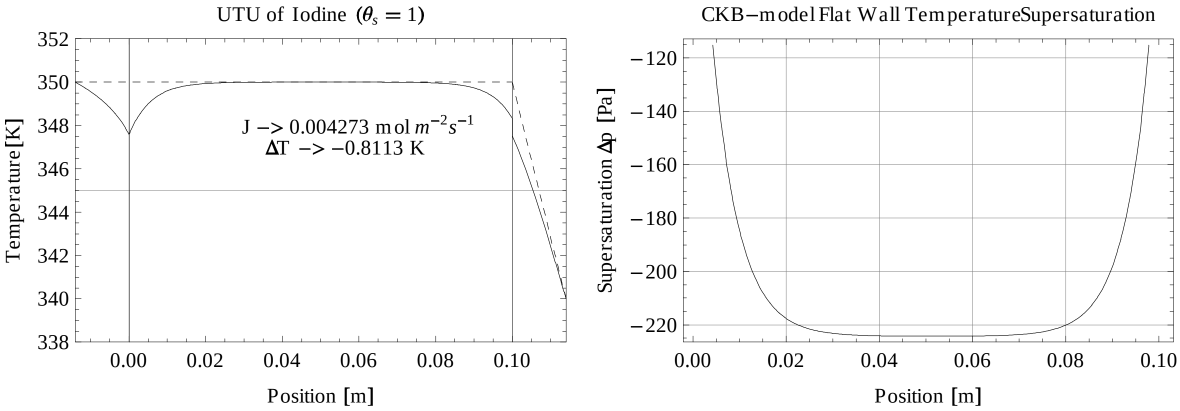

Figure 7.13: In this case, the $T_w(x)$ in the vapor is kept constant. Cooling only occurs at the seed. The vapor Δp is negative right up to the interface; parasitic nucleation is unlikely to occur.

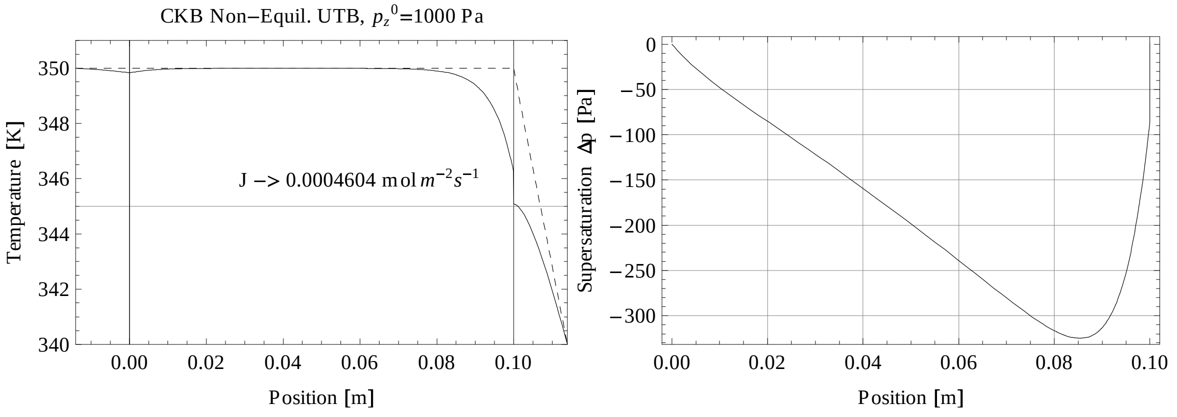

Figure 7.14: The temperature and supersaturation profile in the presence of a background gas. The Δp_a remains negative right up to the interface, where a large pressure jump drives the transport. Parasitic nucleation is unlikely anywhere along the ampoule wall.

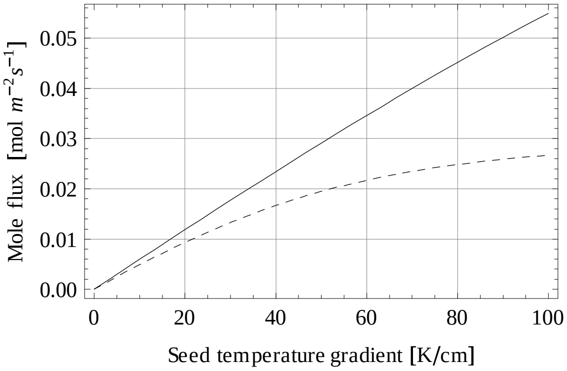

Figure 7.15: The mole flux as a function of temperature gradient in the solid. The solid line represents the relationship for $T(x) = 350\,\mathrm{K}$ in the vapor, the dashed line represents the relationship for $T(x) = 300\,\mathrm{K}$

It is interesting here that a significant transport rate is obtained in a scenario where the imposed interface wall temperatures are equal; the transport must be driven by the temperature profile in the seed only. Thus, a crystal growth model that only tracks the advective-diffusve flow in the vapor such as [9, 13, 12] could not capture this phenomenon. In Fig. 7.15 we plot the transport rate as a function of the temperature gradient in the seed. We see that with a steep enough gradient in the solid, a significant mole flux can be obtained. As we shall see in Chapter 8, this type of temperature profile has been successfully applied for the growth of CdTe.

7.4.2 Polynomial temperature profile

Achieving a steep temperature gradient in the solid seed may be difficult due to limitations in the apparatus used. An alternative commonly used in vapor crystal growth is to use a temperature profile such as the one given in Fig 7.16. We saw profiles such as this one previously in §7.3. Here, the vapor is heated along the length of the ampoule; the supersaturation is kept negative. Near the interface, the wall temperature is reduced rapidly, such that a relatively steep temperature gradient is attained in the solid and in the vapor above the solid. Thus, the transport benefits from both the solid temperature gradient, as well as the temperature difference between the source and the seed, thus giving a high transport rate; again, parasitic nucleation is unlikely anywhere along the ampoule wall, and the CSS criterion is not violated.

In all the above cases, we note that the steeper the temperature gradient at the interface, the larger the interface temperature jump — this relationship was previously shown for liquid-vapor interfaces [19]; we have extended it to solid-vapor interfaces.

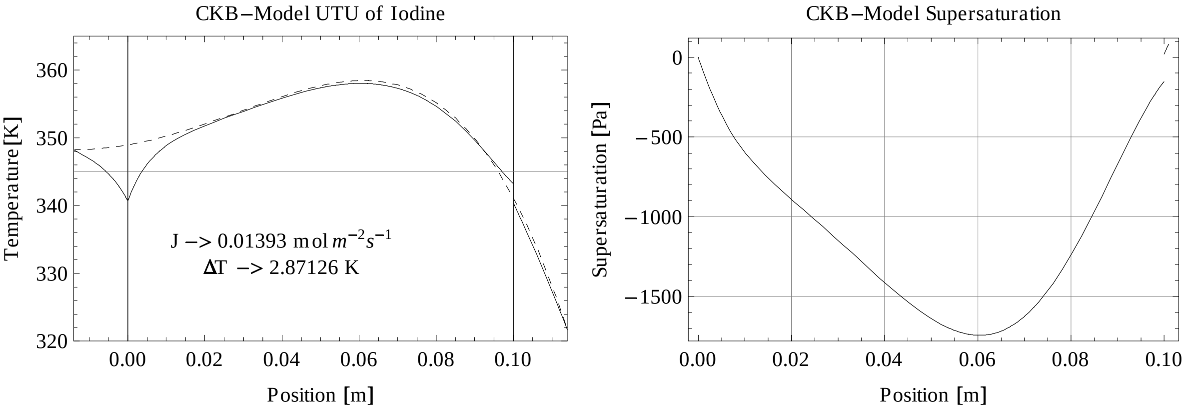

Figure 7.16: A typical vapor growth temperature profile. Here, the vapor has negative supersaturation right up to the interface, where supersaturation is induced by the temperature jump.

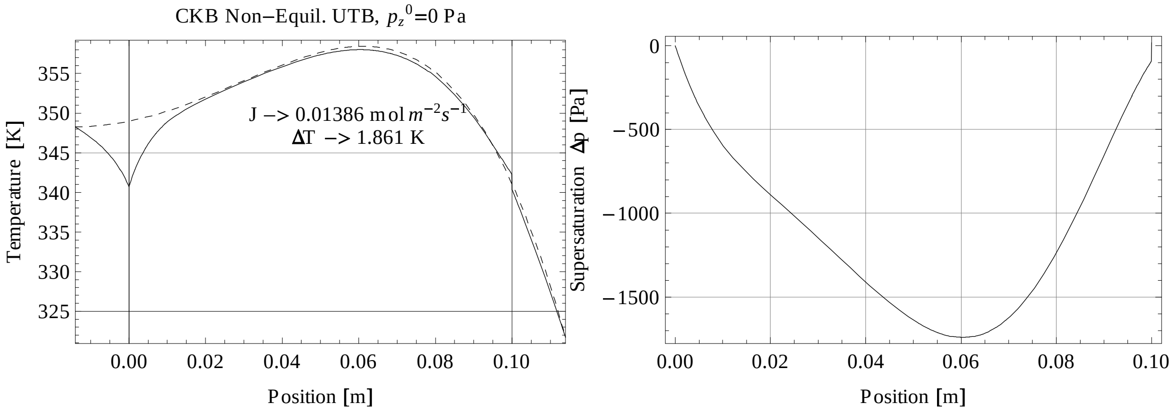

Figure 7.17: The supersaturation in the case of a polynomial temperature profile in the presense of a background gas.

7.5 Discussion

Bulk vapor growth of crystals is seldom conducted within a pure vacuum atmosphere; even if the ampoule were sealed at high vacuum, impurities vapors would still be present, both from outgassing of the ampoule and of impurities present in the source materials [9, 11]. Therefore, the UTU transport solution is illustrative only, as no experimental data is available for a comparison. The UTB model on the other hand shows good agreement with experiment at low temperatures, but deviates from experiment at high temperatures. We initially suspected this error was caused by radiative heat transport or by the viscosity; but we have shown that this cannot be the case. The most likely cause of this error is an incorrect estimate of the wall temperature profile.

7.5.1 Characterization of the thermal impedance

Because our model includes the thermal impedance, the UTU model does solve in the equilibrium case. This is a surprising result, classical PVT models that do not consider heat transport, cannot be solved when diffusive, viscous or kinetic impedances are not considered [9, 11, 13, 25].

We begin with a closer examination of the equilibrium solution. We recall the structure of the equilibrium UTU model as in Tab. 6.1. The boundary conditions (6.20), (6.22), (6.19) and (6.21) do not constrain the mole flux. The mole flux is only defined by the energy conservation equations at the interfaces (6.30) and (6.31). We solve (6.31) and find

$$J = \frac{q_s - q_v}{\Delta h}, \tag{7.6}$$

where $\Delta h = \bar{h}_v - \bar{h}_s$, x_I is the interface position, the subscript v refers to the vapor and s refers to the solid. Setting the solid temperature to the reference temperature gives

$$J = \frac{q_s - q_v}{\Delta h_{sv}}. \tag{7.7}$$

This then is how the latent heat impedance arises in the transport model. The larger the latent heat is, the smaller the possible mole transport rate is, so long as the heat transport rates (i.e. the temperature gradients) at the interface are fixed.

7.5.2 Temperature Jumps

We recall now that the temperature jump is the driving force for the non-convective heat transport across the interface. If a non-convective heat flux occurs across the interface, the CKB model must give a temperature jump. If this heat flux is oriented towards the vapor from the solid, the temperature of the vapor must be lower than the temperature of the solid; the opposite is true if the heat flux is oriented

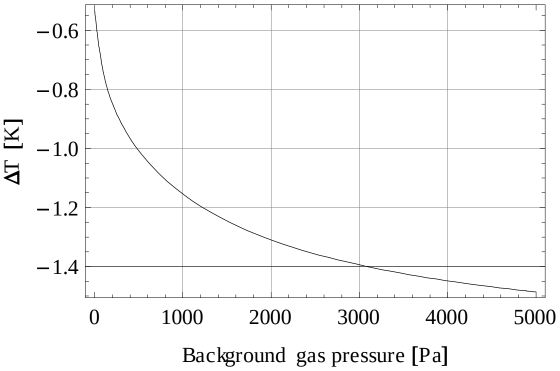

Figure 7.18: The interface temperature jump for a flat vapor temperature profile at $T_w = 350\,\mathrm{K}$. The sticking coefficient has a negligable effect on the jump. The temperature jump increases as background gas is added.

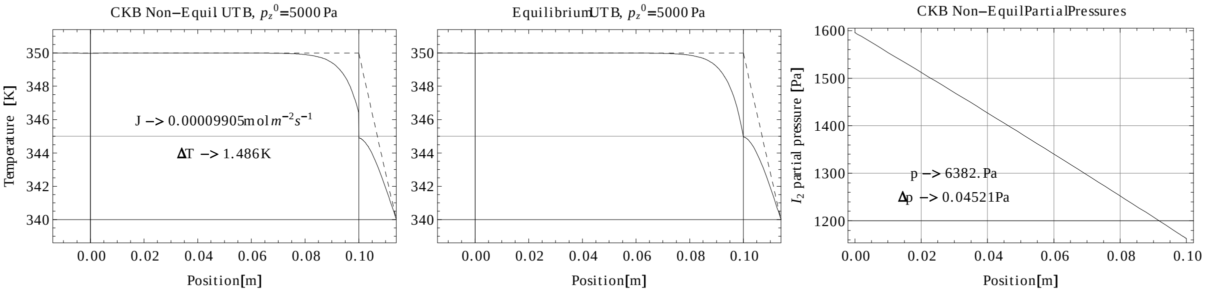

Figure 7.19: The temperature and partial pressure distributions for transport of I_2 with a flat wall temperature profile in the vapor.

into the solid. In Figs. 7.14 and 7.17 we observe that the CKB solution gives significant temperature jumps, even in conditions where a background gas is present. The relationship between the temperature jump and the fill pressure is given in Fig. 7.18 for a flat wall temperature profile in the vapor, as in Fig. 7.14. Interestingly enough, the magnitude of temperature jump increases as the background gas pressure increases. To investigate how this phenomenon arises we examine the equilibrium and CKB solutions to a flat temperature profile, given in Fig 7.19.

Transport from the source to the seed is strongly limited by the diffusive impedance — the background gas pressure is nearly five times greater than the saturation pressure in the ampoule. Therefore, a steep partial pressure gradient appears in the vapor. Due to the equilibrium assumption at the interface, the partial pressure at the interface must equal the saturation vapor pressure. For the solution to be consistent, the temperature of the interface must then be significantly colder than the source temperature for transport to occur at all.

In order to understand how this situation arises at all, we must understand the driving force for the transport — the seed temperature gradient. For this, we imagine how such a steady state solution might arise in a vapor transport experiment. We start by considering an ampoule with constant temperature equal to the wall temperature throughout (e.g. $T_w(x) = 350\,\mathrm{K}$), and no temperature gradient applied in the seed. In such a situation the pressure in the ampoule is equal to

$$p = p_{sat}(T_w) + p_z^0, \tag{7.8}$$

where p_z^0 is the fill pressure of the ampoule. The ampoule is in full equilibrium with no heat or mole transport taking place. If now we induce a steep temperature gradient in the seed, non-convective heat transport occurs following

$$q_s = -\kappa_s \frac{dT}{dx}. \tag{7.9}$$

Heat is transported away from the interface faster than it can be replaced by conduction through the vapor and through the wall; the interface cools. This cooling induces mole transport, a little bit at first, until, between the latent heat and the vapor temperature gradient, enough heat is supplied to the interface to balance the heat being removed. The temperature jump arises in the non-equilibrium solution from the magnitude of heat transfer from the vapor into the interface.

As the quantity of background gas is increased, the transport rate, and therefore the latent heat release at the interface is reduced; the rate of heat transfer from the vapor to the interface must increase to compensate, and thus the temperature jump increases.

7.5.3 The steady state assumption

The UTU and UTB models both assume steady state, as discussed in Chapter 2. In reality, as transport proceeds, the source becomes depleted and the seed grows; as a result, the distance between the ampoule ends and the interfaces changes. In vapor growth experiments, the wall temperature gradients are translated so that the interfaces are kept at a constant temperature; nevertheless, the heat transport in the solids changes as their dimensions change. In Fig. 7.20 we show the effect on the transport rate of altering the source and seed lengths, as might be expected during the course of a vapor growth experiment. We see that so long as the temperature profile in the vapor does not change, the steady state assumptions are valid for the majority of the growth process.

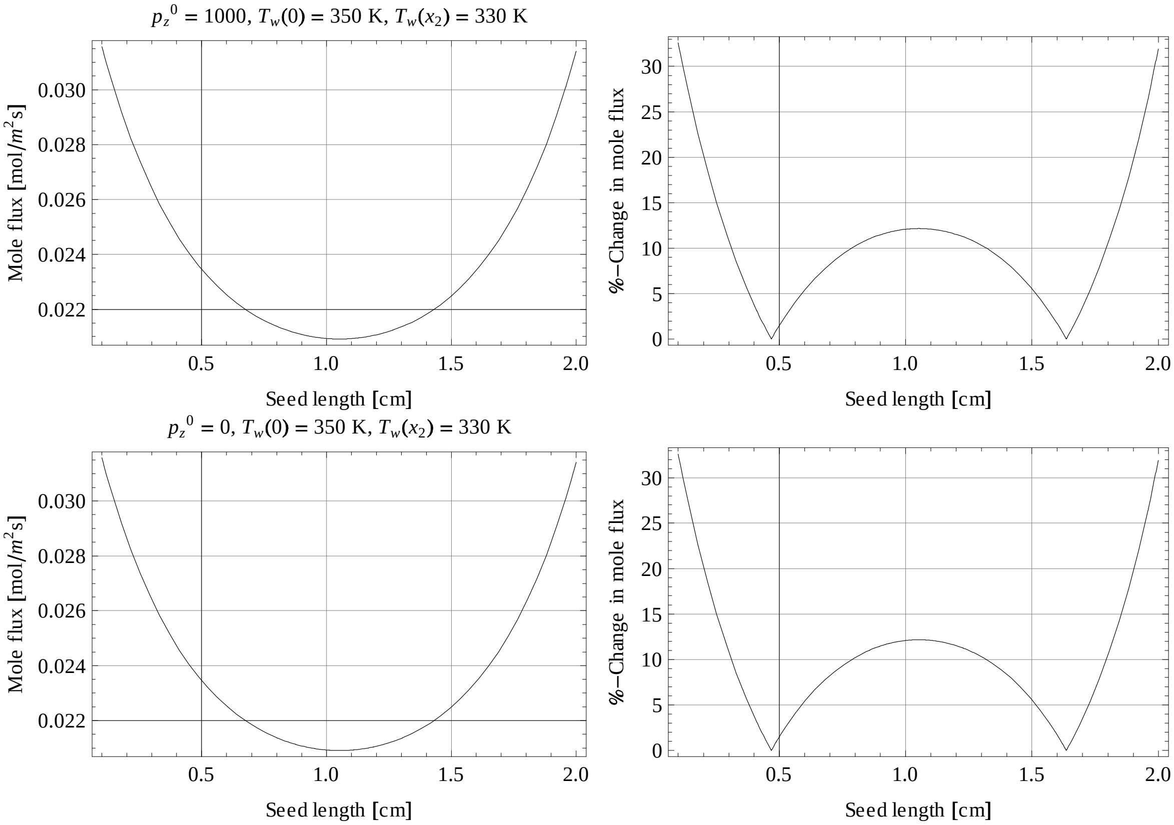

Figure 7.20: The effect of seed length on the transport rate when a linear temperature profile is imposed. The percentage indicated is based upon the absolute value of the difference between the mean transport rate and the instantaneous transport rate.

7.6 Concluding remarks

We have thoroughly investigated the properties of the single species transport models. We have confirmed that the transport rate is limited by the thermal impedance, the kinetic impedance and the diffusive impedance. Generally, one of these impedances dominates over the remaining two impedances, depending upon the conditions. Regarding these conditions, we conclude that:

1. At low temperatures, ($< 310\,\mathrm{K}$) and low background gas pressures, interface kinetics becomes the dominant transport impediment.
2. At high temperatures ($> 330\,\mathrm{K}$) and low background gas pressures, the thermal impedance becomes the dominant transport impedance.
3. At all temperatures, when the background gas pressure approaches and exceeds the mean I_2 partial pressure in the ampoule, diffusion becomes the dominant transport impedance.

These conclusion justify the neglection of non-equilibrium and first law effects in many vapor crystal growth scenarios in the presence of significant background gas pressures. In UTU transport, however, all three impedances should be carefully considered.

Chapter 8

Cadmium Telluride Transport by Dissociative Sublimation

In this Chapter, we study transport of CdTe, both as a binary mixture (BTB) and as a ternary mixture (BTT) with CO as a background gas.

8.1 Dissociative Sublimation

Dissociative sublimation transport of CdTe and other II-VI semiconductor materials has been studied extensively by many researchers; notable works include, but are not limited to [12, 27, 18, 6, 17, 10]. In Chapter 5, we showed how the saturation pressure of CdTe varies with the composition of the solid. Small deviations in solid composition lead to large swings in the saturation pressure of the vapor constituents. This is caused by the dissolution of excess material at interstitial sites in the solid crystal structure. Regardless of vapor composition, the mole transport in the vapor phase is nearly stoichiometric (see 8.2.1). The minority constituent must therefore diffuse through the majority constituent to reach the seed crystal; this induces a significant diffusive impedance, much the same way as a background gas [9]. Depending on the vapor composition, the diffusive impedance can be significant enough to lead to negligible growth rates.

8.1.1 High growth rates in dissociative sublimation

In order to obtain a high growth rate in the transport of CdTe by dissociative sublimation, the composition of the vapor must be kept near the stoichiometric composition[1] ($\zeta = 2$), such that the diffusive impedance is small. Due to the narrow range of existence for solid CdTe, this can be difficult to accomplish. Palosz and Wiedemeier solved this problem by developing a sample preparation technique which produces source material with negligible amounts of excess Te or Cd dissolved in the solid; thus, the resulting vapor compositions were very near to the stoichiometric ratio [12]. An alternative solution is to use the Markov-Davydov method such as was done by Laasch et al .[17]. Here, the excess Te_2 or Cd

---

[1] We recall that $\zeta = \frac{p_{sat}^{Cd}(T)}{p_{sat}^{Te_2}(T)}$.

vapor is vented away though the annulus, thus maintaining a stoichiometric composition throughout the vapor; source composition is less important. A third alternative is to use a separate reservoir of liquid Cd or Te to control the partial pressure of the excess constituent, this was done by Mochizuki [94].

8.1.2 The Equilibrium Pressure Ratio

At this point, the reader might be a little bit confused at to the origin of the equilibrium pressure ratio ζ, which was first discussed in Chapter 5. This value is an equilibrium property of the solid, and is dependent on the composition of the solid CdTe material. When the solid first begins to sublime, the dissolved excess constituent within the solid begins to escape into the vapor, large quantities of the excess constituant may come out of the vapor even before significant quantities of Cd and Te within the lattice begin to sublimate. The vapor pressure of the excess constituant will build up, until an equilibrium between the remaining dissolved excess constituant and excess vapor is reached, and the vapor pressure ratio becomes ζ. If a non-equilibrium is maintained on the solid, the solid now sublimes stoichiometrically, and the actual vapor pressure ratio remains near the equilibrium ratio ζ. If this excess material were constantly removed from the vapor, perhaps by the use of an annular gap, the non-stoichiometric source material would eventually be purified. In a sealed ampoule however, the material does not have a chance to escape. It's too difficult for it all to disolve back into the solids, and thus it remains in the vapor, forming a diffusive impedance to the flux of the minority constituent.

8.1.3 Sticking Coefficients

We discussed sticking coefficients on CdTe surfaces in §4.5.3. In that section, we noted that individual sticking coefficients for Cd and Te_2 have not, to our knowledge, been measured for typical bulk vapor growth conditions ($1073 - 1173\,\mathrm{K}$). In this Chapter, we do investigate the impact of the individual sticking coefficients, but for the most part, we assume the sticking coefficients of Cd and Te_2 to be equal.

8.1.4 Modeling Approach

From our analysis in Chapter 7, it is clear that when the diffusive impedance is dominant over the other impedances, the interface conditions are somewhat irrelevant, at least in terms of mass transport. The transport is governed fully by diffusion. Non-stoichiometric transport cases, where $\zeta \ll 2$ or $\zeta \gg 2$ are therefore not interesting to us in this analysis, as the flow is obviously completely dominated by the diffusive impedance. Furthermore, the objective of any crystal growth model is to, ultimately, determine the optimal conditions for obtaining fast, repeatable growth rates of high quality (i.e., stoichiometric) material; clearly this does not occur when the vapor is non-stoichiometric. We shall therefore stick only

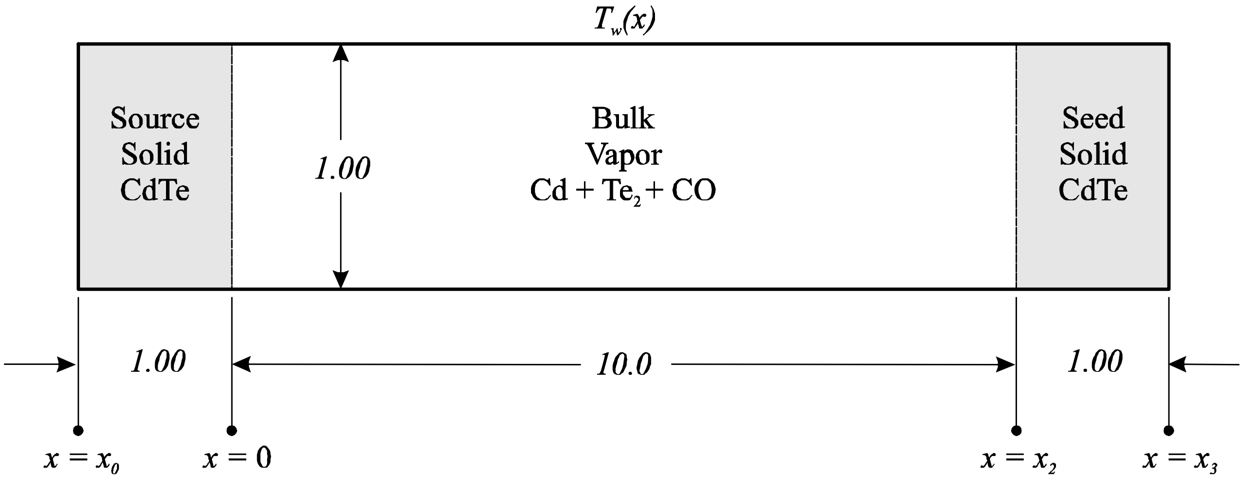

Figure 8.1: The geometry used in the generic CdTe model analysis.

to cases where the deviation from the stoichiometric vapor composition is small.

8.2 Geometry and Assumptions

For our initial testing of the model, we use a generic model geometry, given in Fig 8.1.

8.2.1 Stoichiometric Transport Assumption

In Chapter 5, we set up the solution to BTB and BTT transport by assuming a stoichiometric relationship between the condensing fluxes. This common assumption is made in all of the binary semiconductor transport models that we studied.[12, 27, 18, 6, 17, 10]; it is justified due to the very narrow range of existence of solid CdTe (Fig. 1.14). Thus, the difference between the stoichiometric transport flux and the actual transport flux is less then 1%, especially at the near-stoichiometric compositions that we study. We therefore always assume

$$J_{Cd} = 2J_{Te_2}. \tag{8.1}$$

8.3 BTB Results

For CdTe PVT, BTB is the simplest case. Diffusion only occurs between the two constituents Cd and Te_2 since no background gas is present. We begin by solving the BTB problem with a linear temperature profile and wall temperatures at $T_w(0) = 1150\,\mathrm{K}$ and $T_w(x_2) = 1140\,\mathrm{K}$. These solutions are given for both the equilibrium and CKB interface conditions at Interface 2 in.Fig. 8.2. In each case, the sticking coefficients of both Cd and Te_2 are set to unity.

We see that the temperature profiles have the same general shape as those in Fig. 7.2. The large temperature spikes are, as before, caused by the absorption and release of latent heat at the interfaces. The first row of Fig. 8.2 gives the stoichiometrically dissociating ($\zeta_1 = 2$) case. Here, the vapor maintains its composition along the length of the ampoule during transport; no diffusion takes place. As with the UTU case, the equilibrium solution is limited only by the thermal impedance. The interface temperatures in the equilibrium solution must be equal. The CKB solution is limited by both the thermal and the kinetic impedance. The difference between the equilibrium and CKB transport rate is approximately 8%. The thermal impedance dominates the transport, but not to the extent that the kinetic impedance is totally irrelevant. There is a large positive temperature jump at the interface in the CKB solution, indicating that the non-convective heat flux at the interface is oriented from the solid into the vapor.

Rows 2, 3 and 4 give the solutions for a non-stoichiometric source vapor composition. By (8.1), the mole transport must remain stoichiometric. As expected, the excess constituent forms a diffusion barrier to the transport of the minority constituent. The equilibrium solution is now limited by both the thermal and the diffusive impedance. When $\zeta = 1$, the equilibrium and CKB solutions nearly converge, and the temperature spikes are greatly reduced. Diffusion becomes the dominant transport impedance. The initial non-stoichiometry at the source is amplified along the length of the ampoule, as the minority constituent is consumed at the seed. The overall composition ratio of the system is further from the stoichiometric case than the original source vapor. This behavior is seen in classical theory as well as in experimental systems [12, 6, 9].

In Row 4, a Cd rich source is used, such that $\zeta_1 = 10$. As before, the transport is almost totally limited by diffusion, in the same manner as the cases where $\zeta_1 < 1$.

In the CKB solutions in Fig. 8.2 both the sticking coefficients of Cd and Te_2 are kept at unity. In Fig. 8.3 we plot the difference between the equilibrium and non-equilibrium solutions while varying both sticking coefficients and the source vapor composition. The corresponding equilibrium mole fluxes are plotted in Fig. 8.4. The resulting behavior is similar to what we see in Fig 7.6 for the single species case.

Row 1 of Fig. 8.3 is the high temperature case corresponding to Fig. 8.2. We confirm that the maximum difference between the equilibrium and CKB solutions is 8% for unity sticking coefficients. As the sticking coefficients are reduced, the difference between the equilibrium and non-equilibrium solution becomes significant. Not surprisingly, this effect is damped when the source vapor composition is non-stoichiometric, and the diffusive impedance becomes dominant. Row 2 gives the result for temperatures

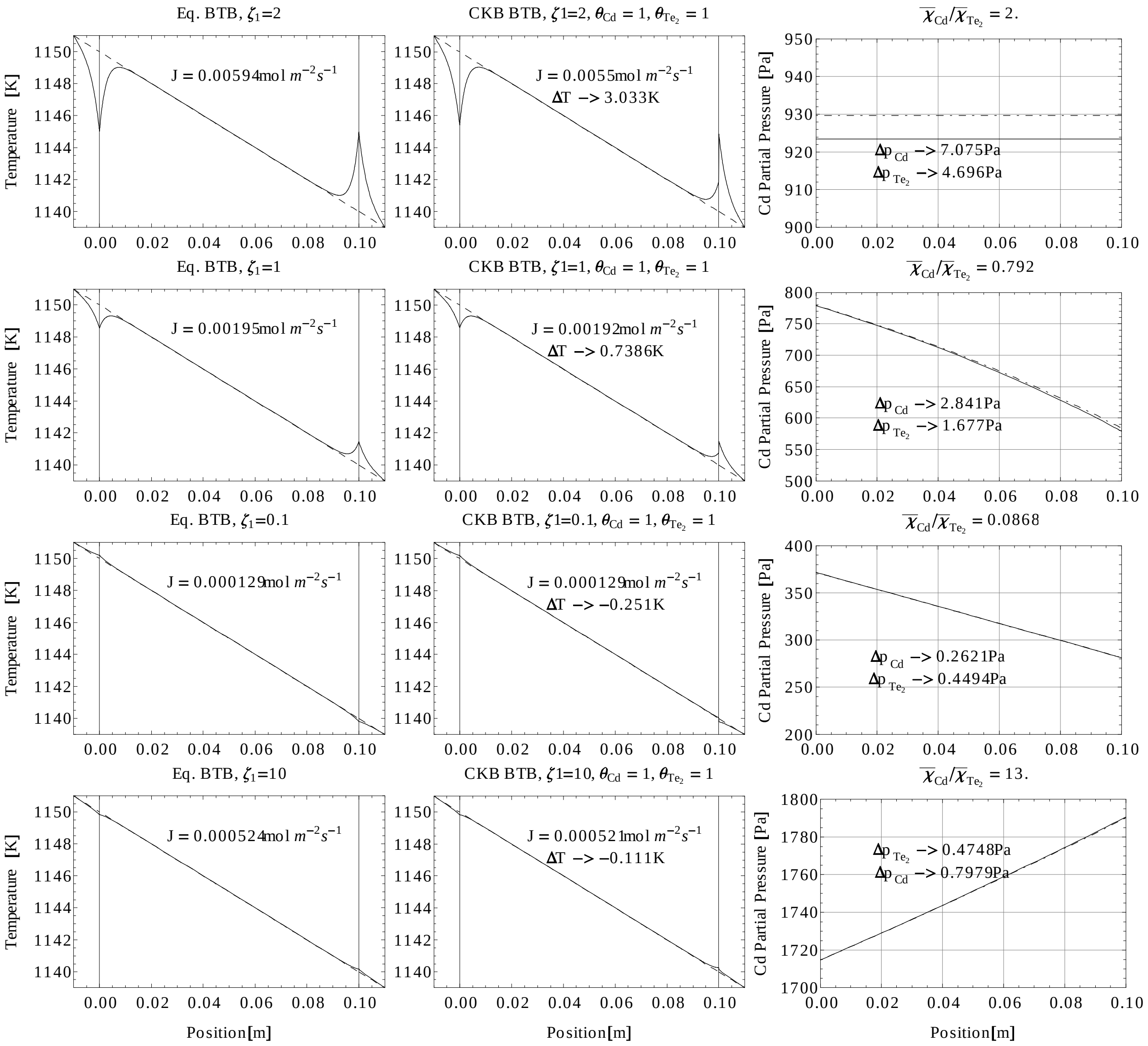

Figure 8.2: Transport of CdTe in BTB. Here, $J = J_{Cd} = J_{CdTe}$. ζ_1 referes to the equilibrium vapor composition of the source material; Δp_{Cd} and Δp_{Te_2} are individual supersaturations at the seed, ΔK is the total chemical supersaturation at the seed, ΔT is the temperature jump. As an increasingly non-stoichiometric source is used, the excess constituent builds up and the transport becomes limited by diffusion.

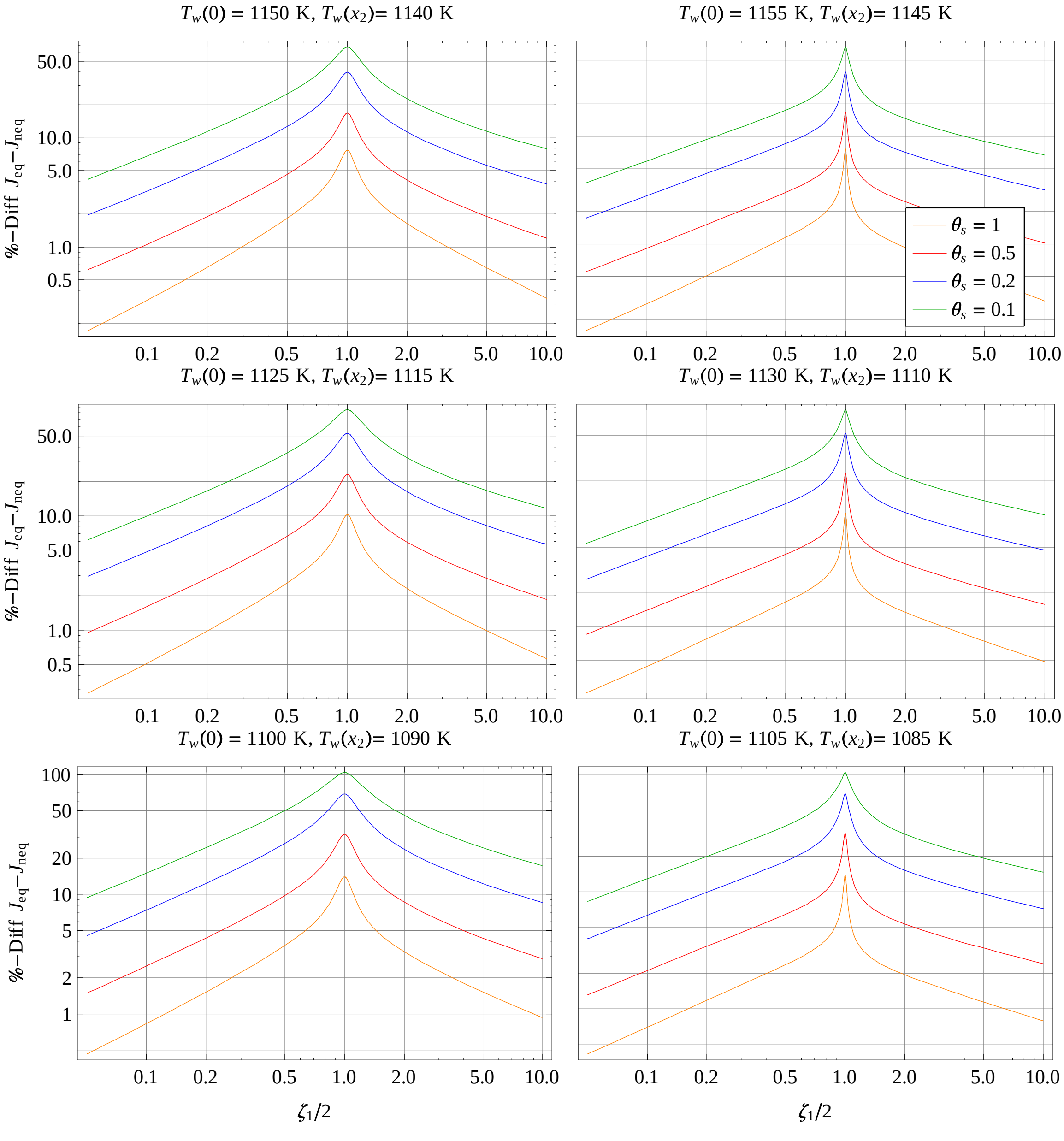

Figure 8.3: The difference between the equilibrium and non-equilibrium solutions as a function of the source composition at various values of the sticking coefficient. In each case, $\theta_s = \theta_{Cd} = \theta_{Te_2}$. The left hand plots have $\frac{dT_w}{dx} = -1\,\mathrm{K/\,cm}$, the right hand plots have $\frac{dT_w}{dx} = -2\,\mathrm{K/\,cm}$.

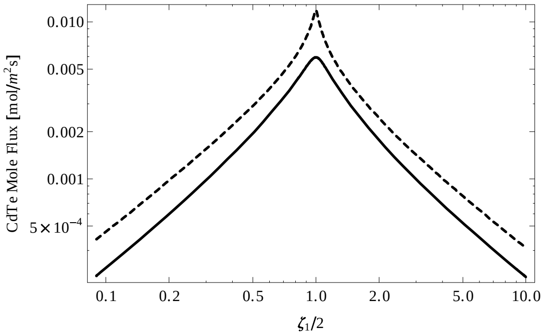

Figure 8.4: Equilibrium mole fluxes corresponding to the results in Fig. 8.3. The dotted line indicates the fluxes when $T_w(0) - T_w(x) = 10\,\mathrm{K}$, the solid like correspond to the case where $T_w(0) - T_w(x) = 5\,\mathrm{K}$. The variation in the fluxes when the overall temperature system of the system is varies is negligible.

that are 25 K lower than the high temperature cases.. The difference between the equilibrium and CKB solutions becomes slightly larger, but not significantly so. In Row 3, the temperatures are reduced a further 25 K. The difference between the equilibrium and CKB solutions increases further. As with the UTU and UTB cases, the kinetic impedance is stronger at lower temperatures in the BTB case.

8.3.1 Effect of the Individual Sticking Coefficients

So far, we have varied the sticking coefficients assuming always that $\theta_s = \theta_{Cd} = \theta_{Te_2}$. Experimental evidence suggests that these sticking coefficients are not, in fact, equal [95]. In Fig. 8.5 we plot the transport rate as a function of only one sticking coefficient, while the other is held at unity for several temperatures. As expected, the overall transport rate tends to zero as either sticking coefficient goes to zero. The transport rate decreases more rapidly when the Cd sticking coefficient is reduced. This is caused by the difference in molecular weights of the two constituents, as they are expressed in the CKB model coefficients.

Fig 8.6 shows that varying the individual sticking coefficients also changes the supersaturation of the vapor constituents, as well as the partial pressure ratio; due to the lower transport rates, the interface temperature is reduced as well.

In Fig. 8.7 two typical mass transport examples are given. In the first, the source is stoichiometric, in the second it is not. The temperature and partial pressure profiles are plotted for $\theta_{Cd} = \theta_{Te_2}$ as we have seen previously, and for $\theta_{Cd} \neq \theta_{Te_2}$. In the stoichiometric source case, one might expect that a difference in the sticking coefficients would lead to non-stoichiometry in the bulk vapor, even if the source composition is stoichiometric. This is, in fact, not the case. Instead, the equilibrium vapor composition of the seed ζ_2 becomes non-stoichiometric, and the total pressure in the ampoule increases, but the

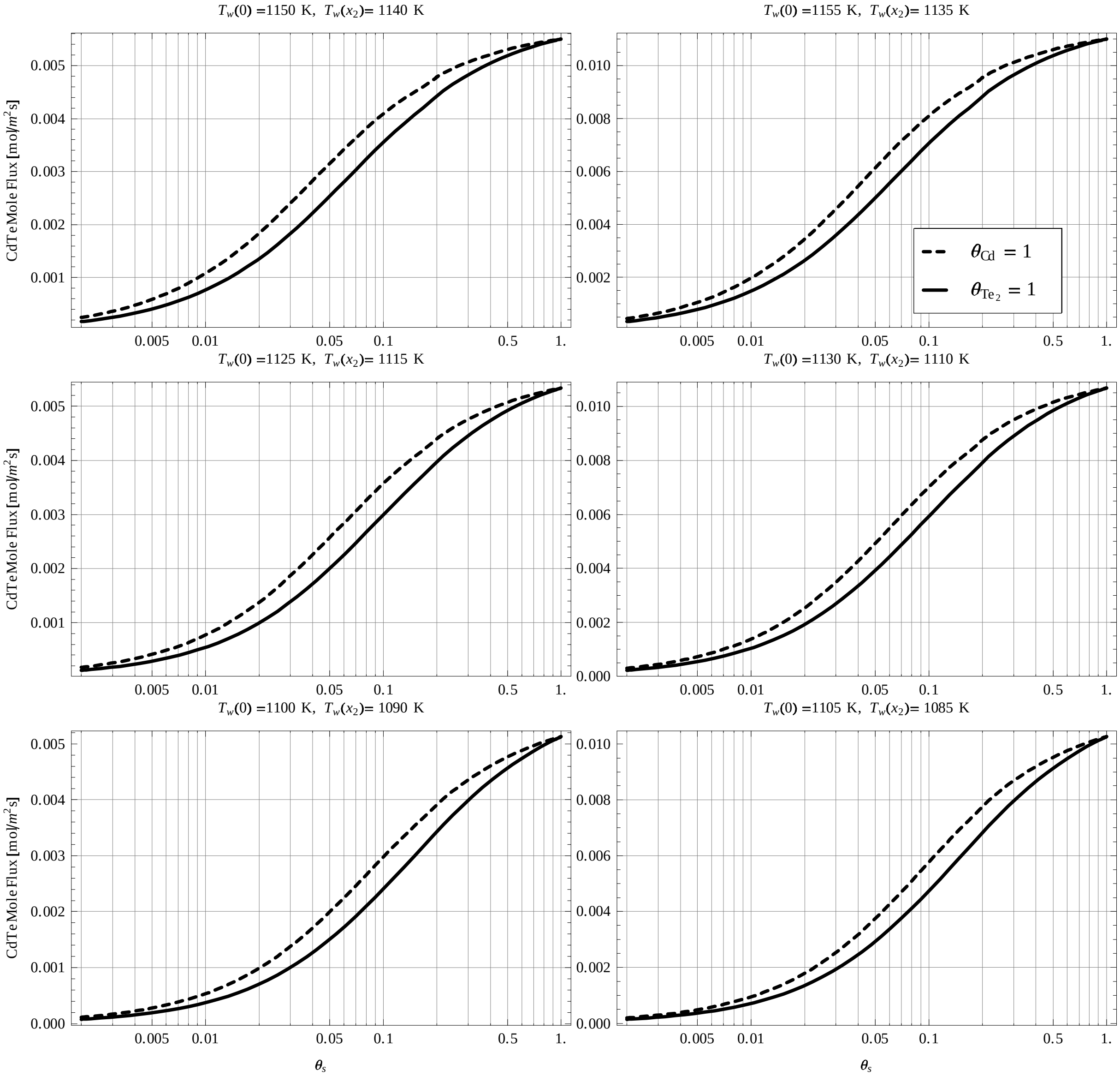

Figure 8.5: The mole flux of CdTe with $\zeta_1 = 2$ as a function of individual sticking coefficients. When one sticking coefficient is changed, the other is held at unity.

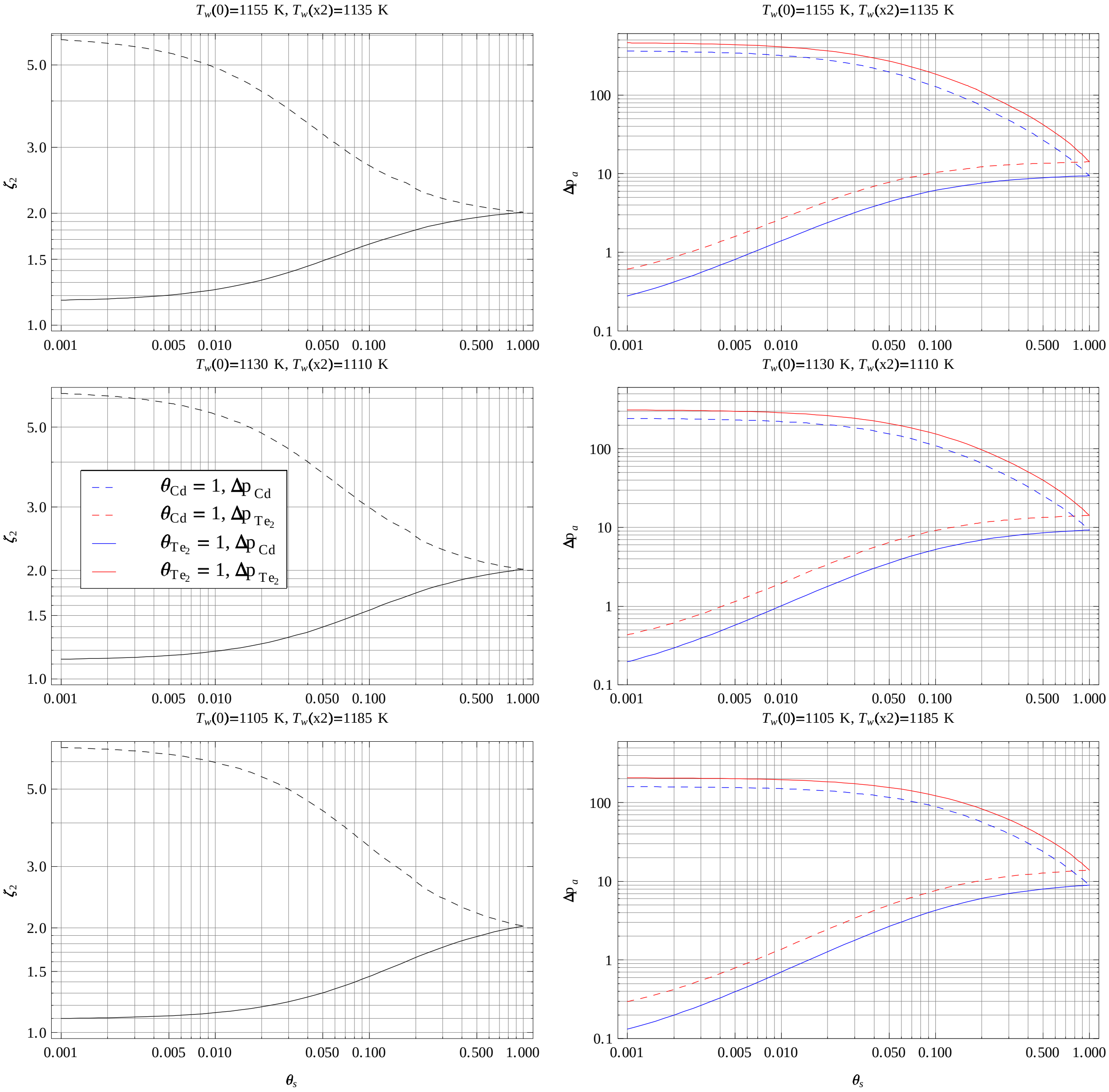

Figure 8.6: The effect of varying one sticking coefficient while keeping the other at unity on the seed equilibrium vapor composition and on the supersaturation of the individual condensing constituents at the seed interface. All values are calculated assuming a stoichiometric source $\zeta_1 = 2$.

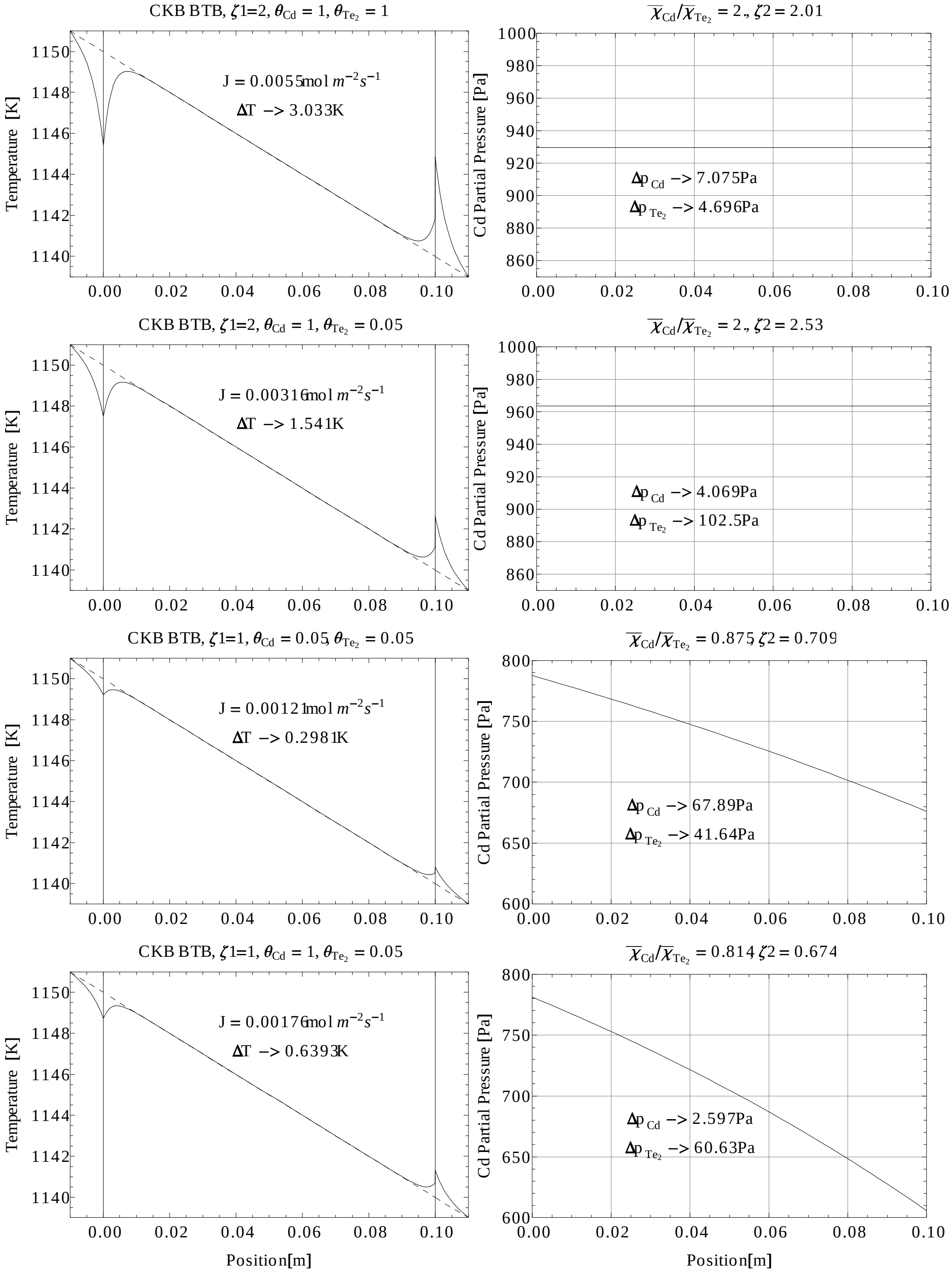

Figure 8.7: Several examples of CdTe transport, some with $\theta_{Cd} = \theta_{Te_2}$, others, at equivelant conditions with $\theta_{Cd} \neq \theta_{Te_2}$.

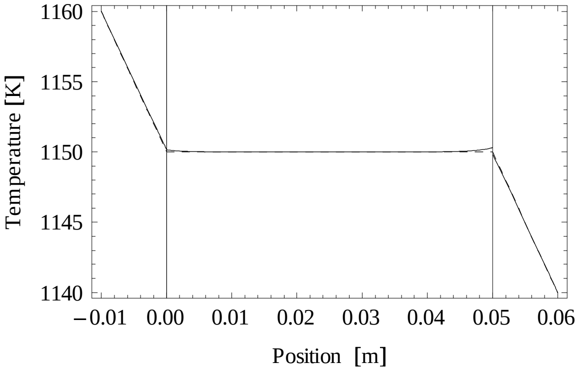

Figure 8.8: The temperature profile used to study the effect of the distance between interface x_2.

bulk composition remains stoichiometric. On the other hand, when the source is non-stoichiometric, the difference in sticking coefficients on the seed does affect the composition of the bulk vapor, along with the total pressures and equilibrium partial pressure ratio of the seed.

8.3.2 The influence of the transport length

As we discussed, Fig. 8.2 shows that non-stoichiometry in the source vapor is amplified along the length of the ampoule as a result of diffusion. The magnitude of this amplification can be reduced by minimizing the transport distance, that is the distance between Interface 1 and Interface 2 [9]. To study this effect, we selected a vapor temperature profile such that the interface temperatures and ampoule temperature gradients are unaffected by variation of x_2; this profile is given in Fig. 8.8. We plot the transport rate against the length of the vapor phase and the source equilibrium vapor composition in Fig 8.9. We confirm that the transport rate is increased when the distance between interfaces is reduced and the source is non-stoichiometric. As expected, when the source vapor is stoichiometric, transport rate is unaffected by changes in transport length.

8.4 BTT Results

The introduction of a background gas (in this case CO) into the system has a similar effect as we have already seen in single species transport — the background gas increases the diffusive impedance to transport, thus reducing the transport rate and decreasing the importance of the other impedances. In Fig. 8.10 some typical BTT solutions for CdTe are given, In Row 1, we give the solution for stoichiometric transport with a very small amount of background gas added. There is a 9% difference between the equilibrium and CKB solutions. This is surprising given that the difference in the BTB solution was 8%

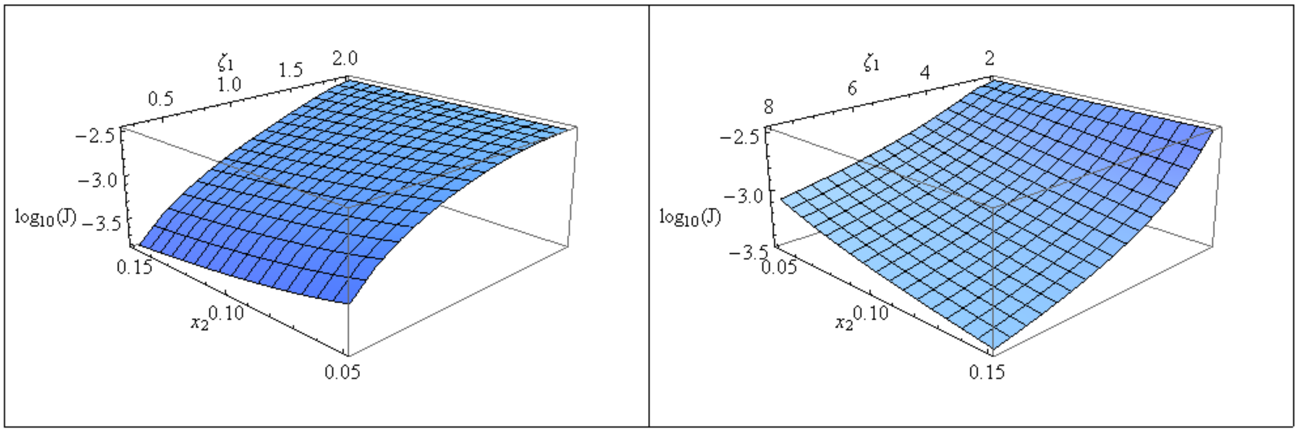

Figure 8.9: The effect of x_2 (the distance between the source and the seed interfaces) on the mole flux at various source compositions. As expected, at non-stoichiometric compositions, the mole flux is inversly proportional to the length x_2. When the source is stoichiometric, length has no effect.

with no background gas added. We would expect that the addition of a background gas would reduce the difference between the equilibrium and CKB solutions, due to the presence of the diffusive impedance. It is likely that this error is rooted in the method used to transform the CKB transport coefficients to include a stagnant constituent (see §4.3.1). Because the error is very small, we do not pursue it further. In the partial pressure profile, we see that the partial pressures of both constituents decrease slightly along the length of the ampoule. This is caused by diffusion in the background gas. In Row 2, we give solutions fro $\zeta_1 = 2$ with a larger amount of background gas added. As expected, the transport rate and the temperature spikes are reduced; the transport is more strongly limited by the diffusive impedance. Consequently, the slope of the partial pressure profiles is steeper. Rows 3 and 4 give the equivalent solutions to Rows 1 and 2, but with $\zeta_1 \neq 2$. Here, the diffusive impedance is stronger since diffusion now takes place not only in a background gas present, but also in the excess constituent.

An interesting consequence of the background gas is that, unlike the BTB solution (Fig 8.2) stoichiometric source compositions do not lead to stoichiometric compositions in the overall vapor or at the seed. The vapor at the seed ends up slightly cadmium rich; this is a result of the binary diffusivity of Cd in CO being greater than the diffusivity of Te_2 in CO (see Tab. 5.6); Cd has an easier time diffusing in CO than Te_2 does.

In Fig. 8.11 the difference between the equilibrium and non-equilibrium mole flux is plotted for different sticking coefficients and background gas pressures. Stoichiometric source compositions are used in all

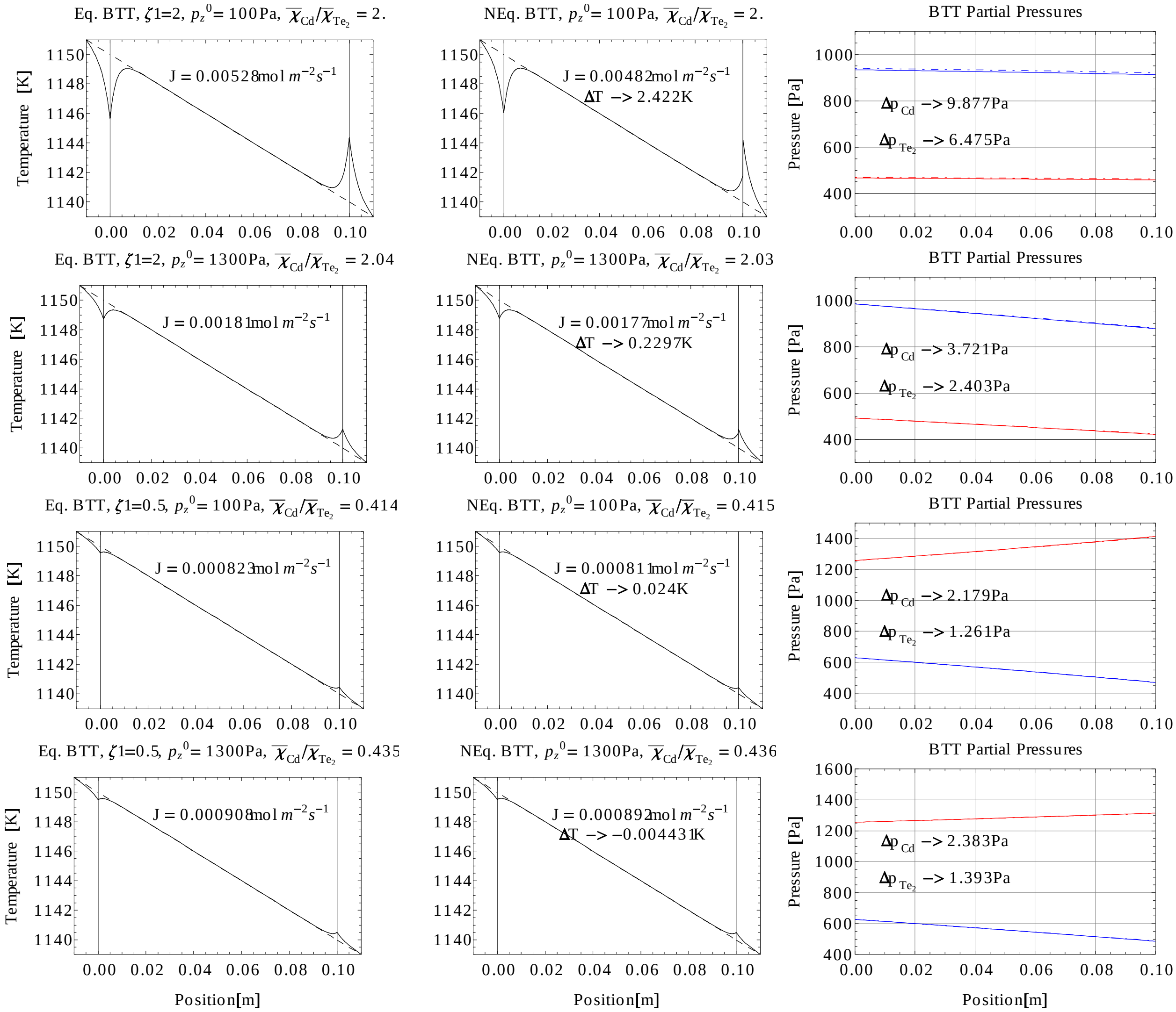

Figure 8.10: Several typical BTT solutions. In the partial pressure profiles, the blue lines indicate p_{Cd}, the red lines indicate p_{Te_2}. All solutions assume unity sticking coefficients for both Cd and Te$_2$.

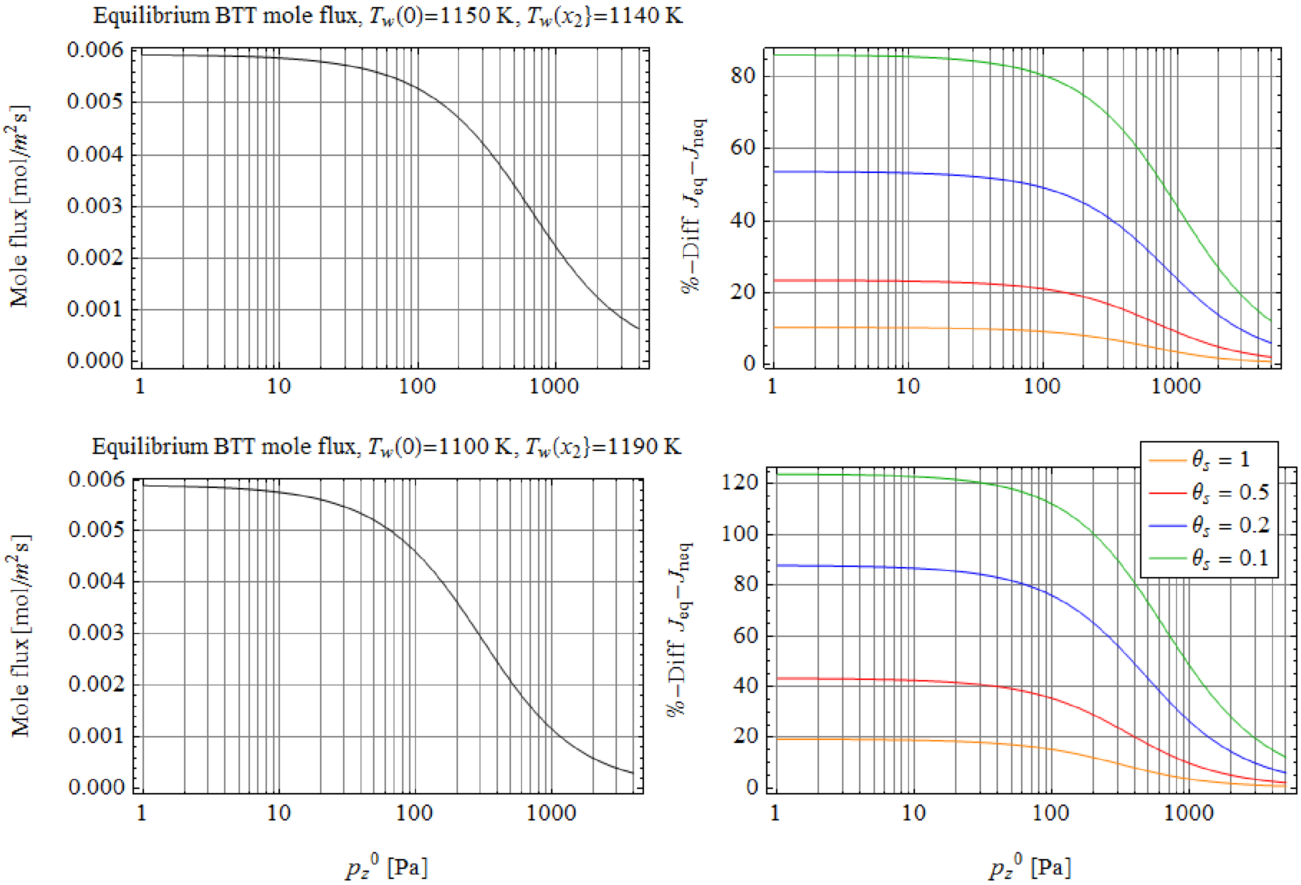

Equilibrium BTT mole flux, $T_w(0)$=1150 K, $T_w(x_2\}$=1140 K

Equilibrium BTT mole flux, $T_w(0)$=1100 K, $T_w(x_2\}$=1190 K

Figure 8.11: The difference between the equilibrium and non-equilibrium BTT solutions at the background gas fill pressure is increased. In all cases a stoichiometric source is assumed ($\zeta_1 = 2$).

cases. We plot a low temperature case and a high temperature case. We find that the BTT system behaves in much the same manner as the UTB case. As before, when no background gas is present, the kinetic impedance becomes significant, especially when the sticking coefficient and temperature is low. Small quantities of background gas do not affect this much, and the kinetic impedance continues to be significant. Once the amount of background gas is high enough, the equilibrium and non-equilibrium solutions begin to converge. The diffusive impedance becomes dominant over the kinetic impedance for all but the lowest sticking coefficients.

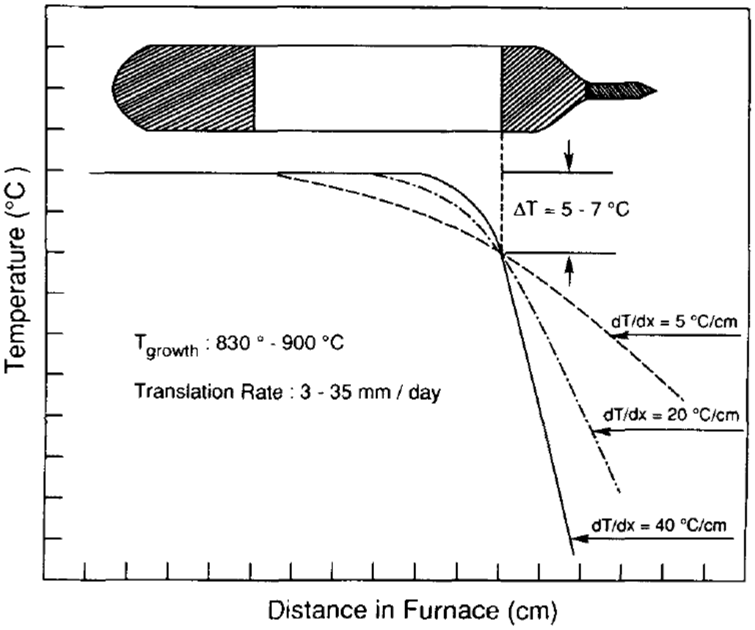

Figure 8.12: A schematic of the arrangement used in the FVG experiment. Figure from [18]. *Used with permission from Springer.*

8.5 Experimental Comparison: BTB

Some of the highest transport rates ever reported in for single crystal CdTe growth in closed ampoules were found by Wiedemeier and Wu in their fast vapor growth (FVG) experiments [18]. We now compare the BTB model to these experimental results.

8.5.1 Experimental Description

Figure 8.12 gives the general experimental arrangement used in the FVG experiments. The ampoules used had a 15 mm inner diameter and a length of 10 cm. The distance between the source and the seed crystal during growth was approximately 6 cm. We consider the steady state at the instant where the source has a length of 3 cm and the seed has a length of 1 cm. This is similar to the situation in Fig. 8.12, though in our model we neglect the complex geometry of the ampoule.

The traveling heater method (THM) was applied in this experiment where the ampoule was translated so that the applied temperature at the seed remained constant during the advancement of the interface. This type of arrangement is common in VPG; we first discussed it in general terms in Chapter 1. The translation rates are given in Fig. 8.12. The furnace used was constructed from a transparent material so that the translation rate could accurately be matched to the advancement rate of the interface.

The source was purified and pretreated carefully such that $\zeta_1 \simeq 2$ following the procedure discussed in [12]. The background gas pressure was estimated to be less than 0.0013 Pa; we shall therefore apply the BTB model to the problem.

The transport rates were reported in $\mathrm{mm/d}$, we use the mole density of CdTe to convert the reported transport rate to $\mathrm{mmol/m^2\,s}$, the measured transport rates are given in Tab. 8.1.

Case	Source Temp. $T_w(0)$ [K]	Undercooling $\Delta \not{T}_u$ [K]	Max. T. Grad $-dT_w/dx$ [K/cm]	Trans. Rate [mm/d]	Mole Flux J_{CdTe} $[\mathrm{mmol/m^2\,s}]$
1	1103	5	5	3	0.8
2	1173	5	5	3	0.8
3	1103	6	20	3	0.8
4	1143	6	20	5	1.3
5	1173	6	20	7.5	2.0
6	1173	7	40	35	9.3

Table 8.1: The transport rates obtained in the Wiedemeier and Wu fast vapor growth of CdTe [18]. The level of undercooling is assumed.

Wiedemeier and Wu found that at small temperature gradients, polycrystalline material was formed at the interfaces; at steeper temperature gradients, the stability of the growing crystal increased, and single crystal material was transported.

8.5.2 Model Assumptions

Before applying the BTB model, several additional assumptions were required. Firstly, the temperature profile shape used in [18] proved to be difficult to fit accurately with a polynomial. We therefore use a discontinuous linear temperature profile to approximate the actual temperature profile, as in Fig. 8.13. Furthermore, because we lack information regarding the individual sticking coefficients of Cd and Te_2, we assume in each case that $\theta_{Cd} = \theta_{Te_2} = \theta_s$. What remains are two free parameters to fit the model to experimental data in Tab. 8.1, ζ_1 and θ_s.

8.5.3 Results

Fig. 8.13 shows the results for fitting in terms of ζ_1; although Wiedemeier and Wu claimed that stoichiometrically dissociating material was used in every run, Palosz and Widemeier suggest that controlling ζ_1 with enough precision to ensure a stoichiometric source composition in every source sample is impossible due to measurement uncertainty [12]. It is therefore perfectly reasonable to assume that the results obtained in [18] are the result of source off-stoichiometry[2]. We observe that the ζ_1 required to fit each

---

[2] We elected to fit the model in terms of a Te_2 rich ($\zeta < 2$) equilibrium vapor composition. An equivelent result could be obtain for Cd rich ($\zeta > 2$) compositions. Given the composition diagram of CdTe, it is more likely that samples are Te-rich than Cd-rich [54].

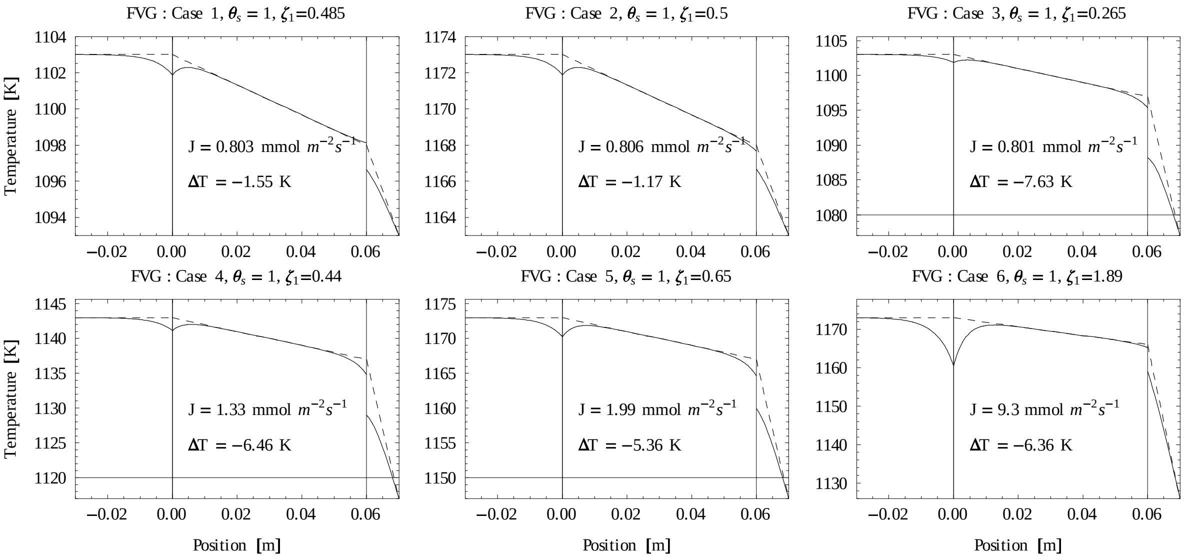

Figure 8.13: The CKB BTB model fitted to the results of [18] in terms of the source equilibrium vapor composition ζ_1 for each series of experimental cases.

case varies significantly.

On the other hand, the results in Tab. 8.1 are the reported average growth rates based upon multiple experimental runs. It is therefore possible that the source composition, averaged over multiple samples was indeed stoichiometric, such that $\zeta_1 = 2$. Fig. 8.14 shows the non-equilibrium BTB model fitted in terms of the overall sticking coefficient θ_s. We observe that cases 1-5 the θ_s required to fit the model is in the range $(0.02 - 0.06)$. This value is an order of magnitude greater than the sticking coefficient value measured by Fiedrele et al. [10]. In case 6, we observe a sticking coefficient value much higher than the previous cases, at $\theta_s = 0.74$. In each case there is a small, negative temperature jump, indicating that the heat transport is directed from the vapor into the solid.

8.5.4 Discussion

In reality, due to the inherent uncertainty associated with CA-PVT, it is difficult to say whether the transport rates obtained in [18] are the result of interface resistivity, the result of source stoichiometry, or caused by some other factor. That being said, the overall consistency of cases 1-5 fitted by the sticking coefficient is quite compelling; indeed cases 2-5 all were fitted with sticking coefficients approximately equal to 0.02. Case 6 is, however, an outlier here; the sticking coefficient used for fitting is dramatically different from those used in cases 1-5.

Wiedemeier and Wu conducted a through study into the morphology of the transported CdTe as a result

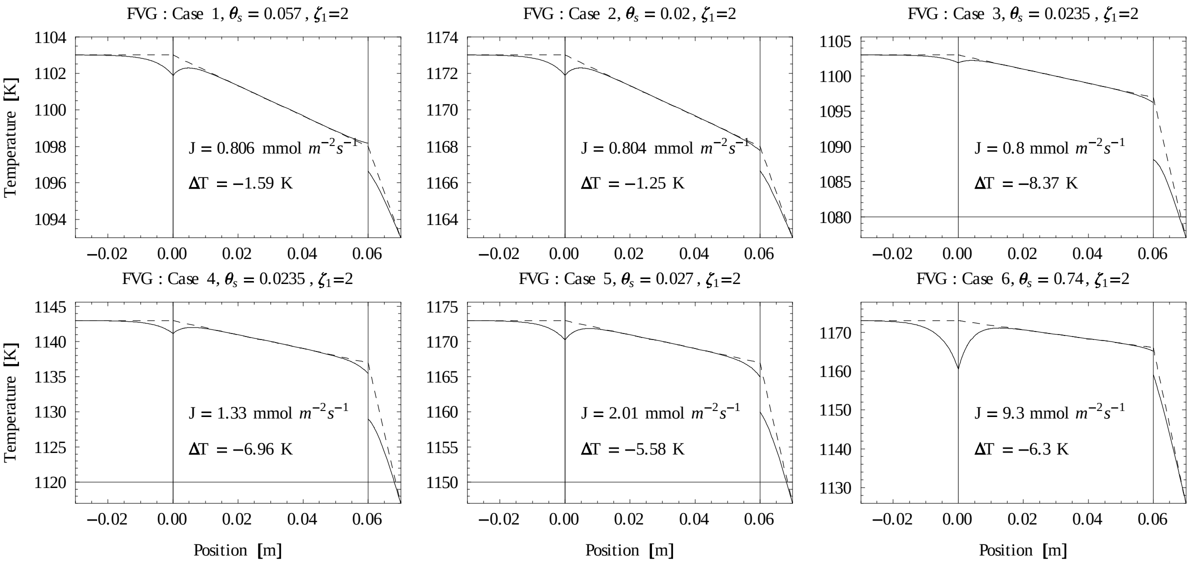

Figure 8.14: The non-equilibrium BTB model fitted to the results of [18] in terms of the source equilibrium vapor composition $\theta_s = \theta_{Cd} = \theta_{Te_2}$ for each series of experimental cases.

of their experiment [18, 96]. Figure 8.15 gives examples of the crystals grown in Cases 1 and 6.

In Case 1, polycrystalline material was grown. Wiedemeier and Wu suggested that the polycrystalline structure of the transported material was a result of high supersaturation ahead of the interface; this supersaturation caused the nucleation of new crystals. This hypothesis corresponds nicely to our findings in Chapter 7 regarding temperature gradients in single crystal growth, especially with the form of the temperature profiles used in FVG experiments (Fig. 8.12) The transported material in Case 1 was polycrystaline, and no crystal plane was dominant during the growth; thus, we expect that the interface structure constituted a rough surface. Cases 2 - 5 produced highly defected single crystals. The densities of these defects decreased with increasing temperature gradient. In Case 6, a single crystal containing a significantly lower defect density was grown. In Cases 2-6, growth proceeded near the (100) plane, with faceting in the (110) direction. This would indicate that growth must have proceeded either by 2D nucleation, spiral growth or step flow growth, or, more likely, a combination of all three.

In Case 1, the interface was concave. Wiedemeier and Wu suggested that the concavity of the crystal was caused by increased latent heat removal from the edge of the crystal due to conduction through the ampoule walls. In Case 6, the interface was flat; the majority of the latent heat was likely removed by conduction through the crystall; conductive effects at the edges were less important.

Encouragingly, we find that the variation of the fitted sticking coefficient values in Fig. 8.14 correspond roughly to the different types of growth in the 6 experimental cases, with the exception of Case 2. Case

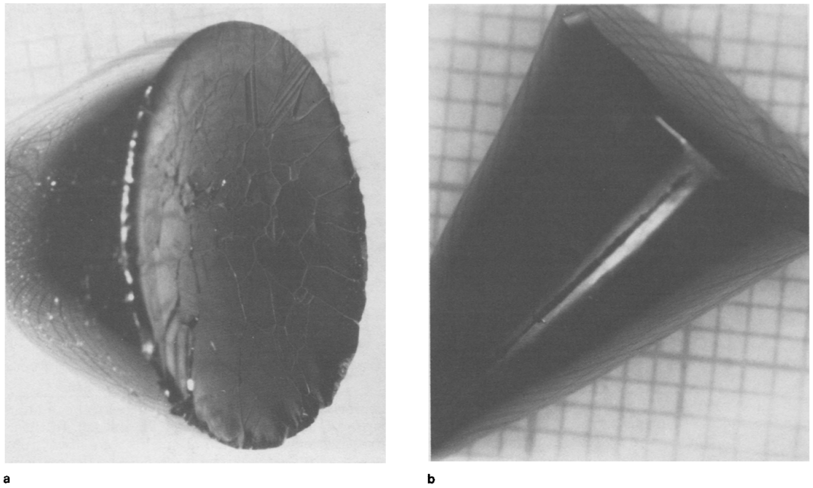

Figure 8.15: Typical transported CdTe boules from WWE. A. corresponds to Case 1; here, the material is polycrystaline, with clearly visible grain boundaries. The interface is concave. B. corresponds to Case 6; here, the interface is flat an the material constitutes a single crystal [18]. *Figure used with permission from Springer.*

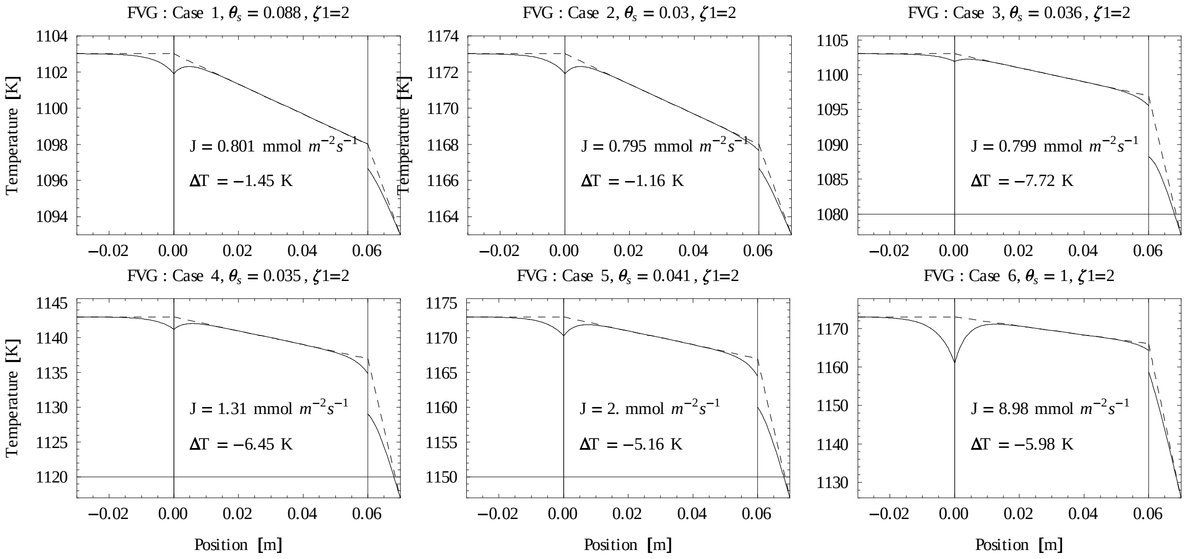

Figure 8.16: The CKB BTT model fitted to the results of [18] in terms of the sticking coefficient with a CO background gas pressure of $p_z^0 = 100\,\mathrm{Pa}$. Note the Case 6 experimental transport rate is $9.2\,\mathrm{mmol\,m^{-2}\,s^{-1}}$.

1 corresponds to a sticking coefficient of 0.05, Cases 3-5 all have sticking coefficients in the range of 0.02-0.03, and Case 6, which may have had different surface kinetics due to the substantially lower defect density and flat interface shape had a much higher sticking coefficient than the other cases, as $\theta_s = 0.74$. We must emphasize that this relationship between the sticking coefficient and the transported material condition may be purely coincidental.

8.5.5 Additional Considerations

It was assumed that the ampoules in the FVG experiments contained no background gas. Other studies have suggested that a background gas in sealed ampoules is unavoidable [97, 98]. For the sake of comparison we re-calculate the FVG experiment, this time with a small amount of CO background gas present[3] ($p_z^0 = 100\,\mathrm{Pa}$). The result is given in Fig. 8.16. We see that this small amount of background gas does not affect the results much. In Cases 1 - 5 the sticking coefficients are increased slightly from the BTB case, but they are still of the same order-of-magnitude. The BTT model cannot be fitted to Case 6 using the sticking coefficients because the experimental transport rate exceeds the BTT rate with unity sticking coefficients.

In Chapter 7, we suggested that the large error between the experimental result and the model result for the high temperature UTB cases resulted from a lack of knowledge of the correct temperature profile used in the experiment. In this case, we believe the temperature profile is captured correctly, as the temperature gradients very nearly match those reported in the experiment; we therefore doubt that these modelling runs contain the same error.

As a final consideration, we note that the results in [18] suffered from a lack of repeatability. These fast growth rates were obtained by gradually increasing the pulling rate of the ampoule right up to the point at which the growth become unstable. There was no knowledge beforehand of what maximum growth rate would be achieved in any particular run [99].

8.6 Experimental Comparison: BTT

We now compare our model to the Palosz and Wiedemeier experiment (PWE) [12]. This set of experiments involved the transport of stoichiometric CdTe in a sealed ampoule; exclusively polycrystalline material was condensed at the seed end of the ampoule.

---

[3] Although the actual background gas is likely not CO, we use this as an apporximation only.

8.6.1 Experimental Description

Source samples were prepared very carefully so as to ensure the source material was as close to the congruent sublimation line (Fig. 1.14) as possible, i.e., the source material had a stoichiometric equilibrium vapor pressure ratio ($\zeta_1 = 2$). A small quantity of background gas, consisting mainly of carbon monoxide (CO) remained in the ampoules as a result of the sealing process. The background gas pressure was estimated to be 1000 Pa at the growth temperature of 1173 K. This estimate was obtained by opening the sealed ampoules under water, and measuring the size of the resulting bubble, assuming the bubble consisted entirely of CO. At the end of their paper, Palosz and Wiedemeier suggest that this estimation method severely overestimated the quantity of background gas [12]. Later studies confirmed that typical quantities of background gas in sealed ampoules are much lower, on the order of 100 Pa [97, 98].

The sealed ampoules were then placed in a three-zone furnace and an undercooling between Interface 1 and Interface 2 was applied; the shape of the temperature profile was not specified. Mass transport rates were measured by weighing the amount of transported material upon completion of the experimental run. The mole flux was determined in relation to the cross sectional area of the ampoule. The transient effects at the beginning and end of each run were assumed to introduce measurement errors of less than 10%; an assumption that, in light of our results regarding the steady state assumption (§7.5.3), may not be correct.

The ampoules were 10 cm long and had an inner diameter of 15 mm. In the cases we examine, the ampoule with a 4 g charge of source material, material was condensed directly upon the glass at the seed end of the ampoule. The dimensions of the source charge were not reported. We must calculate the dimensions based upon the cross sectional area of the ampoule and the mole density of CdTe. We take our steady-state snapshot of the problem when exactly half the material has been transported across the ampoule, meaning that the thickness of the source is equal to the thickness of the seed. The resulting arrangement is given in Fig 8.17.

Although Palosz and Wiedemeier conducted a large number of experiments, with different source compositions and different source preparation procedures, we limit ourselves to the highest quality, repeatable experimental runs using stoichiometric source material ($\zeta_1 = 2$). These results are given in Tab. 8.2.

Case	Interface wall temps.		J - CdTe
	$T_w(0)$ [K]	$T_w(x_2)$ [K]	$\left[\mathrm{mmol/m^2\,s}\right]$
1	1173	1160	11
2	1173	1155	17
3	1173	1146	27
4	1173	1143	31

Table 8.2: Experimental data from Fig. 5 in [12]. Stoichiometric sources ($\zeta_1 = 2$) were used, background gas pressure was estimated at 700 Pa.

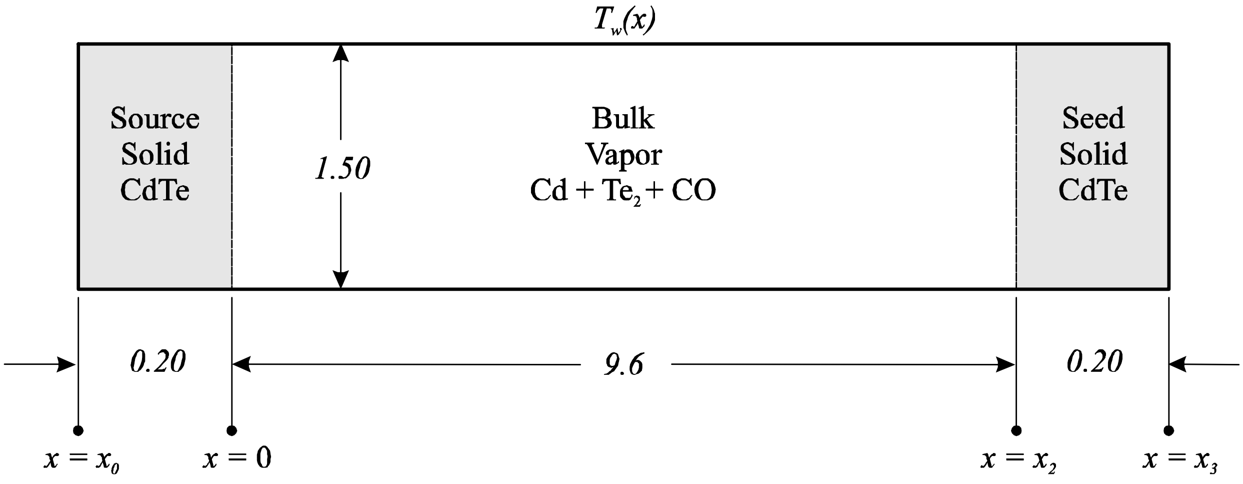

Figure 8.17: The experimental arrangement in the Palosz and Wiedemeier CdTe transport experiments [12]. Dimensions are calculated based upon the instant where half the initial change material (4 g CdTe) is transported. All dimensions reported in centimeters.

We note that these rates are much higher than those reported in [18], this is because polycrystalline material as opposed to a monocrystal was condensed at the seed end.

8.6.2 Model Results

In Fig. 8.18, the results of the CKB model for the PWE are given for a background gas fill pressure of $p_z^0 = 1000\,\mathrm{Pa}$, as estimated in [12]. At this fill pressure, the model transport rate is much smaller than the experimental rate; the model does not predict the mole flux correctly.

In Fig. 8.19 we give the result for a the transport rate with the background gas pressure reduced to 100 Pa. The experimental agreement is significantly improved, especially in the cases where the temperature gradient is lower. At higher temperatures, the error between the model and the experiment is still significant, though greatly improved from the initial case. If we reduce the fill pressure further, to 10 Pa, the agreement between the model and the experiment improves even further, as shown in Fig. 8.20.

Even in the very low fill pressure case, there is still significant error between the model and the experiment for the high temperature gradient cases.

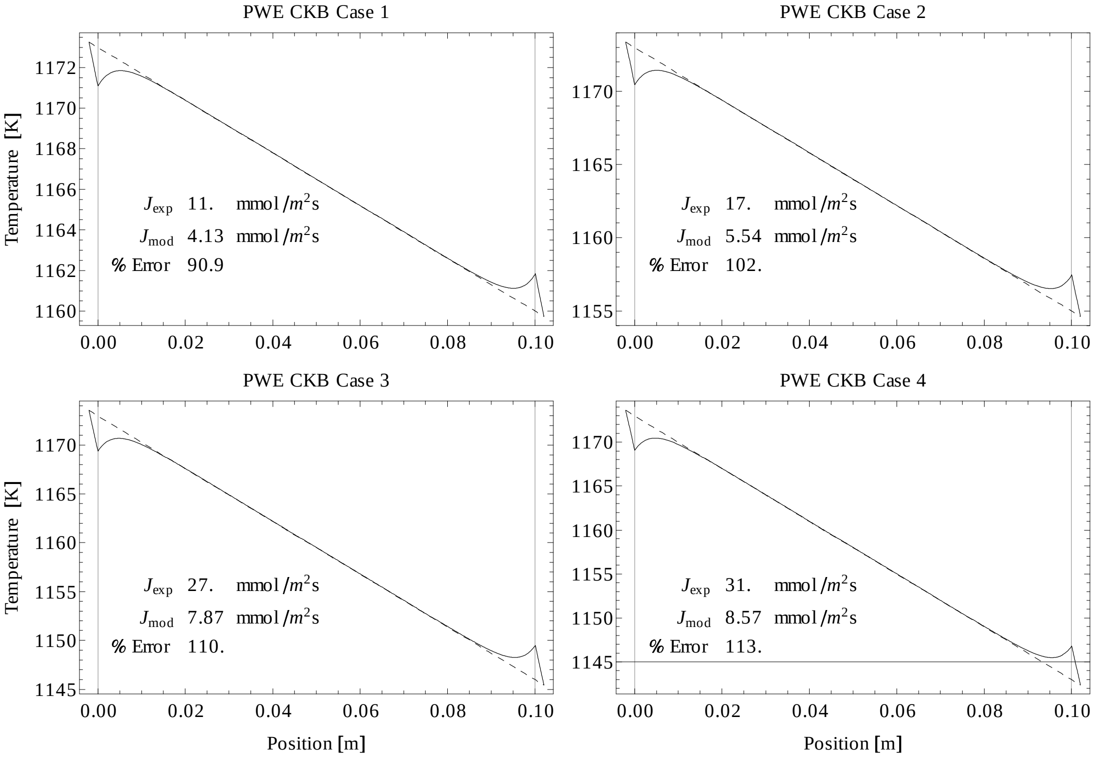
PWE CKB Case 1
PWE CKB Case 2
PWE CKB Case 3
PWE CKB Case 4

Figure 8.18: The CKB model results for the PWE data. Here, $p_z^0 = 1000\,\mathrm{Pa}$ was used, Palosz and Wiedemeier suggest that this estimated background gas pressure is significantly higher than what was actually in the ampoules [12]. Unity sticking coefficinets were used in all cases.

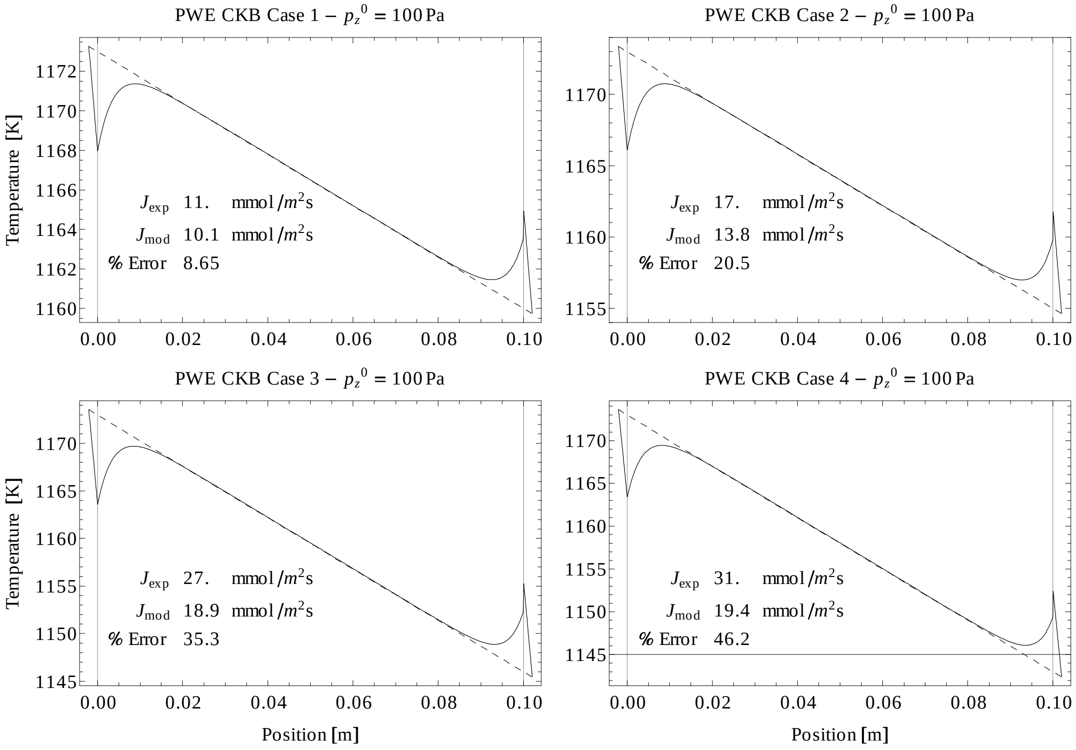

Figure 8.19: The CKB model results for the PWE with fill pressure $p_z^0 = 100\,\mathrm{Pa}$.

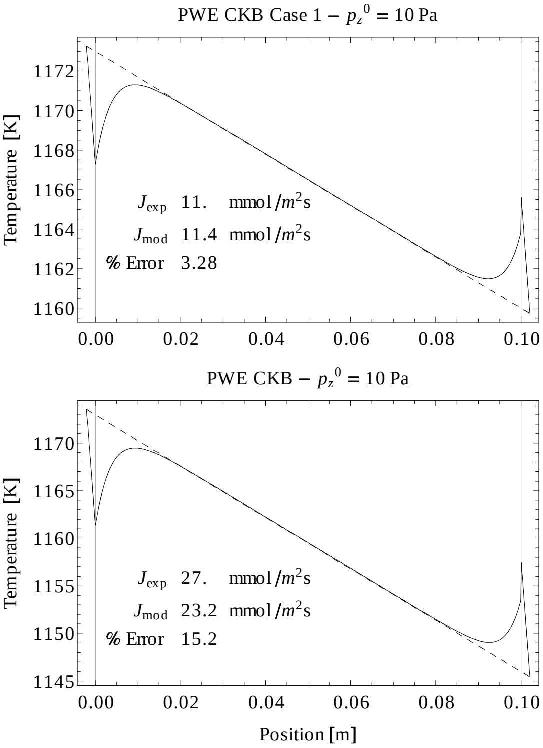

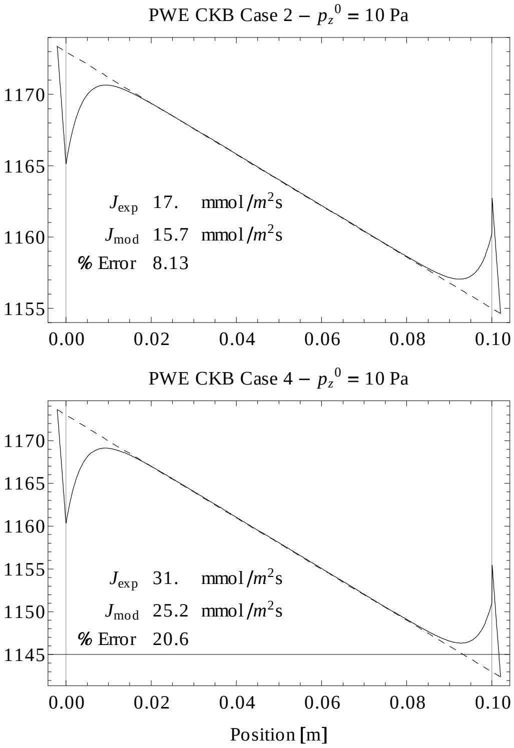

Figure 8.20: The CKB model results for the PWE with fill pressure $p_z^0 = 10\,\mathrm{Pa}$.

8.6.3 Sources of Error

A main cause of the error between the model and the experiment may be lack of information regarding the temperature profile. Palosz and Wiedemeier did not specify in their work what temperature profile was used in the bulk vapor; they only specified the source and seed interface temperatures. From our previous discussion on supersaturation in the vapor (§7.4), it is clear that a linear temperature profile, like the ones we used in this analysis would likely lead to parasitic nucleation along the length of the ampoule. It is therefore likely that Palosz and Wiedemier used a temperature profile that ensured a reduced supersaturation in the vapor; i.e. one in which the average temperature in the bulk vapor was greater than or equal to the source temperature. This type of a temperature profile would invariably lead to a steeper temperature gradient in the seed crystal. Such a gradient would remove more latent heat from the seed, and thus allow for a faster growth rate.

A second source of error stems from the fact that Palosz and Weidemeier did not specify the seed interface shape. The intent of the PWE experiment was not to grow a perfect, single crystal, but to study the effect of sample preparation on the CdTe transport rate, regardless of the growth quality. The transported material was polycrystalline, and no characterization of this material was done [99]. The transport rates were reported in terms of the cross sectional area of the ampoule, *and not of the growing crystal surface.* It is quite likely that this surface had a significantly larger surface area than the cross sectional area of the ampoule. In our analysis we assumed that the ampoule cross sectional area was equal to the actual crystal surface area. If however, the crystal surface area was actually larger, the CKB model would underestimate the mole flux. This may be an additional reason for the large error between the experimental and CKB results.

8.6.4 Conclusion

Our model can be reasonably fitted to the PWE findings by adjustment of the background gas pressure, at least when the temperature gradient is low. The remaining error we attribute to a lack of information regarding the wall temperature profile in [12], and a lack of knowledge regarding the characteristics of the condensed material.

8.7 Concluding Remarks

Much of the phenomena we have seen here in our study of CdTe is similar to what we saw of I_2. We will not repeat the discussion on supersaturation, heat transport, and temperature jumps at the interfaces. In the first section of this Chapter, we confirmed most of the assertions made in standard, equilibrium dissociative sublimation theory [9], including the effect of geometry and the effect of non-stoichiometry in the source material on the transport rate. Kinetic impedances in CdTe vapor crystal growth are likely significant enough to be worthy of further consideration. This is clear from Fig. 8.3, where low sticking coefficients lead to significant differences between equilibrium and non-equilibrium solutions, at least when the source material sublimes stoichiometrically. The limited experimental evidence available suggests that sticking coefficients on CdTe surfaces in the temperature range 1073-1173 K are low [10]. This observation is confirmed in our application of the BTB non-equilibrium model to the FVG experiments [18]; although agreement with these results may be coincidental.

Chapter 9

Transport Coefficients for Cadmium Telluride

In Chapter 8, we studied the transport of CdTe using both equilibrium and non-equilibrium boundary conditions. We enforced a stoichiometric flux relation between the Cd and the Te_2 fluxes and found that under some conditions, especially at low temperatures and low sticking coefficients, the kinetic impedance played an important role in limiting the transport, as in Fig. 8.3. In Chapters 3 and 4, we introduced an alternative formulation of the phenomenological transport coefficients for solids that undergo dissociative sublimation. In the first part of this chapter, we relate the phenomenological coefficients for dissociative sublimation to the CKB coefficients. In the second part, we discuss an experimental method to measure the transport coefficients on CdTe surfaces.

9.1 Phenomenological Coefficients for Dissociative Sublimation Revisited

In §4.3.2 we discussed the form of the phenomenological coefficient matrix for dissociative sublimation. We recall the LIT interface condition,

$$\begin{bmatrix} J_a \\ J_b \\ -\kappa_v \frac{dT_v}{dx} \end{bmatrix} = \mathcal{L}^{(2)}_{AB}(T_1, \zeta, \phi_1) \begin{bmatrix} -\frac{R_u}{p^a_{sat}(T_s)} \Delta p_a \\ -\frac{R_u}{p^b_{sat}(T_s)} \Delta p_b \\ \frac{\Delta T}{T_s^2} \end{bmatrix}. \tag{9.1}$$

The equivalent reactive sublimation interface condition is,

$$\begin{bmatrix} J_{Rx} \\ q \end{bmatrix} = \begin{bmatrix} J_{Rx} \\ -\kappa_v \frac{dT_v}{dx} \end{bmatrix} = \mathcal{L}^{(Rx)}_{AB}(T_1, \zeta, \phi_1) \begin{bmatrix} -\frac{\Delta K}{K_p(T_s)} \\ \frac{\Delta T}{T_s^2} \end{bmatrix}. \tag{9.2}$$

The heat transport coefficients in (9.2) are related to the CKB phenomenological coefficients as

$$l_{qq} = l^{(2)}_{qq}, \tag{9.3a}$$

$$l_{Rq} = l^{(2)}_{aq} + l^{(2)}_{bq}. \tag{9.3b}$$

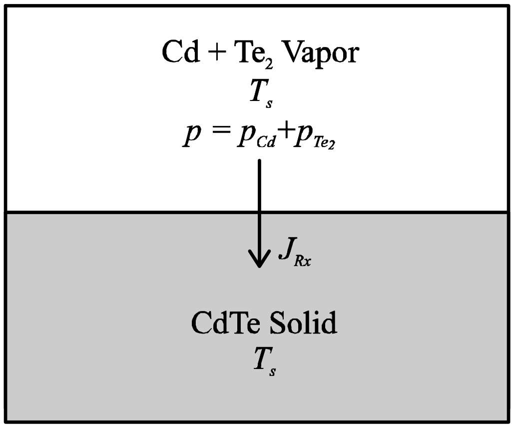

Figure 9.1: A simple, isothermal interface condensation model.

where $l_{qq}^{(2)}$, $l_{aq}^{(2)}$ and $l_{bq}^{(2)}$ are elements of $\mathcal{L}_{AB}^{(2)}(T_1,\zeta,\phi_1)$, l_{qq} and l_{Rq} are elements of $\mathcal{L}_{AB}^{(Rx)}(T_1,\zeta,\phi_1)$. We now address the transport coefficient for the mole flux, l_{RR}, which remains undefined. We begin by recalling (4.26)

$$J_{Rx} = l_{RR}\frac{\Delta K}{R_u K_p(T_s)} = \left(l_{aa}^{(2)} + l_{ab}^{(2)}\right)\frac{\Delta p_a}{p_{sat}^a(T_s)} + \left(l_{bb}^{(2)} + l_{ab}^{(2)}\right)\frac{\Delta p_b}{p_{sat}^b(T_s)}; \tag{9.4}$$

As discussed, we choose not to solve this equation by linearization; instead, we apply both this model, and the CKB model to a simple interface, and compare the result.

9.1.1 Isothermal condensation model

A simple, isothermal system shown in Fig. 9.1. The system consists of a pure mixture of Cd and Te$_2$ over solid CdTe all at temperature T. The Cd and Te$_2$ molecules have sticking coefficients θ_{Cd} and θ_{Te_2} on the solid surface. The equilibrium vapor composition is given by ζ_1.

We assume that the system is very slightly out-of-equilibrium, such that it remains isothermal $T_s = T_v = T$, but the vapor partial pressures are held slightly higher than the corresponding equilibrium pressures by an external Cd and Te$_2$ supply. There must then be a small reaction flux J_{Rx}. We recall the dissociative sublimation reaction of CdTe

$$\mathrm{Cd(v)} + \frac{1}{2}\mathrm{Te_2(v)} \rightleftharpoons \mathrm{CdTe(s)}. \tag{9.5}$$

The assumed mole flux in this calculaiton is very small, such that the latent heat can be neglected. Since the system is isothermal, there is no heat flux at the interface; the only thermodynamic fluxes are the mole fluxes of Cd and Te$_2$; Eq. (3.38) becomes

$$J_{Cd} = \frac{2}{3}J_{Rx} = -l_{aa}^{(2)}\frac{R_u \Delta p_{Cd}}{p_{sat}^{Cd}(T,\zeta_1)} - l_{ab}^{(2)}\frac{R_u \Delta p_{Te_2}}{p_{sat}^{Te_2}(T,\zeta_1)}, \tag{9.6a}$$

$$J_{Te_2} = \frac{1}{3}J_{Rx} = -l_{ab}^{(2)}\frac{R_u \Delta p_{Cd}}{p_{sat}^{Cd}(T,\zeta_1)} - l_{bb}^{(2)}\frac{R_u \Delta p_{Te_2}}{p_{sat}^{Te_2}(T,\zeta_1)}, \tag{9.6b}$$

where $\Delta p_{Cd} = p_{sat}^{Cd}(T,\zeta_1) - p_{Cd}$ and $\Delta p_{Te_2} = p_{sat}^{Te_2}(T,\zeta_1) - p_{Te_2}$. If we prescribe $\{T, J_{Rx}, \zeta_1, \theta_{Cd}, \theta_{Te_2}\}$, (9.6) can be solved for p_{Cd} and p_{Te_2} Once these are known, we may calculate

$$K = \frac{1}{p_0^{3/2}}\left(p_{Cd}\sqrt{p_{Te_2}}\right); \tag{9.7}$$

thus obtaining ΔK. From (3.41)

$$l_{RR}(T, \chi_{sat}^a, \theta_s^a, \theta_s^b) = \frac{J_{Rx}}{\Delta K}K_p(T); \tag{9.8}$$

We expect that this phenomenological coefficient is independent of the mole flux that is selected, at least for small fluxes; this hypothesis is tested in the next section.

9.1.2 Results

Figure 9.2 shows the dependence on the temperature and source composition of l_{RR}. for several choices of the sticking coefficient; in this case $\theta_{Cd} = \theta_{Te_2}$. We see that the transport coefficient varies most significantly with the sticking coefficient and the temperature, although it is not independent of the equilibrium vapor composition. Fig 9.3 shows the relationship between the temperature and the individual sticking coefficients at both stoichiometric and non stoichiometric compositions.

Figure 9.4 shows the influence of the selected J_{Rx} on the value of the coefficient. We see that the coefficient does not vary much when the reaction flux is less than approximately 0.01 $\mathrm{mol/m^2\,s}$. The isothermal transport case could only be accomplished when the flux is small enough that the release of latent heat can be neglected. Furthermore, when the fluxes are high, the degree of non-equilibrium at the interface becomes more significant, and the validity of the linear law becomes questionable. Therefore, Fig. 9.4 confirms our hypothesis that the transport coefficient is independent of the reaction flux when the reaction flux is small.

9.1.3 Comparison to literature

A reactive transport phenomenological coefficient was used by Laasch et al. in their model of Markov-Davydov CdTe growth [17]. Transport of CdTe was modelled at 1118 K; an l_{RR} value of 0.1 and a vapor

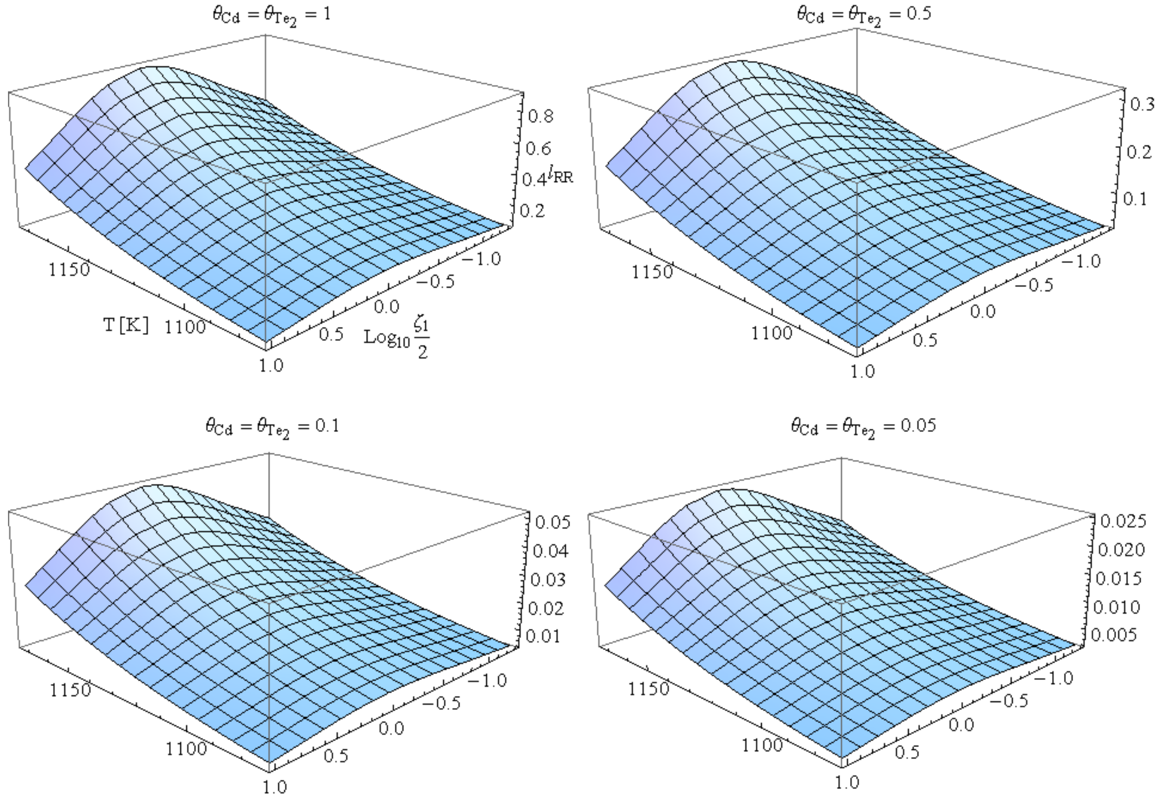

$\theta_{Cd} = \theta_{Te_2} = 1$

$\theta_{Cd} = \theta_{Te_2} = 0.5$

$\theta_{Cd} = \theta_{Te_2} = 0.1$

$\theta_{Cd} = \theta_{Te_2} = 0.05$

Figure 9.2: The phenomenological mole transport coefficient for dissociative sublimation (l_{RR}). For this calculation we assumed a reaction mole flux $J_{Rx} = 0.001\ \mathrm{mol/m^2\,s}$

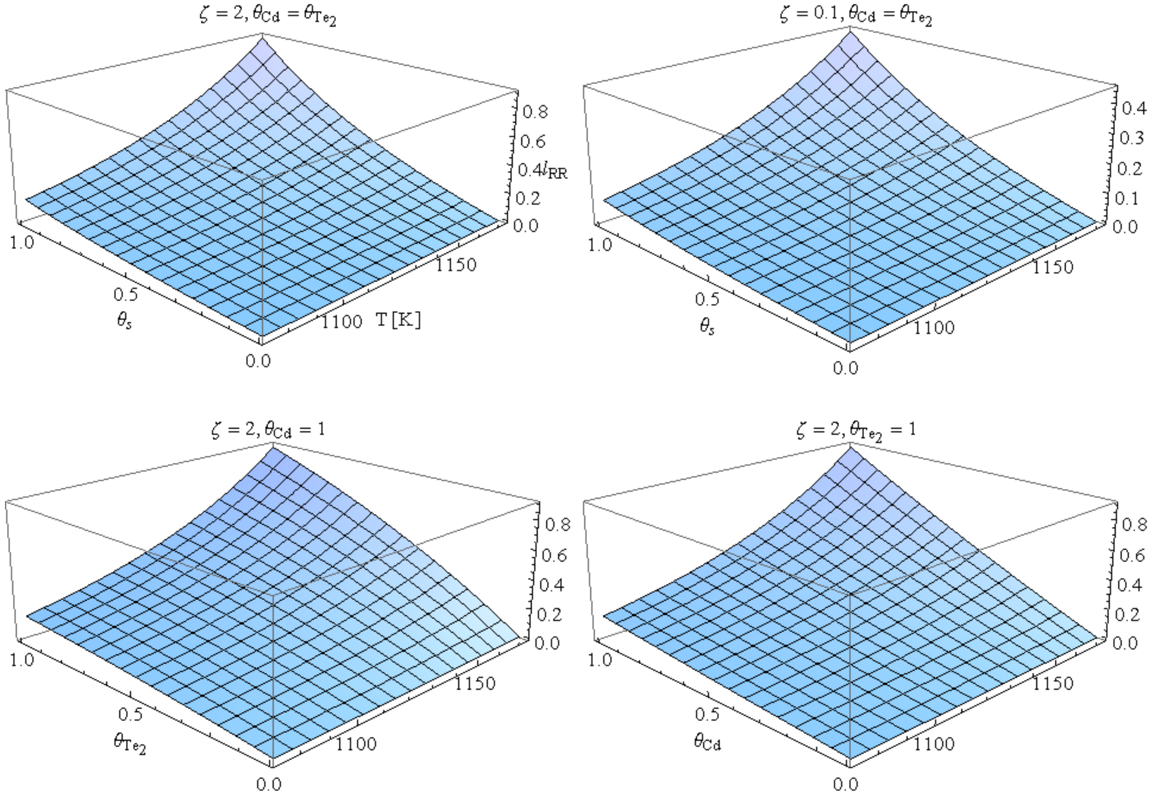

Figure 9.3: The direct influence of the temperature and sticking coefficient on l_{RR} at various temperatures and source compositions

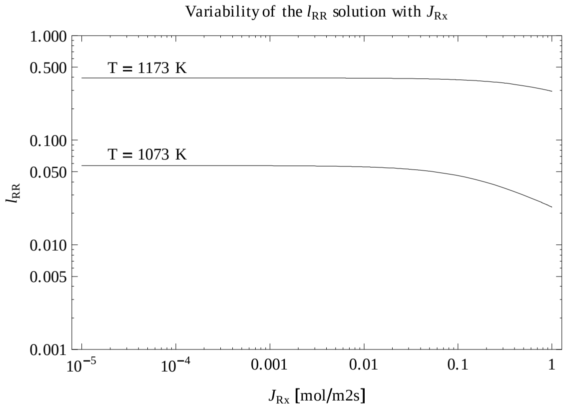

Figure 9.4: The influence of J_{Rx} on the calculation of the coefficient l_{RR}.

composition near the stoichiometric composition was assumed above the seed. Our model gives a value of 0.36 at these conditions when $\theta_s = 1$ and $\zeta_2 = 2$. We match the Laasch result when $\theta_s = 0.41$. Laasch et al. [17] did not provide any justification for their choice of transport coefficient, and instead made an intuitive argument; it turns out their intuition was quite good, and the value they selected is perfectly reasonable.

9.2 Estimating the Phenomenological Coefficient for Dissociative Sublimation

From our results in Chapter 8, it is clear that knowledge of the sticking coefficient is important for modelling PVT of CdTe. If the sticking coefficient is high, equilibrium conditions give a reasonably accurate interface condition, as shown in Fig. 8.3. If, however, the sticking coefficient is low, the difference between the equilibrium and CKB solutions is significant at all temperatures.

In terms of our temperatures of interest, the Fiederle value (0.003) [10] seems to be the only measurement available. This extremely low value for the sticking coefficient would suggest that the kinetic impedance is significant; Fiederle et al. make this claim for temperatures under 900 °C. Since this was the only data we could find for the sticking coefficient on CdTe surfaces, we now propose a method to estimate it.

9.2.1 Concept

Fig. 9.5 shows a system that consists of a solid piece of stoichiometrically subliming CdTe ($\zeta = 2$) placed in a chamber connected to vacuum. The entire chamber is heated to a temperature T_w. As the

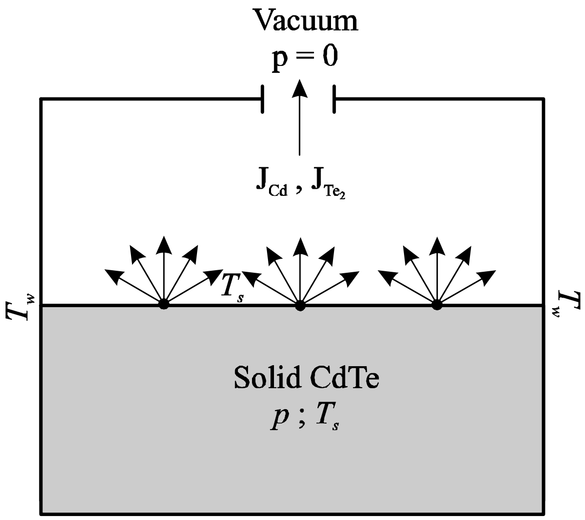

Figure 9.5: A simple, isothermal solid system. Strong non-equilibrium is maintained at the interface by removing all the vapor at the interface. The net particle flux from the interface can be described by a Maxwellian at $p = p_{sat}^{Cd} + p_{sat}^{Te_2}$ and T_s.

temperature of the chamber increases, the solid begins to sublime. The initial mole flux off of the surface can be obtained from kinetic theory using equation (1.6) with the Maxwellian distribution (1.9) The resulting sublimation mole fluxes of Cd and Te_2 are [39].

$$J_{CdTe} = J_{Cd}^{+} = \frac{\theta_{Cd}}{M_{Cd}}\sqrt{\frac{M_{Cd}}{2\pi R_u T_s}}p_{sat}^{Cd}(T_s,\zeta), \tag{9.9a}$$

$$J_{Te_2}^{+} = \frac{1}{2}J_{Cd}^{+} = \frac{\theta_{Te_2}}{M_{Te_2}}\sqrt{\frac{M_{Te_2}}{2\pi R_u T_s}}p_{sat}^{Te_2}(T_s,\zeta). \tag{9.9b}$$

The temperature T_s is the surface temperature of the interface. If $\zeta = 2$ and the flux is stoichiometric, we can equate (9.9a,b) and find a relationship between the sticking coefficients of Cd and Te_2.

$$\frac{\theta_{Cd}}{\theta_{Te_2}} = \frac{M_{Cd}}{M_{Te_2}}\sqrt{\frac{m_{Te_2}}{m_{Cd}}} \tag{9.10}$$

So that if we measure one sticking coefficient, we automatically know the other.

Due to the absorption of latent heat upon sublimation, T_s will not, in general, be equal to the imposed temperature T_w. Fig. 9.6 identifies the heat flows inside the chamber at the solid. The interface receives energy by conduction through the solid and by radiation from the ampoule walls. The latent heat is absorbed at the interface; when a steady state is reached, the interface temperature will be stable at T_s. In this system, we control only T_w. The resulting mole flux is then a function of T_s as well as the

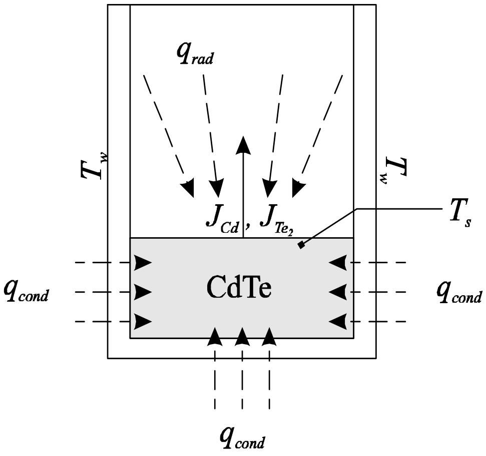

Figure 9.6: The solid sample heat transport. Energy is transported into the solid by conduction through the walls. Energy is also exchanged by radiation, though the direction of the radiative transport is not clear, since radiative heat transport between the cold finger (not shown) and the sample also takes place.

sticking coefficients.

The temperature T_s is unknown, but can be determined from the first law at the interface,

$$q = J\Delta h \tag{9.11}$$

where q is the total non-conductive heat transport to the interface, $J = J^+_{Cd} + J^+_{Te_2}$, and

$$\Delta h = \bar{C}_p\,(T_s - T_{ref}) - \bar{C}_s(T_s - T_{ref}) + \Delta h_{sv}. \tag{9.12}$$

Here, we have assumed sublimation into vacuum. Thus, the temperature of the subliming vapor must be equal to that of the solid. If q and J are known, T_s, θ_{Cd} and θ_{Te_2} can be found from (9.9) and (9.11).

9.2.2 Procedure

We shall obtain high purity, stoichiometric, polycrystalline CdTe samples from our industry partner; 5MPlus. These high purity samples are produced by the THM solution growth method. The test sample will be placed in one end of a sealed ampoule; the other end of the ampoule will be in thermal contact with a cold finger. The cold finger will be set at a low temperature such that the effective Cd and Te_2 saturation pressures at the cold finger end are negligable. The ampoule will then be inserted into the growth furnace and rapidly heated to the test temperature, which, for now, we leave undefined. The furnace will impose a flat temperature profile. The ampoule will be kept within the furnace for a

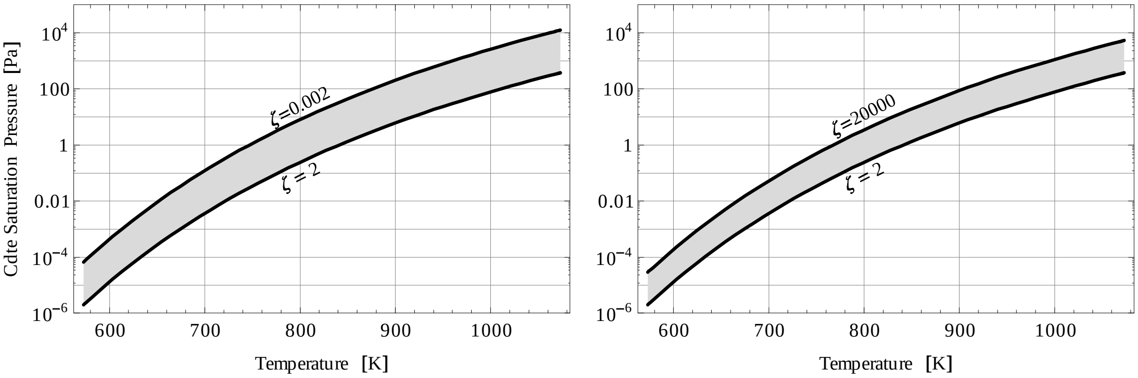

Figure 9.7: Total saturation pressure over solid CdTe as a function of temperature and composition for both Cd rich and Te rich CdTe compositions.

fixed period of time. It will then be removed from the furnace and cooled rapidly so as to minimize transient effects. The quantity of transported CdTe will then be measured. Considering the time within the furnace, and assuming the transient effects are negligible, the mole flux J_{CdTe} will then be obtained. Since all sublimed material will condense upon the glass at the cold finger almost immediately after sublimation from the surface, the actual cadmium and tellurium vapor pressures above the source are nearly equal zero,

$$p_{Cd} \simeq 0, \tag{9.13a}$$

$$p_{Te_2} \simeq 0. \tag{9.13b}$$

Eqs. (9.9) should therefore give an accurate representation of the mole fluxes.

The results of this experiment hinge on (9.13) and on a minimization of any background gases present in the sealed ampoule. In the experimental apparatus, (9.13) is ensured if the temperature of the cold finger is sufficiently low, such that $p_{sat}^{Cd(l)}(T_{cf}) = p_{sat}^{Cd(s)}(T_{cf}) = p_{sat}^{Cd}(T_{cf}) \simeq 0$ and $p_{sat}^{Cd(l)}(T_{cf}) = p_{sat}^{Cd(s)}(T_{cf}) = p_{sat}^{Cd}(T_{cf}) \simeq 0$. Fig. 9.7 gives the saturation pressure of near-stoichiometric CdTe as a function of temperature and composition. Depending of course on the temperature at which we choose to conduct our experiment, a cold finger under 700 K (427 °C) should effectively remove the Cd and Te_2 vapor from the ampoule. The formation of a liquid Te_2 or Cd phase is also possible, and the vapor pressure may be effected accordingly. Evidence of the condensation of a liquid phase will be evident on the transported material, so, as they say, we will cross that bridge when we get there.

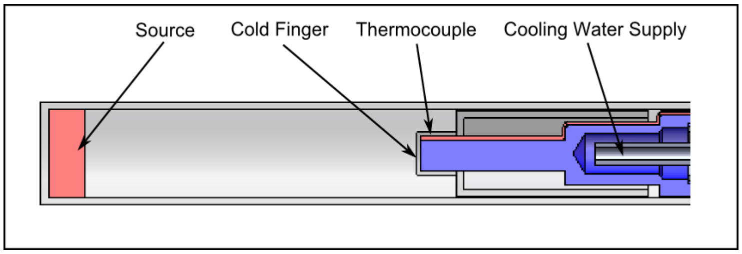

Figure 9.8: A schematic of the sealed ampoule used for the estimation of the sticking coefficient on CdTe.

9.2.3 Apparatus

A schematic of the apparatus is shown in Fig 9.8. The source will be placed at a sufficient distance from the cold finger so as to ensure its thermal isolation. This distance can be set arbitrarily to an upper limit of 100mm. As discussed previously, the cold finger must be maintained below 700 K; this temperature will be actively monitored by the thermocouple. The cold finger is cooled by cold water circulating at one end, as in Fig. 9.8. The whole ampoule can easilly be inserted and removed from the furnace, so heating and cooling can be imposed rapidly, thus reducing transient effects. The sealed ampoule will be made of fused-Quartz glass. The cold finger and thermocouple will be in thermal contact with the glass.The fused quartz ampoule will first be outgassed at a high temperature for a period and then sealed at approximately 150 °C under high vacuum using a hydrogen torch, this is similar to the procedure described in [100]. The background gas pressure should then not exceed 0.01 Pa.

9.2.4 Analysis

In order to measure the sticking coefficients on the CdTe surface, we must know the surface temperature T_s. This temperature is very difficult to measure. Instead, a model can be used to predict T_s based upon T_w.

To predict T_s, we recall the heat transfer schematic for the solid sample in Fig. 9.6. Heat is transported out of the crystal surface by the mole fluxes, and by radiative cooling from the cold finger. Heat flows to the interface by conduction through the ampoule walls and by radiation from the ampoule walls. To simplify this problem somewhat, the use of insulation in the furnace can isolate many of the heat fluxes, thus reducing the required model complexity. Furthermore, at least for a first order estimate, we may assume that the area of the cold finger is small enough that radiative cooling may be ignored. A schematic of this simplified heat transfer system is given in Fig. 9.9.

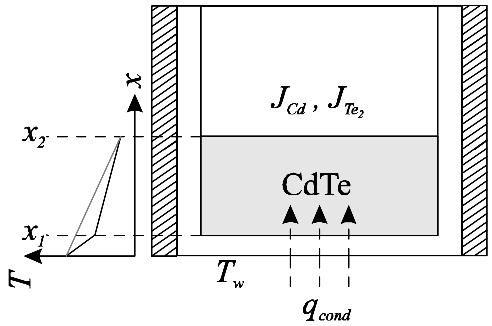

Figure 9.9: The simplified heat transport model. The walls of the ampoule are now insulated, so that heat is only transfered in through the bottom of the ampoule. The interface is radiatively cooled by the cold finger.

In the this scenario, the first law at the interface becomes

$$-\kappa_s \left.\frac{dT}{dx}\right|_{x=x_2} = J\Delta h \tag{9.14}$$

where we have Fourier's law for conduction in the solid. To model the conductive heat transport through the bulk solid, we recall (2.46) given as

$$\frac{d}{dx}\left\{JC_s\left[T\left(x\right)-T_{ref}\right]-\kappa_s\frac{dT}{dx}\right\} = \Lambda\left\{T_w(x)-T(x)\right\}. \tag{9.15}$$

Since the wall is insulated $T(x) \simeq T_w(x)$; the energy balance can be integrated to give

$$JC_s\left[T\left(x\right)-T_{ref}\right]-\kappa_s\frac{dT}{dx} = Q_0. \tag{9.16}$$

Here Q_0 is the heat transfer along the length of the solid, which, in the absence of other fluxes, remains constant along the length of the solid. This equation can be solved for $T(x)$ by using an integrating factor;

$$T(x) = C_8 \exp\left(\frac{JC_s}{\kappa_s}x\right) + \frac{Q_0 + JC_sT_{ref}}{JC_s}. \tag{9.17}$$

What remains are two unknowns, the integration constant C_8, and the unknown heat transport Q_0. Two boundary conditions are required. One is given by (9.14), for a second condition, we must assume a temperature at the edge of the solid. As a first estimate, we neglect discontinuity between the quartz glass and the solid, and instead use the distance averaged thermal conductivity

$$\kappa = \frac{x_1\kappa_q + x_2\kappa_{CdTe}}{x_1+x_2}. \tag{9.18}$$

where $\kappa_q = 3.5\,\mathrm{W/\,m\,K}$ [101]. The temperature profile is then continuous as shown in gray in Fig. 9.9. Thus, for a second boundary condition we assume

$$T\,(0) = T_w(0). \tag{9.19}$$

If J and T_w are known (from the experiment), (9.14) and (9.19) can be solved simultaneously for C_8 and Q_0, and T_s is obtained by

$$T(x_2) = T_s \tag{9.20}$$

Once T_s is known, the sticking coefficients can be obtained from (9.9).

9.2.5 Discussion

In the experiment, we control the imposed temperature T_w; we measure J_{Cd}. Once these are obtained, the sticking coefficient can be calculated using the model described. Fig. 9.10 gives the calculated sticking coefficient for each $T_w(0)$ and the corresponding rate of interface retreat in $\mathrm{mm/\,h}$, defined as

$$\dot{x} = \frac{J_{CdTe}}{c_{CdTe}}, \tag{9.21}$$

within our temperature range of interest, and the corresponding interface temperature. Not surprisingly, when the sticking coefficient is large, the sublimation rate is high, and limited by the amount of heat that can be supplied to the seed. Since we assume that the heat source temperature is fixed, the temperature of the interface must drop significantly when the transport rate is high, so that a sufficient amount of energy is transferred to the interface to maintain the sublimation rate. If the insulation were removed, more heat would be transferred to the interface and the result of the curves in Fig. 9.10 would all be altered. It is clear therefore that the accuracy of this experiment is dependent upon how well heat transport through the system is understood.

The results in Fig. 9.10 are calculated assuming the source material dissociates stoichiometrically ($\zeta = 2$). But according to [12], it is likely that the source material will exist over a range of ζ values, regardless of how pure the material is, due to the extreme sensitivity of ζ to the material composition. In Fig. 9.11 we show how the result of the experiment would be effected if the material were Te rich for $T_w(0)$ corresponding to Fig. 9.10. The sensitivity to off-stoichiometry of the sample is low; therefore, even if the sample is not perfectly stoichiometric, the experiment should still give useful results.

There is also the question of the quantity of material required for the experimental run, as material will inevitably become exhausted as the experiment proceeds. This actually introduces additional problems related to the moving interface in the problem. As the solid source sublimes, the interface will retreat.

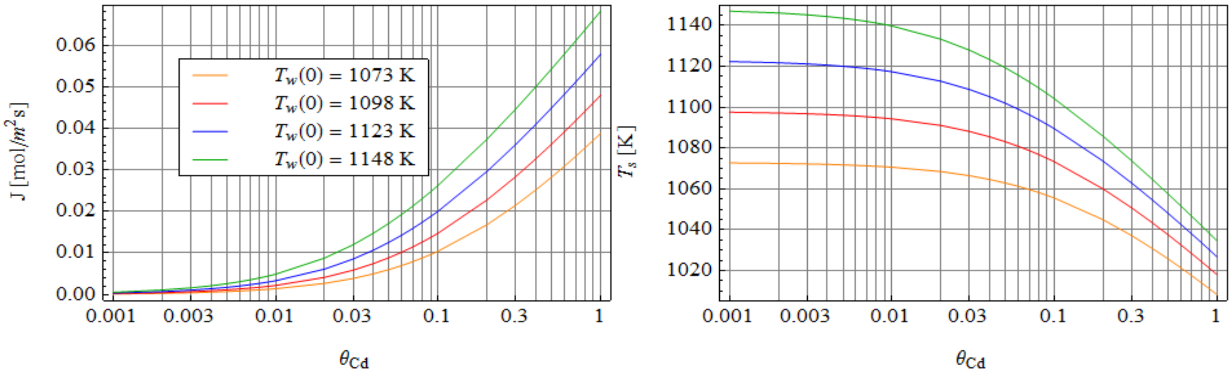

Figure 9.10: The predicted results of the experiment. The temperature $T_w(0)$ is controlled, $\dot{x}$ is measured and θ_{Cd} can be obtained from these. The corresponding interface temperature T_s is also given.

The thickness of the sample will decrease. This will cause the temperature of the interface T_s to rise, increasing the transport rate. Thus, if the transport rate is high, the data collected cannot be reliably used to measure the sticking coefficient. Fortunately, if Fig. 9.10 we show that the rates of retreat of the interface are slow for the temperatures selected, due to the limited amount of latent heat that can be supplied to the interface.

The intent of this experiment is to estimate the sticking coefficient of CdTe surfaces, we do not, at this point, require a high precision measurement. Indeed, due to uncertainties associated with the build up background gases as well as the constituent gas in the ampoule, the results will necessarily be uncertain with the type of apparatus described herein. If the sticking coefficient is found to be high, we can assume that the interfacial non-equilibrium is not especially important. If however, the sticking coefficient is found to be low, a more through investigation is recommended. This apparatus could be improved significantly if the growth vessel were semi-open, along the same lines at the Markov-Davydov system (see Chapter 1).

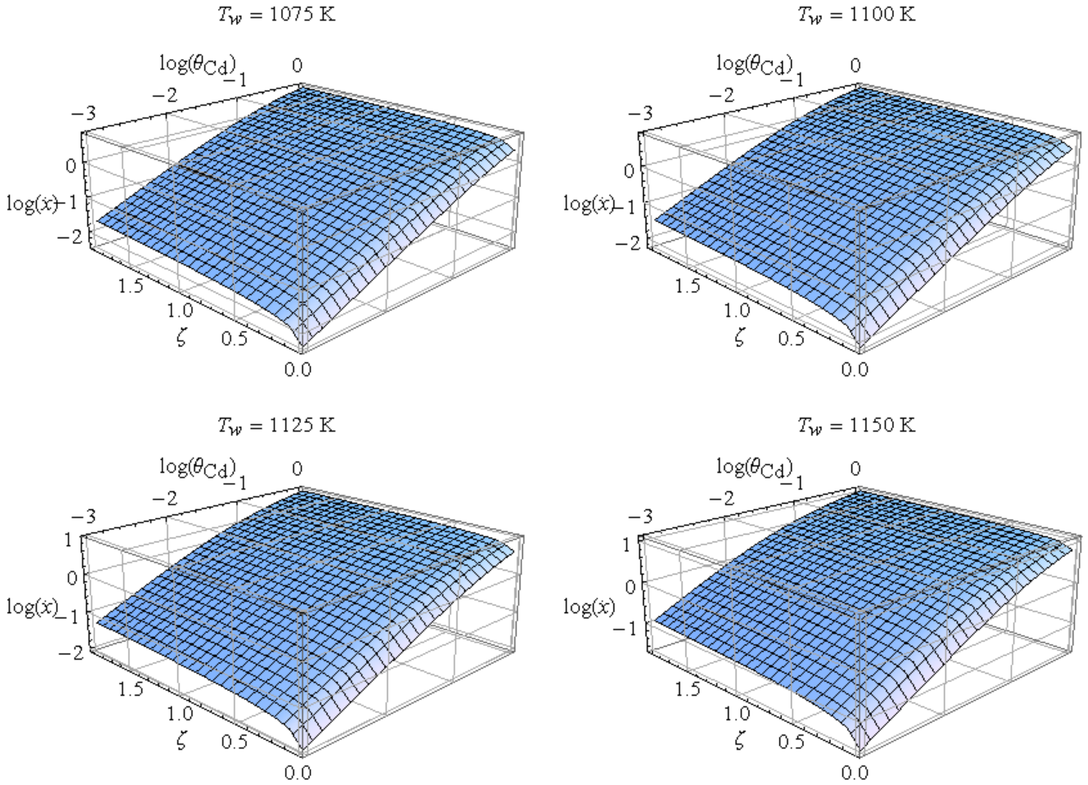

Figure 9.11: The sensitivity of the experimental result to the source ζ shown for Te rich compositions ($\zeta < 2$). For small deviations from stoichiometry ($0.1 < \zeta < 2$) the sensitivity is very low.

Chapter 10

Conclusions

In this thesis, a 1D heat and mass transport model was applied to CA-PVT crystal growth. Both equilibrium and non-equilibrium interface conditions were used. In this final chapter we discuss our findings.

10.1 Findings

The choice of interface conditions for PVT models depends upon the magnitude of the three main transport impedances in the system: the kinetic impedance, the thermal impedance and the diffusive impedance.

10.1.1 The kinetic impedance

The kinetic impedance is caused by the resistance of particles to transition between the vapor to the solid phases. This is governed by the phenomena of particle-surface interaction, adsorption and surface diffusion. The magnitude of the this impedance is inversely proportional to the temperature, and to the sticking coefficient(s). At lower temperatures, the vapor particles have a more difficult time transitioning between the solid and vapor phase; they require a harder push (i.e., a greater supersaturation). Non-equilibrium interface conditions can correctly incorporate the kinetic impedance into the model.

In single species transport of iodine, it was found that when the temperature is high, the kinetic impedance becomes small, even when the sticking coefficient is low. At lower temperatures, the impedance begins to play a more significant role, even when the sticking coefficient is high. Therefore, for iodine transport careful attention must be paid to the temperature of the system, as an equilibrium model is likely to become increasingly inaccurate at lower temperatures.

In the temperature range typically used for CdTe transport, it was found that the kinetic impedance is significant, even at the higher end of the typical temperature range and unity sticking coefficients.

10.1.2 The thermal impedance

The thermal impedance is the result of the exchange of latent heat at the interfaces. In condensation, this heat must be removed from the interface to maintain the transport. If more heat is removed, more material can release latent heat, and thus the mass transport rate increases. Therefore, the faster heat can be removed from the interface, the smaller the thermal impedance becomes. At the source interface, the latent heat is absorbed as molecules sublime. The faster heat can be supplied to the interface, the smaller the thermal impedance at the source becomes.

The thermal impedance is incorporated into the model through proper reference adjustment in the first law at the interfaces. So long as the model considers both the interphase heat and mass transport, the thermal impedance is included, regardless of the choice of interface conditions. The magnitude of the thermal impedance is not strongly dependent on the temperature, as the variation of the latent heat with temperature is small.

We found that the thermal impedance is important only when the diffusive and kinetic impedances are small. For situations where either of these is large, the thermal impedance can be neglected; this is commonly done in PVT models [9, 13, 5].

10.1.3 The diffusive impedance

The diffusive impedance is unique among the impedances in that it can be easily controlled. The magnitude of this impedance is directly proportional to the amount of background gas in the ampoule. In both the cases of I_2 and CdTe, the diffusive impedance becomes dominant roughly when the background or excess gas pressure exceeds the stoichiometric source saturation pressure of the active constituent(s).

10.1.4 Interplay between the impedances

The importance of each impedance is dictated by the conditions of the experiment. We propose the following guidelines:

1. The kinetic impedance is significant when the temperature of the interface is low, and/or when the sticking coefficient is low. The magnitude of this impedance can be easily found using the CKB model if the interface temperature and the sticking coefficient(s) are known.

2. The magnitude of the thermal impedance is determined by the latent heat of sublimation, and by the total convective and non-convective heat transport at the interface. As the mole transport rate increases, the thermal impedance increases as more latent heat is released. This impedance is

independent of the temperature of the interface, at least when Δh_{sv} is considered independent of temperature. However, it is strongly dependent on the temperature gradients at the interface; the steeper the temperature gradients, the faster the latent heat can be added or removed (as required). The importance of this impedance can only be determined in relation to the other impedances.

3. While the kinetic and thermal impedance depend upon the properties of the materials used, the diffusive impedance can be controlled directly in an experiment by setting the background gas pressure. When the background gas pressure is high enough, this impedance dominates over the others, and they can be effectively ignored. A large diffusive impedance makes it possible to model vapor transport between the interfaces without regard of the heat transport in the vapor and solid phases. This type of model is frequently seen in the literature.

The overall message here is that the transport impedances must be carefully analyzed before constructing a PVT model. A 1D model such as the one developed in the preceding is useful for such an analysis.

10.1.5 Temperature Jumps

When the CKB non-equilibrium interface model is used, temperature jumps in both directions are found in all four transport problems. These temperature jumps are the result of the non-convective heat flux across the interface. A positive temperature jump is found when the heat flows from the solid into the vapor and a negative jump is found when the heat flows from the vapor into the solid. These types of jumps have been experimentally observed at liquid-vapor interfaces [67, 16]. To our knowledge, temperature jumps at solid-vapor interfaces have not been measured. It is known that the CKB model underestimates the magnitude of temperature jumps at liquid-vapor interfaces [20]. This is likely the case at solid-vapor interfaces as well. In the equilibrium and CKB models, the solid interface temperatures were nearly identical for each solution; the temperature jumps affected the vapor phase much more strongly, and the difference between the equilibrium interface vapor temperature and CKB interface vapor temperature were significant.

10.2 Recommendations

Since our research group is mainly interested in the growth of binary and ternary semiconductor materials, these recommendations are made exclusively in the context of their growth; we leave iodine behind.

10.2.1 Further work with the 1D models

There remains additional work that should be done with 1D models. With some modification, the 1D models developed here could easily be extended to other vapor crystal growth techniques, such as the Markov-Davydov method, as done by Laasch et al. [17]. Additional features which we neglected but are worthy of further exploration are thermal diffusion, and the effects of surface energy (surface tension). The 1D models considered here have all been steady state models; as we discussed in Chapter 7, the steady state approach may not always be the best way to proceed. The incorporation of transient effects into the 1D model may be useful for capturing the entire lifecycle of an experimental run, and better predict the total mole flux. Finally, the 1D ternary transport (BTT) model could easily be extended to the growth of ternary semiconductor materials such as $\mathrm{Cd}_{1-n}\mathrm{Zn}_n\mathrm{Te}$.

Of additional interest is the stability of interfaces. It has been known for a long time that the constitutional supersaturation stability criterion we discussed briefly in Chapter 7 is inadequate for vapor crystal growth, as the conditions for stability are substantially stronger than what is actually observed in experiments [93]. The most detailed stability analysis of vapor growth was done for a single species by Louchev [75]. Louchev included the effects of the interface heat transport and surface kinetics as well as diffusive effects in the vapor into his stability model. Although the interface stability of CdTe has been studied experimentally [102, 103], the Louchev model has not been applied to interface stability in CdTe vapor growth. An important further step therefore is to couple the Louchev model with the CKB model to identify the optimal interface conditions for rapid, stable growth of CdTe.

10.2.2 2D and 3D Models

The limitations of 1D models are significant; firstly, while our 1D models were able to closely predict the mole fluxes under experimental conditions, they shed no light upon the ongoing evolution of the crystal shape. Furthermore, 1D models ignore heat and mass transfer by gravity driven convection. Both theoretical [11] and experimental [62] studies have shown that convective flows are significant in PVT, even under low pressure conditions. We therefore recommend the development of 2D and possibly 3D models [11] of binary and ternary PVT; some of this work has already been done by other groups [10].

It is clear from our analysis that in conditions under which rapid vapor growth of CdTe takes place, kinetic impedances play a significant role, even if the sticking coefficients for CdTe surface are high. Therefore, any 2D or 3D modelling should take these into account. The incorporation of the CKB interface model to 2D or 3D models should not be difficult, though obtaining stable numerical solutions with CKB interface conditions may be a significant challenge. The addition of a background gas or the modelling of non-stoichiometric compounds should damp out the kinetic impedance. This is an attractive approach to building these 2D or 3D models, as equilibrium interface conditions make it easier to obtain stable solutions. Ultimately though, to make these higher dimensional models useful for predicting actual high-speed (i.e. stoichiometric) vapor growth experiments, the full non-equilibrium boundary conditions should be used.

Finally, in this thesis, we predicted the presence of large temperature jumps under many conditions typically found in PVT. Though experimental confirmation is lacking, these temperature jumps will have a significant impact on the vapor temperature field predicted by 2D and 3D PVT models, as they do on the temperature field of the 1D model. It therefore would be very interesting to build 2D and 3D models both with and without the presence of temperature jumps to observe how the thermal field is affected. To our knowledge, no such analysis has been done for PVT.

10.2.3 Experimentation

The low hanging fruit in terms of experimentation is the experiment discussed in Chapter 9. The attempts to measure the sticking coefficients on CdTe surfaces have been limited; yet this information is critically important for selecting appropriate interface conditions for PVT models. We therefore recommend these experiments be conducted as the next logical step of this research.

In terms of growth techniques, the lack of repeatability and other problems associated with CA-PVT suggest that this technique is somewhat of a dead end in terms of progress in vapor crystal growth. Techniques such as the Markov-Davydov and Multi-Tube method have been much more successful in repeatedly producing high quality, stoichiometric CdTe crystals. Nevertheless, some of the highest growth rates of CdTe monocrystals have been observed in closed ampoules, though these experiments suffered from a lack of repeatability [99]. We recommend that the findings of the FVG experiment [18] be coupled with a vapor growth method that allows for the removal of impurities and excess constituent build up, such as the Markov-Davydov method so to see if the results of [18] could be reproduced reliably.

10.2.4 Cadmium Telluride Growth Optimization

Though the 1D model discussed here is limited in scope, we feel prepared to make some statements regarding the optimization of CdTe growth. We refer back to the phase diagram of CdTe in Fig. 1.14. To ensure the highest possible quality semiconductor material, we must ensure that the transported material is stoichiometric. The range of possible stoichiometry for CdTe reaches a maximum at approximately 1140 K and decreases rapidly below this temperature. Yellin and Szapiro [53] showed that the equilibrium pressure ratio is least sensitive to composition where the range of possible compositions is at a maximum. Therefore, a source temperature around 1140 K would increase the probability that the vapor itself is near stoichiometric. We wish to grow a stoichiometric sample of CdTe. Therefore, it makes sense to reduce the seed temperature significantly, so as to reduce the possible range of non-stoichiometry in the grown material.

In terms of maximizing the growth rate, it appears that stable growth of CdTe is possible even when the growth rate is very high, as in the FVG experiment [18]. Experimental evidence suggests that there is a point at which surface kinetics cannot keep up with the amount of material condensing upon the interface, and polycrystalline material is grown [103]. This is likely the effect of the surface diffusion not being able to keep up with the rate of condensation. Unfortunately, given that our stability analysis of the interface is incomplete, we are not prepared to give a recommend optimal conditions that maximize the growth rate in terms of interface stability at this time.

10.3 Contributions

In the course of this work, we have carefully examined the interplay between the kinetic, thermal and diffusive impedances in CA-PVT as outlined above. We have demonstrated that non-equilibrium interface effects can, under many common bulk vapor growth conditions, contribute significantly to limiting the mole transport. We have also demonstrated that theory predicts temperature jumps at solid-vapor interfaces resulting from the non-convective heat transfer across these interfaces. Furthermore, for the first time, we have coupled the Chapman-Enskog kinetic theory interface model with sublimating interfaces under bulk growth conditions using the framework of linear irreversible thermodynamics, as per the CKB model. The interface model developed in this work can now be used to determine interface conditions in 2D and 3D vapor growth models.

References

[1] A. Levi and M. Kotrla, “Theory and simulation of crystal growth,” *Journal of Physics: Condensed Matter*, vol. 9, pp. 299–344, 1997.

[2] W. Burton, N. Cabrera, and F. Frank, “The growth of crystals and the equilibrium structure of their surfaces,” *Transations of the Royal Society of London A*, vol. 243, pp. 299–358, 1951.

[3] I. Markov, *Crystal Growth for Beginners.* Singapore: World Scientific, 2003.

[4] J. Greenberg, “Vapor pressure scanning implications o cdte crystal growth,” *Journal of Crystal Growth*, vol. 197, pp. 406–412, 1999.

[5] C. Paorici and G. Attolini, “Vapour growth of bulk crystals by pvt and cvt,” *Progress in Crystal Growth and Characterization of Materials*, vol. 48-9, pp. 2–41, 2004.

[6] K. Benz, V. Babentsov, and M. Fiederle, “Growth of cadmium telluride from the vapor phase under low gravity conditions,” *Progress in Crystal Growth and Characterization of Mateirals*, vol. 48/49, pp. 189–208, 2004.

[7] E. Kaldis and M. Piechotka, *Handbook of Crystal Growth.* North-Holland, 1994, vol. 2a, ch. 11, pp. 615–656.

[8] A. W. Brinkman and J. Carles, “The growth of crystals from the vapour,” *Progress in Crystal Growth and Characterization of Materials*, vol. 37, pp. 169–209, 1998.

[9] M. Faktor and I. Garrett, *Growth of Crystals from The Vapour.* London: Chapman and Hall, 1974.

[10] M. Fiederle, K. W. Benz, A. Croll, A. Zappettini, D. Calestani, E. Dieguez, L. Carotenuto, and E. Bassano, “Deposition of cdte films under microgravity: Foton m3 mission,” *Crystal Research and Technology*, vol. 44, pp. 1059–1066, 2009.

[11] F. Rosenberger, J. Ouazzani, I. Viohl, and N. Buchan, “Physical vapor transport revisited,” *Journal of Crystal Growth*, vol. 171, pp. 270–287, 1997.

[12] W. Palosz and H. Wiedemeier, “Physical vapor transport of cadmium telluride in closed ampoules,” *Journal of Crystal Growth*, vol. 129, pp. 653–665, 1993.

[13] C. Paorici, C. Razzetti, M. Zha, L. Zanotti, L. Carotenuto, and M. Ceglia, “Physical vapour transport of urotropine: one-dimensional model,” *Materials Chemistry and Physics*, vol. 66, pp. 132–137, 2000.

[14] R. Ma, H. Zhang, V. Prasad, and M. Dudley, “Growth kinetics and thermal stress in the sublimation growth of silicon carbide,” *Crystal Growth and Design*, vol. 2, pp. 213–220, 2002.

[15] M. Faktor and I. Garrett, “Interplay of activation and diffusion in crystal growth from the vapour phase,” *Journal of Crystal Growth*, vol. 9, pp. 12–16, 1971.

[16] M. Bond and H. Struchtrup, “Mean evaporation and condensation coefficients based on energy dependent condensation probability,” *Physical Review E.*, vol. 70, p. 0610605, 2004.

[17] M. Laasch, T. Kunz, C. Eiche, M. Fiederle, W. Joerger, G. Kloess, and K. W. Benz, “Growth of twin-free cdte single crystals in a semi-closed vapour phase system,” *Journal of Crystal Growth*, vol. 174, pp. 696–707, 1997.

[18] H. Wiedemeier and G. Wu, “Fast vapor growth of cadmium telluride single crystals,” *Journal of Electronic Materials*, vol. 22, pp. 1121–1127, 1993.

[19] M. Bond, “Non-equilibrium evaporation and condensation,” Master’s thesis, University of Victoria, 2004.

[20] S. Kjelstrup and D. Bedeaux, *Non-Equilibrium Thermodynamics of Heterogeneous Systems.* Singapore: World Scientific, 2008.

[21] J. Cipolla, H. Lang, and S. Loyalka, *Rarified Gas Dynamics.* DFVLR-Press, 1974, ch. Vol. II, pp. F.4–1 to F.4–10.

[22] ——, “Kinetic theory of condensation and evaporation,” *Journal of Chemical Physics*, vol. 61, pp. 69–78, 1974.

[23] J. Mullins, J. Carles, N. Aitken, and A. Brinkman, “A novel multi-tube vapour growth system and its application to the growth of bulk crystals of cadmium telluride,” *Journal of Crystal Growth*, vol. 208, pp. 211–218, 2000.

[24] A. Pimpinelli and J. Villain, *Physics of Crystal Growth.* Cambridge University Press, 1998.

[25] J. Abernathey, D. Greenwell, and F. Rosenberger, “Congruent (diffusionless) vapor transport,” *Journal of Crystal Growth*, vol. 47, pp. 145–154, 1979.

[26] M. Faktor, R. Heckingbottom, and I. Garrett, “Growth of crystals from the gas phase. part i. diffusional limitations and interfacial stability in crystal growth by dissociative sublimation,” *Journal of the Chemical Society*, vol. A, pp. 2657–2664, 1970.

[27] N. Yellin and S. Szapiro, “Vapor transport of nonstoichiometric cdte in closed ampoules,” *Journal of Crystal Growth*, vol. 69, pp. 555–560, 1984.

[28] K. Grasza and W. Palosz, “Some aspects of pvt low-supersaturation nucleation and contactless crystal growth,” *Crystal Research and Technology*, vol. 34, pp. 565–571, 1999.

[29] L. Onsager, “Reciprocal relations in irreversible processes i.” *Physical Review*, vol. 37, pp. 405–426, February 1931.

[30] ——, “Reciprocal relations in irreversible processes II.” *Physical Review*, vol. 38, pp. 2265–2279, December 1931.

[31] S. de Groot and P. Mazuer, *Non-Equilibrium Thermodynamics.* Dover, 1984.

[32] R. Taylor and R. Krishna, *Multicomponent Mass Transfer.* Wiley, 1993.

[33] H. Ottinger, *Beyond Equilibrium Thermodynamics.* New Jersey: Wiley, 2005.

[34] G. Lebon, D. Jou, and J. Casas-Vazquez, *Understanding Non-Equilibrium Thermodynamics.* Berlin: Springer-Velag, 2008.

[35] C. Cercignani, *Rarefied Gas Dynamics From Basic Concepts to Actual Calculations.* Cambridge University Press, 2000.

[36] H. Struchtrup, *Macroscopic Transport Equations for Rarefied Gas Flows.* Springer, 2005.

[37] C. Cercignani, *Theory and Application of the Boltzmann Equation.* Scottish Academic Press, 1975.

[38] G. Bird, *Molecular Gas Dynamics and Simulation of Gas Flows.* Oxford: Clarendon Press, 1994.

[39] K. Kolasinski, *Surface Science: Foundations of Catalysis and Nanoscience.* Wiley, 2008.

[40] J. Caputa and H. Struchtrup, “Interface model for non-equilibrium condensation,” *Physica A*, vol. 390, pp. 31–42, 2011.

[41] I. Kuscer and M. Robnik, “Semi-microscopic description of evaporation and condensation,” *Journal of Physics A*, vol. 13, p. 621, 1980.

[42] I. Kuscer, “Reciprocity in scattering of gas molecules by surfaces,” *Surface Science*, vol. 25, p. 225, 1971.

[43] D. Askeland, *The Science and Engineering of Materials*, 3rd ed. PWS Publishing, 1994.

[44] W. Kossel, *Nachrichten der Gesellschaft der Wissenschaften Gttingen, Mathematisch-Physikalische Klasse.* Band, 1927, p. 135.

[45] I. Stranski, “Zur theorie des kristallwachstums,” *Zeitschrift fr Physikalische Chemie*, vol. 136, pp. 259–278, 1928.

[46] G. Iche and P. Nozires, “A simple stochastic description of desorption rates,” *Le Journal de Physique*, vol. 37, pp. 1313–1323, 1976.

[47] G. Antczak and G. Ehrlich, “Jump processes in surface diffusion,” *Surface Science Reports*, vol. 62, pp. 39–61, 2007.

[48] P. Bennema and C. V. Leeuwen, “Crystal growth from the vapour phase: confrontation of theory with experiment,” *Journal of Crystal Growth*, vol. 31, pp. 3–19, 1975.

[49] H. Neureiter, S. Schinzer, W. Kinzel, S. Tatarenko, and M. Sokolowski, “Simultaneous layer-by-layer and step-flow sublimation on the cdte(001) surface derived from a diffraction analysis,” *Physical Review B*, vol. 61, pp. 5408–5415, 2000.

[50] D. Bloor and R. W. Cahn, *The Encyclopedia of advanced materials*, 1st ed. Oxford, England ; Tarrytown, N.Y.: Pergamon, 1994.

[51] C. Kittel, *Introduction to Solid State Physics*, 7th ed. Wiley, 1995.

[52] Y. Tanigaki, Y. Kimura, H. Suzuki, and C. Kaito, “Direct observation of sublimation process on a cdte(111) surface using an ultrafine particle,” *Journal of Crystal Growth*, vol. 260, pp. 298–303, 2004.

[53] N. Yellin and S. Szapiro, “Calculation of the partial vapor pressures of tellurium and cadmium over non-stoichiometric cdte in the temperature range 750-1050c,” *Journal of Crystal Growth*, vol. 73, pp. 77–82, 1985.

[54] J. Greenberg, “P-t-x phase equilibrium and vapor pressure scanning of non-stoichiometry in cdte,” *Journal of Crystal Growth*, vol. 161, pp. 1–11, 1996.

[55] S. Sze and K. Ng, *Physics of Semiconductor Devices*, 3rd ed. New Jersey: Wiley-Interscience, 2007.

[56] Y. Cengel and M. Boles, *Thermodynamics, An Engineering Approach*, 4th ed. McGraw Hill, 2002.

[57] I. Muller, *Thermodynamics.* Pitman Advanced Publishing Program, 1985.

[58] R. Aris, *Vectors, Tensors and the Basic Equations of Fluid Mechanics.* New York: Dover, 1989.

[59] R. Bird, W. Stewart, and E. Lightfoot, *Transport Phenomena*, 2nd ed. New Jersey: Willey, 2002.

[60] F. Incropera, D. DeWitt, T. Bergman, and A. Lavine, *Fundmentals of Heat and Mass Transfer*, 6th ed. Wiley, 2007.

[61] B. Poling, J. Prausnitz, and J. O'Connell, *The Properties of Gasses and Liquids.* McGraw Hill, 2001.

[62] M. Piechotka, E. Kaldis, G. Wetzel, and A. Flisch, "Kinetics of physical vapour transport at low pressure under microgravity conditions ii. results of the dcmf space experiment," *Journal of Crystal Growth*, vol. 193, pp. 90–100, 1998.

[63] T. Ytrehus, "Molecular-flow effects in evaporation and condensation at interfaces," *Multiphase Science and Technology*, vol. 9, pp. 205–327, 1997.

[64] J. Delhaye, "Jump conditions and entropy sources in two-phase systems." *International Journal of Multiphase Flow*, vol. 1, pp. 395–409, 1974.

[65] S. Lowell, J. Shields, and M. Thommes, *Characterization of Porous Solids and Powders: Surface Area, Pore Size and Density.* Kluwer Academic Publishers, 2004.

[66] T. Tsuruta, H. Tanaka, and T. Masuoka, "Condensation/evaporation coefficient and velocity distributions at liquid-vapor interface," *International Journal of Heat and Mass Transfer*, vol. 42, pp. 4107–4116, 1999.

[67] C. Ward, "Liquid-vapor phase change rates and interfacial entropy production," *Journal of Non-Equilibrium Thermodynamics*, vol. 27, no. 3, pp. 289–303, 2002.

[68] P. Raback, "Modeling of the sublimation growth of silicon carbide crystals," Ph.D. dissertation, Helsinki University of Technology, 1999.

[69] A. Zangwill, *Physics at Surfaces.* Canbrudge University Press, 1988.

[70] H. Hertz, "Ueber die verdunstung der flussigkeiten, insbesondere des quecksilbers, im luftleeren raume," *Annalen der Physik und Chemie*, vol. 17, pp. 177–200, 1882.

[71] M. Knudsen, “Die maximale verdampfunggeschwindigkeit des quecksilbers,” *Annalen der Physik und Chemie*, vol. 47, pp. 697–708, 1915.

[72] P. Tempest and D. Ballentyne, “Supersaturation control in crystal growth of ii-vi componds for the vapour,” *Journal of Crystal Growth*, vol. 21, pp. 219–226, 1974.

[73] D. Ballentyne and L. Rouse, “The growth of cadmium sulphide from the vapour phase - surface kinetics,” *Journal of Crystal Growth*, vol. 39, pp. 231–240, 1977.

[74] T. Ytrehus, “Theory and experiments on gas kinetics in evaporation,” *Rarefied Gas Dynamics*, vol. 51, no. 2, pp. 1197–1212, 1977.

[75] O. Louchev, “Diffusion, heat transfer, equilibrium molecular density and kinetic mechanism of morphological instability in physical vapor deposition,” *Journal of Crystal Growth*, vol. 140, pp. 216–236, 1994.

[76] R. W. Schrage, *A Theoretical Study of Interphase Mass Transfer.* New York: Columbia University Press, 1953.

[77] J. Barrett and C. Clement, “Kinetic evaporation and condensation rates and their coefficients,” *Journal of Colloid and Interface Science*, vol. 150, no. 2, pp. 352–364, May 1992.

[78] D. Labuntsov, “An analysis of intensive evaporation and condensation,” *High Temperature (English Translation)*, vol. 5, pp. 579–647, 1967.

[79] A. Waag, T. Bher, T. Litz, B. Kuhn-Heinrich, D. Hommel, and G. Landwehr, “Rheed stuides of mbe growth mechanisms of cdte and cdmnte,” *Materials Science and Engineering*, vol. B16, pp. 103–107, 1993.

[80] M. Gauthier, Ed., *Engineered materials handbook.* Ohio: ASM International, 1995.

[81] J. Butler, “The thermal decomposition of octafluorocyclobutane,” *Journal of the American Chemical Society*, vol. 84, pp. 1393–1398, 1962.

[82] D. Shirley and W. Giauque, “The entropy of iodine. heat capacity from 13 to 327 k. heat of sublimation,” *Journal of the American Chemical Society*, vol. 81, pp. 4778–4779, 1959.

[83] A. Nesmeyanov, *Vapor pressure of the chemical elements*, R. Gary, Ed. Elsevier Publishing Company, 1963.

[84] (2010, November) Air liquide gas encyclopedia - octafluorocyclobutane. Air Liquide. [Online]. Available: http://encyclopedia.airliquide.com

[85] D. Palmer. (2010) Semiconductor information. [Online]. Available: http://www.semiconductors.co.uk

[86] H. Ouyang and W. Shyy, "Numerical simulation of cdte vertical bridgman growth," *Journal of Crystal Growth*, vol. 173, pp. 352–356, 1997.

[87] A. Malkova, V. Zharov, G. Shmoilova, and A. Pashinkin, "Specific heat of zinc andcadmium tellurides in the range 360-760k," *Russian Journal of Physical Chemistry*, vol. 63, pp. 21–22, 1989.

[88] B. DeLargy, A. Finch, and P. Gardner, "Thermodynamic functions for the congruant sublimation of cadmium telluride," *Journal of Crystal Growth*, vol. 61, pp. 194–198, 1983.

[89] (2010, November) Wolfram mathematica 7 documentation. [Online]. Available: http://reference.wolfram.com/mathematica/guide/Mathematica.html

[90] Q. Chen, H. Zhang, and V. Prasad, "Modeling of heat transfer and kinetics of physical vapor transport growth of silicon carbide crystals," *Journal of Heat Transfer*, vol. 123, pp. 1098–1110, 2001.

[91] F. White, *Fluid Mechanics*, 6th ed. McGraw Hill, 2008.

[92] T. Reed, W. LaFleur, and A. Strauss, "Diffusion and convection in vapor crystal growth," *Journal of Crystal Growth*, vol. 3/4, pp. 115–121, 1968.

[93] F. Rosenberger, M. Delong, D. Greenwell, J. Olson, and G. Westphal, "Constitutional supersaturation revisited," *Journal of Crystal Growth*, vol. 29, pp. 49–54, 1975.

[94] K. Mochizuki, "Effect of the deviation from stoichiometry of a source specimen on the vapor transport of cdte," *Journal of Crystal Growth*, vol. 51, pp. 453–456, 1981.

[95] Y. Wu, C. Becker, A. Waag, K. von Schierstedt, R. Bicknell-Tassius, and G. Landwehr, "Surface sublimation of zinc blende cdte," *Applied Physics Letters*, vol. 62, pp. 1510–1512, 1993.

[96] H. Wiedemeier and G. Wu, "Defects in cdte single crystals grown by very fast vapor growth technique," *Journal of Electronic Materials*, vol. 24, pp. 1007–1015, 1995.

[97] W. Palosz and H. Wiedemeier, "Residual gas pressures in sealed fused silica glass ampoules," *Journal of Crystal Growth*, vol. 131, pp. 193–198, 1993.

[98] W. Palosz, "Residual gas in closed systemsi: development of gas in fused silica ampoules," *Journal of Crystal Growth*, vol. 267, pp. 475–483, 2004.

[99] ——, “Personnal communication,” November 2010, email exchange.

[100] F. Rosenberger, J. Olson, and M. Delong, “A gas handling system for extacting crystal growth preparations,” *Journal of Crystal Growth*, vol. 47, pp. 321–325, 1979.

[101] W. Wolfe and G. Zissis, *The Infrared Handbook.* Washington: Office of Naval Research, Dept. of the Navy, 1985.

[102] K. Grasza and A. Jdrzejczak, “Growth stability in high temperature vapour growth,” *Journal of Crystal Growth*, vol. 162, pp. 173–177, 1996.

[103] K. Grasza, “A stability diagram for crystal growth from the vapor - a review,” *Crystal Research and Technology*, vol. 42, pp. 1202–1206, 2007.